COMPUTATIONAL INSIGHTS OF CATALYTIC CARBON DIOXIDE VALORIZATION AND CIRCULAR RECYCLING PROCESSES

Alba Villar Yanez

UNIVERSITAT ROVIRA i VIRGILI

Computational Insights of Catalytic Carbon Dioxide Valorization and Circular Recycling Processes

Alba Villar Yanez

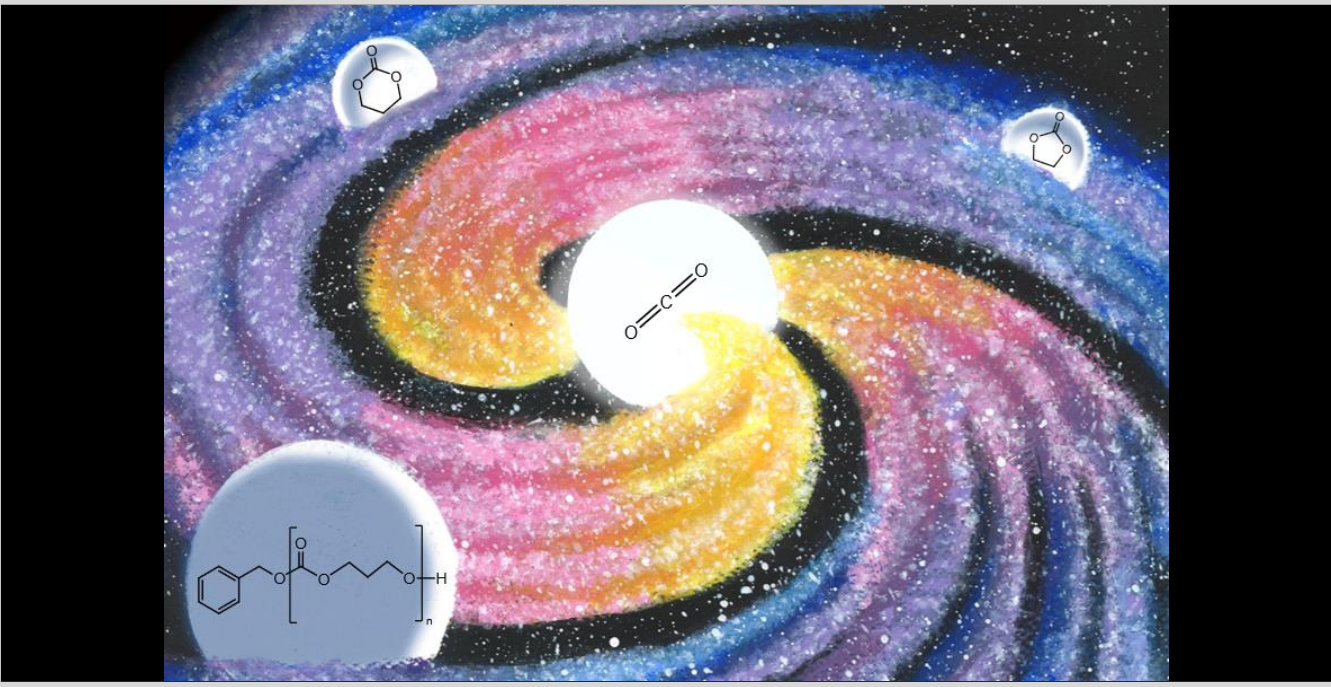

DOCTORAL THESIS
2024

UNIVERSITAT ROVIRA I VIRGILI
COMPUTATIONAL INSIGHTS OF CATALYTIC CARBON DIOXIDE VALORIZATION AND CIRCULAR RECYCLING PROCESSES
Alba Villar Yanez

Alba Villar Yanez

Computational Insights of Catalytic Carbon Dioxide Valorization and Circular Recycling Processes

Doctoral Thesis

Supervised by Prof. Arjan W. Kleij and Prof. Carles Bo Jané

Tarragona

2024

UNIVERSITAT ROVIRA I VIRGILI
COMPUTATIONAL INSIGHTS OF CATALYTIC CARBON DIOXIDE VALORIZATION AND CIRCULAR RECYCLING PROCESSES
Alba Villar Yanez

UNIVERSITAT ROVIRA i VIRGILI

ICIQ Institut Català d'Investigació Química

Prof. Dr. Arjan W. Kleij, Group Leader at the Institute of Chemical Research of Catalonia (ICIQ) and Research Professor at the Catalan Institution for Research and Advanced Studies (ICREA) and Prof. Dr. Carles Bo i Jané, Group Leader at the Institute of Chemical Research of Catalonia (ICIQ) and professor at Universitat Rovira i Virgili (URV):

WE STATE that the present study, entitled "**Computational Insights of Catalytic Carbon Dioxide Valorization and Circular Recycling Processes**", presented by Alba Villar Yanez for the award of the degree of Doctor, has been carried out under our supervision at the Institute of Chemical Research of Catalonia (ICIQ).

Tarragona, May 2024

Doctoral Thesis Supervisor/s:

Arjan Willem Kleij - DNI X8048279G (TCAT)
Digitally signed by Arjan Willem Kleij - DNI X8048279G (TCAT)
Date: 2024.05.30 08:20:23 +02'00'

Carles Bo Jané
29 May 2024 17:32:36 CEST
Certificat emès per: EC-SectorPublic
Número de serie: 837732019611299763846668177670313345 72
Fundació Institut Català d'Investigació Química (ICIQ)

Prof. Dr. Arjan W. Kleij

Prof. Dr. Carles Bo i Jané

UNIVERSITAT ROVIRA I VIRGILI
COMPUTATIONAL INSIGHTS OF CATALYTIC CARBON DIOXIDE VALORIZATION AND CIRCULAR RECYCLING PROCESSES
Alba Villar Yanez

Funding

The work presented in this Ph.D. thesis has been funded by the Institute of Chemical Research of Catalonia (ICIQ) and by a FPI grand (PRE2018-083947) from the Spanish Ministry of Science and Innovation.

UNIVERSITAT ROVIRA I VIRGILI
COMPUTATIONAL INSIGHTS OF CATALYTIC CARBON DIOXIDE VALORIZATION AND CIRCULAR RECYCLING PROCESSES
Alba Villar Yanez

Acknowledgments

En primer lloc vull agrair als meus supervisors Arjan W. Kleij i Carles Bo Jané la paciència i dedicació que he rebut al llarg d'aquests anys. Ha estat un plaer formar part dels vostres equips ja que he pogut aprendre moltes coses que sens dubte formen part de la meva riquesa personal.
En segon lloc vull donar les gràcies a tots els meus companys de l'ICIQ, res hagués estat el mateix sense vosaltres, em sento molt afortunada d'haver-vos conegut i que formeu part de la meva vida. I que malgrat viure a ciutats diferents, haguem pogut compartir tants riures, festes, converses i moments de tot tipus. Gràcies per tot el suport i alegries que m'heu donat al llarg d'aquesta etapa, sou genials. En especial vull agraïr als meus companys i ex-companys de grup (Hartree-Foca): Aleix, Diego, Enric P., Jordi B., Marco, Mireia. I també al Martin, Moisés, Núria Vendrell i l'Ingrid per solucionar-me tots els problemes informàtics i gestions. Al grup de computacionals anomenats "Gnus": Albert S.R., Albert S.D., Andrea, Bruna, Enric I., Isabel, Javier, Jordi M., José Manuel, Julian, Lucía, Marina, Oliver, Pavle, Raúl, Sara, Santiago i Sergio. I als meus companys i ex-companys experimentals del grup Kleij: Alèria, Alejandro, Àlex, Arianna, Balázs, Bart, Chang, Chenyang, Cristina, David, Debasish, Enrico, Francesco, Fengyun, Jianing, Jixiang, Kun, Matteo, Nicola, Qian, Sijing, Thiru, Wangyu i Xuetong.

I am very grateful to my Amsterdam internship supervisor, Bernd Ensing. Thank you for making me feel comfortable during these months; I've learned a lot at UvA. I also want to thank Adam, Albert S.D., Alberto, Alwan, Ashique, Bernadette, Daria, Eline, Ferry, Hannah, Jacobus, Lingshu, Longjiao, Lucas, Massimiliano, Rahavendra, Tamika, Thor, Toon, and Yingying.

La música és una part essencial de la meva vida i cantar a l'Orfeó Català és un privilegi que em permet expressar la meva creativitat. Però encara és millor quan tinc companys que fan que els assajos, concerts i gires siguin molt millors. Gràcies per alegrar-me les tardes i gràcies per interessar-vos pel meu

benestar durant la meva tesi. En especial a la Raquel, Marina, Núria i Maria.

No podien faltar els agraïments per tu, Èric. Que has tingut tota la paciència del món, m'has cuidat, m'has donat suport i has fet que els meus pitjors dies fossin millors. Gràcies per tot l'amor que em dones cada dia, per estar sempre al meu costat i per estimar-me com ho fas.
Finalment, vull donar les gràcies a la meva família i als meus amics, m'heu animat sempre, m'heu donat suport i m'heu fet sentir molt estimada. Vull dedicar aquesta tesi als meus avis, que malgrat ja no hi són, sempre m'han encoratjat a aprendre, lluitar per la vida i seguir sempre endavant. Sé que els ompliria d'orgull saber que he arribat fins on he arribat. Sempre els duré al meu cor.

List of publications

1. **Organocatalytic Trapping of Elusive Carbon Dioxide Based Heterocycles by a Kinetically Controlled Cascade Process**, Chang Qiao, Alba Villar-Yanez, Josefine Sprachmann, Bart Limburg, Carles Bo, Arjan W. Kleij, *Angewandte Chemie International Edition* (2020), 59, 18446 – 18451
   DOI: 10.1002/anie.202007350

2. **Cascade Transformation of Carbon Dioxide and Alkyne-1,*n*-diols into Densely Substituted Cyclic Carbonates**, Xuetong Li*, Alba Villar-Yanez*, Charlene Ngassam Tounzoua*, Jordi Benet-Buchholz, Bruno Grignard, Carles Bo, Christophe Detrembleur, and Arjan W. Kleij, *ACS Catalysis* (2022), 12, 5, 2854–2860
   DOI: 10.1021/acscatal.1c05773
   **[equal contribution]*

3. **Bicyclic Guanidine Promoted Mechanistically Divergent Depolymerization and Recycling of a Biobased Polycarbonate**, David H. Lamparelli*, Alba Villar-Yanez*, Lorenz Dittrich, Jeroen Rintjema, Fernando Bravo, Carles Bo, Arjan W. Kleij, *Angewandte Chemie International Edition*, (2023) 62, e202314659
   DOI: 10.1002/anie.202314659
   **[equal contribution]*

Publications non-related with the thesis

4. **Ni-Catalyzed Decarboxylative Silylation of Alkynyl Carbonates: Access to Chiral Allenes via Enantiospecific Conversions**, Kun Guo, Qian Zeng, Alba Villar-Yanez, Carles Bo, and Arjan W. Kleij, *Organic Letters*, (2022), 24, 2, 637–641
   DOI: 10.1021/acs.orglett.1c04086

5. **Domino Synthesis of Bicyclic 3,5-Anhydro Furanose Mimics Using a Binary Al(III) Complex/Halide Catalyst**, Chang Qiao, Alba Villar-Yanez, Diego Garay-Ruiz, Jordi-Benet Buchholz, Carles Bo, and Arjan W. Kleij, *ACS Catalysis* (2022), 12, 9, 5464–5469
DOI: 10.1021/acscatal.2c00925

List of Abbreviations

In this doctoral thesis, the abbreviations and acronyms most commonly used in organic chemistry are based on the recommendations of the ACS "Guidelines for authors". Additional abbreviations are listed below:

ACN	Acetonitrile
APC	Aliphatic Polycarbonates
AROP	Anionic Ring-Opening Polymerization
BnOH	Benzyl Alcohol
CO_2	Carbon Dioxide
DFT	Density Functional Theory
GPC	Gel Permeation Chromatography
HF	Hartree-Fock
LC	Limonene carbonate
LO	Limonene oxide
MD	Molecular Dynamics
NMR	Nuclear Magnetic resonance
PES	Potential Energy Surface
PLC	Poly(limonene carbonate)
ROCOP	Ring-Opening Copolymerization
ROP	Ring-Opening Polymerization
TBD	1,5,7-Triazabicyclo[4.4.0]dec-5-ene
TOF	Turnover Frequency
TS	Transition State
5MCC	Five-Membered cyclic carbonate
6MCC	Six-Membered cyclic carbonate
7MCC	Seven-Membered cyclic carbonate
8MCC	Eight-Membered cyclic carbonate

UNIVERSITAT ROVIRA I VIRGILI
COMPUTATIONAL INSIGHTS OF CATALYTIC CARBON DIOXIDE VALORIZATION AND CIRCULAR RECYCLING PROCESSES
Alba Villar Yanez

Abstract

Two of the major environmental challenges in today's society are CO_2 emissions and waste management surrounding plastics. The inability to properly recycle plastic materials (polymers) not only creates pollution issues related to microplastics present in our eco-systems, but also directly relates to the carbon emitted causing a major impact on global warming and climate change.

It is thus essential to create new strategies to reduce these negative effects, and chemistry offers a tool to access polymers using circular economy principles, which utilize CO_2 as a reactant. This minimizes our dependency on fossil fuels, while new types of monomers can be made from CO_2 (cyclic carbonates) used to produce degradable polymers within a circular economy approach.

This thesis focuses on computational analysis (DFT) of CO_2 valorization/recycling processes through homogeneous catalysis, and creating a predictive reactivity model. In each chapter, I studied a specific part of process circularity or CO_2 recycling, starting with the conversion of CO_2 into five-membered cyclic carbonates from alkyne-1,2-diols using a Ag catalyst. Then, the creation of larger-ring carbonates (six-membered) from smaller ones is presented via a unique organocatalytic strategy. As these cyclic carbonates can be used as monomers, though not in all cases, I conducted an extensive study of the Ring-Opening Polymerization (ROP) reaction of cyclic carbonates using BnOH as initiator and an organocatalyst. This exploration led to defining a main ROP pathway for a wide range of monomers and model that can predict the polymerization ability of a monomer. Finally, I studied the organocatalyzed depolymerization of a polycarbonate, that selectively breaks down the polymer into a trans-cyclic carbonate, or an epoxide and CO_2. This ultimate study provides deep insights for CO_2 valorization, complemented by experimental results offering a more complete view on how to effective convert and recycle CO_2 within a circular approximation.

UNIVERSITAT ROVIRA I VIRGILI
COMPUTATIONAL INSIGHTS OF CATALYTIC CARBON DIOXIDE VALORIZATION AND CIRCULAR RECYCLING PROCESSES
Alba Villar Yanez

Contents

UNIVERSITAT ROVIRA I VIRGILI
COMPUTATIONAL INSIGHTS OF CATALYTIC CARBON DIOXIDE VALORIZATION AND CIRCULAR RECYCLING PROCESSES
Alba Villar Yanez

CHAPTER

1 Introduction

1.1 Climate change and CO_2 problems

Carbon dioxide (CO_2) is a linear gaseous molecule present in the atmosphere as one of its main components. This gas is vital for maintaining Earth's habitable conditions as it can absorb infrared radiation. The amount of CO_2 in the atmosphere directly affects the greenhouse effect also known as global warming.

According to the sixth assessment report by the Intergovernmental Panel on Climate Change (IPCC), emissions of greenhouse gases from human activities are responsible for about 1.11°C of global warming since the beginning of the 20^{th} century. These activities include for example the burning of coal, oil and gas, deforestation and farming. A study made by the European Environment Agency (EEA) in 2019[1,2], describes that the most emitted greenhouse gas is CO_2 (around 80%), followed by methane (CH_4, 11%), nitrous oxide (N_2O, 6%) and hydrofluorocarbons (HFCs, 2%). Despite the fact that other greenhouse gases are emitted in smaller amounts, they are much more effective at trapping heat compared to CO_2. For example, methane is above 80 times more potent than CO_2.

A 2019 study reported by the EEA describes that the main origin for the gas emissions is in the energy sector (77%), while agriculture contributes with 10.6%, industrial processes and products emit 9.1% and waste management another 3.3%.

1.1.1 Circular Recycling Processes

The circular economy is a sustainable model based on three principles: Reduce, Reuse and Recycle. The idea is to minimize the use of raw materials and reducing waste through efficient processes and technologies, and extend the life cycle of products and recover materials from end-of-life products by reusing them[3].

The international community has recognized that the principal phenomenon responsible for global warming is the accumulation of carbon dioxide (CO_2) emissions in the atmosphere. Consequently, the greenhouse effect is increased,

causing the Earth's atmosphere to become warmer, leading to global warming and its associated adverse impacts. Therefore, the main challenge is to create sustainable methods for reducing greenhouse gas emissions and using CO_2 as a renewable carbon resource in the chemical industry to mitigate climate change. To reach this goal some strategies have been developed such as CO_2 capture and storage (CCS) and CO_2 capture and usage (CCU). CCS is the principal method to reduce the CO_2 in the environment through long-term storage. However, CCU is particularly promising because involves the chemical conversion of CO_2 into high value products, such as organic molecules or polymers. Another problem is plastic waste and recycling, only a third part of the plastic waste in Europe is recycled while around 25% is landfilled. At a global level, experts estimate that in 2019, over 850 million tonnes of greenhouse gases were released into the atmosphere due to the manufacturing and burning of plastic. Therefore, the European Union is looking for solutions involving circular recycling processes of plastics.

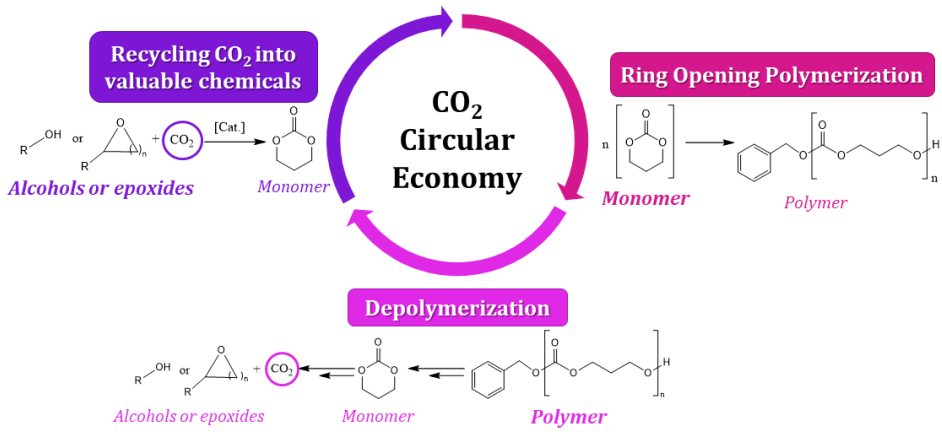

Figure 1.1: Circular recycling of CO_2 considered in this thesis. 1. Synthesis of cyclic carbonates from CO_2 from alcohols or epoxides. 2. Use cyclic carbonates as a monomers to obtain polycarbonates via Ring-Opening Polymerization reaction. 3. Depolymerization of polycarbonates into its precursors (monomers or CO_2 + alcohols or epoxides)

Taking into account these concepts, one example of non-reductive approaches to use CO_2 is the synthesis of cyclic carbonates. These molecules can be typically prepared from epoxides, halohydrins, or propargyl alcohols

with CO_2 as a co-reactant. The cyclic carbonates can be used as monomers to produce polymers that can be depolymerized into its precursors as a prime example of circular economy of CO_2 (**Figure 1.1**). Furthermore, this process creates polymers (plastic ingredients) that can be easily depolymerized into their corresponding monomers or epoxides and CO_2 using a catalyst, thereby reducing the greenhouse gas emissions associated with plastic recycling.

1.2 The importance of Chemistry and Catalysis

Chemistry is everywhere, it is present in every aspect of our daily lives, from the food we consume, the medicines we take to, the materials we use, and the environment we live in. This field of science studies the properties and behaviour of the substances, which are all made by the combination of atoms in the periodic table. "There are just over a hundred kinds of chemical atoms, corresponding to the different kinds of chemical elements, but their possible and actual combinations are so many as to seem infinite"[4] (*T. H. Levere, 2001*).

The ubiquitous nature of chemistry means that it is crucial towards developing new products and technologies that improve our quality of life. However, the production and disposal of chemicals can also result in environmental pollution, health hazards, and resource exhaustion. Maintaining a balance between the benefits and disadvantages of chemistry is a continuous challenge that requires ongoing research and responsible practices in order to obtain the benefits of chemical innovations while minimizing their negative impacts on health and the environment. "Many of the necessities for our crowded planet are made possible by the application of chemistry. Many of the problems that we have created while providing those necessities are also tied to chemistry, and so too will be their solutions"[4] (*T. H. Levere, 2001*).

A catalyst is defined as a "substance that increases the rate of a chemical reaction without itself undergoing any permanent chemical change"[5] (*Atkins et al., 2008*). The catalyst decreases the activation barrier of the reaction providing an alternative path for the slowest rate determining step for the noncatalyzed

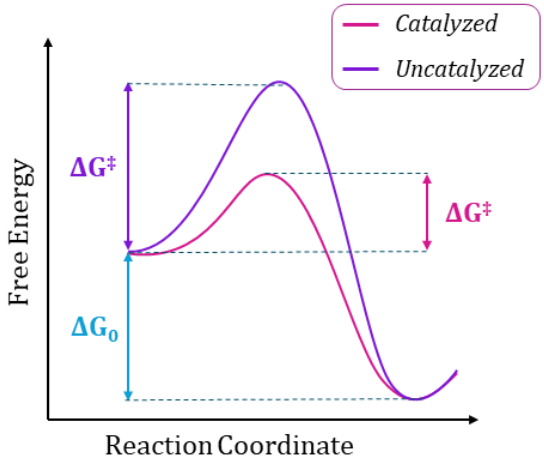

Figure 1.2: Example of free energy profile for a catalyzed and uncatalyzed chemical reaction

reaction (**Figure 1.2**) without being consumed in the process. Moreover, catalysts can also enable alternative reactions that would not be obtained under other conditions, offering a powerful level of control over the chemical process.

Catalysis processes are traditionally classified in three different areas[5]:

- **Homogeneous catalysis**: The reactants and the catalyst are in the same physical phase (usually a liquid one)[6]. Therefore, the catalyst is uniformly distributed throughout the reaction mixture making it more prone to react. Other advantages are the catalyst ability towards high selectivity when interacting with specific molecules, and the relative ease (compared with heterogeneous catalysis) of studying reaction mechanisms and kinetics as all reaction molecules are in the same phase. The disadvantages are connected to the lack of catalyst separation from the mixture, which often is challenging, and the lower stability of the catalyst compared with heterogeneous ones, limiting in that way its reusability.

  - Enzymatic catalysis: Enzymes are biological homogeneous catalysts. These molecules (usually proteins) have an active site where the substrate is prone to be bound and undergo the reaction[7]. Enzymes are

highly specific, biodegradable and non-toxic, reducing the environmental impact and the catalytic reactions typically occur under mild conditions. However, they are expensive to produce and purify, are limited to pre-set environmental conditions that, if altered, lowers their reaction efficacy, and have limited stability over time and requiring thus specific storage conditions.

- **Heterogeneous catalysis**: The reactants (usually gases or compounds distributed in a solvent) and the catalyst (usually a solid components) are in different phases[8]. The main advantages are catalyst recovery, the application of continuous and large-scale industrial processes, and the reusability of heterogeneous systems that are often more stable than homogeneous ones making them more cost-effective within industrial environments. However, only the atoms in contact with the reactants are active and therefore, their efficiency heavily relies on the characteristics of the surface layer. Due to this behaviour, the selectivity may be low, and the diffusion of the reactants through the catalyst sublayers can slow down the reaction progress and potentially poison the catalyst. Consequently, the reaction mechanisms can be more complex making them harder to study.

1.2.1 Catalysts in homogeneous catalysis

A wide portfolio of catalysts is available in homogeneous catalysis depending on the reaction to study, selectivity to achieve or cost to reduce. Organometallic catalysts[9] have been widely used along the years because they provide high selectivity and are highly effective in a huge variety of chemical processes such as hydrogenation, hydroformylation, cross-coupling and polymerization reactions. However, the separation between the products and the organometallic catalyst to allow for its subsequent reuse can be challenging, Moreover, if the catalysts have a transition metal, it should not be released to the environment and therefore, an extra cost is introduced when disposing its waste. Over the last years, the use of metal-free organocatalysts[10,11] has grown rep-

resenting a "green" and cheaper alternative to transition metal-based catalysts also offering to prepare high-purity products, creating process versatility and considerably reducing the environmental footprint.

TBD: a versatile organocatalyst

TBD (1,5,7-Triazabicyclo[4.4.0]dec-5-ene)[12] is a unique superbase type catalyst characterized by its high basicity and bifunctionality with two reactive sites located at close distance in the molecular structure. This makes TBD superior to other N-derived superbases such as TMG (1,1,3,3-tetramethylguanidine), DBN (1,5-diazabicyclo(4.3.0)non-5-ene), and DBU (1,8-diazabicyclo(5.4.0)undec-7-ene).

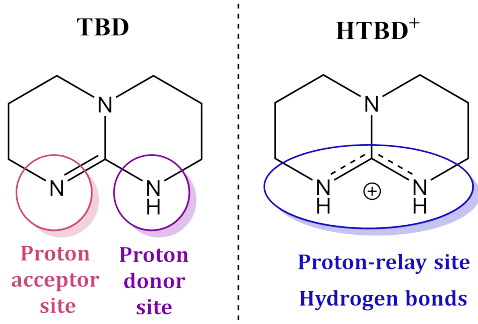

Figure 1.3: Dual functionality of TBD and its protonated form $HTBD^+$

Figure 1.3 illustrates that TBD structure is a bicyclic guanidine that has nucleophilic character due to the lone pair of electrons on the secondary, sp^3-hybridized nitrogen atom. Once TBD is protonated ($HTBD^+$), both -NH groups can create hydrogen bonds and also can operate in a formal proton-rely process. The proximity between these reactive sides makes the TBD highly versatile, so it can catalyze several reactions such as transesterification, amidation, Michael and aldol reactions, polymerization (including ROP), and depolymerization. In the case of cyclic carbonates and polycarbonates[13], TBD interacts with the carbonate oxygen atoms, locating itself close to the reactive centre while it is able to exchange protons with other carbonate units. The proximity of various active sites near the catalyst structure makes it exceptionally effec-

tive for carbonate and polycarbonate formation reactions. Therefore, TBD is widely studied in this thesis, and more specifically in **Chapter 5, 6** and **7**.

1.2.2 Synergy between computational and experimental studies

The synergy between computational and experimental studies is crucial for the investigation of chemical reactions[14]. On one hand, computational chemistry provides important insights at an atomic level that unveils the mechanisms and energy changes involved in the reaction to study. This information helps to investigate different mechanistic pathways and model the chemical system to predict its behaviour on the basis of the interactions between the molecules involved. The computational effectiveness and its accuracy, however, depends on the models used. On the other hand, experimental studies provide real-world results, allow to characterize and isolate products and intermediates involved in the reaction, and to obtain kinetic information. Experimental data offer the opportunity to validate computational predictions, providing feedback on the accuracy and reliability of the theoretical models. Though, experimental studies cannot provide detailed information at an atomic-level of the reaction manifold.

Therefore, the combination of both experimental and computational studies provides a deeper understanding of complex reaction processes produce more detailed information of the mechanistic pathways. Considering the importance of the synergy between computational and experimental studies, this thesis will demonstrate the value of these hybrid approaches as to unravel detailed information of reaction intermediates and the most likely manifolds that lead to the specific target molecules discussed in each chapter.

1.3 Synthesis of CO_2-based cyclic carbonates

The synthesis of cyclic carbonates using carbon dioxide (CO_2) is an attractive and sustainable approach in green chemistry. Cyclic carbonates are versatile heterocycles that have been widely used such as electrolytes for lithium

batteries, polar aprotic solvents, fine chemical intermediates and polymerizable monomers[15–17]. The traditional method to synthesize cyclic carbonates in high yield involves the use of phosgene, a very toxic chemical that releases corrosive HCl upon reacting, with a wide range of precursors such as glycerol, amino acids, and sugars. Consequently, in the last decades alternative and environmentally more friendly strategies have been developed towards cyclic carbonates. These methods use CO_2, a greenhouse gas, as a raw material in combination with typical molecules such as epoxides or alcohols[18,19]. The most predominant synthesis involves the coupling between carbon dioxide and epoxides, with the latter being reactive substrates that helps to overcome the thermodynamic hurdle in converting CO_2. Other precursors such as homoallylic alcohols, halohydrines, ethylene glycol, oxetanes and propargylic alcohols have also been used to generate cyclic carbonates[20,21].

Several strategies/examples to obtain cyclic carbonates using CO_2 and diverse precursors as reported in the literature are depicted in **Figure 1.4**. The reactions studied by the Tomishige, Buchard and Dyson groups (**Figure 1.4 (a)**) involve 1,n-diols and CO_2 as reactants to produce cyclic carbonates[22–24]. Due to the versatility of the diol precursors, it is possible to obtain cyclic carbonates with various substituents and different ring sizes. The Johnston group discovered that it is possible to synthesise six-membered cyclic carbonates (6MCCs) from homoallylic alcohols using a chiral amine catalyst[25,26] (**Figure 1.4 (c)**). The Kleij group reported the synthesis of 6MCCs from oxetanes[27] (**Figure 1.4 (b)**) or epoxides (**Figure 1.4(e)**) with CO_2 as a reactant, catalyzed by an aluminium-based catalyst[28]. Dabral and Schaub[29] (**Figure 1.4(d)**) described the synthesis of an α-alkylidene carbonate using a Buchwald phosphine and silver(I) salt.

Generally, five-membered cyclic carbonates (5MCCs) are easier to be synthesized compared to larger ring congeners, such as six-membered (6MCC), seven-membered (7MCC), and even eight-membered cyclic carbonates (8MCCs). Additionally, the number and disposition of the substituents bound to the cyclic carbonate ring depend mainly on the precursor structures and the mechanistic pathway to synthesise the product.

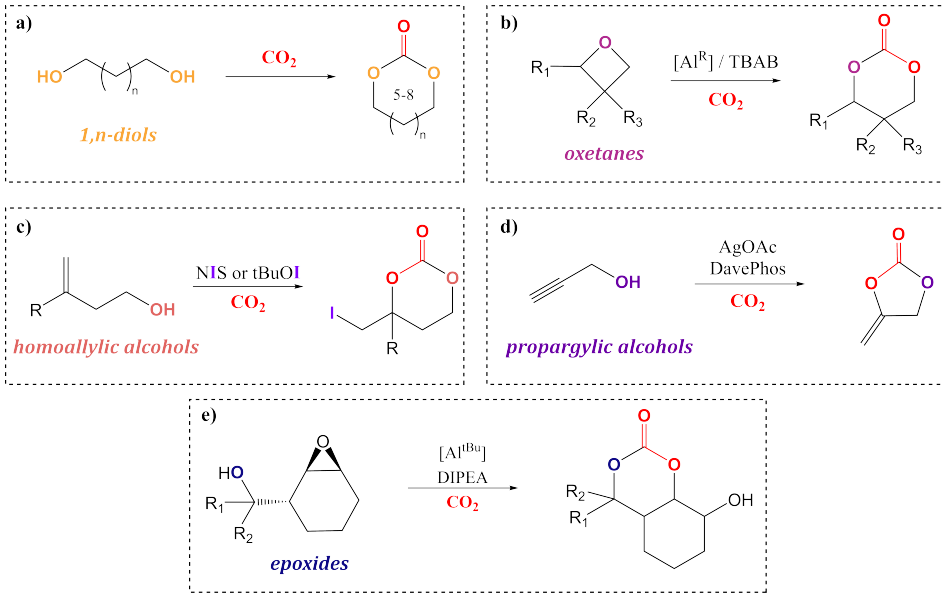

Figure 1.4: Schematic synthetic routes reported in the literature for the synthesis of cyclic carbonates using CO_2 as a reagent

1.4 Ring-opening polymerization of cyclic carbonates

Ring-opening polymerization (ROP) is a method used to synthesize linear polymers by opening cyclic monomers such as lactones[30–33], lactides[34], cyclic esters or cyclic carbonates under appropriate conditions using an initiator[35]. A standard polymerization manifold consists of three main steps: the *initiation* (when a molecule initiates the reaction by activating another one), the *propagation* (the active site leads to the addition of the next monomer thus growing the chain), and *termination* (polymerization ends). These steps are typically catalyzed by various metal-based initiators or organic catalysts. The ring strain of the monomer (cyclic carbonate) is an important thermodynamic driving force for the ROP, therefore, larger rings such as six- seven- or eight-membered cyclic carbonates are more prone to ROP and releasing relatively free energy-stable polycarbonate chains. Smaller cyclic carbonates (5MCC) typically suffer from decarboxylation during the ROP reaction thereby leading to poly(ether carbonate)s.

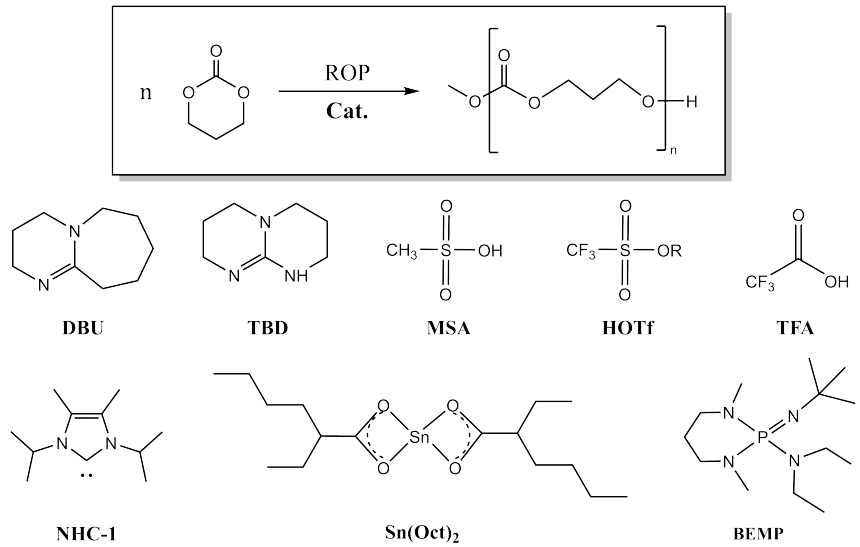

Figure 1.5: Ring-opening polymerization scheme with different catalysts from the cationic, anionic and coordination-insertion ROP strategies

The ROP reaction can take place through different mechanisms depending on the chemical nature of the initiators and catalysts:

Cationic ROP[36,37]: The monomer acts as a Lewis base due to the dipolar moment of the cyclic carbonate group when reacting with an electrophilic initiator, which can be a Brønsted or Lewis acid such as MSA (methane sulfonic acid), HOTf (triflic acid), DPP (diphenylphosphate) or TFA (trifluoro acetic acid. The polymerization is initiated by the protonation or alkylation of a carbonyl oxygen by the electrophile initiator, and then there are two possible pathways: the activated monomer (AM) and the active chain end (ACE) mechanisms[38,39]. The cationic ROP is suitable for a wide range of cyclic carbonates, however, during the polymerization side reactions such as backbiting or chain transfer can occur, which makes it difficult to control the molecular weight and distribution of the polymer obtained.

Anionic ROP[39,40]: The polymerization is initiated by nucleophiles such as alkoxides, carbanions, or amines due to the electrophilic nature of the car-

bonyl group. The reaction starts with a nucleophilic attack by the initiator on the carbonyl carbon of the cyclic carbonate, opening the ring and generating an alkoxide intermediate that will attack subsequent monomers thereby extending the polymer chain. The reaction ends when a proton donor neutralizes the active alkoxide. There are different catalysts that can enable an anionic ROP, including phosphazene bases, N-Heterocyclic carbenes (NHCs) and several Brønsted base initiators such as DBU, TBD and N-methylated MTBD. In general, these catalysts allow for good control over the molecular weight and produce polymers with narrow molecular weight distributions.

Coordination-Insertion ROP[39]: A metallo-organic catalyst attacks the cyclic carbonate by means of two possible different mechanisms. The first one consists of an insertion reaction that involves a Lewis acid metal (a metal halide, oxide or carbonate) and water or alcohol. The second one is a coordination-insertion mechanism, which involves a metal alkoxide that interacts with the cyclic carbonate, followed by a rearrangement that results into the breaking of a metal-oxygen bond and an acyl-oxygen bond of the cyclic carbonate[38]. The typical metallo-organic catalysts used in this kind of ROP contain zinc, tin or aluminium such as $SnOct_2$[a], or zinc stearate. These processes generally lead to high selectivity and control over the polymer structures. However, their high cost, toxicity, and the difficulty in removing the catalysts from the products make their use challenging.

Enzymatic ROP[38,41–44]: The ring-opening of the cyclic carbonate is performed by an enzyme (e.g., lipases or *Novozym-435*). This procedure operates under mild and environmentally friendly conditions with high specificity and selectivity. However, these enzymatic ROPs have usually slower reaction rates compared to the other ROP methods, and hence is limited to specific monomers that are compatible with the enzyme.

[a] Stannous octoate

1.5 Depolymerization

Polymers are ubiquitous materials widely used because of their low-cost production and versatility. However, many of them have short lifetimes or are limited to single use. As a consequence, plastic waste has been accumulating in the environment for decades. A 2024 review[45] shows that 91% of all plastic ever produced has been incinerated or discarded[46], leading to widespread microplastics[47,48], environmental pollution (specially marine)[49] and severe quality air issues from open burning[50]. The overall impact of plastic consumption on climate change is substantial, as it has been estimated that by 2050, plastic production and incineration could consume up to 13% of the remaining carbon budget connected to a maximum level of global warming to 1.5°C[51]. Despite this environmental problem not being new, concerns about plastic recycling efficiency and the linear way to consume plastics are more recent. Actually, many economic and environmental incentives related to plastic recycling are focused on solving plastic waste treatment problems, but the current approaches still remain limited. Therefore, to mitigate the waste impact, a circular plastic economy, in which the materials are reused and recycled as much and as long as possible through repeated cycles of use, needs to be implemented.

On the one hand, ***mechanical recycling*** strategies represent traditional ways to recycle plastic through physical recycling or pyrolysis, which is not efficient enough. Over 99% of plastic recycling in Europe is mechanical[52], and faces several limitations such as lowering the material quality after recycling, and being sensitive to contaminants or polymer mixtures thus needing expensive waste management systems.

On the other hand, ***chemical recycling*** has grown both academically and commercially, and involves converting plastic waste polymers into smaller molecules with high purity and yield[53]. There are two known chemical recycling strategies:

- **Thermochemical Recycling:** This process mainly uses heat to break down polymers into small(er) molecules. This process is generally nons-

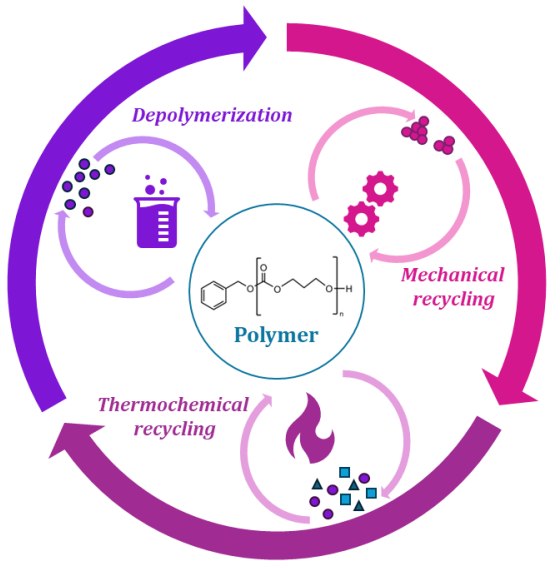

Figure 1.6: Schematic representation of circular polymer recycling processes

elective, producing a mixture of monomers, oligomers, feedstock chemicals, and fuels.

- **Chemical Depolymerization:** This strategy intends to selectively convert polymers into monomers or specific chemicals, typically using solvents, catalysts, and heat. These monomers can then be repolymerized obtaining high-quality polymers, or be repurposed towards the fabrication of other value-added chemicals.

With these latter chemical recycling processes, the use of catalysts is needed to enhance the efficiency of the depolymerization reaction. Metal-based catalysts such as zinc or lead acetates, sodium/potassium sulphate, and titanium phosphate are widely used in depolymerization strategies, having as disadvantage a difficulty of separating them from the crude product, leading to poor chemo-selectivity, and high environmental/economic cost. In the case of organic catalysts, a wide range of them are used in polymerization reactions, while in depolymerization reactions their use is still limited. Organocatalysts can facilitate the depolymerization mechanisms to produce highly pure, small

molecules, suitable for subsequent polymerizations. In many cases, hydrogen-bond interactions involved in the depolymerization mechanism promoted by organocatalysts such as TBD are crucial for controlling the catalytic activity and selectivity of the depolymerization reaction.

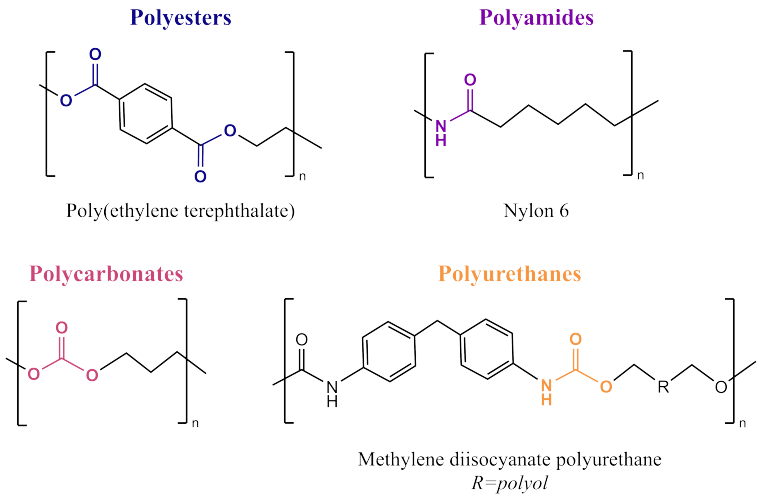

Figure 1.7: Active sides susceptible to a scission during the depolymerization process for the most common polymers

The chemical structure of a polymer is crucial to the process efficiency of the depolymerization reaction. In particular, polymers with C-C backbones are challenging to depolymerize due to the lack of polarity and high bond dissociation energies of C-C bonds, while polymers with backbones containing C-X bonds (X is a heteroatom) are more susceptible and depolymerize faster[54]. For polycarbonates, the carbonate carbonyl group is targeted for nucleophilic attack, which may lead to CO_2 release or to the formation of cyclic carbonates (monomers), depending on the chemistry used.

In this thesis (**Chapter 7**), we address the depolymerization of polycarbonates, which are thermoplastic polymers widely used in several applications. In particular, we focus on the depolymerization reaction of poly(limonene carbonate) (PLC) using an organocatalyst (TBD) that allows obtaining the monomer, limonene carbonate (LC), as a major product, and limonene oxide (LO) and CO_2 as potential side-products. This process could be regarded

as a proof-of-concept study that should spur further activities in the area of polymer science with a focus on circularity.

CHAPTER

2 Objectives

2.1 Main objectives and outline

The main objective of this thesis is to study the recycling of CO_2 itself and CO_2-based polymers obtained by homogeneous catalysis, and studying the mechanistic pathways involved in every step to create a deeper understanding how to design more efficient recycling processes. CO_2 is a carbon renewable that can be used as a reactant combined with alcohols and cyclic ethers to obtain cyclic carbonates. The most common synthesis, the coupling between epoxides or alcohols and CO_2, is typically performed to obtain five-membered cyclic carbonate (5MCCs) (the focus in **Chapter 4**). Even though 5MCCs can be polymerized by a ring-opening polymerization (ROP) reaction, larger-ring heterocycles such as six-, seven- or eight-membered cyclic carbonates can lead to more stable polymers. However, in general, these polymers are generally more difficult to synthesize. Therefore, a conversion from five- to six-membered cyclic carbonate (**Chapter 5**) is an interesting alternative route to obtain functionalized 6MCCs. These monomers can then be polymerized with an organocatalyst under mild conditions. However, not all cyclic carbonates are prone to undergo a ROP reaction to obtain their respective polycarbonates. To optimize available time and resources, a predictive model was designed to classify which monomers can undergo the ROP under certain conditions (**Chapter 6**), and more specifically how their substitution and functionality influence the ROP process. Finally, polycarbonates can be depolymerized using an organocatalyst (shown in **Chapter 7**), obtaining an epoxide, CO_2 and a trans-configured cyclic carbonate (monomer). The latter is particularly interesting as it can be re-polymerized, thereby creating a step closer to a circular use of polycarbonates.

In this thesis, computational studies are complemented with experimental data provided by other Kleij group members. The synergy between theoretical and experimental results provides a deeper understanding of the reaction mechanisms. In terms of structure, this thesis describes first a theoretical background used to perform the calculations throughout the thesis, followed by the chapters that describe various transformative CO_2 processes addressing the

reuse/recycling of this carbon feedstock. The following paragraphs outline the contents and objectives of each chapter.

In **Chapter 3: Computational Methods**, the theoretical background of the methodology used along this thesis is outlined. All reactions studied involve homogeneous catalysis, and therefore, we have focused on Density Functional Theory (DFT) since it is widely used in modelling mechanistic pathways. This offers high accuracy in describing the reactivity, and low computational cost.

In **Chapter 4: Using CO_2 to obtain Five-Membered Cyclic Carbonates with a Silver-based Catalyst**, we describe a novel cascade process to synthesise keto-substituted five-membered cyclic carbonates that are built from alkyne-1,2-diol as a key substrate together with CO_2 as a renewable carbon reagent. This process is promoted by a Ag-based catalyst composed of a Buchwald phosphine-ligand (DavePhos or BrettPhos) coordinated to a silver(I) salt (AgOAc). As the substrate has a chiral center, in order to fully understand the mechanistic pathway, DFT calculations will be performed for each catalyst complex while taking into account the chirality of the substrate. The computational results obtained will be supported with experimental data provided by Xuetong Li (another Kleij group member).

In **Chapter 5: From Five- to Six-Membered Cyclic Carbonates**, a unique organocatalytic manifold has been discovered for the formation of six-membered cyclic carbonates starting with five-membered cyclic carbonates. The reaction begins with a five-membered cyclic carbonate possessing a tertiary alcohol, 1,5,7-triazabicyclodec-5-ene (TBD) as a catalyst, and acetyl imidazole (AcIm) as an acylating agent. This cascade reaction yields an elusive six-membered cyclic carbonate product with a primary alcohol, which can be trapped by protecting the pendent alcohol. The mechanistic pathway involved in this reaction will be examined in detail by performing DFT calculations reinforced by experimental data from Chang Qiao's research (another Kleij group member). Furthermore, alternative mechanistic pathways will be also calculated, such

as the acylation of the alcohol from the reactant and the five-membered cyclic carbonate isomerization into a seven-membered cyclic carbonate.

In **Chapter 6: Ring-Opening Polymerization**, an extensive computational study will be performed. Firstly, we will study the mechanistic pathway involved in a ROP reaction for a six-membered cyclic carbonate using benzyl alcohol (BnOH) as an initiator, catalyzed by TBD (an often used and highly effective organocatalyst) in toluene solution at room temperature. To comprehend the effect of the ring size of the cyclic carbonates (5MCC, 6MCC and 7MCC), several mechanistic pathways will be calculated and compared. Monomers (cyclic carbonates) polymerizable under the same conditions will then studied and the results will be benchmarked against experimental data provided by various Kleij group members. Moreover, a predictive model correlating the energy span of the reaction and the polymer stability could be generated. The data points within this plot indicate whether the ROP reaction is energetically feasible and the resulting polymer stability is thermodynamically favoured. Thus, if the specific data points fall within a specific region, it shows that the monomer has good potential to be polymerized. Monomers with a different number of substituents, or difference in the chemical nature and size of ring-substituents in the cyclic carbonate will be also calculated. For some of these monomers, experimental data have been reported in the literature and helped to validate the predictive model. Finally, an additional computational study on the influence of the polymer conformation on the ROP efficiency was performed taking into account more configurations.

In **Chapter 7: Depolymerization**, we will study the mechanistic pathways involved in the depolymerization of poly(limonene carbonate) abbreviated as PLC, using TBD as a catalyst at 80°C in acetonitrile solution by exploring two different mechanisms: end-group based depolymerization and main-chain scission. Both mechanisms will be investigated through DFT calculations supported by experimental results obtained from David Lamparelli (a former Kleij group member). The combination of these mechanisms offers a successful

and efficient depolymerization that provides an appreciable yield of *trans*-limonene-carbonates (i.e., monomers), and limonene-oxides and CO_2 as alternative products. The cyclic carbonate repolymerization into PLC via ROP using the same organocatalyst will be also considered, being this depolymerization/repolymerization sequence a nice example of a potential circular use of polycarbonates.

UNIVERSITAT ROVIRA I VIRGILI
COMPUTATIONAL INSIGHTS OF CATALYTIC CARBON DIOXIDE VALORIZATION AND CIRCULAR RECYCLING PROCESSES
Alba Villar Yanez

CHAPTER

3 Computational Methods

3.1 Quantum Chemistry

Quantum chemistry[55–57], is a field in physical chemistry that applies quantum mechanics to chemical systems in order to describe their interatomic interactions. Its main goal is to calculate the electronic effects on the physical and chemical properties of molecules, materials, and solutions at atomic scale. In this thesis, the mechanistic pathways of chemical reactions were computed by using quantum mechanics calculations to determine the intermediates and transition states.

3.1.1 Schrödinger equation

Erwin Schrödinger[58] proposed that physical systems can be described by means of wave functions.

The time-dependent Schrödinger equation is:

$$i\hbar\frac{\partial\psi(\mathbf{r},t)}{\partial t} = \hat{H}\psi(\mathbf{r},t) \tag{3.1}$$

The time-independent Schrödinger equation is:

$$\hat{H}\psi(\mathbf{r}) = E\psi(\mathbf{r}) \tag{3.2}$$

Where $\hat{H}$ is the Hamiltonian operator representing the total energy of the system, $\psi(\mathbf{r})$ is the wavefunction dependent on spatial coordinates $\mathbf{r}$, and E is the energy associated with the state represented by the wavefunction.

The total molecular wavefunction depends on the nuclei position ($\mathbf{R}$) and the electron coordinates ($\mathbf{r}$), giving the Equation 3.3:

$$\hat{H}\psi(\mathbf{r},\mathbf{R}) = E\psi(\mathbf{r},\mathbf{R}) \tag{3.3}$$

The *Born-Oppenheimer approximation*[59] is a fundamental assumption in quantum chemistry and molecular physics that assumes that the nuclei are much more heavier than the electrons, resulting in a much more slower movement. Consequently, it separates the motion of the nuclei and the electrons

based on their mass difference in the total molecular wavefunction $\Psi(\mathbf{r},\mathbf{R})$ by separating the variables as a product of the electronic wavefunction $\psi(\mathbf{r};\mathbf{R})$ and the nuclear wavefunction $\chi(\mathbf{R})$ (Equation 3.4)

$$\Psi(\mathbf{r},\mathbf{R}) \approx \psi(\mathbf{r};\mathbf{R})\chi(\mathbf{R}). \tag{3.4}$$

Then, the electronic wavefunction is obtained from the electronic Hamiltonian. The electronic Schrödinger equation, with the nuclei fixed at positions $\mathbf{R}$ is represented in Equation 3.5:

$$\hat{H}_{\text{elec}}\psi(\mathbf{r};\mathbf{R}) = E_{\text{elec}}(\mathbf{R})\psi(\mathbf{r};\mathbf{R}) \tag{3.5}$$

The electronic Hamiltonian ($\hat{H}_{\text{elec}}$) is described in Equation 3.6:

$$\hat{H}_{\text{elec}} = \hat{T}_{\text{elec}} + \hat{V}_{\text{elec-elec}} + \hat{V}_{\text{elec-nuc}} \tag{3.6}$$

Where $\hat{T}_{\text{elec}}$ is the kinetic energy operator of the electrons, $\hat{V}_{\text{elec-elec}}$ is the electron-electron repulsion potential, and $\hat{V}_{\text{elec-nuc}}$ is the electron-nucleus attraction potential.

3.1.2 Potential Energy surface

The concept of Potential Energy surface (PES)[57] derives directly form the Born-Oppenheimer approximation explained above. Solving the electronic Schrödinger equation $E_{\text{elec}}(\mathbf{R})$, the energy for a determined nuclear configuration is found. The value for this energy (potential energy) acts as a potential energy surface (PES) for the nuclei, allowing the nuclear Schrödinger equation (Equation 3.7) to be solved:

$$\left[\hat{T}_{\text{nuc}} + E_{\text{elec}}(\mathbf{R}) + \hat{V}_{\text{nuc-nuc}}\right]\chi(\mathbf{R}) = E_{\text{total}}\chi(\mathbf{R}) \tag{3.7}$$

Where $\hat{T}_{\text{nuc}}$ is the kinetic energy operator of the nuclei, $\hat{V}_{\text{nuc-nuc}}$ is the nucleus-nucleus repulsion potential, and E_{total} is the total energy of the molecule.

Gradient

The gradient of the potential energy is a vector of first-order partial derivatives of the potential energy function with respect to the nuclear coordinates. It indicates the direction and rate of the steepest descent in the energy landscape. It is defined as:

$$\nabla E(\mathbf{R}) = \left(\frac{\partial E(\mathbf{R})}{\partial R_1}, \frac{\partial E(\mathbf{R})}{\partial R_2}, \ldots, \frac{\partial E(\mathbf{R})}{\partial R_n} \right) \tag{3.8}$$

Where $E(\mathbf{R})$ is the potential energy function, and $R_1, R_2, \ldots, R_n$ are the nuclear coordinates.

Hessian Matrix

The Hessian Matrix is a square matrix of second-order partial derivatives of the potential energy function with respect to the nuclear coordinates. It provides information about the curvature of the PES. It is defined as:

$$H_{ij} = \frac{\partial^2 E(\mathbf{R})}{\partial R_i \partial R_j} \tag{3.9}$$

Where $E(\mathbf{R})$ is the potential energy function, and R_i and R_j are the nuclear coordinates.

Stationary Points

An stationary point in the Potential Energy Surface is defined as a point with zero gradient (Equation 3.8, **Figure 3.1**), which can be:

- **Local Minima:** Is the point where the Hessian matrix has all positive eigenvalues. It describes energy minima that correspond to physically stable chemical species that can be reactants, products or intermediates.
- **Saddle Point:** Is the point where the Hessian matrix has exactly one negative eigenvalue, indicating a local maximum in one direction (reaction coordinate) and the other eigenvalues are positive indicating a local minima in all other directions, describing a transition state (TS).

- **n-order Saddle Point:** Is the point where the Hessian matrix has n (*where n>1*) negative eigenvalues, and the other are positive. These kind of points are not chemical relevant.

In **Figure 3.1** are represented an example of PES with the stationary points both minima and Transition State (TS). The reaction path must connect the local minimum (Reactants, Products) through the TS, which has to be energetically higher than the minima and has to accomplish the definition of Saddle Point described above.

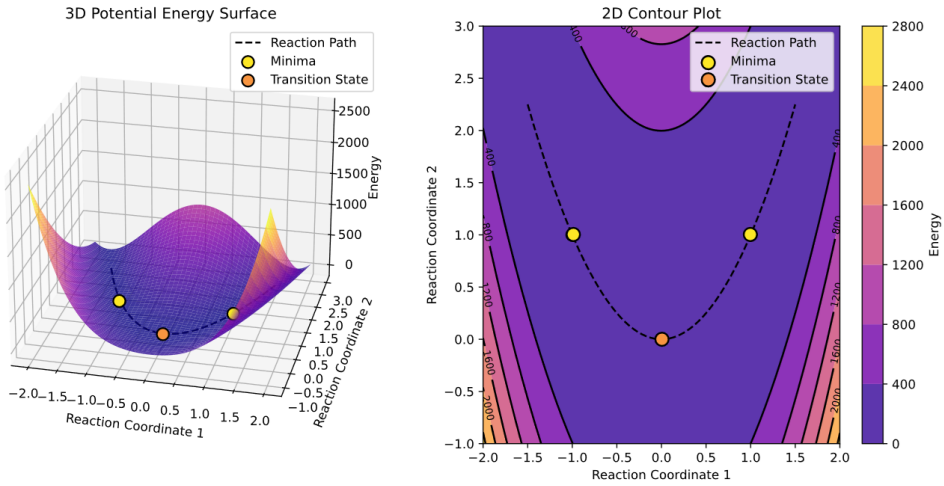

Figure 3.1: Example of Potential Energy Surface (PES) representation with stationary points (Minima and TS) depicted as circles and Reaction Path drawn as a dashed line

The main problem to obtain a Potential Energy surface (PES) in molecular systems is the dimensionality, particularly in chemical systems that include several atoms. It describes the exponential growth in computational complexity when the system increases, namely the number of atoms to describe. Using Cartesian coordinates (x, y, z), the dimension of a molecular system of N atoms, becomes $3N$ (nuclear coordinates). The internal coordinates allow to eliminate the system's global translations and rotations degrees of freedom, thus resulting in a $3N\text{-}6$ of total coordinates and $3N\text{-}5$ for linear molecules. This dimensionality issue becomes particularly challenging in quantum chemistry calculations

where the Schrödinger equation needs to be solved for the entire molecular system.

Representing the PES entirely is not feasible, as for example a small molecular system with 10 atoms, has 24 degrees of freedom. Considering that an acceptable representation of the PES is by representing 10 points for each degree of freedom, the total number of calculations need to obtain the PES is 10^{24}, which is totally unfeasible. To address this challenge several approximations and computational methods were developed, therefore, computational chemistry focuses in the description to the stationary points along the PES to describe the reaction path without the need of calculating the complete PES.

3.1.3 Solvation Models

In chemical reactivity and properties, the solvation effects are crucial to describe the chemical reactions. There are two methods to take into account the solvation effects in computational chemistry, explicit solvation and implicit solvation.

The explicit solvation consists in introducing explicitly a certain amount of solvent molecules around the studied molecule. This method provides an accurate description of solute-solvent interaction in the studied system. However, the inconvenient in adding the number of solvent molecules needed to mimic the real concentration of the chemical system is the computational cost, which is inaccessible in DFT calculations. For that reason, the explicit solvation is commonly used in Molecular Dynamics calculations.

The implicit solvation consists in considering that the solvent molecules are modelled as a continuum medium with a dielectric constant ϵ[60]. The solute molecule is located in a cavity within the continuum medium, usually shaped to fit the solute molecule. Then, the dielectric medium models the electrostatic interaction between the solute and the solvent, which is typically described by the Poisson or Poisson-Boltzmann equation that considers the dielectric properties of the solvent and the solute charge distribution. The response of the solvent to the solute's charge distribution, named reaction field, is determined in a

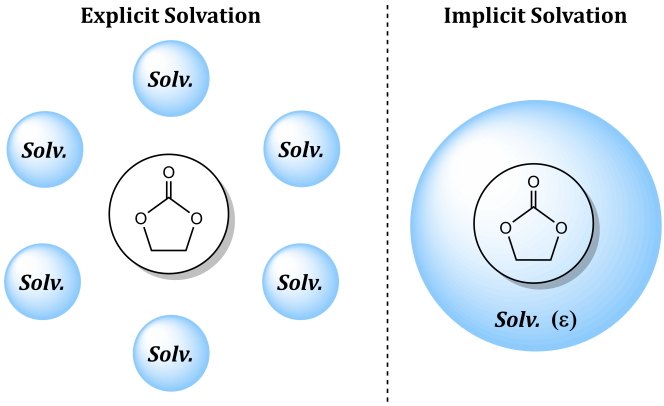

Figure 3.2: Schematic representation of the explicit and implicit solvation models

self-consistent manner that consists in iterating the solute's electronic structure and the solvent's reaction field until convergence is achieved (Self-Consistent Reaction Field (SCRF))[61]. One of many internal parameters used to define solvents (SCRF) in Gaussian 16 rev. A.03[62] are ϵ=2.3741 for toluene, and ϵ=35.688 for acetonitrile.

The most used implicit solvent continuum models implemented in Gaussian 16[62] software are the Polarized Continuum Model (PCM)[63,64] and the Solvation Model based on Density (SMD)[65].

The PCM method is focused on electrostatic interactions by solving the Poisson-Boltzmann equation. The solute cavity is created by a set of overlapping spheres centred on atoms or groups of atoms. This method is generally used for molecular geometry optimization in solution, calculating solvation energies and studying reaction mechanisms.

The SMD method, is based on the generalized Born equation, it solves the Poisson-Boltzmann equation similarly to PCM, but uses a set of specifically parametrised Coulomb radii to construct the solute cavity. The non-electrostatic contributions are explicitly included by the cavity-dispersion-solvent-structure (CDS) protocol[65]. This method is widely used to calculate thermodynamic properties, solvation energies, spectral properties and reaction mechanisms.

In this Thesis the SCRF=SMD for toluene and acetonitrile implemented in Gaussian 16 rev. A.03[62] were used to calculate the solvation effects in the reaction mechanisms.

3.1.4 Entropic Corrections

The gas-phase Gibbs free energies for mechanistic pathways with a high degree of association or dissociation tend to not describe correctly the entropic effects in solution. For example, in a polymerization reaction, the reaction starts with n molecules (monomers and initiator) that become in an unique macromolecule (polymer) as a product. In this case, if we use the uncorrected Gibbs free energies, the final product will be too entropically disfavoured due to the overestimation of the entropic penalty. Therefore, in **Chapter 6** and **7**, where a polymerization and depolymerization reactions are described, it is necessary to apply entropic corrections to the Gibbs free energies. Specifically, we applied the Standard state correction[66], which consists in assuming a 1.0 M concentration instead of a 1 atm of pressure. The correction could be applied by applying the ideal gas equation related by concentrations and pressure (Equation 3.10).

$$PV = nRT \rightarrow P = \frac{nRT}{V} \rightarrow P = \frac{n}{V}RT \rightarrow P = cRT \tag{3.10}$$

Where c = 1.0 mol/L, P = 1atm and R = 0.082(atm·L)/(mol·K)

$$P^* = \left(\frac{1.0mol}{L}RT\right) \tag{3.11}$$

$$G^* = G^\circ + RTlog\left(\frac{P^*}{P^\circ}\right) \tag{3.12}$$

Then, substituting the Equation 3.11 with Equation 3.12:

$$G^* = G^\circ + RTlog\left(\frac{c^*RT}{P^\circ}\right) = G^\circ + RTlog\left(\frac{1.0M}{1.0atm}RT\right) = G^\circ + RTlog|RT| \tag{3.13}$$

Note that the units of R inside the logarithm should be in atm·L/mol·K for simplicity, while the R located outside the logarithm should be in the same units as G°.

Therefore, the Equation 3.13 at 298.15K is:

$$G^* = G^\circ + 1.89 kcal \cdot mol^{-1} \tag{3.14}$$

With these corrections, the entropic effects in solution along the reactions depicted in **Chapter 6** and **7** are described more accurately.

3.1.5 Energy Span Model

The Energy Span Model (ESM) developed by Kozuch and Shaik[67,68], provides an understanding of the catalytic efficiency of a chemical reaction by analyzing the turnover frequency (TOF) of catalytic cycles by means of the intermediates and transition state energies involved in the catalytic process.

- **Turnover Frequency (TOF)** can be described as the number of catalytic cycles per unit of time and is it used to measure the catalytic activity of the system.
- **Energy Span (δE)** is defined as the difference in energy between the highest energy transition state (TS) and the lowest energy intermediate (Int) in the catalytic cycle.

In brief, the application of the Energy Span Model starts by identifying key intermediates and transition states named TOF-determining transition state (TDTS) and the TOF-determining intermediate (TDI). In this model the TDI and TDTS are not necessarily the highest and lowest states, and they do not need to be connected in a single process. Once both identified, the TOF is calculated. Note that the TOF is inversely proportional to the exponential of the energy span, therefore, a higher TOF corresponds to smaller energy span, indicating a better efficiency of the catalyst. The model assists in identifying which steps of the catalytic cycle are kinetically controlling.

3.2 Outline of *ab initio* Methods

In this section, we will only summarize a basic overview about this methods to understand the foundations and differences. The *ab initio* methods[55–57]

solves the Schrödinger equation using only the Born-Oppenheimer approximation, without adding empirical information.

3.2.1 Hartree-Fock

The Hartree equation as an approximate solution of the time-independent Schrödinger (Equation 3.2) for a multi-electron atom or molecule. The energy for the many-electron wavefunction (Ψ_{HF}) is approximated by a single Slater determinant (Equation 3.15), which is a product of one-electron wavefunctions (orbitals).

$$\Psi_{\mathrm{HF}} = \frac{1}{\sqrt{N!}} \begin{vmatrix} \phi_1(\mathbf{x}_1) & \phi_2(\mathbf{x}_1) & \cdots & \phi_N(\mathbf{x}_1) \\ \phi_1(\mathbf{x}_2) & \phi_2(\mathbf{x}_2) & \cdots & \phi_N(\mathbf{x}_2) \\ \vdots & \vdots & \ddots & \vdots \\ \phi_1(\mathbf{x}_N) & \phi_2(\mathbf{x}_N) & \cdots & \phi_N(\mathbf{x}_N) \end{vmatrix} \tag{3.15}$$

Where $\phi_i(\mathbf{x}_j)$ are the spin-orbitals of the electrons.

The Fock operator $\hat{F}_i$ (Equation 3.16) is defined as an effective one-electron Hamiltonian that includes the effects of electron-electron repulsion.

$$\hat{F}_i = \hat{h}_i + \sum_{j \neq i} \left(\hat{J}_j - \hat{K}_j \right) \tag{3.16}$$

Where $\hat{h}_i$ is the one-electron Hamiltonian, $\hat{J}_j$ is the Coulomb operator, and $\hat{K}_j$ is the exchange operator.

The Hartree-Fock equations (Equation 3.17) are derived from the variational principle applied to the Slater determinant.

$$\hat{F}_i \phi_i = \epsilon_i \phi_i \tag{3.17}$$

Where ϵ_i are the orbital energies and ϕ_i the molecular orbitals
These equations must be solved iteratively because the Fock operator depends on the orbitals themselves. Therefore, the Hartree-Fock Method is a

Self-Consistent Field (SCF)[69] method. The procedure consists in starting with an initial guess for the spin-orbitals ϕ_i, then apply the Fock operator using the current orbitals ϕ_i (Equation 3.16), and solve the HF-equations to obtain new ones. This process is iterated until convergence (when the energies and orbitals do not have significant changes), which means the system reaches the self-consistency and the spin-orbitals are consistent with their own potential The total Hartree-Fock energy of the system is described as:

$$E_{\mathrm{HF}} = \sum_{i=1}^{N} \langle \phi_i | \hat{h} | \phi_i \rangle + \frac{1}{2} \sum_{i=1}^{N} \sum_{j=1}^{N} \left(\langle \phi_i \phi_j | \frac{1}{r_{12}} | \phi_i \phi_j \rangle - \langle \phi_i \phi_j | \frac{1}{r_{12}} | \phi_j \phi_i \rangle \right) \tag{3.18}$$

Where, the first term represents the sum of one-electron energies, and the second term accounts for the electron-electron repulsion composed by Coulomb ($\hat{J}_j$) and exchange ($\hat{K}_j$) terms.

In summary, the Hartree-Fock offers an approximate solution for the time-independent Schrödinger equation considering the many-electron wavefunction as a single Slater determinant. This method is also named as Self-Consistent Field, which obtains the optimal group of single-electron orbitals and the related overall energy by iterating the solution of HF equations until they converge. Although HF has its limitations in accounting for electron correlation, it plays a fundamental role in quantum chemistry calculations being the basis of many computational methods.

3.2.2 Basis set

The Basis set is a set of guess functions χ_i used to approximate the molecular orbitals[57]. It is used to represent the electronic wave function in Hartree-Fock or DFT calculations. The most known are:

- **Slater Type Orbitals (STOs)**: They provide a more accurate representation of atomic orbitals, but unfortunately calculating the integrals is computationally difficult.

- **Gaussian Type Orbitals (GTOs)**: These orbitals involves a Gaussian function in their expression. The main advantage is the simplification of the computation of interaction integrals because the product of two Gaussian functions (from different atoms) is another Gaussian function. Despite the representation of atomic orbitals are less accurate than the STOs, the GTOs are the most often used due to the simplicity of solving interaction integrals with a lower computational cost, and allow efficient implementations in the post-HF methods.

3.2.3 Semiempirical Methods

The semiempirical methods balance between accuracy and computational efficiency by simplifying the Schrödinger equation calculations. In particular, they use parametrized Hamiltonians that are derived from experimental data or higher-level calculations to reproduce known properties of molecules such geometric parameters or energies. They neglect certain integrals to reduce the computational cost, and use empirical data to tune their parameters, being reasonable accurate for a wide range of molecular properties. The main advantages are the computational efficiency, being significantly faster than *ab initio* methods, and their reasonable accuracy for well parametrized properties. As an inconvenient, the accuracy depends on the quality of the empirical data used to parametrize, and the parameters optimized for a specific type of molecules may not describe well other molecules.

This method is mainly used to studying large molecule simulations for large molecules such polymers, preliminary screening, and qualitative analysis for chemical reactivity and electronic structure.

3.2.4 Post-Hartree-Fock Methods

The main inconvenient of the Hartree-Fock method is that it does not consider the electron correlation. In order to improve the approximations, the post-Hartree-Fock methods uses the HF function as a basis and add the elec-

tron correlation in different ways. These methods are extremely accurate but computationally expensive[56,57]. The most important methods are:

- **Møller-Plesset Perturbation Theory (MPn)**: Includes the electron correlation through perturbation theory. The notation "MPn" denotes that the energy has been corrected in n-order.
- **Configuration Interaction (CI)**: The wavefunction is expressed as a linear combination of multiple Slater determinants constructed from the orbital spins obtained with the Hatree-Fock method, representing different electron configurations to account for electron correlation. If the wavefunction include all possible excitations as a linear combination of Slater determinants, the exact non-relativistic energy of the system of N electrons would be obtained. This function is named *Full Configuration Interaction (Full CI)*, and is considered one of the most complete description of electron correlation, however the computational cost associated is unavailable. Methods derived from the CI approach include *Multi-Configurational Self-Consistent Field (MCSCF)*, which prominent examples are *Complete Active Space Self-Consistent Field (CASSCF)* and *Multi-Reference Configuration Interaction (MRCI)*.
- **Coupled Cluster (CC)**: It considers excitations (singles, double, triple..) of electron pairs through an operator $\hat{T}$ to introduce the electron correlation. Is a self-consistent and highly accurate method, specifically the CCSD(T) *Coupled Cluster Singles and Doubles with approximating the triple excitations* is considered one of the most precise methods in the actuality.

3.3 Density Functional Theory

The basis of the Density Functional Theory (DFT)[70,71] relies on the Hohenberg-Kohn theorem[72], which postulates that the energy of the ground state of any electronic system can be described to its electron density $\rho(\mathbf{r})$ that only depends on three spatial coordinates. And also postulates about a functional

that relates the energy of the system and the electron density (Equation 3.19), whose form is not described.

$$E[\rho(\mathbf{r})] = T[\rho(\mathbf{r})] + V_{\text{ext}}[\rho(\mathbf{r})] + E_{\text{int}}[\rho(\mathbf{r})] \tag{3.19}$$

Where $T[\rho(\mathbf{r})]$ is the kinetic energy functional, $V_{\text{ext}}[\rho(\mathbf{r})]$ is the external potential energy functional, and $E_{\text{int}}[\rho(\mathbf{r})]$ is the electron-electron interaction energy functional.

The Kohn-Sham[73] formalism is a DFT foundational method based on implementing the Hohenberg-Kohn theorem, that offers a solution for the intractable many-body problem of interacting electrons in a static external potential, by reducing it to a solvable problem of non-interacting electrons moving in an effective potential that includes the Coulomb interactions between electrons and the external potential. The Kohn-Sham equations and its terms are described below:

$$\hat{h}_{KS}\psi_i(\mathbf{r}) = \epsilon_i\psi_i(\mathbf{r}) \tag{3.20}$$

$$\hat{h}_{KS} = \left(-\frac{\hbar^2}{2m}\nabla^2 + V_{\text{eff}}(\mathbf{r})\right) \tag{3.21}$$

Where the first term is the kinetic Energy $T[\rho]$, and the second is the effective potential $V_{\text{eff}}(\mathbf{r})$ which is described in Equation 3.22.

$$V_{\text{eff}}(\mathbf{r}) = V_{\text{ext}}(\mathbf{r}) + V_{\text{H}}(\mathbf{r}) + V_{xc}(\mathbf{r}) \tag{3.22}$$

This effective potential consists in the $V_{\text{ext}}(\mathbf{r})$ that is the interaction energy electron-nuclei, $V_{\text{H}}(\mathbf{r})$ is the Hartree potential (Equation 3.23), and $V_{xc}(\mathbf{r})$ is the exchange-correlation potential (Equation 3.24)

$$V_{\text{H}}(\mathbf{r}) = \int \frac{\rho(\mathbf{r}')}{|\mathbf{r}-\mathbf{r}'|}\, d\mathbf{r}' \tag{3.23}$$

$$V_{xc}(\mathbf{r}) = \frac{\delta E_{xc}[\rho]}{\delta\rho(\mathbf{r})} \tag{3.24}$$

The Kohn-Sham equations are solved iteratively using the SCF method analogous as the Hartree-Fock explained above. In this case, it starts with an initial guess for the electron density $\rho(\mathbf{r})$, then the Kohn-Sham equations are solved to obtain the orbitals $\psi_i(\mathbf{r})$ and the corresponding energies ϵ_i and a new electron density is calculated from the orbitals. This process is repeated until the density converges. As the true form of the functional postulated by Hohenberg-Kohn is not known, approximate Exchange-Correlation functionals must be proposed. Therefore, the accuracy of the DFT method relies in the approximation of the Exchange-Correlation functional. Therefore, different functionals were developed (LDA, GGA, and Hybrid) depending on the description of this Exchange-Correlation functional.

3.3.1 Local Density Approximation (LDA)

The main assumption in the Local Density Approximation (LDA)[57,70] is that the functional only depends on the density, which is considered as an uniform gas of electrons. The exchange energy is obtained from the Dirac formula, and the correlation energy term is obtained from quantum Monte-Carlo simulations.

$$E_{\mathrm{xc}}^{\mathrm{LDA}}[\rho] = \int \rho(\mathbf{r})\epsilon_{\mathrm{xc}}(\rho(\mathbf{r}))d\mathbf{r} \tag{3.25}$$

In general, LDA provides good results for solid structure properties, however, overestimates the binding energy and underestimate ground-state and ionization energies. It obtains accurate results for many systems, but fails in describing situations where the electronic density changes fast.

3.3.2 Generalized Gradient Approximation (GGA)

To improve the LDA, the Generalized Gradient Approximation (GGA)[57,70] exchange-correlation energies not only depend on the electronic density but also for its gradient ($\nabla\rho(\vec{r})$).

$$E_{\mathrm{xc}}^{\mathrm{GGA}}[\rho] = \int f(\rho(\mathbf{r}), \nabla\rho(\mathbf{r}))d\mathbf{r} \tag{3.26}$$

Compared to LDA, the GGA functional compensates the LDA over-binding tendency obtaining in general better total energies, structural energy differences, energy barriers, and atomization energies. However, GGA does not describe correctly the van der Waals interactions and sometimes it describe the solid-state properties worse than LDA.

3.3.3 Hybrid Density functionals

The Hybrid Density functionals (H-GGA)[57,70] combine a part of the exact Hartree-Fock's exchange Energy E_{ex}^{HF} with the exchange-correlation functional of GGA. Consequently, improves the accuracy for the description of several molecular properties although has some difficulties in describing solid-state systems.

In this Thesis, the functional ωB97X-D introduced by Chai and Head-Gordon in 2008, which includes empirical dispersion[74], is widely used in **Chapters 5, 6 and 7**. The central part of this functional is based on B97 functional, modified to include a long-range correction and incorporating a fraction of Hartree-Fock (HF) exchange, which improves the treatment of long-range electron-electron interactions. The X indicates the inclusion of exact (Hartree-Fock) exchange, and the -D correspond to the Grimme's D2 empirical dispersion correction to describe the van der Waals (vdW) interactions that are not well-described by standard DFT methods. This functional is widely used for optimization of molecular geometries, calculating reaction energies and enthalpies, studying non-covalent interactions and computing electronic spectra and properties related to excited states.

In **Chapter 4** the method used is PBE0-D3(BJ)/SDD/def2tzv. The PBE0 functional incorporates a part of the exact Hartree-Fock echange into the Perdew-Burke-Ernzerhof (PBE)[75] that is a GGA functional. The -D3(BJ) corresponds to the D3 Grimme dispersion correction with Becke-Johnson damping (more details explained below). The basis set consists in a Stuttgart/Dresden effective core potential (SDD) and a split-valence basis set developed by

the Karlsruhe group (def2)[76]. The SDD is a relativistic effective core potential (ECP) that substitutes the inner core electrons of heavier elements with a potential, decreasing computational cost while preserving accuracy. The def2-tzv[77] means "triple-zeta valence", which includes three basis functions for each valence orbital. This basis set is often used for lighter elements, while the SDD basis set works well for transition metals and heavier elements. Therefore the combination of both, describe well the metal-based catalyst system studied in **Chapter 4**.

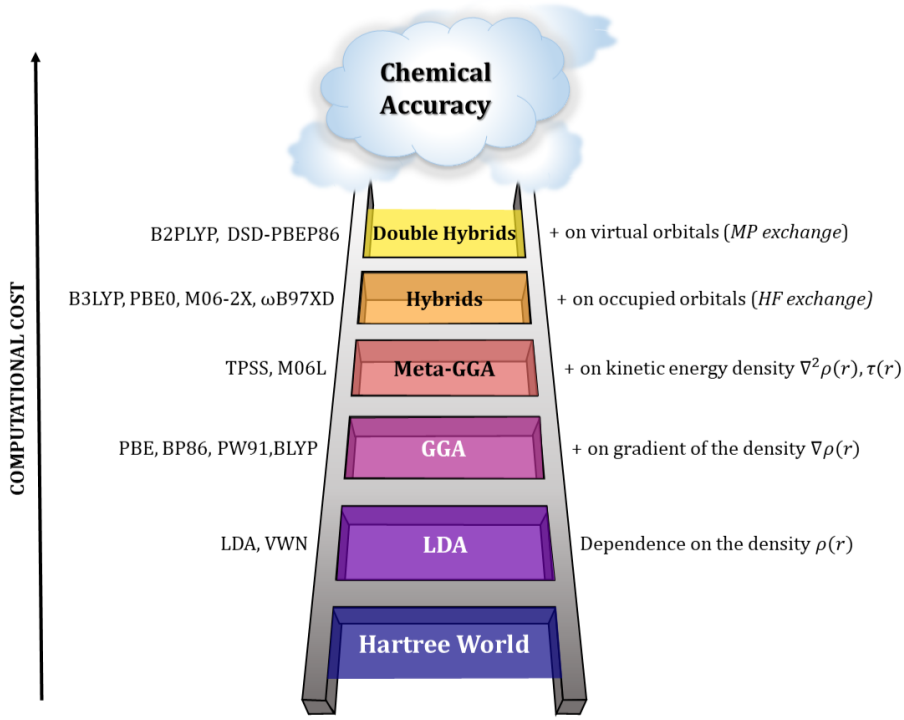

Figure 3.3: Jacob's ladder of DFT representation proposed by Perdew[78], which defines the path from the "Earth Hartree World" towards to "Heaven of chemical accuracy". In the left side are written the main DFT functionals for each method. In the right side are included the principal feature added to the functional

The number of DFT functionals and sophistication were increased significantly, as a consequence, John Perdew in June 2000 proposed a idea named "Jacob's Ladder of DFT"[78] (**Figure 3.3**) visualizing the DFT functionals as

a succession of ladder steps that categorizes various approximations of the exchange-correlation functional based on their accuracy and complexity. The ladder comprises five rungs, each one corresponding to five generations of DFT functionals (LDA, GGA, meta-GGA, Hybrids and Double-hybrids). Climbing the Jacob's ladder from the "Hartree World" towards the "Heaven of Chemical Accuracy", the accuracy of the functionals improves, but also the computational cost.

3.3.4 Dispersion Correction

As seen in the section above, sometimes the DFT method does not describe accurately the weak intermolecular forces, such as hydrogen bonds or van der Waals interactions. To solve this problem, dispersion corrections are added to the total energy calculated by DFT. In this thesis, we use Grimme's empirical dispersion correction D2, and D3 with Becke-Johnson (BJ) damping. The D2 correction is included in the DFT functional ωB97X-D used in **Chapters 5, 6, and 7**, and the D3 (BJ) is used in **Chapter 4**.

The Grimme's D2 correction[79] adds pairwise dispersion energy terms to the DFT energy, considering only the C_6 term for pairwise atomic interactions.

The total dispersion energy $E_{\text{disp}}^{\text{D2}}$ is given by:

$$E_{\text{disp}}^{\text{D2}} = -s_6 \sum_{A<B} \frac{C_6^{AB}}{R_{AB}^6} f_{\text{damp}}(R_{AB}) \tag{3.27}$$

Where s_6 is a global scaling factor, C_6^{AB} is the dispersion coefficient for the C_6 term between atoms A and B, R_{AB} is the distance between atoms A and B, $f_{\text{damp}}(R_{AB})$ is the damping function.

The damping function is usually defined as:

$$f_{\text{damp}}(R_{AB}) = \frac{1}{1 + e^{-d(R_{AB}/R_0 - 1)}} \tag{3.28}$$

The Grimme's D3 (BJ)[80,81] correction adds pairwise dispersion energy terms with higher-order contributions, considering C_6, C_8, and C_{10} terms for

pairwise atomic interactions. The Becke-Johnson (BJ) damping helps to avoid overestimation at short distances.

The total dispersion energy $E_{\text{disp}}^{\text{D3(BJ)}}$ is given by:

$$E_{\text{disp}}^{\text{D3(BJ)}} = -\sum_{A<B}\sum_{n=6,8,10} s_n \frac{C_n^{AB}}{R_{AB}^n} f_{\text{damp}}^{(n)}(R_{AB}) \tag{3.29}$$

Where s_n are the global scaling factors for each term, C_n^{AB} is the dispersion coefficients for the n-th term between atoms A and B, R_{AB} is the distance between atoms A and B, and $f_{\text{damp}}^{(n)}(R_{AB})$ is the Becke-Johnson damping function.

The Becke-Johnson (BJ) damping function is defined as:

$$f_{\text{damp}}^{(n)}(R_{AB}) = \frac{1}{1+e^{-d_n(R_{AB}/R_0-1)}} \tag{3.30}$$

Where d_n is the damping parameter for the n-th term, R_0 is the reference distance related to the sum of atomic van der Waals radii.

The Grimme's Dispersion Corrections D2 and D3 described in this section are implemented in Gaussian 16 rev. A.03[62], implicitly within a functional as ωB97X-D, or explicitly as a keyword to request.

3.3.5 GFN2-xTB

Grimme and Bannwarth[82]defined the GFN2-xTB method as a "Semiempirical quantum mechanical method, which represents the first broadly parametrized tight-binding method to include electrostatic and exchange-correlation Hamiltonian terms beyond the monopole approximation." This method combines theoretical foundations from Hartree-Fock and DFT methods, incorporating a self-consistent D4 dispersion model. As GFN2-xTB method is implemented in xtb software developed by Grimme[83] (coded with Fortran), the calculations are very fast, making it extremely useful for exploring conformations, performing MD simulations, and scanning the PES.

In particular, in this thesis we used GFN2-xTB to explore the initial geometries for the transition states by scanning the PES. Additionally, in **Chapter 6** we

also studied the conformations of a polymer by means of an alternative procedure that involves an initial molecular dynamics simulations with GFN2-xTB. The resultant molecular geometries are a good starting point before performing more detailed calculations (DFT).

CHAPTER

4 Using CO_2 to obtain Five Membered Cyclic Carbonates with a Silver-based Catalyst

4.1 Introduction

In the context of a circular chemistry, an attractive route consists in the re-utilization of carbon-based waste into value added products via catalysis[84–86]. The utilization of circular principles, will improve the usage of the natural resources, which will lead to a sustainable future and a more efficient carbon management[87]. Carbon dioxide (CO_2) is a simple carbon-based reactant that is attractive for the synthesis of diverse products such polymerizable monomers[88–92], pharmaceuticals[93–96], bulk chemicals[97,98] and synthetic intermediates[99–103].

In the last 10 years and despite the difficulties, the catalytic conversion of CO_2 has been advanced and reported for both reductive[104–107] and nonreductive transformations[108–114]. More specifically, a notable nonreductive conversion to obtain cyclic carbonates is the [3+2] cycloaddition of CO_2 to epoxides. In the last few years, cyclic carbonates gained synthetic importance as starting points for the formation of decarboxylated compounds with elusive stereocenters[115,116] and CO_2-based polymers and more sustainable materials[117–121]. Cyclic carbonates synthesis based on the [3+2] cycloaddition works well for mono- and di-substituted epoxides in general, however this approach is still limited for sterically demanding oxiranes. To face this challenge, new conceptual designs have arisen that rely on alternative reactivity patterns, some examples are presented in **Figure 4.1**.

A substrate-controlled manifold example is represented in **Figure 4.1 (a)** where a cascade process with a suitable trapping mechanism offers access to highly elusive cyclic carbonates[122,123]. Another cascade process is depicted in **Figure 4.1 (b)**, starting with an α-alkylidene carbonate (prepared *in* or *ex-situ*) and a diol reagent, which leads to a domino transesterification process that produces a 1:1 mixture of an α-hydroxy ketone and different cyclic carbonate[124–126]. Whereas the latter cascade process is able to obtain a high but quite limited degree of structural diversity, the formation of a ketone by-product makes it atom inefficient. The preparation of α-alkylidene carbonate is represented in **Figure 4.1 (c)**[29], which involves a propargyl alcohol and

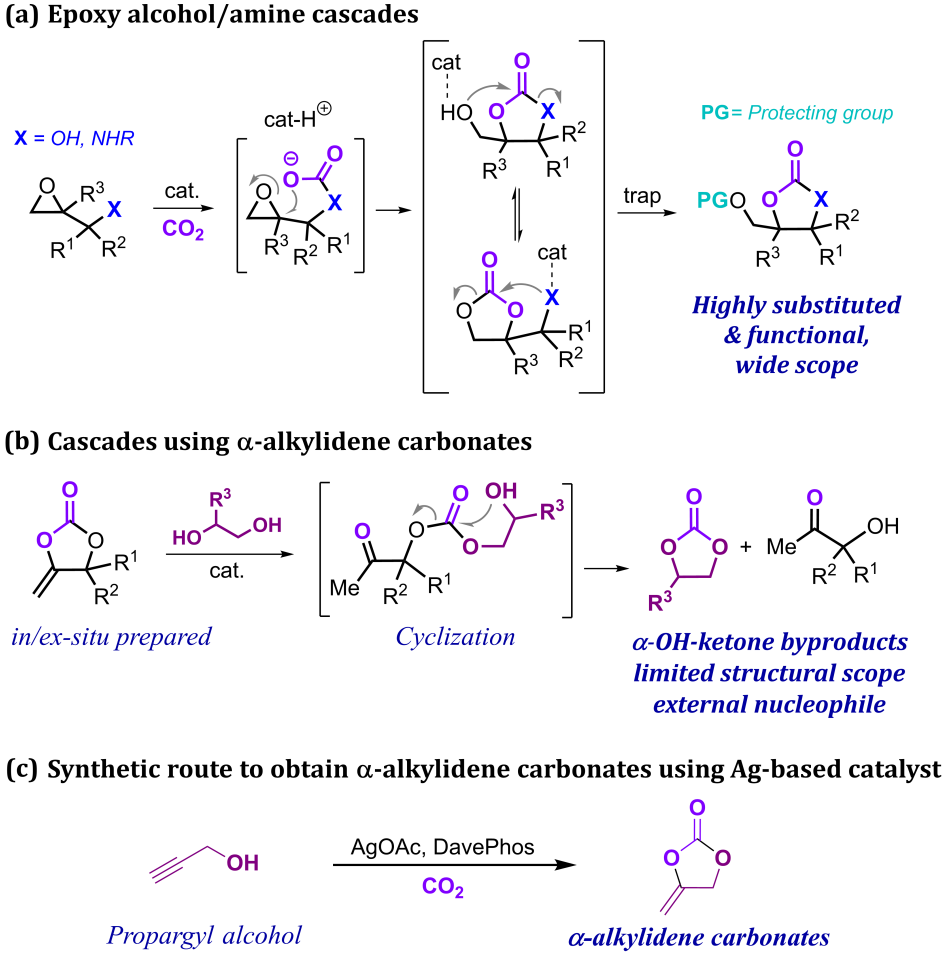

Figure 4.1: (a) Substrate-controlled cascade leading to highly substituted cyclic carbonates, (b) Domino transesterification process involving external diols, (c) Synthesis of α-alkylidene carbonate using a Buchwald-phosphine ligand with a silver(I) salt as a pre-catalyst

CO_2 as a reactants and a Ag-based catalyst. The catalyst choice is due to the assumption of the Thorpe-Ingold effect[127–129], which enhances the cyclization of an α-substituted tertiary or secondary propargyl alcohol. Therefore, a bulky-donor ligand such as Buchwald-phosphine ligands in combination with a silver(I) salt (see **Figure 4.2**) could produce an angle compression effect with a wider population of the appropriate conformer which will initiate the car-

boxylative cyclization.

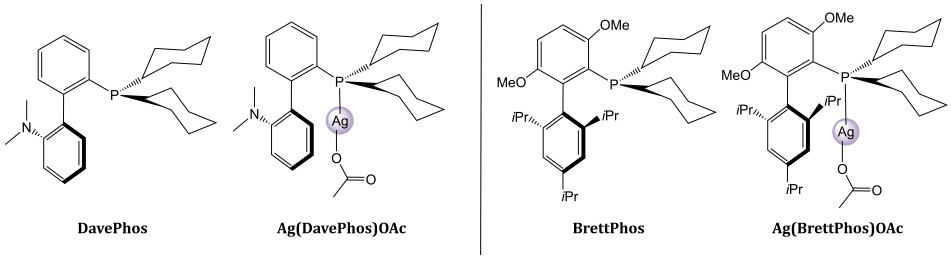

Figure 4.2: Scheme of the Buchwald phosphines DavePhos and BrettPhos and their pre-catalyst complexes when combined with the silver salt AgOAc

To enhance the creation of new cyclic carbonates via a novel cascade process, the Kleij's group members developed the reaction presented in **Figure 4.3** is developed[130]. This procedure consists of the combination of the presence of an intramolecular alcohol (pro)nucleophile with a reactive exocyclic double bond, which will lead to the formation of a keto-functionalized cyclic carbonate, that also will enable a large substitution and functionality scope. The key for this novel path is the use of an alkyne-1,2-diol which induces a skeletal rearrangement of an initially created α-alkylidene carbonate with the building of the keto group as a thermodynamic driving force. Therefore, the reaction to study is the conversion from an alkyne-1,2-diol with CO_2 to a keto-functionalized five-membered cyclic carbonates using Buchwald-phosphines combined with a silver(I) salt as a pre-catalyst under mild conditions. Specifically, the phosphines chosen are commonly named DavePhos and BrettPhos, which will be combined with silver acetate (AgOAc) to create the catalyst complexes studied in this chapter, abbreviated as Ag(DavePhos)OAc and Ag(BrettPhos)OAc respectively (see **Figure 4.2**).

4.2 Objective/Motivation

The objective of this chapter is to understand the mechanistic pathway involved for the novel catalytic domino process based on the transformation of an alkyne-1,2-diol with CO_2 into a highly substituted (saturated) keto-carbonate

in acetonitrile solution at room temperature. To accomplish this goal, DFT calculations were performed considering:

- Two different Buchwald-phosphine ligands, named DavePhos and BrettPhos, each of them bonded to a silver(I) salt (AgOAc) used as a catalyst
- As the substrate has a chiral centre, R- and S-pathways were calculated for each catalyst complex.

The computed mechanistic pathways are supported by the experimental data provided by X.Li, Kleij's group member.

4.3 Computational Details

All calculations were performed using Gaussian 16 version A.03[62]. Due to the nature of the catalyst, which contains a silver atom and a phosphine ligand, the functional and basis set chosen is PBE0-D3(BJ)/SDD/def2tzv[131,132] using dispersion correction with Becke-Johnson damping[133,134]. The temperature chosen is 298 K and an implicit solvent model SMD[65] with parameters for acetonitrile were used. An unrestricted optimization and frequencies analysis were performed to determine the transition state structures and intermediates involved in the mechanistic pathway.

Full access to the computational data stored in ioChem-BD[135] repository is provided through: http://dx.doi.org/10.19061/iochem-bd-1-214

4.4 Results and Discussion

The reaction to study represented in **Figure 4.3** starts with an *alkyne-1,2-diol* as a substrate in the presence of CO_2, using acetonitrile as a solvent and AgOAc with DavePhos as catalyst components. Under these conditions, instead of an expected *α-alkylidene carbonate*, a highly substituted *keto-carbonate* is obtained.

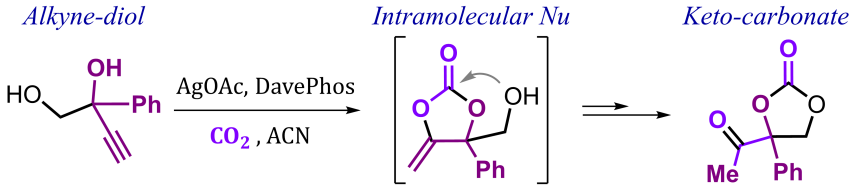

Figure 4.3: Overall computed reaction scheme for the CO_2-based domino synthesis

The silver salt or the phosphine ligand alone do not catalyze the reaction, however, their combination generates a silver complex named from now on *Ag(DavePhos)OAc* (**Figure 4.2**), which induces a high substrate conversion and moderate yield (entry 1, **Table 4.1**). The nature of the phosphine is essential considering that the use of a bulky monophosphine ligand as BrettPhos provides a full conversion and excellent yield (entries 2 and 3, **Table 4.1**). Another silver salt was tested (AgF), and while the reaction time and amount of catalyst is lower than in the other cases, the reaction temperature had to be increased a bit to obtain the same conversion and yield. These last conditions are considered the most favoured ones (entry 3, **Table 4.1**).

Table 4.1: Highlighted screening and optimization data of the Ag- catalyzed conversion of alkyne-1,2-diol and CO_2 into keto-substituted cyclic carbonate[130]

Ag Salt	Phosphine	time (h)	Temp °C	Conv. (%)	Yield (%)
AgOAc	DavePhos	48	25	83	62
AgOAc	BrettPhos	24	25	>99	91 (85)
AgF	BrettPhos	6	40	>99	91 (88)

The nature of the catalyst has been described as a complex generated from a silver(I) salt with a Buchwald-phosphine-ligand as DavePhos or BrettPhos[29]. Notably, the expected product is an *α-alkylidene carbonate* (**Figure 4.1 (c)**) however, the use of an alkyne-1,2-diol causes the *α-alkylidene carbonate* becoming an intermediate instead of a final product. The nature of the catalyst and the initial substrate help to isomerize this last intermediate into a *keto-carbonate* as shown in **Figure 4.3**.

The combination of the phosphine ligands with the silver(I) salt are repre-

sented in **Figure 4.2**, the phosphor atom makes a coordinative bond with the silver atom from the AgOAc salt. The P-Ag-O geometry is totally linear with an angle near to 180°. The biphenyl fragment bonded to the phosphor atom can rotate at room temperature, thus making different configurations for DavePhos possible.

4.4.1 Mechanistic Pathway

The mechanistic pathway and its relative Gibbs free energy profile involved in this reaction are represented in **Figure 4.4**. Since the substrate has a chiral centre, there are diastereoisomeric intermediates and transition states, and to see more clearly the mechanism, only the lowest energetic pathway (based on (R)-substrate) is represented. However, the energetic profiles for both diastereoisomer formations are compared in **Figure 4.5** to describe the complete analysis of this reaction.

In **Figure 4.2** the Ag(DavePhos)OAc catalyst structure is represented, note that the phosphine substituents are not symmetric and can rotate at room temperature. Hence, to correctly understand the reactivity of this reaction, all structures showed in **Figure 4.4** and **Figure 4.5** were calculated with the same fixed chiral phosphine conformation. This catalyst was chosen since it was able to compare directly with a previous work[29] which computed the conversion of a simpler propargylic alcohol precursor into an *α-alkylidene carbonate* using Ag(DavePhos)OAc as a catalyst.

The mechanism starts with the *(R)*-substrate, CO_2 and the pre-catalyst complex Ag(DavePhos)OAc used as a reference (0.0 kcal·mol^{-1}) and known as **Reactants**. The first transition state **TS-1** (4.7 kcal·mol^{-1}) is the concerted reaction of the deprotonation of the tertiary alcohol of the substrate, which is bonded through the triple bond to the silver atom, followed by CO_2 activation by the newly created alkoxide (geometry showed in **Figure 4.7**). This concerted transition state results in the intermediate **A** (3.7 kcal·mol^{-1}) which includes the catalyst complex bound to the substrate with a terminal carbonate

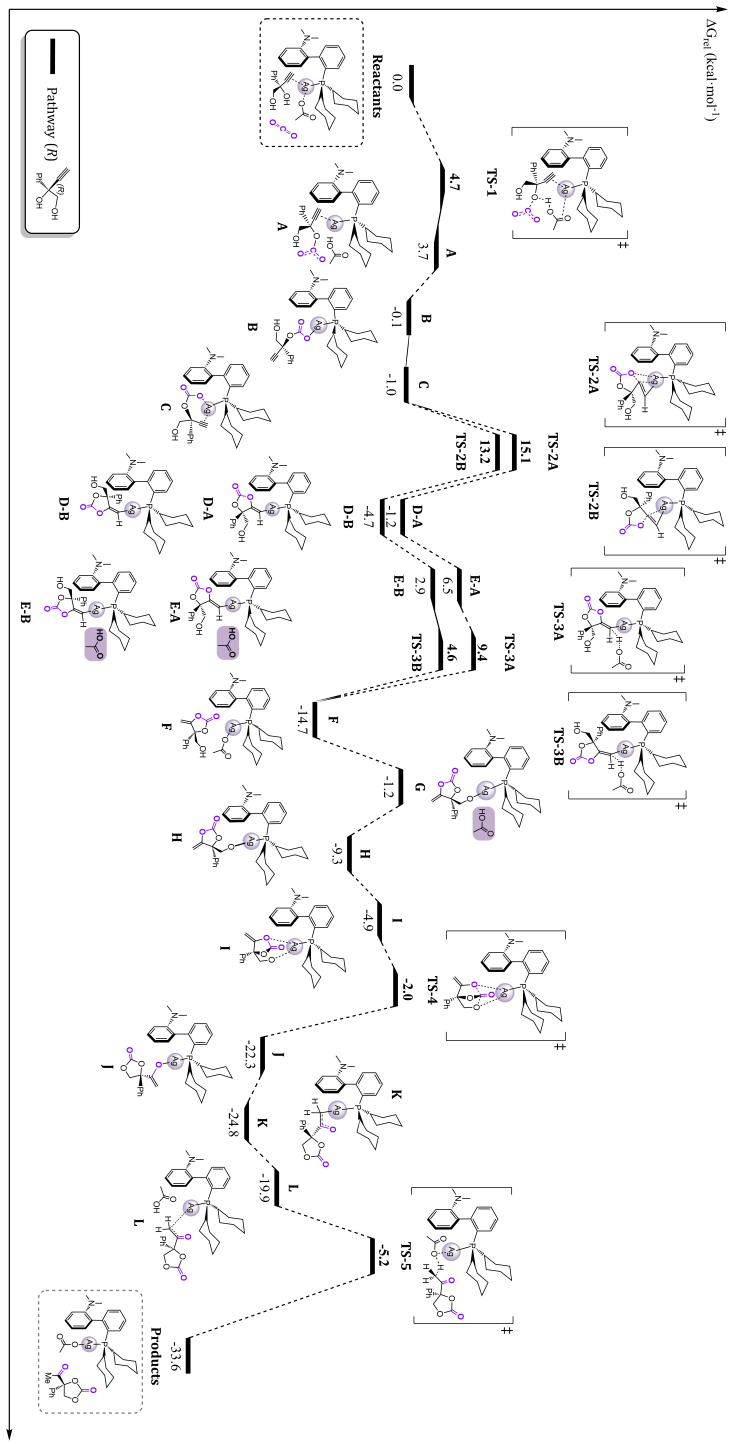

Figure 4.4: Gibbs Free Energy profile in kcal·mol^{-1} for the mechanistic pathway (R)

anion and an acetic acid molecule. The latter will not be involved during the formation of the further intermediates and transition states until **E-A** and **E-B**.

The intermediate **B** (-0.1 kcal·mol^{-1}) has a linear O-coordination through the carbonate which replaces the initial alkyne coordination to the silver atom, although it will be restored in the intermediate **C** (-1.0 kcal·mol^{-1}), via a bidentate coordination mode. The next transition state **TS-2** is the alkylidene cyclic carbonate formation starting from the intermediate **C**. The five-membered cyclic carbonate that is created during this transition state could be obtained through two possible orientations with respect to the fixed conformation of Ag(DavePhos). This results into two different diastereoisomers, both differ in the double-bond configuration where **TS-2A** (15.1 kcal·mol^{-1}) corresponds to a ***Z*** configuration and **TS-2B** (13.2 kcal·mol^{-1}) to ***E*** (geometries for both **TS-2A** and **TS-2B** are represented in **Figure 4.8**). From now on, all structures and intermediates **"A"** will be referred to the starting configuration ***Z*** and **"B"** to the ***E***.

The following structures **D-A** (-1.2 kcal·mol^{-1}) and **D-B** (-4.7 kcal·mol^{-1}) shown an alkene carbon to the silver centre from Ag(DavePhos). These structures are similar to the ones reported[29] before the final protodemetalation takes place providing alkylidene carbonates. Nevertheless, the reaction studied in this chapter corresponds to a more substituted substrate, which leads to more complex pathways where ***Z***- and ***E***- configurations are feasible in addition to the ***(R)*** and ***(S)*** ones from the substrate.

The next structures **E-A** (6.5 kcal·mol^{-1}) and **E-B** (2.9 kcal·mol^{-1}) include a molecule of the acetic acid which enables the protodemetalation through **TS-3A** (9.4 kcal·mol^{-1}) and **TS-3B** (4.6 kcal·mol^{-1}) by means of a proton transfer from the acetic acid's hydrogen to the alkene carbon bound to the Ag(DavePhos) complex (geometries for **TS-3A** and **TS-3B** shown in **Figure 4.9**). During these last steps, the (***E***) isomer structures are more energetically favoured than the (***Z***) ones, nonetheless, the energetic difference shows that both pathways are equally feasible under these conditions. As a result, intermediate **F** (-14.7 kcal·mol^{-1}) has the α-alkylidene cyclic carbonate released with the Ag(DavePhos) bound to the oxygen alkoxide from the acetate. The pendant

alcohol from the newly synthesised cyclic carbonate is then deprotonated by the acetate bound to the silver centre obtaining structure **G** (-1.2 kcal·mol^{-1}), which is the pendent alkoxide bound to the Ag(DavePhos) complex and an acetate acid. It was not possible to identify the transition state involved during this deprotonation for this uphill process. Again, the acetic acid is not present in the following structures until intermediate **L**. The de-coordination of the O-carbonate in **H** (-9.3 kcal·mol^{-1}) followed by a rotation and re-coordination of the outer oxygen next to the olefin results into intermediate **I** (-4.9 kcal·mol^{-1}). An isomerization process occurs in the transition state **TS-4** (-2.0 kcal·mol^{-1}), with a tetrahedral geometry for the carbon centre (geometry showed in **Figure 4.10**), a new five-membered cyclic carbonate is obtained with an enol coordinated to the Ag(DavePhos) complex by its oxygen atom as represented in structure **J** (-22.3 kcal·mol^{-1}). The most thermodynamically stable intermediate is **K** (-24.8 kcal·mol^{-1}), resulting from an oxygen to carbon rearrangement with the enolate coordinated by the terminal carbon to the catalyst. As said before, the acetic acid plays a key role in the last part of the reaction approaching the complex in structure **L** (-19.9 kcal·mol^{-1}). The last transition state **TS-5** (-5.2 kcal·mol^{-1}) is the proton transfer from the acetic acid to the carbon atom of the enolate fragment (geometry represented in **Figure 4.11**), forging the *keto-carbonate* with the regenerated catalyst complex Ag(DavePhos)OAc named as **Products** with the most stable energetic value (-33.6 kcal·mol^{-1}).

As seen in **Figure 4.4** and **Figure 4.5**, the overall mechanistic pathway for the conversion of the substrate includes different key steps: a CO_2 activation by a propargylic diol succeeded by a triple bond attack, a carbonate isomerization step including a pendant alcohol and a tautomerization. All of these steps are promoted by proton transfer/H-abstraction. The determining transition state is **TS-2** with a maximum energetic span of 16.1 kcal·mol^{-1} for the R-substrate and 16.6 kcal·mol^{-1} for the S-substrate. These data concur with the experimental finding that the substrate (regardless of its stereochemistry), may undergo the reaction at room temperature to obtain a *keto-carbonate* using a Ag(DavePhos)OAc as a pre-catalyst and acetonitrile as a solvent.

The comparison showed in **Figure 4.5** represents both pathways for the

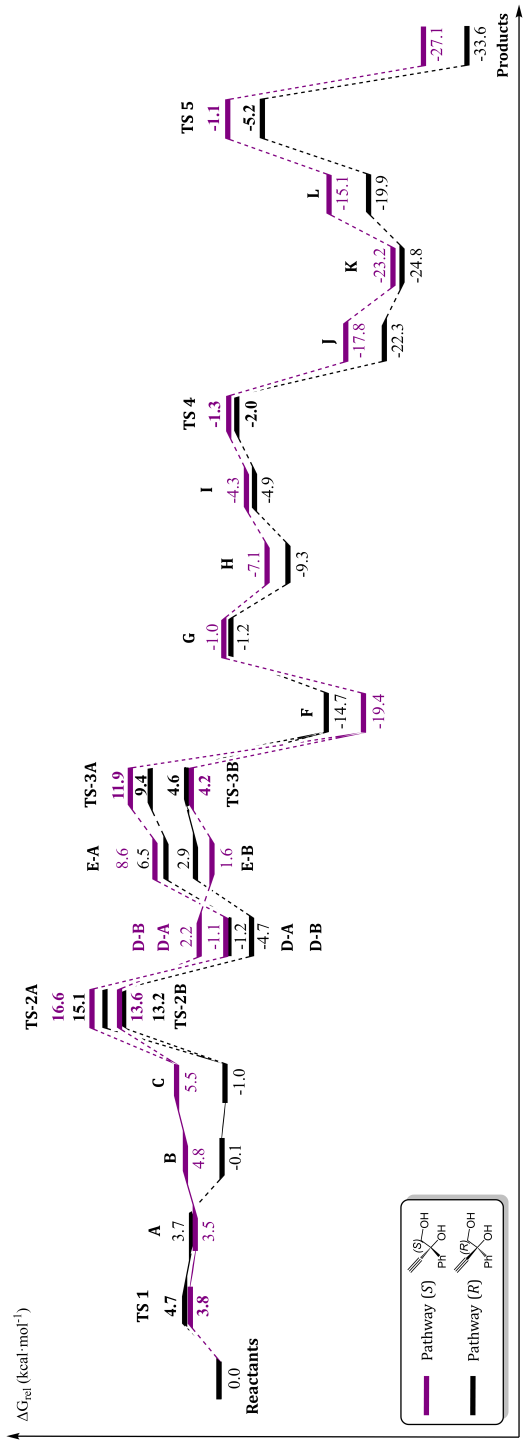

Figure 4.5: Comparison between Gibbs free energy profiles for the pathways (R) and (S) in kcal·mol^{-1}

conversion of R- and S- configured substrates. Whereas the pathway-S is more energetically disfavoured than the pathway-R, both substrates are able to undergo the reaction successfully through a cascade process. The S-pathway is initially slightly more feasible than the R one with energetic values for **TS-1** and **A** of 3.8 and 3.5 kcal·mol^{-1} respectively. However, when the acetic acid is not present, the energies become more unstable than those in the R-pathway in the following structures with a 4.8 kcal·mol^{-1} for **B**, and 5.5 kcal·mol^{-1} for **C**. The determining transition state **TS-2A** related to the ***Z***-isomer remains being the most disfavoured for both structures having a value of 16.6 kcal·mol^{-1} for the S-pathway. The **TS-2B** (***E***-isomer) has also similar values for both isomers, with a value of 13.6 kcal·mol^{-1}. The behaviour changes in the resulting intermediates because the structure **D-B** (***E***) at 2.2 kcal·mol^{-1} is more disfavoured than the **D-A** (***Z***) at -1.1 kcal·mol^{-1}, contrary than R-pathway. Nevertheless, the reactivity changes again for the following structures having similar values for **E-A** and **TS-3A** having a Z-configuration (8.6 and 11.9 kcal·mol^{-1}), and **E-B** and **TS-3B** with E-configuration (1.6 and 4.2 kcal·mol^{-1}).

The intermediate **F** in the S-pathway is more thermodynamically favoured located at -19.4 kcal·mol^{-1}. The last structures and transition states of the manifold are energetically higher for the S-pathway, starting with the **G**, **H** and **I** intermediates that have relative energies of -1.0, -7.1 and -4.3 kcal·mol^{-1} respectively. The energetic values in this latter portion of the computed profiles are very close for both pathways. The transition state **TS-4** for the S-pathway has an energetic value of -1.3 kcal·mol^{-1}, which leads to **J** located at -17.8 kcal·mol^{-1}. The next structure **K** is the most feasible intermediate with an energy of -23.2 kcal·mol^{-1}. The last intermediate **L** and transition state **TS-5** were calculated at -15.1 and -1.1 kcal·mol^{-1} respectively. The mechanistic profile ends with the most thermodynamically stable structure at -27.1 kcal·mol^{-1} and corresponds to the *keto-carbonate* product and the recovered catalyst.

Taking into account the data listed in **Table 4.1**, the mechanistic profile using the Ag(BrettPhos)OAc complex was calculated and is represented in **Figure 4.6**. This catalyst was chosen due to the similar successful results between AgF and AgOAc salts, with the conversion and yield being really close, and there-

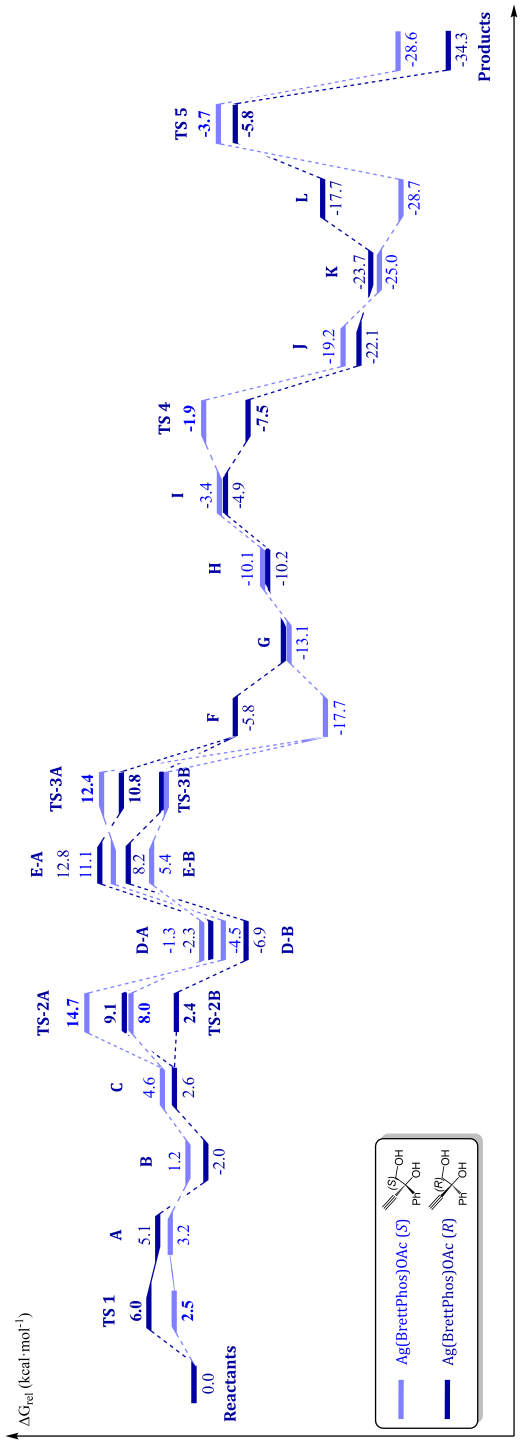

Figure 4.6: Comparison between Gibbs free energy profiles for the pathways (R) and (S) in kcal·mol^{-1} using Ag(BrettPhos)OAc

fore, both salts are effective precursors to obtain the *keto-carbonate*. Whereas the phosphine ligand BrettPhos is more sterically hindered than DavePhos, the reactivity related with the counterion of the AgOAc salt has to be similar. Considering the deep knowledge for the mechanistic pathway obtained by the calculations showed above, the silver salt AgOAc was chosen.

The overall mechanism shown in **Figure 4.6** is slightly more energetically favoured than the one represented in **Figure 4.5**, nevertheless, the energetic differences have not a significant effect on the outcome of the reaction. For the BrettPhos profile, the first transition states **TS-1** have an energetic value of 6.0 and 2.5 kcal·mol^{-1} respectively, for the R- and S-pathway in comparison with the DavePhos pathway with these transition states located at 4.7, and 3.8 kcal·mol^{-1}. While this first transition state is more disfavoured for the R-pathway than the S-based one, the following transition states show a different relationship. The determining transition state (TDTS) for both DavePhos pathways is **TS-2**. While the S-BrettPhos pathway follows the same trend, the R-BrettPhos pathway is different at at the stage of **TS-3**, which corresponds to the H-transfer to the alkene carbon bound to the Ag atom to release the five-membered cyclic carbonate instead of carbonate ring closure. The energies involved in S-BrettPhos pathway are 14.7 and 8.0 kcal·mol^{-1} for **TS-2A** and **TS-2B**, while for the R-Brettphos manifold these values are 9.1 and 2.4 kcal·mol^{-1}. The **TS-3A** is slightly more favoured than the last transition state in the S-BrettPhos path (12.4 kcal·mol^{-1}), and a bit less stable in the R-BrettPhos mechanism (10.8 kcal·mol^{-1}). The following structures have a similar pattern as already noted in **Figure 4.5** and refers to all intermediates and transition states being more stable than the initial reference. While the profile for R-pathway has less energetic differences between the structures computed for the S-pathway display larger differentiation. In this latter part, the structures involved in the R-pathway are not always the most feasible ones, nonetheless, the transition state **TS-4** (-7.5 kcal·mol^{-1} for R, and -1.9 kcal·mol^{-1} forS), the last transition state **TS-5** (-5.8 and -3.7 kcal·mol^{-1}) and the **Products** (-34.3 and -28.6 kcal·mol^{-1}) keep the same behaviour as seen before with the DavePhos complex.

The results shown during this computational process are not relevant to

compare directly with the experimental results. Note that the calculations carried out for the Ag(DavePhos) complex were fixed because the structure can rotate, and there is a realistic possibility that the conformation depends on the position of the ligands. On the other hand, Ag(BrettPhos) is more sterically hindered but the rotation of the rings could be similar, thereby creating more similarities in the reactivity compared to DavePhos. Moreover, in the case of DavePhos it is possible to keep the reactants and acetic acid more close to the reactive centre due to this geometry. Therefore, this computational study allows to understand the reaction with both catalysts by thermodynamic forces, but does not allow to determine the relative rate of the reaction depending on the concentration of the reactants and catalyst.

4.4.2 Mechanistic Pathway Structures

The following figures describe the geometries for the transition states involved in the mechanistic pathway shown in **Figure 4.4**. In this section, key distances and angles will be included in a Table to combine them with the respective Figure which illustrate the schematic and tridimensional representations.

The first transition state **TS-1** is represented in **Figure 4.7** and its key angle and distances values are provided in **Table 4.2**. As described before, **TS-1** corresponds to a concerted transition state that involves CO_2 activation and a proton transfer. The oxygen atom O1 from the complex Ag(DavePhos)OAc deprotonates the tertiary alcohol from the (R)-substrate (H2 and O3), and consequently, the angle O1-H2-O3 is linear with a value of 175.2°. The distances O1-H2 (1.31 Å) and H2-O3 (1.10 Å) are longer than expected for an O-H bond. At the same time, the oxygen atom O3 from the generated alkoxide attacks the carbon C4 from the CO_2 molecule, bending its linear molecular geometry to 151.1°, which will become an approximately 120° when the carbonate is formed in the next structure **A**.

The second transition state for both structures **TS-2A** and **TS-2B** are shown in **Figure 4.8**, and their key geometry values are represented in **Table 4.3**, cor-

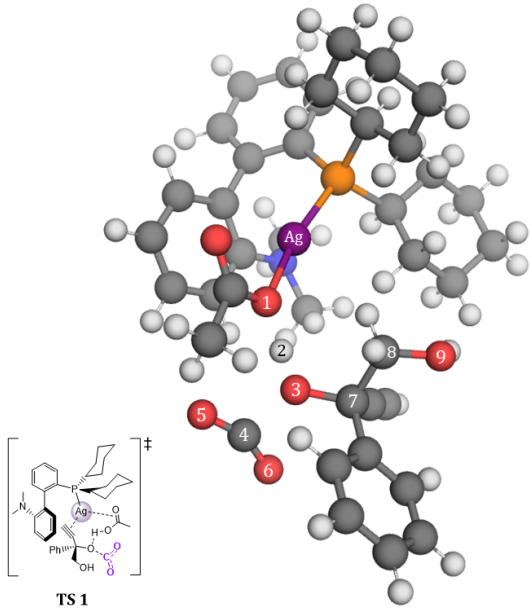

Figure 4.7: Geometry for the transition state **TS-1** for the (R)-pathway using Ag(DavePhos)

Table 4.2: Angles and distances for the geometry of **TS-1** presented in **Figure 4.7**

Atom labels	Angle (°)
O1-H2-O3	175.2
Ag-O1-H2	115.9
H2-O3-C4	117.1
O3-C4-O5	102.7
O6-C4-O3	106.2
O5-C4-O6	151.1

Atom labels	Distance (Å)
Ag-O1	2.14
O1-H2	1.31
H2-O3	1.10
O3-C4	1.86
O5-C4	1.22
O6-C4	1.21

responding to a ring closure from two different sides. The orientation of the substrate bound to Ag(DavePhos) for **TS-2A** matches with the ***Z***-isomer, while **TS-2B** with the ***E***-isomer. Despite the energetic differences shown in **Figure 4.4**, the distances and angles for the ring closure step are very close, the outer oxygen atoms from the carbonate anion O6 are located within 2 Å and the angle related with the closure O6-C11-C12 is 112° for both structures. The distance between C11 and C12 for the alkene part is near 1.25 Å, and the angle related

with the alkene and the Ag atom from the catalyst C11-C12-Ag is around 113° for both structures. The five-membered cyclic carbonate bound by the alkene carbon C12 to the catalyst is represented in the following structures **D-A** and **D-B**, with the release of the α-alkylidene carbonate intermediate occurring in the next transition state, with an active role for acetic acid.

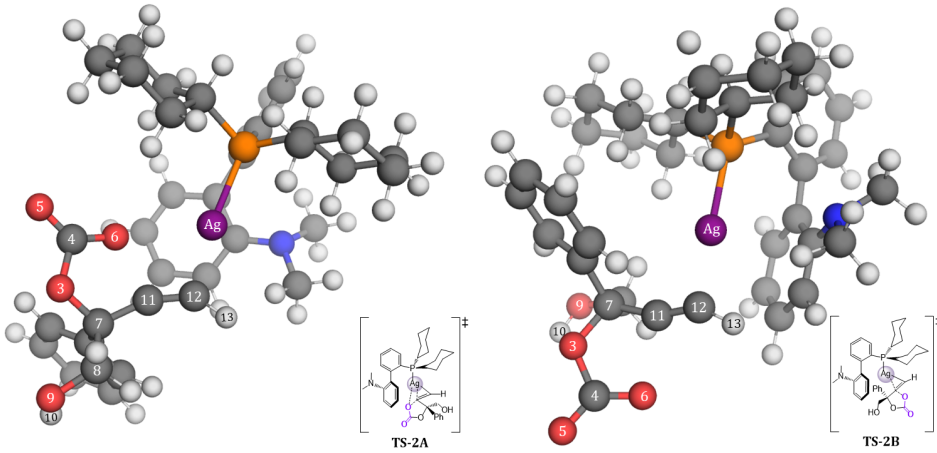

Figure 4.8: Geometry for the transition states **TS-2A** and **TS-2B** in the (R)-pathway using Ag(DavePhos)

Table 4.3: Angles and distances for the geometry of **TS-2A** and **TS-2B** presented in **Figure 4.8**

	Atom labels	**Angle (°)**
TS-2A	O6-C11-C12	112.6
	C11-C12-Ag	106.7
	H13-C12-Ag	113.7
TS-2B	O6-C11-C12	112.8
	C11-C12-Ag	99.3
	H13-C12-Ag	112.5

	Atom labels	**Distance (Å)**
TS-2A	Ag-C12	2.18
	C11-C12	1.26
	O6-C11	2.07
TS-2B	Ag-C12	2.20
	C11-C12	1.25
	O6-C11	2.21

In **Figure 4.9** and **Table 4.4** are presented the structures and key geometry values for the **TS-3A** and **TS-3B**. These transition states illustrate a proton transfer made by the acetic acid, releasing the five-membered cyclic carbonate in the next intermediate and the recovered catalyst complex Ag(DavePhos)OAc. The

stereochemical ***Z***- and ***E***-configuration is maintained from **TS-3A** and **TS-3B** respectively. During this latter transition state, the distances for the proton transfer are slightly different, while **TS-3A** has the distance for alkene carbon C12 and the hydrogen H2 from acetic acid at 1.44 Å, while for **TS-3B** this is closer with a value of 1.36 Å. The other relevant distance related with this proton transfer is between the oxygen O1 from the acetic acid and its proton H2, which has a value of 1.19 Å for **TS-3A** and 1.25 Å for **TS-3B**. These slight differences are due to the orientation of the substrate related with the catalyst which could be a bit more accessible. Consequently, the relative Gibbs free energy profile in **Figure 4.4** shows an energetic preference for one of these structures although both of them are feasible. Despite of that, the angle C12-H2-O1 related with this reaction is very similar for both structures, being around 177°. Such an angle as consequence, enables a successful proton transfer and allows for subsequent α-alkylidene cyclic carbonate release in **F** and to be bound again in intermediate **G**.

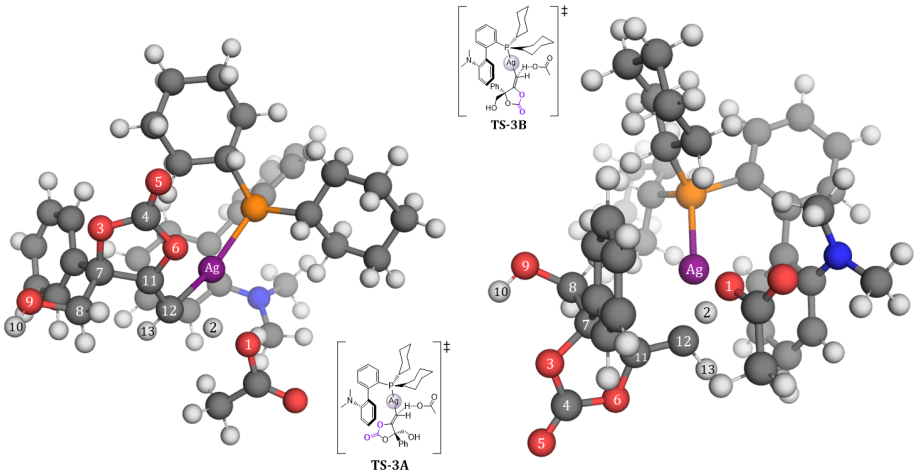

Figure 4.9: Geometry for the transition states **TS-3A** and **TS-3B** in the (R)-pathway using Ag(DavePhos)

The transition state **TS-4** presented in **Figure 4.10** and its key geometric values collected in **Table 4.5**, describe an isomerization process. From the tetrahedral intermediate **I**, the new *keto-carbonate* is generated during **TS-4** through

Table 4.4: Angles and distances for the geometry for **TS-3A** and **TS-3B** presented in **Figure 4.9**

	Atom labels	**Angle (°)**
TS-3A	C12-H2-O1	176.4
	C11-C12-Ag	104.6
	H13-C12-H2	115.8
TS-3B	C12-H2-O1	177.6
	C11-C12-Ag	111.6
	H13-C12-H2	115.0

	Atom labels	**Distance (Å)**
TS-3A	Ag-C12	2.23
	C12-H2	1.44
	H2-O1	1.19
TS-3B	Ag-C12	2.21
	C12-H2	1.36
	H2-O1	1.25

a ring closure involving C4 and O9 (distance is 1.53 Å) and simultaneously a ring opening that comprise O6 and carbon C4 (distance 1.70 Å). The Ag atom from the catalyst complex Ag(DavePhos) has similar distances to the carbonyl carbon C4, and both outer oxygens O6 and O9, while the Ag-C4 distance is the longest one being 2.92 Å, while the distance to O6 and O9 are 2.48 Å and 2.36 Å respectively. Thus, the silver atom could easily change its coordination by the substrate along the conformational conversion, making this transition state feasible geometrically. The tetrahedral geometry around the (initial) carbonyl carbon C4 enhances the reactivity, and the angles related between the outer oxygens O6 or O9 and the carbonyl carbon C4 and the oxygen O5 are 114.6° and 118.3° respectively. In the resulting product, the oxygen O6 will be bound to the silver atom once the new cyclic carbonate is created in intermediate **J** (**Figure 4.4**).

Table 4.5: Angles and distances for the geometry for **TS-4** presented in **Figure 4.10**

Atom labels	**Angle (°)**
O6-C4-O5	114.6
O9-C4-O5	118.3
O6-C4-Ag	58.1
O9-C4-Ag	53.6
O6-C4-O3	97.5
O3-C4-O9	102.8

Atom labels	**Distance (Å)**
Ag-C4	2.92
Ag-O6	2.48
Ag-O9	2.36
O6-C4	1.70
O9-C4	1.53
O3-C4	1.44

In **Figure 4.11** and **Table 4.6**, the geometry scheme and values for the last

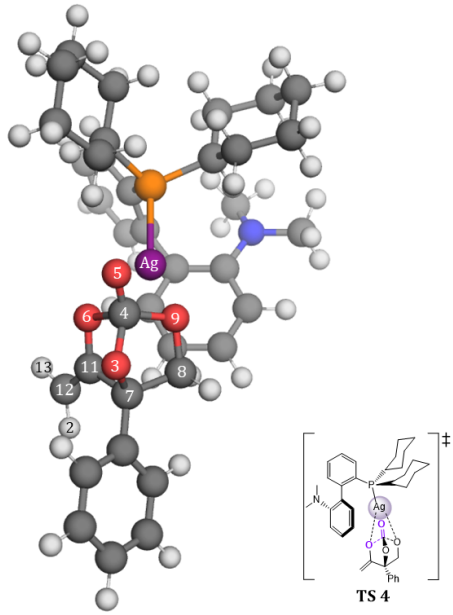

Figure 4.10: Geometry for the transition state **TS-4** in the (R)-pathway using Ag(DavePhos)

transition state **TS-5** are shown, which relate to a proton transfer that releases the final product, a *keto-carbonate*. This process consists of a protonation of carbon C12 by the H10 from the acetic acid group. This protonation causes a change in the hybridation of C12 connected to C11, with an interatomic value of 1.46 Å which is in the middle of an alkene and alkane C-C bond *(note that theoretical values are 1.54 Å and 1.35 Åfor a C-C and a C=C bond, respectively)*. The aforementioned change in hybridization will help to create a ketone in the final product, and moreover, the angle C12-C11-O6 is already trigonal with a value of 123.8°. The proton transfer itself results in an angle of 164.1°, and despite being less linear than **TS-3** and **TS-1** structures, it is feasible. The distance from the acetic acid oxygen O1 and hydrogen H10 is 1.30 Å, which is similar to the distance between carbon C12 and hydrogen H10 (1.36 Å).

Note that only transition states are discussed in this section, and there were selected to better understand the geometries involved in the key steps during the reaction. With these structures, it is possible to imagine the intermediates

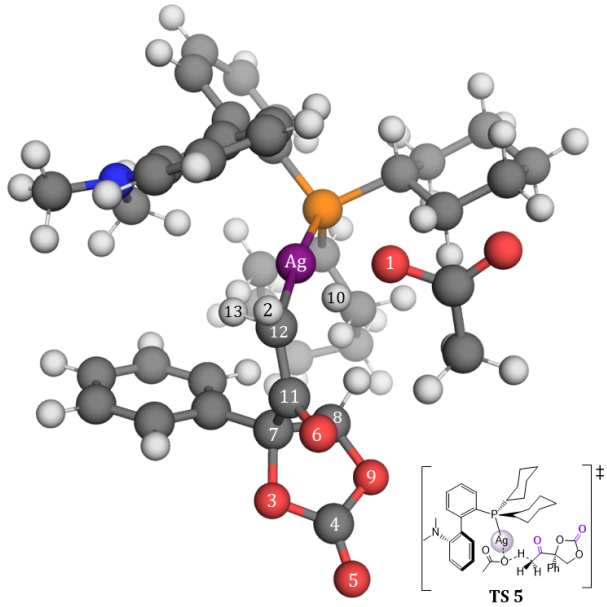

Figure 4.11: Geometry for the transition state **TS-5** for the (R)-pathway using Ag(DavePhos)

Table 4.6: Angles and distances for the geometry of **TS-5** presented in **Figure 4.11**

Atom labels	**Angle (°)**
C12-H10-O1	164.1
H13-C12-H2	126.8
H2-C12-H10	90.5
C12-C11-O6	123.8

Atom labels	**Distance (Å)**
Ag-C12	2.42
C12-H10	1.36
H10-O1	1.30
C11-C12	1.46

through the geometry and reactivity described in each transition state which supports the schematic mechanism shown in the **Figure 4.4**, thus creating a specific and overall understanding of the mechanism.

4.5 Conclusions

The central focus of this chapter was to examine the mechanistic pathway involved with the synthesis of keto-substituted five-membered cyclic carbonates, starting from alkyne-1,2-diols as modular substrates, CO_2 as a renewable

carbon reagent and promoted by a Ag-based catalyst. In pursuit of this aim, a detailed computational analysis based on DFT calculations has revealed the main mechanistic features of this process and how the catalyst composed of a different phosphine-ligand (DavePhos or BrettPhos) coordinated to a silver(I) salt (AgOAc) operates, all supported by experimental data provided by X. Li (Kleij's group member). Moreover, the chiral centre of the substrate has also been considered in this mechanistic pathway, thus offering a complete understanding of this reaction including all possible scenarios.

The pathway related to the R-substrate is more favoured than the S-substrate for both Ag(DavePhos)OAc and Ag(BrettPhos)OAc catalysts. Furthermore, the formation of an α-alkylidene carbonate as an intermediate instead of being a final product is demonstrated by the higher thermodynamic stability of the keto-carbonate (product) which concurs with the experimental data. The determining transition state (TDTS) for both R- and S- Pathways using the Ag(DavePhos)OAc catalyst corresponds to the ring closure, with the ***E***-configuration being more energetically favoured than the ***Z***.

The mechanistic profile for the path catalyzed by Ag(BrettPhos)OAc is slightly more energetically feasible compared to Ag(DavePhos)OAc. However, the energetic differences are not directly comparable with the experimental behaviours that have a moderate yield for Ag(DavePhos)OAc and high yield for Ag(BrettPhos)OAc. A potential explanation could be that the catalyst complex can rotate, leading to conformational changes that depends on the position of the ligands, thereby favouring the reaction catalyzed by Ag(BrettPhos)OAc. Therefore, the computational study allows to understand the reaction with both catalysts by thermodynamic forces but does not enable the determination of the relative reaction rates depending on the concentration of the reactants and catalyst.

In summary, a new cascade process has been discovered, which begins with alkyne-1,2-diol and CO_2, catalyzed by an Ag-based catalyst in acetonitrile solution at room temperature, obtaining a wide scope of keto-substituted five-membered cyclic carbonates. The catalyst is composed by a Buchwald phosphine-ligand (DavePhos or BrettPhos) coordinated to a silver(I) salt (AgOAc)

and the substrate has a chiral centre. All of these pathways were calculated, providing insights into the mechanism involved in this reaction and demonstrating the feasibility of both pathways catalyzed by Ag(BrettPhos)OAc or Ag(DavePhos)OAc.

UNIVERSITAT ROVIRA I VIRGILI
COMPUTATIONAL INSIGHTS OF CATALYTIC CARBON DIOXIDE VALORIZATION AND CIRCULAR RECYCLING PROCESSES
Alba Villar Yanez

CHAPTER

5 From Five to Six Membered Cyclic Carbonates

5.1 Introduction

During the last decade, there has been a growing interest in new catalytic processes focused on the valorisation of carbon dioxide (CO_2)[136–139] to provide organic molecules used as precursors for polymers[140–143], fine chemicals[144–146] and pharmaceuticals[147–149]. The preparation of heterocycles such as cyclic carbonates[150–152], carbamates[153–155] and ureas[156,157] by a non-reductive transformation of CO_2 is one of the most applied valorisation routes. Both organocatalysts[158–160] and metal-based catalysts[130,161–163] are able to activate a co-reactant such as cyclic ethers, to produce a nucleophilic intermediate species that activates CO_2 to obtain the desired product. In general, the synthesis of larger rings remains as a challenging target due to the difficulties related to both thermodynamic and kinetic aspects. In particular, routes to generate six-membered cyclic carbonates are scarce[164–169] and often depend on stoichiometric approaches. As an exception, successful coupling reactions between oxetanes and CO_2 have been discovered, though currently there is still a lack of effective catalysts for these substrates[170–173] and oxetanes are less common substrates than epoxides. Therefore, new ideas are required to obtain larger functionalized heterocycles that can be used as a synthetic intermediates[174,175] and polymerizable monomers, and specifically, cyclic carbonates[176–180].

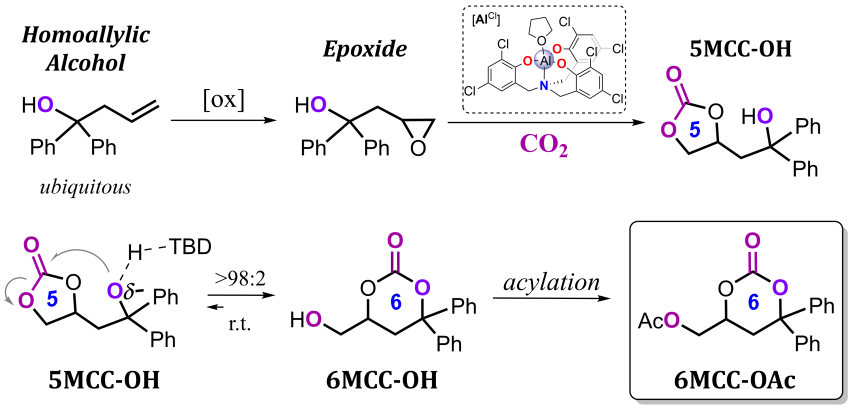

Figure 5.1: Scheme for the synthesis of the 5MCC-OH from homoallylic alcohols and its isomerization and acylation into 6MCC-OAc

A study made by Kleij group[88] examined the synthesis of a five-membered cyclic carbonate and its subsequent organocatalytic trapping to form elusive six-membered cyclic carbonates (**Figure 5.1**). The synthesis of the five-membered cyclic carbonate uses a homoallylic alcohol as a reactant because it is a ubiquitous precursor with an important role in organic synthesis[181–183]. The terminal alkene group from the homoallylic alcohol can be converted into an epoxide, that combined with CO_2 can be transformed into a five-membered cyclic carbonate[184–188] with a tertiary alcohol (**5MCC-OH**) in high yield using a Al(III) based binary catalyst[189,190].

This chapter will focus on the reaction presented in **Figure 5.1**, which starts with the activation of five-membered cyclic carbonate **5MCC-OH** catalyzed by TBD (1.5.7-triazabicyclo-[4.4.0]dec-5-ene)) and evolves into a six-membered cyclic carbonate with a primary alcohol group (**6MCC-OH**). The pendant alcohol from **6MCC-OH** can be protected using acetyl imidazole (AcIm), resulting in the acylated product of six-membered cyclic carbonate (**6MCC-OAc**).

5.2 Objective/Motivation

The main objective of the work reported in this chapter is to study the mechanistic pathway involved in the conversion of a five-membered cyclic carbonate with a tertiary alcohol (5MCC-OH) into an acylated six-membered cyclic carbonate (6MCC-OAC) using TBD as a catalyst and AcIm as an acylating agent in acetonitrile solution under mild conditions. Two kinds of computational studies were performed:

- DFT studies to understand the mechanistic pathway involved from 5MCC-OH to 6MCC-OAc.
- Exploration of alternative mechanistic pathways via DFT calculations to complete the knowledge about the entire process.

The synergy between the experimental data provided by the Kleij group[88] and computational studies allows to gain a deeper understanding of the studied reaction.

5.3 Computational Details

DFT calculations were performed using ωB97X-D functional[191] and the 6–311G**[192,193] basis set. All structures in this study were calculated by using Gaussian 16 program, revision A.03[62]. Unconstrained optimizations and vibrational analysis were carried out in order to find the nature of the intermediates and transition states. To emulate the experimental conditions, all calculations were performed at 298.15 K (room temperature) including an implicit solvent model SMD[65] with parameters for acetonitrile. Full access to the computational data is provided through ioChem-BD repository[135]: https://dx.doi.org/10.19061/iochem-bd-1-171.

To find the initial geometries for the transition states, the Potential Energy Surface (PES) was scanned using Gaussian 16 rev. A.03[62] at the same DFT level outlined above. For faster or multi-dimensional scans in the potential energy surface, the GFN-xTB[83] version 6.4.1 program was used. The temperature chosen was the same as in Gaussian calculations (298.15 K), and the implicit solvent model used was GBSA with acetonitrile parameters.

5.4 Results and Discussion

The reaction studied is presented in **Figure 5.2**, it starts with a five-membered cyclic carbonate with a tertiary alcohol and two phenyl groups as a substituents (**5MCC-OH**), which isomerizes into an intermediate six-membered cyclic carbonate with a primary alcohol (**6MCC-OH**) that is trapped by acylating the pendent alcohol resulting into an acylated six-membered cyclic carbonate (**6MCC-OAc**). The overall reaction is catalyzed by the organocatalyst TBD, the acylating agent is AcIm in acetonitrile solution under mild conditions.

Despite the effectiveness of other bases such as DBU[a], DABCO[b], DBN[c], TEA[d] etc., the best results were achieved for TBD due to its versatility, capable

[a] DBU=1,8-diazabicyclo[5.4.0]-undec-7-ene
[b] DABCO=1,4-diazabicyclo[2.2.2]octane
[c] DBN=1,5-diazabicyclo[4.3.0]non-5-ene
[d] TEA=triethylamine

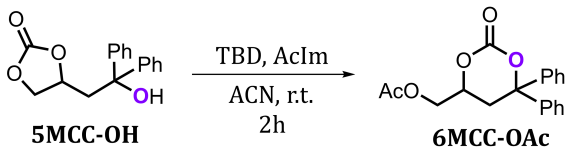

Figure 5.2: Scheme showing the optimized experimental conditions for the conversion from **5MCC-OH** into **6MCC-OAc**

of functioning both as a base and as a proton-relayspecies involved in breaking and creating hydrogen bonds. In particular, the best experimental conditions for this reaction to reach high substrate conversion and a 93% NMR yield (91% - yield of isolated 6MCC-OAc)) were achieved by using TBD, AcIm, in acetonitrile solution, at room temperature under inert atmosphere (N_2 or Ar)[88]. (Experimental data provided by Chang Qiao, an ex-member of Kleij group)

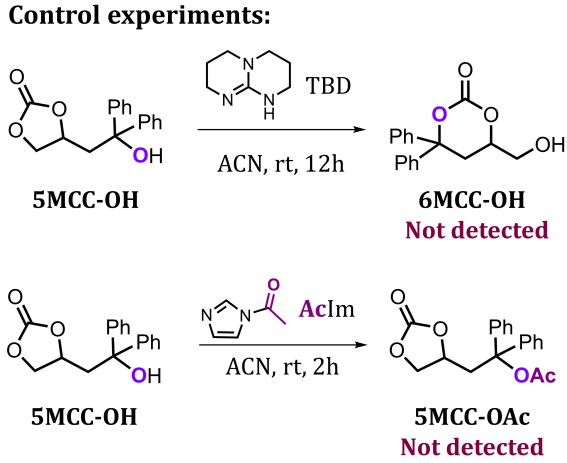

Figure 5.3: Control experiments starting with the reactant **5MCC-OH** using catalyst (TBD), and the influence of the acylating agent (AcIm) on the conversion of **5MCC-OH**

Figure 5.3 depicts two of the control experiments performed during the investigation to examine the role of carbonate isomerization and the steric bulk on the O-protection. The first experiment focuses on the preparation of a six-membered cyclic carbonate with a primary alcohol (**6MCC-OH**) using only the catalyst TBD. The target product **6MCC-OH** was not detected, suggesting that

the reactant **5MCC-OH** is thermodynamically more stable. The second control experiment involves the absence of the catalyst TBD, with only the acylating agent AcIm present. The envisioned product is the five-membered cyclic carbonate with the tertiary alcohol protected, named **5MCC-OAc**; however, this product was also not detected suggesting that the reactant is kinetically stable.

With the experimental conditions reported and control experiments carried out, is possible to conclude that both TBD and AcIm are required to facilitate the reaction. The catalyst (TBD) is crucial to perform the isomerization process from a five- to a six-membered cyclic carbonate, and the combination of both catalyst (TBD) and acylating agent (AcIm) leads to the formation of the acylated six-membered cyclic carbonate (**6MCC-OAc**) by trapping the product in this formal cascade process

5.4.1 Mechanistic Pathway

The overall cascade mechanistic pathway showed in **Figure 5.4** can be described as two consecutive reactions: a conversion from a five- (**5MCC-OH**) to a six- membered cyclic carbonate (**6MCC-OH**) named "isomerization part", followed by an alcohol protection using acetyl imidazole (AcIm) to obtain the final product **6MCC-OAc** named "acylation part", all catalyzed with TBD.

The first part of the mechanism (isomerization) involves the five-membered membered cyclic carbonate **5MCC-OH** and the catalyst TBD, while the AcIm acts as a spectator and will start its role in the second part (acylation). The adduct with **5MCC-OH** and the TBD is used as a reference (0.0 kcal·mol^{-1}), followed by the first transition state **TS 1** which consists of a deprotonation of the tertiary alcohol by TBD with an energetic value of 4.2 kcal·mol^{-1} (geometry represented in **Figure 5.5**). As a result, the structure for the corresponding alkoxide **5MCC-O** and the protonated catalyst HTBD^{+} (3.0 kcal·mol^{-1}) is obtained. The oxygen atom from this alkoxide approaches the carbonyl carbon from the cyclic carbonate and generates the intermediate **5MCC-Int** with a value of 13.8 kcal·mol^{-1} (geometry represented in **Figure 5.6**). This interme-

diate has a tetrahedral carbon centre that leads to **TS 2** (geometry represented in **Figure 5.7**), in which the bond related to the five-membered cyclic carbonate is broken, creating a new one thereby obtaining a six-membered one with a pendent alkoxide. This transition state is the most unstable along the entire mechanism with an energetic value of 17.6 kcal·mol^{-1}. The next structure **6MCC-Int1** (9.0 kcal·mol^{-1}) represents a six-membered cyclic carbonate with an alkoxide group close to the carbonyl carbon. The role of the protonated catalyst HTBD^{+} during this process (from **5MCC-Int** to **6MCC-Int1**) is to maintain a close interaction between the alkoxide and the carbonyl group by means of hydrogen bonds.

Then, a proton transfer from the protonated catalyst HTBD^{+} to the alkoxide through transition state **TS 3** (8.8 kcal·mol^{-1}), produces a six-membered cyclic carbonate with a primary alcohol **6MCC-OH** (2.9 kcal·mol^{-1}). This is an important step since it changes the conformation from the alkoxide, placing this group away from the carbonate, thus avoiding a back-reaction to produce **5MCC-Int** or even the starting reactant **5MCC-OH**. Note that the **6MCC-OH** is thermodynamically less stable than reactant **5MCC-OH** (nearly 3 kcal·mol^{-1}), hence, corroborating with the control experiment presented in **Figure 5.3**, which determined that the intermediate **6MCC-OH** is not detectable without the O-protection by ImAc. Therefore, the only way to trap the six-membered cyclic carbonate product during this cascade process is by means of an acylation reaction.

The second part of the cascade process consists of the acylation of the primary alcohol of the six-membered cyclic carbonate **6MCC-OH** to obtain the product **6MCC-OAc**. This step uses AcIm as the acylating agent and TBD as a catalyst. The acylation part starts with a deprotonation of the primary alcohol of the **6MCC-OH** in **TS 4** with an energetic value of 7.7 kcal·mol^{-1}, which results into a six-membered cyclic carbonate with an alkoxide group and the protonated catalyst HTBD^{+} as intermediate **6MCC-O-1** (9.1 kcal·mol^{-1}). Note that in this last structure (**6MCC-O-1**) the alkoxide is located further away from the carbonate carbon centre, different than the geometry involved in the intermediate **6MCC-Int1**. This larger separation is still present in the next interme-

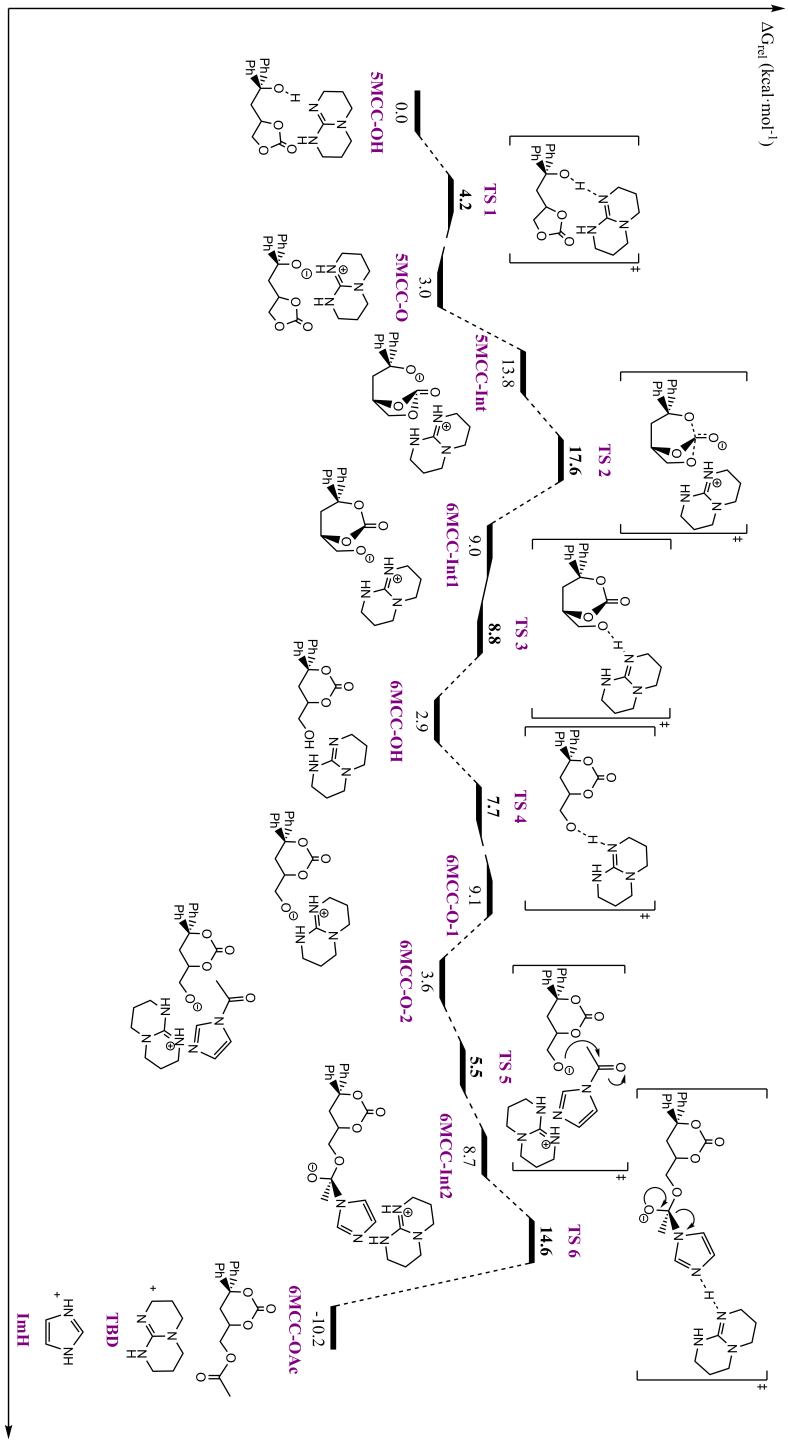

Figure 5.4: Relative Gibbs Free energy profile in kcal·mol^{-1} for the mechanistic pathway for the conversion and acylation of 5MCC-OH to give 6MCC-OAc using TBD as a catalyst and AcIm as acylating agent

diate **6MCC-O-2** (3.6 kcal·mol^{-1}), which gathers the six-membered cyclic carbonate, the protonated catalyst HTBD^{+} and AcIm. This ensemble evolves into the next transition state **TS 5** (geometry represented in **Figure 5.8**) with an energetic value of 5.5 kcal·mol^{-1}, and the HTBD^{+} allows the nucleophilic alkoxide to attack the carbonyl carbon fragment from the AcIm. As a consequence, the intermediate **6MCC-Int2** (8.7 kcal·mol^{-1}) includes a tetrahedral carbon centre with the Imidazole bound. The last step hence leads to the last transition state **TS 6** (geometry represented in **Figure 5.9**) where the carbonyl carbon bound to the AcIm changes its hybridization from sp^3 to sp^2. The protonated catalyst HTBD^{+} undergoes a proton transfer reaction to the outer nitrogen of the imidazole group which induces an electronic rearrangement that delivers the final product **6MCC-OAc**, with the ImH as a by-product while regenerating the catalyst TBD with an stable energetic value of -10.2 kcal·mol^{-1}. This final product **6MCC-OAc** is thermodynamically more stable than the initial reactants **5MCC-OH**, and since all intermediates and transition states are in dynamic equilibrium, the acylation to achieve O-protection makes the cascade process irreversible at room temperature.

The determining transition state (TDTS) for the overall reaction corresponds to **TS 2**, which has an energy span of 17.6 kcal·mol^{-1}. This transition state is crucial as it determines the isomerization from five- to six-membered cyclic carbonate. Interestingly, there is another transition state, **TS 6**, with a slightly lower energy span of 14.6 kcal·mol^{-1}, which is close to the TDTS. This transition state also plays a significant role in trapping the product by acylating the pendent alcohol of the six-membered cyclic carbonate.

Mechanistic pathway structures

For an in-depth analysis of the mechanism depicted in **Figure 5.4**, specific transition states and intermediates were chosen to closely examine their geometric parameters.

The structure presented in **Figure 5.5** and some geometric values described in **Table 5.1**, corresponds to the first transition state **TS 1** that consists of a pro-

ton transfer for the tertiary alcohol from **5MCC-OH** (O9-H10) through the nitrogen atom N11 from the catalyst TBD. The angle O9-H10-N11 related with the proton transfer is fairly linear with a value of 162.7°. The N-H bond distances related to this proton transfer are similar, which involve TBD and the H10 from the tertiary alcohol and O9-H10 (from the alcohol group) and are 1.24 Å and 1.23 Å respectively.

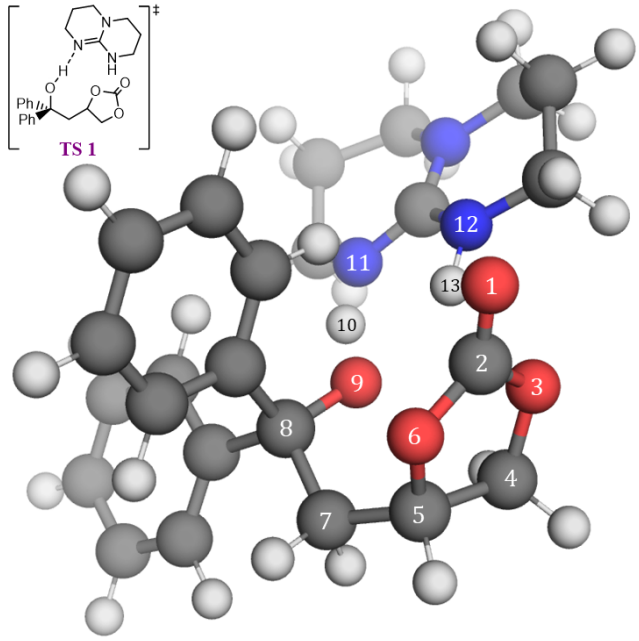

Figure 5.5: Molecular structure for the transition state **TS 1** from **Figure 5.4** including atom labels

Table 5.1: Angles and distances for the geometry of **TS 1** presented in **Figure 5.5**

Atom labels	Angle (°)
O3-C2-O6	111.7
O9-H10-N11	162.7
C8-C7-C5	117.1

Atom labels	Distance (Å)
O9-H10	1.23
H10-N11	1.24
O9-C2	3.30

The intermediate **5MCC-Int** is shown in **Figure 5.6** and some relevant bonds and angles are listed in **Table 5.2**. This structure is crucial for the next

transition state **TS 2** in which the isomerization occurs through a tetrahedral carbon centre C2 connected to O1, O3, O6 and O9 providing an intermediate for advancing towards the product. The angle O6-C2-O3 corresponding to the initial five-membered cyclic carbonate is 102.2°, which is close to the angle (O9-C2-O6) that corresponds to the final six-membered cyclic carbonate having a value of 107.0°. Moreover, the C-O bond distances are similar with values close to 1.45 Å. In this intermediate, the catalyst TBD does not interact with the substrate directly, but has an important role of keeping close the O-atoms surrounding the tetrahedral carbon center via hydrogen bonds. Hence, the angle O3-H13-N12 (outer oxygen O3 and H13-N12 from TBD) has an rather linear geometry with a value of 169.1°, and the distance from O3 (substrate) and H13 (TBD) is 1.89 Å.

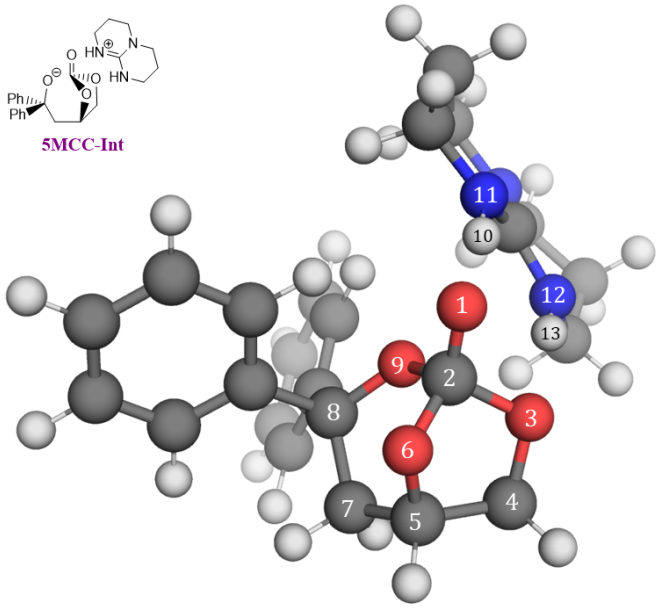

Figure 5.6: Molecular structure for the intermediate **5MCC-Int** from **Figure 5.4** including atom labels

The second transition state **TS 2** is presented in **Figure 5.7** and some geometrical parameters such as bond distances and angles are described in **Table 5.3**. This is the determining transition state (TDTS) that represents an isomer-

Table 5.2: Angles and distances for the geometry of **5MCC-Int** presented in **Figure 5.6**

Atom labels	**Angle (°)**
O6-C2-O3	102.2
O9-C2-O6	107.0
C5-C4-O3	104.0
O3-H13-N12	169.1

Atom labels	**Distance (Å)**
O9-C2	1.48
C2-O6	1.42
C2-O3	1.47
O3-H13	1.89

ization of the five- to six-membered cyclic carbonate.

During this transition state, the carbonyl carbon centre C2 from the previous intermediate **5MCC-Int** is separated from O3 (a C-O bond present in the initial 5MCC) by a distance of 1.91 Å. Simultaneously, the C2-O bond lengths involving O9 and O6 become smaller and amount to 1.39 Å and 1.37 Å respectively, facilitating the formation of the six-membered cyclic carbonate (6MCC). The catalyst TBD does not react directly with the substrate, but its role during this process is to keep the oxygen atoms bound to the carbon centre enhancing their interaction through hydrogen bonds. Specifically, the distance between O3 and H13 from the TBD is 1.60 Å, and the angle is rather linear (170°). The distance is shorter than that within the previous intermediate **5MCC-Int**, as such it favours the next transition state **TS 3** depicted in **Figure 5.4**.

Table 5.3: Angles and distances for the geometry of **TS 2** presented in **Figure 5.7**

Atom labels	**Angle (°)**
O6-C2-O3	93.7
O9-C2-O6	112.0
C5-C4-O3	104.0
O3-H13-N12	170.4

Atom labels	**Distance (Å)**
O9-C2	1.39
C2-O6	1.37
C2-O3	1.91
O3-H13	1.60

The next transition states, **TS 3** and **TS 4**, involve proton transfer reactions. Initially, the pendent alkoxide from **6MCC-Int** is protonated to obtain a six-membered cyclic carbonate with a primary alcohol, **6MCC-OH**, which is then deprotonated into an alkoxide providing structure **6MCC-O-1**. The proton transfer reactivity can be described as a process analogous to **TS 1**, hence, it will not be further discussed here.

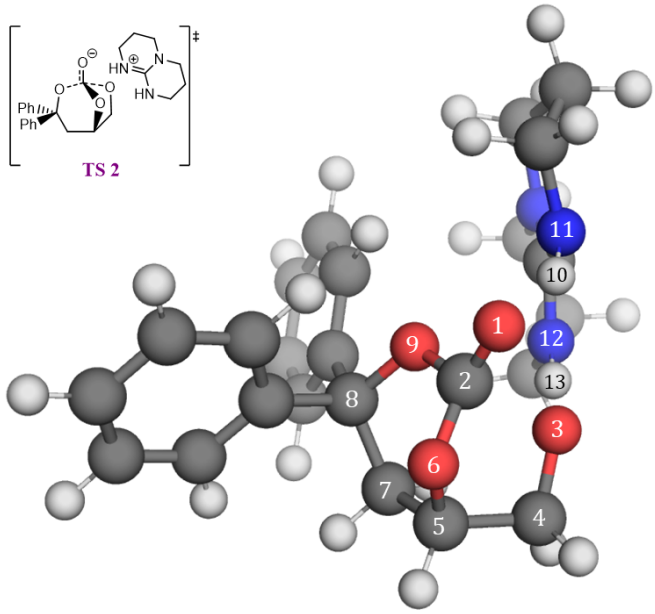

Figure 5.7: Molecular structure for the transition state **TS 2** from **Figure 5.4** including atom labels

The transition state **TS 5** is presented in **Figure 5.8** and some of its geometrical parameters are described in **Table 5.4**. This structure entails a six-membered cyclic carbonate (6MCC) with a primary alkoxide, the protonated catalyst $HTBD^+$ and the acylating agent ImAc. The process involves the attack of alkoxide O3 onto the carbonyl carbon C14 from the ImAc, with an interatomic distance of 2.04 Å, and an angle O3-C14-N16 of 91.7°. This arrangement leads to the formation of an intermediate with a tetrahedral carbon centre in the next structure **6MCC-Int2** (**Figure 5.4**). During this transition state, the role of the catalyst is to bring the alkoxide O3 from the 6MCC and H13 in close proximity via hydrogen bonding with the formed O3-H13 distance being 1.75 Å.

The last transition state **TS 6** is presented in **Figure 5.9** and some of its bond lengths and angles are given in **Table 5.5**. This transition state is the second most energetically disfavoured after **TS 2** in the entire mechanism. It involves a protonation of the outer nitrogen atom N17 from the ImAc by H13 from the catalyst $HTBD^+$, followed by an electronic rearrangement that involves the car-

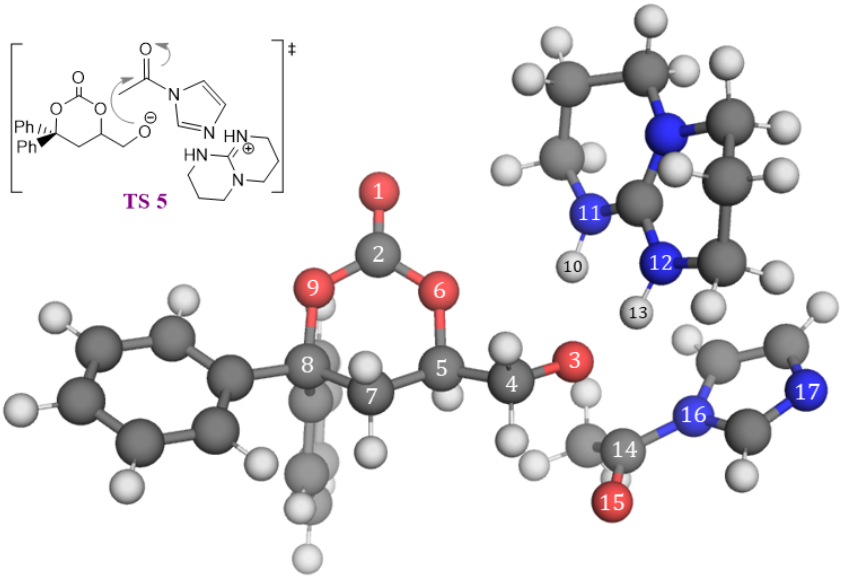

Figure 5.8: Molecular structure for the transition state **TS 5** from **Figure 5.4** including atom labels

Table 5.4: Angles and distances for the geometry of **TS 5** presented in **Figure 5.8**

Atom labels	Angle (°)
O3-C14-N16	91.7
O15-C14-N16	117.2
C5-C4-O3	112.9
O3-H13-N12	153.4

Atom labels	Distance (Å)
O3-C14	2.04
C14-N16	1.46
C14-O15	1.22
O3-H13	1.75

bon centre C14. This reaction overall results into an acylation of the alkoxide O3 by breaking the bond between the imidazole-N16 and C14, thereby releasing a molecule of Im-H.

Table 5.5: Angles and distances for the geometry of **TS 6** presented in **Figure 5.9**

Atom labels	Angle (°)
O3-C14-N16	101.6
O15-C14-N16	108.5
C5-C4-O3	116.8
N17-H13-N12	171.0

Atom labels	Distance (Å)
O3-C14	1.46
C14-N16	1.65
N17-H13	1.20
H13-N12	1.36

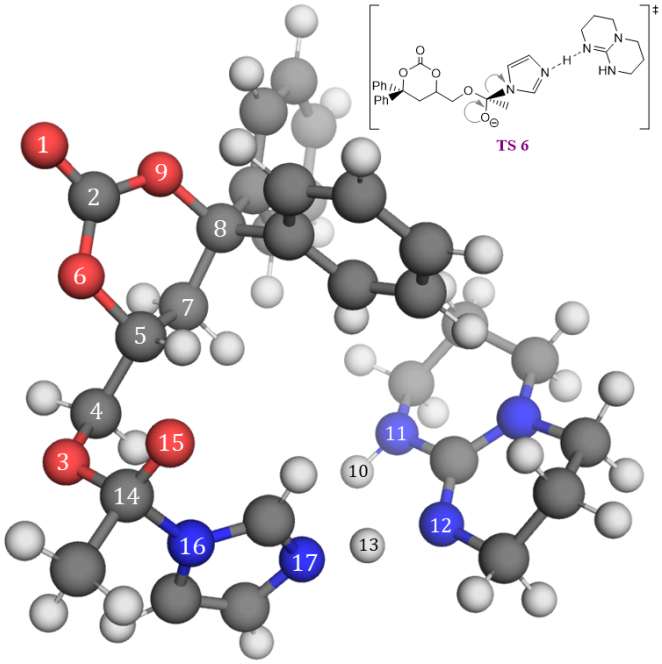

Figure 5.9: Molecular structure for the transition state **TS 6** from **Figure 5.4** including atom labels

The protonation step that involves H13 from $HTBD^+$ and N17 from the imidazole group results into a linear angle N17-H13-N12 of 171.0°. The distance between the carbon C14 from the acetate group and the nitrogen N16 from the imidazole is 1.65 Å, which is larger than that in the previous transition state **TS 5** (1.22 Å), due to the subsequent release of ImH. All of these consecutive reactions in this transition state give rise to the formation of the final product **6MCC-OAc**, which is a six-membered cyclic carbonate with a pendent primary alcohol (O3) protected by an acetate group, a molecule of ImH as a byproduct and the regenerated catalyst TBD.

5.4.2 Alternative routes

As described above, the reaction starts with the reactant (**5MCC-OH**), catalyst (TBD) and Imidazole Acetate (ImAc). Although the most feasible mechanism is described in **Figure 5.4**, these molecules may be involved in different

mechanistic pathways that lead other products than **6MCC-OAc**. In this section, the most relevant alternative routes (acylation of 5MCC and isomerization into a seven-membered cyclic carbonate 7MCC) will be described.

Acylation of 5MCC

The acylation mechanism of the pendent alcohol converting **6MCC-OH** into **6MCC-OAc** requires the close proximity between the substrate having an alcohol group (**6MCC-OH**), the catalyst (TBD) and the acylating agent(ImAc). All three molecules involved in this protecting step are similar to the combination of the reactants (**5MCC-OH**, TBD and ImAc), and question could come to mind: Why is the initial **5MCC-OH** not acylated?

To explore this hypothesis, the acylation mechanism for the five-membered cyclic carbonate **5MCC-OH** was investigated and the findings are depicted in **Figure 5.10**, following the same pathway as described for **6MCC-OH** in **Figure 5.4**.

The reaction starts in the same way as the main mechanism presented in **Figure 5.4** using the adduct of 5MCC-OH and TBD with the addition of ImAc as a reference (0.0 kcal·mol^{-1}). This is followed by the deprotonation of the alcohol in **TS 1** (4.2 kcal·mol^{-1}) to form a newly generated alkoxide **5MCC-O** (3.0 kcal·mol^{-1}). The differences start with the next structure **5MCC-O-2**, which includes the adduct of the 5MCC alkoxide, ImAc and TBD (8.6 kcal·mol^{-1}). This leads to the next transition state **TS 5.1**, in which the alkoxide attacks the carbonyl carbon from the acetate group in ImAc, and the protonated catalyst HTBD^{+} keeps the involved species close by making several hydrogen bonds (18.2 kcal·mol^{-1}). As a result, the intermediate **5MCC-Int2** has a tetrahedral carbon centre due to its bonding with the Imidazole group (20.1 kcal·mol^{-1}). The last transition state **TS 6.1** is the most disfavoured one with an energy of 24.8 kcal·mol^{-1}. At this stage, the HTBD^{+} protonates the outer nitrogen atom of the Imidazole, releasing ImH, while simultaneously there is an electronic rearrangement that changes the geometry of the tetrahedral carbon centre, result-

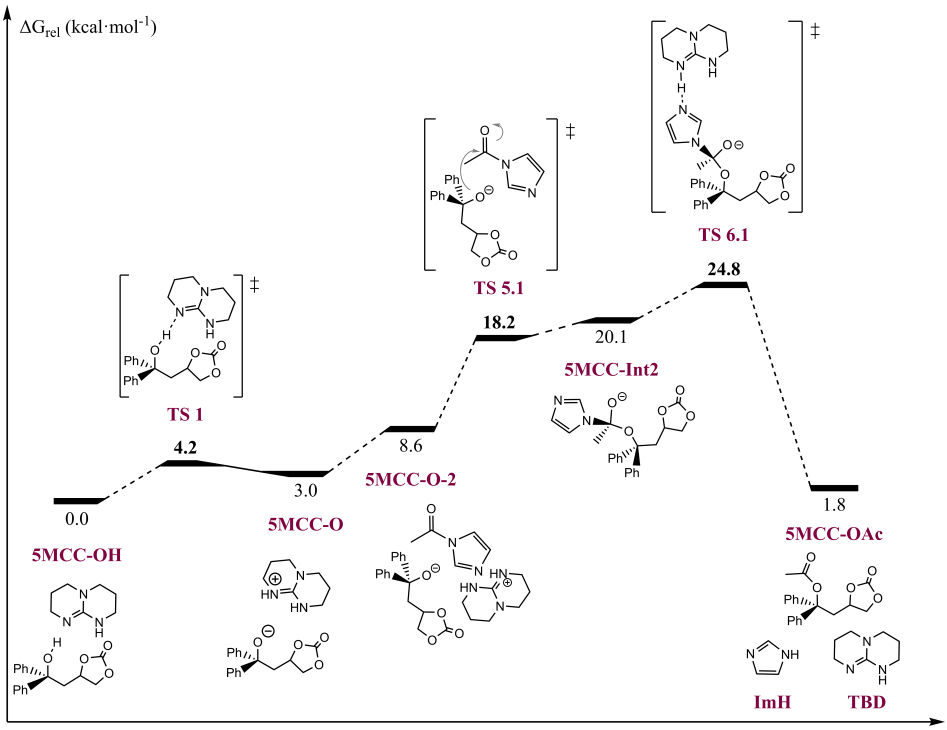

Figure 5.10: Relative Gibbs free energy profile in kcal·mol^{-1} for the acylation of the **5MCC-OH** into **5MCC-OAc**

ing in the formal acylation of the five-membered cyclic carbonate. The final product **5MCC-OAc** includes the acylated 5MCC, the recovered catalyst TBD and ImH (1.8 kcal·mol^{-1}).

The energy span[67] for the acylation of **5MCC-OH** (**Figure 5.10**) is 24.8 kcal·mol^{-1}, while for the overall mechanism reported in **Figure 5.4**, a span of is 17.6 kcal·mol^{-1} was determined. Comparing both mechanisms, it becomes evident that there is an energetic preference for the mechanism involving both isomerization and acylation to obtain **6MCC-OAc** rather than the acylation of the reactant **5MCC-OH**. Additionally, the product resulting from this latter acylation mechanism **5MCC-OAc** (1.8 kcal·mol^{-1}) is more unstable than the product for the overall mechanism **6MCC-OAc** (-10.2 kcal·mol^{-1}). This suggests that the alcohol protection for **6MCC-OH** is irreversible, resulting in a stable product (**6MCC-OAc**), while the **5MCC-OAc** mechanism is energetically

disfavoured and reversible and can led to *in situ* back-equilibration to the unprotected alcohol **5MCC-OH**.

These results indicate that at room temperature, the acylation of the **5MCC-OH** is not energetically competitive with the five-to-six carbonate isomerization/acylation cascade, and a kinetic differentiation between both alcohol protection pathways allows for the selective trapping of **6MCC-OAc** in high yield, which is consistent with the experimental data reported above (*control experiments* - **Figure 5.3**, and *main mechanistic pathway* - **Figure 5.4**).

Isomerization into 7MCC

The isomerization from a five- to six-membered cyclic carbonate in **TS 2** corresponds to the TOF-determining transition state (TDTS) in the overall mechanism reported in **Figure 5.4**. The process starts with **5MCC-Int** that has a tetrahedral carbon centre (**Figure 5.6**) between C2 and the oxygens O1, O3, O6 and O9. During **TS 2**, the bond between C2 and O3 is broken, resulting into a six-membered cyclic carbonate (**Figure 5.7**). However, if the bond scission occurs between C2 and O6, a seven-membered cyclic carbonate with a secondary alcohol (**7MCC-OH**) could also be obtained. To investigate this option, a computational study was performed calculating the intermediates and transition states for the conversion of the **5MCC-OH** into **7MCC-OH** (**Figure 5.11**) and comparedto the isomerization part reported in **Figure 5.4**, which involves the isomerization of **5MCC-OH** into **6MCC-OH**.

The energetic profile presented in **Figure 5.11**, starts with the same intermediates and transition states as reported in **Figure 5.4**. The **5MCC-OH** is deprotonated in **TS 1**, culminating into **5MCC-O** as a resultant alkoxide, and this latter species approaches the carbonyl carbon in intermediate **5MCC-Int**. From this point onwards, two possible isomerization transition states may be accessed, both creating a new bond between C2 and O9 (see **Figure 5.6**). However, depending on which bond is broken in the initial 5MCC (O3 or O6), the resulting product could be either a 6MCC or a 7MCC.

On the one hand, **TS 2** describes the separation between C2 and O3, re-

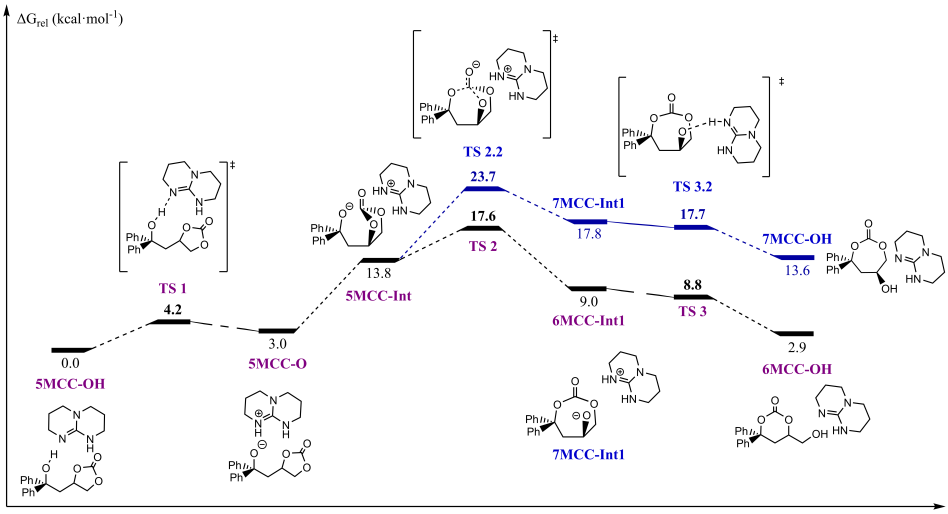

Figure 5.11: Relative Gibbs free energy profiles for the isomerization part in kcal·mol^{-1} for the formation of **6MCC-OH** and **7MCC-OH**

sulting in a six-membered cyclic carbonate structure at 17.6 kcal·mol^{-1}, which determines the energy span of the entire process. On the other hand, the transition state **TS 2.2** promotes the separation of C2 and O6, obtaining a seven-membered cyclic carbonate, which is also the most energetically disfavoured one for this alternative mechanism at 23.7 kcal·mol^{-1} (see **Figure 5.11**). The intermediate alkoxide **7MCC-Int1** has an energetic value of 17.8 kcal·mol^{-1}, and thus more unstable than the TDTS (**TS 2**) in the other mechanism leading to **6MCC-OAc**. The protonation of the alkoxide during the transition state **TS 3.2** is also energetically disfavoured at 17.7 kcal·mol^{-1}. Finally, the free energy product of the isomerization **7MCC-OH** has a value of 13.6 kcal·mol^{-1}, which is much higher compared to **6MCC-OH** (2.9 kcal·mol^{-1}).

Note that the control experiment in (**Figure 5.3** did not result in detecting the presence of **6MCC-OH** due to its relative instability compared with the reactants and the acylated product. Therefore, the energy values determined for the structures and transition states in the 7MCC formation pathway are too high, which is in line with the experimental observations by various Kleij group members who did not detect such species by any means[88].

In summary, the mechanistic pathway for the isomerization from 5MCC to 7MCC is energetically unfavourable, with an energetic span of 23.7 kcal·mol^{-1}. In contrast, the isomerization from 5MCC to 6MCC followed by an O-protection step to capture the product, presents a significant more favourable energetic span of 17.6 kcal·mol^{-1}.

5.5 Conclusions

In this chapter, the main objective was to investigate the mechanistic pathway involved in the formation of six-membered cyclic carbonate **6MCC-OAc** starting with a five-membered cyclic carbonate **5MCC-OH**, catalyzed by TBD, using AcIm as an acylating agent in acetonitrile solution at room temperature. To achieve this goal, DFT studies were performed to calculate the mechanistic pathway for this reaction, as well as alternative routes, supported by experimental data/observations provided by Chang Qiao (a former Kleij group member), to gain a better understanding of the role of each molecule/species during this reaction.

The main computed mechanism can be divided into two parts, an isomerization step followed by O-acylation. The reaction starts with a five-membered cyclic carbonate featuring a tertiary alcohol (**5MCC-OH**), which is first isomerized into a six-membered cyclic carbonate having a primary alcohol (**6MCC-OH**) by the organocatalyst TBD. During this phase, the acylating agent remains a spectator. The second part begins with the six-membered cyclic carbonate **6MCC-OH** that is acylated by AcIm in the presence of TBD to obtain the final product **6MCC-OAc**. During this second phase, both TBD and AcIm are required to successfully facilitate the reaction. All intermediates and transition states involved in this reaction are thermodynamically more unstable compared to the reactant **5MCC-OH**, with the exception of the final product **6MCC-OAc**. This suggests that these structures remain in equilibrium until they reach the last transition state, through which the final product is trapped and thus obtained in high yield. The energetic span of this reaction is 17 kcal·mol^{-1}, which enables a room temperature conversion.

The alternative routes that were considered, the acylation of the reactant **5MCC-OH** into a **5MCC-OAc**, and the isomerization of **5MCC-OH** into a **7MCC-OH**, involve both more unstable intermediates and transition states, and consequently have higher energetic spans (24.8 and 23.7 kcal·mol^{-1} respectively) compared to those involved in the main reaction.

In summary, a unique organocatalytic manifold for the formation of six-membered cyclic carbonates has been developed starting from five-membered cyclic carbonates. These products (6MCC) are highly versatile and may include the presence of several aryl- and alkyl-ring substituents. This computational study complements the experimental data and control experiments previously obtained, and emphasizes the importance of a kinetic differentiation between the protecting of the pendent alcohol groups. This chapter describes the overall mechanistic pathway that involves an isomerization followed by an acylation step. The isomerization step includes the rate-determining transition state for the overall reaction, while the acylation step traps the elusive six-membered cyclic carbonate. To consider other possible scenarios, alternative routes such as the acylation of **5MCC-OH** and the isomerization from a **5MCC-OH** to a **7MCC-OH** have also been considered. Both of these routes are energetically not competitive compared to the observed manifold leading to **6MCC-OAc**.

UNIVERSITAT ROVIRA I VIRGILI
COMPUTATIONAL INSIGHTS OF CATALYTIC CARBON DIOXIDE VALORIZATION AND CIRCULAR RECYCLING PROCESSES
Alba Villar Yanez

CHAPTER

6 Ring Opening Polymerization

6.1 Introduction

A major challenge in materials science is to develop biomaterials that meet the criteria of biocompatibility, controlled degradation, and high performance. Synthetic polymers, particularly aliphatic polycarbonates (APCs) have been considered as promising sustainable materials, as they can be obtained from a range of natural or renewable sources, and they are potentially biodegradable. The APCs are excellent biocompatible materials due to their low toxicity, degradability and mechanical properties, making them particularly suitable for medical devices and drug delivery systems. The potential for these polycarbonates over the natural ones lies in their versatility with respect to the chemical structure and the ease of manipulation. These APCs can be synthesized through different routes including: polycondensation of aliphatic polyols and dialkyl carbonates[194], Ring-Opening Copolymerization of carbon dioxide with epoxides (ROCOP)[195–201] or Ring-Opening Polymerization (ROP) using cyclic carbonates as monomers[35,38,39,202]. Currently, many polymers can be synthesised through a ring-opening polymerization reaction starting from lactones[30–33], lactides[34], or cyclic carbonates. These ROP reactions may proceed via cationic[36,37], anionic[40], coordination-insertion or enzymatic[38,41–44] mechanisms. The ring strain of the monomers play a key role to facilitate a successful ROP (**Figure 6.1**). The ROP of larger-ring, six- to eight-membered cyclic carbonates will lead to stable polymer chains, contrary to five-membered cyclic carbonates, whose ROP is far more difficult. Without using a fused ring-structure making the whole system more strained, the ROP of 5MCCs can only occur at high temperatures, leading to decarboxylation during the process[203,204] obtaining thereby a poly(ether-carbonates).

In the ring-opening polymerization (ROP) of cyclic carbonates, catalysts play a key role in controlling polymerization kinetics, achieving high molecular weights, and maintaining end-group fidelity. Two main types of catalysts commonly employed in this process are metal-based catalysts and organocatalysts.

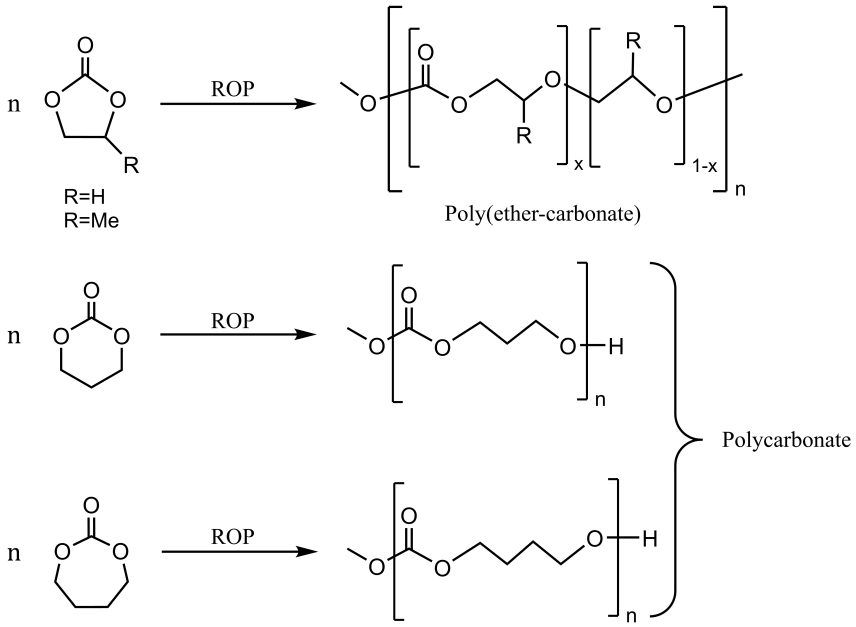

Figure 6.1: Ring-Opening Polymerization scheme products for five-, six- and seven-membered cyclic carbonates and their polymer products

On the one hand, metal-based catalysts are often transition metal complexes, which have been extensively studied and utilized in ROP reactions. These catalysts typically coordinate the cyclic carbonate monomer, activating it towards ring-opening polymerization. Some of the most used metals present in catalysts include tin(II)[205,206], zinc(II)[30,207,208], and aluminium-based[209,210]. They typically offer high catalytic activity and these metal-based catalysts can polymerize a wide range of cyclic carbonates under mild reaction conditions. However, an inconvenience of metal-based catalysts is the residual metal that could remain within the polymer product, which may lead to cytotoxicity in biomedical applications.

On the other hand, organocatalysts have gained attention as alternative catalysts for ROP reactions due to their biocompatibility and potential to produce metal-free polymers[44,211]. The most used organocatalysts, presented in the **Figure 6.2**, offer precise control over polymerization kinetics and can produce polymers with low dispersity and well-defined end-groups. Additionally,

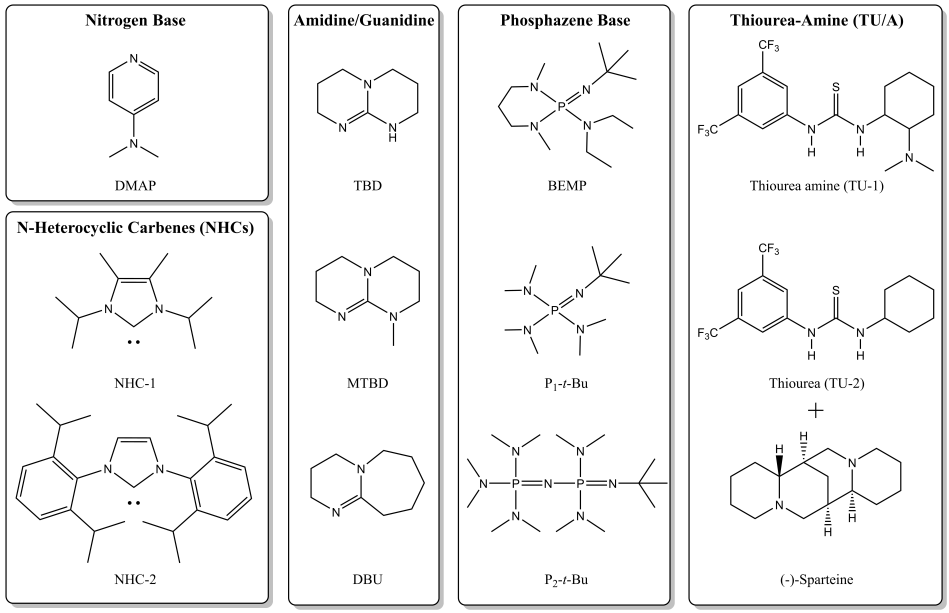

Figure 6.2: Organocatalysts used in ROP of cyclic carbonates

organocatalysts often exhibit high efficiency and selectivity in ROP reactions.

The organocatalysts represented in **Figure 6.2** correspond to the main organic bases used in an Anionic Ring-Opening Polymerization (AROP). A simple nitrogen-based catalyst is DMAP[a], the N-heterocyclic carbene (NHCs) group includes catalysts that may have either alkyl or aryl substituents such as NHC-1[b] and NHC-2[c] respectively. The next group gathers two commercially available guanidines being TBD[d] and MTBD[e], and the amidine-base DBU[f]. Typical phosphazene bases are BEMP[g], P_1-*t*-Bu[h] and P_2-*t*-Bu[i]. The last group includes the bifunctional thiourea-tertiary amine catalyst TU-1[j], and a catalyst mixture

[a] 4-dimethylamino pyridine
[b] 1,3-diisopropyl- 4,5-dimethyl-imidazol-2-ylidene
[c] 1,3-bis(2,6-diisopropylphenyl)- imidazol-2-ylidene
[d] 1.5.7-triazabicyclo-[4.4.0]dec-5-ene
[e] 7-methyl-1.5.7-triazabicyclo-[4.4.0]dec-5-ene
[f] 1,8-diazabicyclo[5.4.0]undec-7-ene
[g] 2-tert-Butylimino-2-diethylamino-1,3-dimethylperhydro-1,3,2-diazaphosphorine
[h] tert-Butylimino-tris(dimethylamino)phosphorane
[i] 1-tert-butyl-2,2,4,4,4-pentakis(dimethylamino)-2λ^5,4λ^5-catenadi(phosphazene)
[j] 1-(3,5-bis(trifluoromethyl)phenyl)-3-(2-(dimethylamino)cyclohexyl)thiourea

of thiourea TU-2[k] with (-)-Sparteine.

In this chapter, the organocatalyst selected for the ROP reactions is TBD because its properties combine strong basicity, steric hindrance, nucleophilicity, and versatility making it a highly efficient catalyst for ROP reactions[12,13]. As aprotic solvents, toluene, methylene chloride (CH_2Cl_2), THF, benzene, acetonitrile and DMF are preferred, contrary to protic solvents as methanol, which can be involved in the initiation step. Solvation affects the reactivity of the monomers, catalysts and initiators in some cases, hence, low or non-polar solvents are favoured[39]. The typical initiators are molecules with a terminal alcohol group such as benzyl alcohol (BnOH), glycerol (GLY), and diethylene glycol (DEG)[212]. In these cases, it is believed that the ROP is facilitated by the bifunctional activation of an initiator alcohol through an ionic nucleophilic interaction. In summary, the conditions studied for the ROP reaction in this chapter include the use of cyclic carbonates as monomers, TBD as a catalyst, BnOH as an initiator in toluene solution at room temperature.

The building blocks (monomers) for polycarbonates are cyclic carbonates, which can be prepared in three ways: ring-closing, ring-expansion and backbiting. The most common method is ring-closing of α,ω-diols with carbonylation reagents such as phosgene and its derivatives[32,213,214]. Despite being high yielding, the main reagent is highly toxic and laborious, as work-up needs to be conducted at low temperatures with rigorous purification steps, making this chemistry difficult to scale up. Some alternative strategies have been developed such as ring-expansion reaction of cyclic ethers (mainly epoxides and oxetanes) with CO_2, the latter gaining a lot of attention as a way to utilize a renewable feedstock. In addition, the direct coupling of carbon dioxide with different starting materials (1,3-diols or sugars[195,215,216]) allow to obtain functionalized 6MCCs[201,217–219].

Despite the availability of different methods to obtain cyclic carbonates with different substituents and ring sizes, their synthesis still remains challeng-

[k] 1-(3,5-bis(trifluoromethyl)phenyl)-3-cyclohexylthiourea

ing in certain aspects. Larger ring cyclic carbonates like 6MCCs and 7MCCs have become popular monomers over time due to their propensity to be polymerized via ROP[220] using generally organocatalysts under mild conditions. However, their preparation is still challenging because it often involves the use of harmful and low-atom economy reagents such as phosgene and its derivatives. Additionally, not all cyclic carbonates that are synthesised can easily undergo a successful polymerization reaction because of steric and electronic limitations.

6.1.1 Previous Studies reported in the literature

There exists experimental data in the literature that reports successful ROP reactions for different monomers. Depending on the type of ROP reaction (anionic, cationic, immortal...), each study uses different kinds of catalysts such as metal-based complexes, enzymes and organocatalysts. This section gathers experimental data found in the literature for some monomers that will be further studied in this chapter.

Taking into account that the conditions are different for each study, thus making these results not directly comparable among them, they are still useful to gather knowledge about the potential of each monomer to be polymerized. The most studied monomer is the simplest six-membered cyclic carbonate 6MCC, namely Trimethylene carbonate (TMC). This monomer has good commercial availability and can be ring-open polymerized with high activity. In the last decades, its polymerization has been investigated using different catalysts, solvents and condition[30,31,35,36,38,195,202,207,208,212,213,221,222]. In general, the use of metal-based catalysts leads to higher activities and regio-selectivity, however, the use of organocatalysts have recently been shown to offer reasonable alternatives to give access to polycarbonates devoid of any metal impurities. In this chapter we will focus on the TBD as a catalyst[12,13].

In **Table 6.1** are gathered the data for the ROP reaction performed by various Kleij group members[28,223], which are helpful because the polymerization reactions were carried out under the same conditions used as a benchmark in

this chapter.

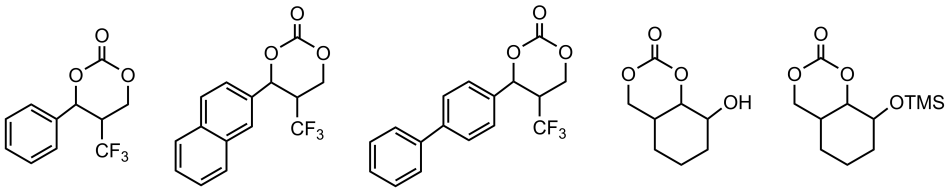

CF_3-Ph **CF_3-Naph** **CF_3-Biphen** **Bicyc-OH** **Bicyc-OTMS**

Figure 6.3: Monomers tested in Kleij laboratory: CF_3-Ph[223], CF_3-Naph[223], CF_3-Biphen[223], Bicyc-OH[28] and Bicyc-OTMS[28]

Table 6.1: Experimental conditions reported in literature[28,223] for monomers tested by the Kleij group: CF_3-Ph[223], CF_3-Naph[223], CF_3-Biphen[223], Bicyc-OH[28] and Bicyc-OTMS[28]

Monomer	Initiator	Catalyst	Solvent	Temp.	M_n	Đ
CF_3-Ph	BnOH	TBD	Toluene	r.t.	5.2	1.42
CF_3-Naph	BnOH	TBD	Toluene	r.t.	5.0	1.23
CF_3-Biphen	BnOH	TBD	Toluene	r.t.	2.6	1.41
Bicyc-OH	BnOH	TBD	Toluene	r.t.	1.7	1.47
Bicyc-OTMS	BnOH	TBD	Toluene	r.t.	8.6	1.27

Temperature in °C, M_n in kg·mol^{-1}, Đ = M_w/M_n

Maquilón *et al.*[223] tested three monomers with a CF_3 and aryl substituent (phenyl, Naphthyl and biphenyl), which are abbreviated as CF_3-Ph, CF_3-Naph and CF_3-Biphen respectively, that undergo a ROP successfully. Specifically, the monomers CF_3-Ph and CF_3-Naph were converted with moderate-to-high conversion (78 and 83% respectively), and they have similar values for the polymer molecular weight (M_n). For CF_3-Biphen, the conversion (59%) and M_n are lower even though the molecular weight distribution (Đ) is comparable with the CF_3-Ph.

For the six-membered cyclic carbonates having a fused cyclohexyl (Bicyc-OH and Bicyc-OTMS)[28], Qiao *et al.* found that Bicyc-OH could be oligomerized at incomplete conversion in 20h (**Table 6.1**, entry 4). Moreover, if the reaction time was prolonged to 48h, the initial oligocarbonate suffered a partial

degradation. Therefore, the free alcohol from Bicyc-OH may interfere during the ROP reaction. For that reason, the authors protected the free alcohol with trimethylsilyl (TMS) to afford the Bicyc-OTMS monomer, which undergoes a ROP reaction with full monomer conversion in 20 h and providing relatively high molecular weight ($M_n \sim 8$ kg/mol).

In the last decades, different six-membered cyclic carbonates have been synthesized and polymerized using diverse catalysts and conditions. The most common monomers include one or two ring substituents due to their easy synthesis from substituted diols. In **Figure 6.4** are presented six-membered cyclic carbonates with one or two substituents reported in the literature that will be considered in this chapter.

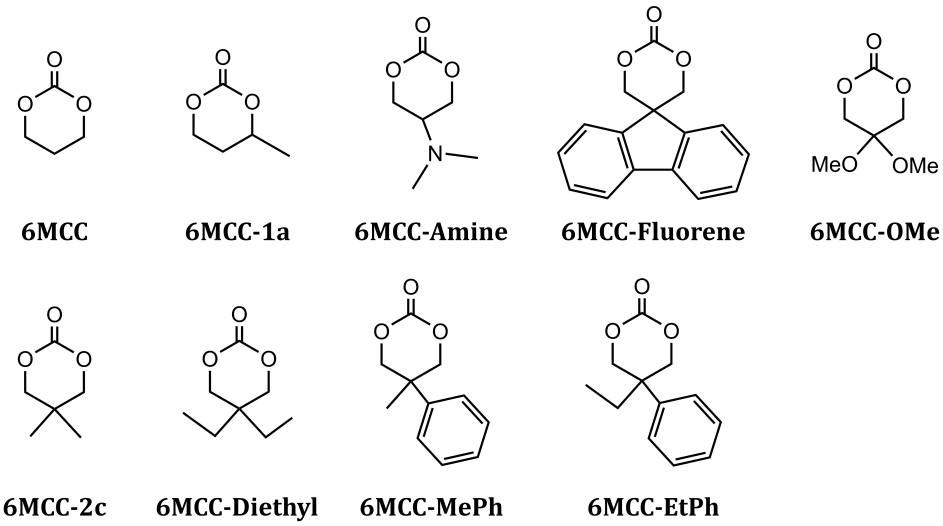

Figure 6.4: Six-membered cyclic carbonates with one or two substituents reported in the literature: 6MCC[219], 6MCC-1a[209,224,225], 6MCC-Amine[41,226], 6MCC-Fluorene[227], 6MCC-OMe[228], 6MCC-2c[219], 6MCC-Diethyl[219], 6MCC-MePh[219] and 6MCC-EtPh[219]

An AROP for different six-membered cyclic carbonates was performed by Matsuo *et al.*[219], and they used only *t*-BuOK at low temperature to enable the reaction. They tried different substituents in the same positions in order to see their effect in the ROP reaction. Specifically, they tried the unsubstituted

6MCC and the disubstituted monomers 6MCC- 2c (two methyl groups), 6MCC-Diethyl (two ethyl groups), 6MCC-MePh (a methyl and a phenyl group) and 6MCC-EtPh (an ethyl and a phenyl group). All of them are susceptible towards ROP under the conditions reported in **Table 6.2**, with the monomer having ethyl substituents 6MCC-Diethyl and 6MCC-EtPh providing under ROP conditions smaller polymer chains than monomers equipped with methyl groups (6MCC-2c and 6MCC-MePh, respectively).

Table 6.2: Experimental conditions for six-membered cyclic carbonates with two substituents and 6MCC reported in literature[219]: 6MCC-2c, 6MCC-Diethyl, 6MCC-MePh and 6MCC-EtPh

Monomer	Initiator	Solvent	Temp.	M_n	Đ
6MCC	*t*-BuOK	THF	0	32.6	1.5
6MCC-2c	*t*-BuOK	THF	0	54.0	1.4
6MCC-Diethyl	*t*-BuOK	THF	0	48.1	1.4
6MCC-MePh	*t*-BuOK	THF	0	51.9	1.4
6MCC-EtPh	*t*-BuOK	THF	0	12.7	1.5

Temperature in °C, M_n in kg·mol^{-1}, Đ = M_w/M_n

Table 6.3: Experimental conditions reported in the literature for 6MCC-Amine[41], 6MCC-Fluorene[227] and 6MCC-1a[209]

Monomer	Initiator	Catalyst	Solvent	Temp.	M_n	Đ
6MCC-Amine	-	Novozym	Toluene	60	4900	1.4
6MCC-Fluorene	BnOH	DBU	CH_2Cl_2	r.t.	~4.0*	~1.17
6MCC-1a	BnOH	TBD	Toluene	60	10.9	1.85

*Novozym = Novozym-435 / *(Data in kDa)*

Temperature in °C, M_n in kg·mol^{-1}, Đ = M_w/M_n

The 6MCC-Amine can be synthesised from a diol with triphosgene[226], and it can be polymerized by an enzymatic ROP using Novozym-435[41] as catalyst. Zhang *et al.* also tried a metal-based catalyst ($Sn(Oct)_2$), but they observed an unsuccessful ROP attempt. Unfortunately, the study did not include any organocatalyst.

For the monomer 6MCC-Fluorene[227], the authors made a kinetic study for its polymerization reaction with the conditions provided in **Table 6.2** (entry 2). Therefore, the data of M_n and Đ are approximate since they are derived from a kinetic plot. The principal motivation in this study was the development of amphiphiles containing fluorene units, they used as macro-initiatiors commercially available mPEG-OH of different molecular weights (1.6 – 10.0 kDa). This way, they developed diblock copolymers in a single step.

The monomer with a methyl group in α position, 6MCC-1a[209,224,225], was polymerized successfully using different organocatalysts and metal-based (Zn, Al) complexes. On the one hand, Hua[224] and Derosa[225] centred their focus in the regioselectiviy of the polymerization to investigate which is the preferred configuration of the intermediate resulting from the ring-opening, i.e., the way the different repeat units (RUs) are spatially connected with another. These RUs can be connected via head-to-head (HH), head-to-tail (HT), or tail-to-tail (TT) arrangements. Hua *et al.*[224] tried DBU, TBD and P2-*t*-Bu to polymerize *rac*-6MCC-1a at -40°C, and they found that the slowest polymerization rate is observed when using DBU, while the presence of TBD and P2-*t*-Bu allows for faster polymerization rates in comparison. The best results were observed for the phosphazene base under all conditions. If the reaction is performed at room temperature, TBD increases the polymerization rate although it being lower than that of P2-*t*-Bu. Derosa *et al.*[225] performed an study using (R)- and (S)- monomers with Zn- and Al-based catalysts to test their catalytic performance. Complementary, Brignou *et al.*[209] performed a ROP reaction using various metallic and organic catalysts with BnOH as an initiator at 60 and 110°C. The lewis acid $Al(OTf)_3$ was not able to promote the ROP at the lower temperature, while all other tested catalysts ($([(BDI^{iPr})\text{-}Zn(N(SiMe_3)_2)]$[a], TBD, BEMP and DMAP) were capable of polymerizing the respective monomer at both temperatures. The best activities for this ROP reaction reported in this latter study were noted when using either the zinc β-diiminate complex, TBD (**Table 6.2**, entry 3) or BEMP.

[a] (BDI^{iPr}) = 2-((2,6-diisopropylphenyl)-amido)-4-((2,6-diisopropylphenyl)-imino)-2-pentene

Table 6.4: Experimental conditions for the ROP reaction of 6MCC and 6MCC-OMe reported in literature[228]

Monomer	Initiator	Catalyst	Solvent	Temp.	M_n	Đ
6MCC	BnOH	TBD	CH_2Cl_2	r.t.	42.85	1.31
6MCC*	Glycerol	BEMP	-	60	9.1	1.57
6MCC-OMe*	BnOH	BEMP	-	90	14	1.66

**(iROP)*

Temperature in °C, $\boldsymbol{M}_n$ *in kg·mol*$^{-1}$, Đ = M_w/M_n

Helou *et al.*[228] studied the catalytic activity for different organocatalysts such as DMAP, TBD, BEMP, and some metal-based catalysts for bulk ROP under immortal conditions. The "immortal" ROP (iROP) of carbonates is based on using a catalytic amount of metal complex and a large excess of an aprotic source (typically alcohols), which act as a co-initiator and chain-transfer agent. The 6MCC was tested using TBD and BnOH at room temperature (**Table 6.4**, entry 1), and led to a high M_n value. Additionally, the same monomer was tested under iROP also using TBD, and they found that the guanidine catalyst was clearly much more active in the bulk "immortal" process. It mediates the polymerization reaction faster and its use leads to larger values for M_n although the reaction temperature in this latter regime was higher (60-110°C). Both 6MCC and 6MCC-OMe were polymerized under immortal conditions, which take place at a higher temperature and solvent-free conditions thereby offering simple access to polycarbonate macromolecules.

The simplest five-membered cyclic carbonates 5MCC (ethylene carbonate) and 5MCC-Me (propylene carbonate), have difficulties to undergo a Ring-Opening Polymerization reaction. In the last decades, several studies have been reported concerning their polymerizations using mainly metal-based catalysts at high temperatures above 100°C[203,204,214,220,222,229–234]. Specifically, for 5MCC the typical reaction temperature is around 170°C, and 180°C for 5MCC-Me. The polymerization involves partial decarboxylation, hence, it leads primarily to poly(ether-carbonate)s with a carbonate content of inferior than 50%. This resultant polymer is more flexible than a simple polycarbonate,

however, the carbonate/ether ratio depends on the catalytic system, and different properties can be obtained depending on the ration of the different repeat units.

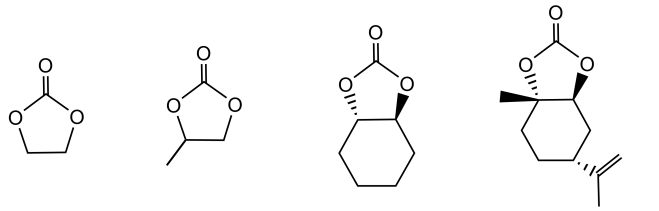

Figure 6.5: Five-membered cyclic carbonates reported in the literature that have been studied in this chapter: 5MCC[203,204,214,222,232], 5MCC-Me[233], 5MCC-Cyc[235,236] and 5MCC-Limonene[237]

For the five-membered cyclic carbonates[203,204,222] 5MCC and 5MCC-Me, the polymer obtained is a poly(ethylene-carbonate) as reported by different authors[214,232,233]. The ROP study for 5MCC performed by Kapiti *et al.*[203] uses TBD catalyst and 3-phenyl-1-propanol (3PP) as an initiator at high temperature (heated with microwave reactor, see **Table 6.5**, entry 1). They obtained a poly(ethylene-carbonate) with 70% ethylene oxide and 30% ethylene carbonate repeating units. These results are comparable with the study made by Lee *et al.*[204] who used sodium hydroxide as initiator and obtained a polymer with a carbonate content below 30%. Yang *et al.*[214] performed a ROP reaction for 5MCC using a phosphazene catalyst (P_4-*t*-Bu) at high temperature (**Table 6.5**, entry 2) and obtained a larger poly(ethylene-carbonate).

Recent studies made by Abdul-Karim *et al.*, demonstrated the ROP for 5MCC[232] (**Table 6.5**, entry 3) and 5MCC-Me[233] (**Table 6.5**, entry 4) using sodium stannate trihydrate as catalyst ($Na_2SnO_3{\cdot}3H_2O$) and diethylene glycol (DEG) at high temperature (175 and 180°C, respectively). The resultant poly(ethylene oxide-*co*-ethylene carbonate)s were analyzed using different spectroscopic techniques to evaluate the composition of the microstructure.

The five-membered cyclic carbonates fused with cycloalkyl, cycloalkene and sugar groups[215,216], include mostly strained ring, which enhance the ROP

Table 6.5: Experimental conditions reported in the literature for the five-membered cyclic carbonates: 5MCC[203,214,232], 5MCC-Me[233], 5MCC-Cyc[236] and 5MCC-Limonene[237]

Monomer	Initiator	Catalyst	Solvent	Temp.	M_n	Đ
5MCC[203]	3PP	TBD	-	180	3.1	1.7
5MCC[214]	-	P$_4$-*t*-Bu	THF	180	14.02	1.66
5MCC[232]	DEG	Na_2SnO_3*	-	175	7.5	~1.7
5MCC-Me	DEG	Na_2SnO_3*	-	210	4.8	1.5
5MCC-Cyc	BnOH	TBD	Toluene	60	18.1	1.54
5MCC-Limonene	BnOH	TBD	Toluene	80	7.29	1.60

3PP = 3-phenyl-1-propanol / DEG = diethylene glycol

Na_2SnO_3 = sodium stannate trihydrate ($Na_2SnO_3 \cdot 3H_2O$)*

Temperature in °C, $\boldsymbol{M}_n$ in kg·mol^{-1}, Đ = M_w/M_n

potential to form polycarbonates without decarboxylation. For 5MCC-Cyc[236], Tezuka *et al.*[235], performed an anionic ROP using *t*-BuOK as catalysts and *trans*-5MCC-Cyc and *cis*-5MCC-Cyc as monomers. They found that the polymerization of *trans*-5MCC-Cyc proceeds without the elimination of CO_2, while the ROP attempt of *cis*-5MCC-Cyc did not provide polymeric products. With these results in mind, Guerin *et al.*[236] used various metal-based (M = Zn, Y) catalysts and TBD as organocatalyst to mediate a successful polymerization reaction. They studied the stereoselectivity performing the ROP of a racemic mixture of *trans*-5MCC-Cyc, obtaining a polymer majorly formed *(R,R)*-5MCC-Cyc in high yield, contrary to *cis*-5MCC-Cyc that was not able to undergo the polymerization.

Another five-membered cyclic carbonate with a fused ring is the limonene carbonate, 5MCC-Limonene[237], which is a versatile monomer that can be polymerized and depolymerized (*more details in* ***Chapter 7 - Depolymerization***) using TBD as a catalyst and applying different temperatures for each of these processes.

There are few studies reported in the literature about the polymerization of seven-membered cyclic carbonates (7MCCs) due to their difficult synthesis.

Moreover, in the past studies focused on the unsubstituted 7MCC using metal-based catalysts. **Table 6.6** contains the data from the literature related with the monomers considered in this chapter. Another monomer reported in the literature is a 7MCC with a fused acetonide[38,44]. It is synthesised from L-tartaric acid, and can be polymerized under enzymatic conditions using a Lipase as a catalyst[43] (*this monomer will not be further discussed in this chapter*).

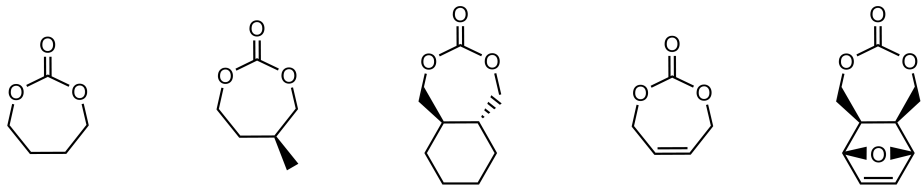

7MCC **7MCC-Me** **7MCC-Cyc** **7MCC-C=C** **7MCC-Ocyc**

Figure 6.6: Seven-membered cyclic carbonates tested in the literature that are studied in this chapter: 7MCC[36,40], 7MCC-Me[210], 7MCC-Cyc[238], 7MCC-C=C[90] and 7MCC-Ocyc[239]

For the seven-membered cyclic carbonate 7MCC, Matsuo *et al.*[36] performed a cationic Ring-Opening Polymerization using different initiators derived from sulfonic acids (TfOMe and TfOEt) and tetrachlorostannane ($SnCl_4$) at 20°C (**Table 6.6**, entry 1). They performed the same polymerization protocol as used for 6MCC, finding that 7MCC undergoes ROP about 100 times faster[222]. The same group also performed an anionic ROP[40] using *sec*-BuLi as initiator which results in the corresponding polycarbonate in a high yield and short time (**Table 6.6**, entry 2).

Brignou *et al.*[210] and Matsuo *et al.*[37] reported a substituent effect in the α- or β- positions of 7MCCs. Matsuo *et al.* performed a cationic ROP using triflic acid (TfOH) and derivates (TfOMe or TfOEt), or tetrachlorostannane ($SnCl_4$) as initiators for α-substituted 7MCC monomers with methyl and phenyl substituents, and a β-substituted 7MCC with a phenyl group. In this chapter, the mono-substituted 7MCC-Me corresponds to the seven-membered cyclic carbonate with a methyl group in the β-position, as studied by the Brignou group. They reported a successful ROP for β-methyl-7MCC using organocatalysts

Table 6.6: Experimental conditions for the ROP of seven-membered cyclic carbonates reported in literature: 7MCC[36,40], 7MCC-Me[210], 7MCC-Cyc[238], 7MCC-C=C[90] and 7MCC-Ocyc[239]

Monomer	Initiator	Catalyst	Solvent	Temp.	M_n	Đ
7MCC[36]	TfOEt	-	Toluene	20	57.6	1.5
7MCC[40]	*sec*-BuLi	-	THF	20	22.8	1.61
7MCC-Me	BnOH	TBD	Toluene	110	10.35	1.40
7MCC-Cyc	BnOH	(Y1)	Toluene	r.t.	22.4	1.28
7MCC-C=C	4-MeBnOH	TBD	CH_2Cl_2	r.t.	18.1	1.53
7MCC-Ocyc	*p*-tolylMeOH	TBD	Toluene	100	75.2*	1.49

*Temperature in °C, $\boldsymbol{M}_n$ in kg·mol^{-1}, Đ = M_w/M_n / *(Data in kDa)*

(TBD, BEMP and DMAP) and metal-based catalysts, namely, aluminium trifluoromethanesulfonate ($Al(OTf)_3$), zinc and yttrium-based organometallic complexes ([(BDI^{iPr})-Zn(N(SiMe$_3$)$_2$)][a] and [(ONOO^{tBu})Y(N(SiHMe$_2$)$_2$)(THF)][b] respectively). Focusing on the organocatalyzed ROP, TBD stands out as a catalytic system giving the highest values of M_n compared with the other organocatalysts under the same conditions (**Table 6.6**, entry 3).

The seven-membered cyclic carbonate fused to cyclohexane ring, 7MCC-Cyc[238], was polymerized by Zhang *et al.* via coordination-insertion ROP using an yttrium alkyl complex supported by a tetradentate amino-bisphenolate ligand catalyst (Y1). The monomers tested with the monomer/catalyst/initiator ratio ([M]:[Y1]:[I]) of 100:1:1, proceeded really fast and approached full conversion within 0.5 min. Notably, when the ratio [M]:[Y1]:[I] was increased to 20000:1:1 they obtained a polymer with M_n of 540 kg·mol^{-1} and Đ of 1.21 in just 11 minutes. They also found interesting properties for this polymer, whose degradation gave access to a cyclic dimer by means a depolymerization reaction. The dimer could be re-polymerized with a base catalyst while increasing the temperature to 150°C.

For 7MCC-C=C[90], the study made by Buchard *et al.* showed that TBD is the

[a](BDI^{iPr}) = 2-((2,6-diisopropylphenyl)-amido)-4-((2,6-diisopropylphenyl)-imino)-2-pentene

[b](ONOO^{tBu}) = amino-alkoxy-bis(phenolate)

best catalyst to enable a ROP,and they obtained a total conversion and a 100:0 *cis/trans*, which thus gives a polymer with a throughout *cis* configuration in the repeat units (**Table 6.6**, entry 5). They also exmined a metal-based catalyst as $Sn(Oct)_2$ at 60°C, thereby obtaining a lower conversion and M_n. Finally, to synthesise a predominantly *trans*-polycarbonate, they uses second-generation Grubbs catalyst (GII), that allowed to obtain a full conversion and a polymer having a 10:90 *cis/trans* ratio with higher M_n than that facilitated by TBD.

The study of the monomer 7MCC-Ocyc reported by Wu *et al.*[239], illustrates a ROP reaction using organo- and metal-based catalyst (TBD and zinc β-diiminatecomplex) with p-tolylmethanol as an initiator, obtaining the desired polycarbonates (**Table 6.6**, entry 6). Moreover, the latter can undergo a ROMP (Ring-Opening Metathesis Polymerization) with first and third generation Grubbs catalysts (GI and GIII). Interestingly compared with the ROP reaction, the ROMP enables the formation of polymers with hydrocarbon backbones, which may provide excellent thermal and hydrolytic stability to the resulting polymers. In summary, Wu *et al.* prepared 7MCC-Ocyc and other 7MCC monomers from bio-renewable materials, which are suitable for both ROP and ROMP, thereby obtaining aliphatic polycarbonates with high molecular weight.

The most common eight-membered cyclic carbonates (8MCCs) reported in the literature are N-Substituted eight-membered cyclic carbonates[164,226,240–244], which undergo a successful Ring-Opening Polymerization reaction using organocatalysts as DBU, TBD or thioureas.

6.2 Objective/Motivation

The aims of the work described in this chapter are:

- To understand the Ring-Opening Polymerization reaction for cyclic carbonates using TBD as a benchmark catalyst and BnOH as an initiator at room temperature in toluene solution.
- To comprehend the effect of the ring size of the cyclic carbonates (5MCC, 6MCC and 7MCC) on its intrinsic reactivity and on the stability of the

polymer

- To compare the reactivity for monomers with a different number, chemical nature and size of substituents in the cyclic carbonate.
- To create a predictive model in order to anticipate which monomers will be likely polymerized under ambient temperature conditions.

Understanding which monomers are prone to be polymerized before trying them in the laboratory could be extremely helpful for experimental chemists. In this way, the developed model would allow to identify the monomers with the highest ROP-probability before their synthesis, thus optimizing time and resources in the lab.

6.3 Computational Details

DFT calculations were performed using ωB97X-D functional[191] and the 6–311G** basis set[192,193]. All structures in this study were calculated with the Gaussian 16 program, revision A.03[62] at room temperature with an implicit solvent model SMD[65] with parameters for toluene. To determine the nature of the structures involved in the mechanisms (intermediates or transition states), an unconstrained optimization with a vibrational analysis were performed.

During the Ring-Opening polymerization reaction described in this chapter, monomers are added along the pathway, hence, the entropy of the system changes significantly in this steps. Consequently, standard state entropic corrections were applied to the Gibbs free energies[66,67].

To find the initial structures for the transition states, a Potential Energy Surface (PES) scan were performed using Gaussian16 program, revision A.03[62] at same DFT level, temperature and solvation model than described above. For some structures, the PES scan was initially calculated using GFN2-xTB, version 6.4.1 (program developed by Grimme)[83], at room temperature with implicit solvent model GBSA2 with toluene parameters. The resulting geometry found

from this calculations, is re-calculated at DFT level with Gaussian 16 with the same conditions described above. The advantage to use GFN-xTB is the lowest computational cost and time to scan more than one geometric parameter (distance, angle or dihedral) simultaneously or sequentially. In that way, it is possible to evaluate more extensively the possible conformations in a transition state without spending so much time.

To calculate these mechanistic pathways for monomers that have substituents in a non-symmetric positions, the most favourable scenario was considered. Specifically, the initiation, propagation and ring-opening parts are performed for the side which is less sterically hindered, thus obtaining structures thermodynamically favoured and more realistic geometries under these conditions.[39]

The alternative method used in **Section 6.4.8** to determine a Gibbs free energy for the polymer, starts performing a molecular dynamics simulation of 50 ps long (4 fs time-step) using the GFN2-xTB, version 6.4.1[83], at room temperature using an implicit solvent model GBSA2 with toluene parameters. To find the most relevant conformations from the molecular dynamics trajectory, above 1000 structures from the trajectory were divided into 5 clusters via K-Means[245] clustering method. For each centre of cluster, the geometry was re-optimized and a vibrational analysis was also performed at the same DFT level outlined above with Gaussian 16 program, revision A.03[62]. The final averaged Gibbs free energy is obtained by adding the energy of each conformer weighted according to a Boltzmann distribution (**Equation 6.1 - Section 6.4.8**).

6.4 Results and Discussion

To accomplish the objectives described in the section above, an extensive study of the Ring-Opening Polymerization reaction was developed. The applied procedure consists of finding the most thermodynamically favoured mechanistic pathway after considering all possibilities. Once the most reliable reaction mechanism is defined, the effect of the ring size of the cyclic carbon-

ates ring sizes was evaluated to understand the relative reactivity and compared with the experimental studies reported in the literature[31,35,38,39,195,220,228,246]. Then, a set of cyclic carbonates polymerized under the same experimental conditions[28,223], and their TBD-mediated ROP calculated to verify whether the mechanistic pathway and computational model agree with real cases. This theoretical study also considers the number of substituents present in the six-membered cyclic carbonates, followed by a deeper investigation of the effect of the nature and size of the substituents in this ROP reaction. The combined information helped to develop a predictive model that, is able to indicate which monomers can be polymerized by ROP using TBD as a catalyst, BnOH as an initiator, and performed at room temperature in toluene solution.

6.4.1 Mechanistic Pathway

The reaction under study is represented in **Figure 6.7**. The typical steps for a standard polymerization reaction consist of an initiation, propagation and termination. The number of propagation steps depends on the concentration of the monomers, initiator, and catalyst. To limit the computational cost, the polymer model system chosen is a trimer, and its preparation involves an initiation and two propagation steps. The tendency of the ROP reaction can be determined with these steps, without requiring too many computational resources.

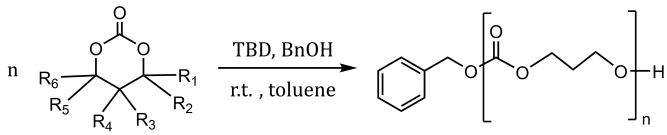

Figure 6.7: Schematic representation for the ROP reaction studied

The mechanistic studies started considering the simplest route, namely a stepwise pathway showed in **Figure 6.8**. This mechanism starts when the initiator (BnOH) is deprotonated by the catalyst (TBD) obtaining an alkoxide (BnO^-) and the protonated form for the catalyst ($HTBD^+$). The alkoxide attacks the carbonate carbon of the cyclic carbonate making a bond, and creating a tetra-

hedral intermediate. The ring-opening step occurs due to an electronic rearrangement, obtaining an oligomer-alkoxide. The termination step occurs when the $HTBD^+$ protonates the alkoxide end-group obtaining thus a released polymer and the regenerated catalyst. Unfortunately, the transition states and some intermediates calculated for this mechanism are remarkably energetically disfavoured, therefore, and thus this reaction has to occur in a different way.

While the initiation (**TS 1**) and termination (**TS 4**) based transition states and intermediates are energetically feasible, the propagation (**TS 2**) and ring-opening (**TS 3**) are extremely high in energy at room temperature. The structures from **C1** till **F1** include only the initiator (BnOH) and 6MCC, indicating that the substrate might be able to react without the presence of the catalyst albeit at relatively high reaction temperatures. All these structures have extremely high energy values (from 44.3 to 68.1 kcal·mol^{-1}), which means that the TBD presence during this process is essential to reduce the high kinetic barrier. Also notice that other transition states include the catalyst, highlighting the importance of its presence in the overall manifold.

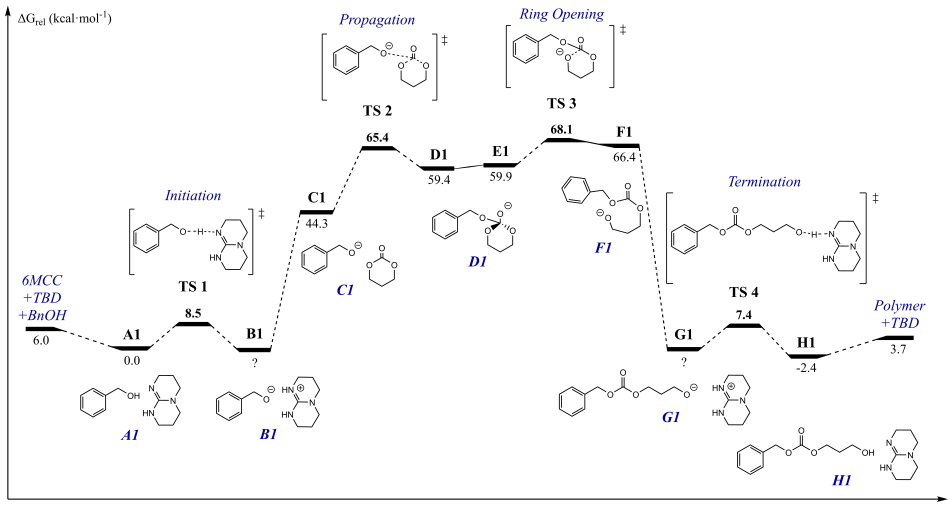

Figure 6.8: Relative Gibbs Free energy profile and structures for the unsuccessful ROP mechanistic pathway

*(Note that some structures are missing in **Figure 6.8**. This is due to the high*

energy values for some structures, that corroborates with the view that this is likely not the mechanistic pathway involved in this ROP reaction under these conditions. Therefore, there was no need to calculate the entire mechanism nor the synthesis of the trimer.)

Considering this results and the nature of the catalyst[12,13], another mechanistic pathway was calculated and depicted in **Figure 6.9**. In this case, the catalyst role in all steps and transition states was considered, and these include the initiator, catalyst and monomer interacting simultaneously.

The mechanism represented in **Figure 6.9** can be divided in different parts, the first one involves the initiation step and the first ring-opening. Followed by a propagation part which consists of a propagation and a ring-opening step, and all this is repated one time to end up with a trimer product.

The mechanism starts with the separated structures: the monomers, catalyst and initiator (at 6.7 kcal·mol^{-1}), and the first intermediate **A** is an adduct that includes the catalyst (TBD), the initiator (BnOH) and the monomer (6MCC) used as a reference (0.0 kcal·mol^{-1}). Then, the initiation step occurs in **TS 1.1** (at 14.9 kcal·mol^{-1}), the nitrogen atom from the TBD deprotonates the primary alcohol from the initiator (BnOH) obtaining an alkoxide that attacks the carbonate carbon from the monomer at the same time, through a concerted transition state.

The structure **B** (at 12.2 kcal·mol^{-1}) is the result of this interaction, where TBD is protonated and the initiator is bound with the monomer obtaining an intermediate with a tetrahedrally surrounded carbon. In the structure **C** (at 14.1 kcal·mol^{-1}), the HTBD^{+} is located in a different place, having an hydrogen bond with the oxygen atom from the carbonate and the other hydrogen is located near to the outer oxygen of this structure. The first ring-opening occurs in **TS 1.2** (at 19.0 kcal·mol^{-1}) where the HTBD^{+} protonates the outer oxygen followed by an electronic rearrangement that opens the ring. The structure **D** (at 1.1 kcal·mol^{-1}) is the adduct of the oligomer with the catalyst recovered.

The propagation part starts with structure **E** (at -1.9 kcal·mol^{-1}) that includes the oligomer, the catalyst and another monomer. The propagation step

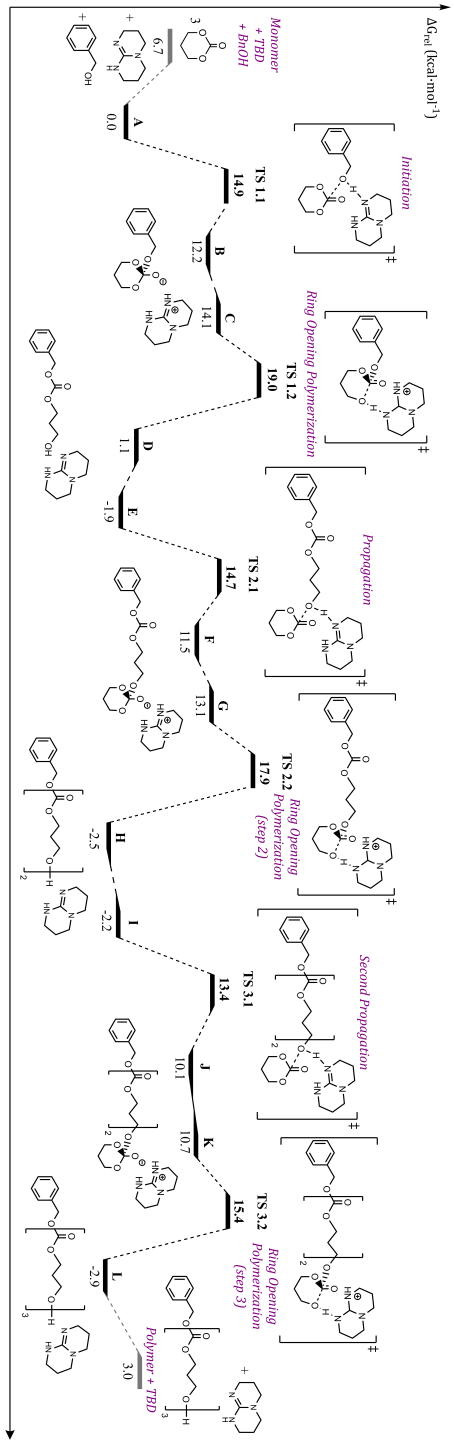

Figure 6.9: Mechanistic Pathway for the ROP of the simplest six-membered cyclic carbonate (6MCC) giving a trimerix carbonate

is shown in the transition state **TS 2.1** (at 14.7 kcal·mol^{-1}), where the oligomer is deprotonated by the TBD and the alkoxide attacks another monomer simultaneously. This transition state leads to structure **F** (at 11.5 kcal·mol^{-1}), that is an intermediate with a tetrahedral carbon. The structure **G** (at 13.1 kcal·mol^{-1}) is quite similar to structure **C**, that is, the protonated TBD is located nearby via one hydrogen bond made to the outer oxygen of this structure and the other hydrogen is located near one of the C-O bonds. Due to the nature of the catalyst, HTBD^{+} stablized the ensemble and allows the reaction to continue towards the transition state **TS 2.2** (at 17.9 kcal·mol^{-1}). Here, the HTBD^{+} protonates the outer oxygen of this structure, breaking the ring, obtaining a dimer and the recovered catalyst in structure **H** (at -2.5 kcal·mol^{-1}).

As in a typical polymerization, the second propagation part (from structure **I** to **L**) proceeds in a similar way as discussed above. In order to not being redundant, it will not be described in detail. It starts with the structure **I** (at -2.2 kcal·mol^{-1}) that is the adduct of the dimer, catalyst and another monomer to undergo the propagation step **TS 3.1** (at 13.4 kcal·mol^{-1}), obtaining the intermediate **J** (at 10.1 kcal·mol^{-1}). The last ring-opening starts with structure **K** (at 10.7 kcal·mol^{-1}) that continues towards transition state **TS 3.2** (at 15.4 kcal·mol^{-1}) where ring-opening happens producing structure **L** (at -2.9 kcal·mol^{-1}) as a product. Finally, the last structure corresponds to the separated components including a trimer, and the recovered catalyst at 3.0 kcal·mol^{-1}.

In summary, the initiation and propagation transition states for each part are lower in energy than their corresponding ring-opening transition states. Moreover, the overall tendency for this ROP reaction is to be energetically more stable after each subsequent propagation, and longer oligomer/polymer chains will thus be favoured.

Mechanistic Pathway Structures

To analyse in more detail the mechanism described in **Figure 6.9**, the geometries for key structures were scrutinized in more detail with respect to their

bond distances, and (dihedral) angles.

The first transition state (labelled as **TS 1.1**) geometry is presented in **Figure 6.10** and selected geometrical data are listed in **Table 6.7**. As mentioned above, **TS 1.1** is a concerted transition state where the BnOH is deprotonated by TBD, and the newly-created alkoxide attacks the carbonate carbon from the 6MCC.

Following the imaginary frequency, the motion seen consists of the deprotonation of the initiator which is the breaking of the bond between oxygen O5 and hydrogen H6 (1.53 Å), followed by an approach of the oxygen O5 towards carbon C2 making a new bond, and simultaneously another bond between hydrogen H6 and nitrogen N7 resulting in the protonated catalyst $HTBD^+$ (1.02 Å). The similarities between the angles computed for O5-H6-N7 and O4-H9-N8, which are close to 180°, emphasize the role of TBD, which is enable a proton transfer in the first, and a hydrogen bond in the second case. The carbon C2, once bound to oxygen O5 from the BnOH, changes its geometry into tetrahedral and during this transition state **TS 1.1**, the angle O1-C2-O3 is 115.4°.

Table 6.7: Angles, dihedral angles and distances for the geometry for the **TS 1.1** represented in **Figure 6.10**

Atom labels	**Angle (°)**
O1-C2-O3	115.4
O1-C2-O5	94.8
C2-O5-H6	100.5
O5-H6-N7	174.3
N8-H9-O4	172.2
C2-O5-H6-N7	-170.7
O4-H9-N8-N7	163.5
H6-N7-N8-H9	-9.7

Atom labels	**Distance (Å)**
C2-O5	1.95
O5-H6	1.53
H6-N7	1.02
N8-H9	1.03
H9-O4	1.75
O1-C2	1.37
C2-O3	1.36
C2-O4	1.23

The intermediate presented in **Figure 6.11** corresponds to the structure **C** in **Figure 6.3**. The latter structure is chosen to show in detail the tetrahedral intermediate obtained as a product of the first transition state **TS 1.1**. Note that the orientation of the $HTBD^+$ is different than that in structure **B**, which is the direct product for the first transition state, in contrast to structure **C**, which is ready to evolve into the next transition state **TS 1.2**.

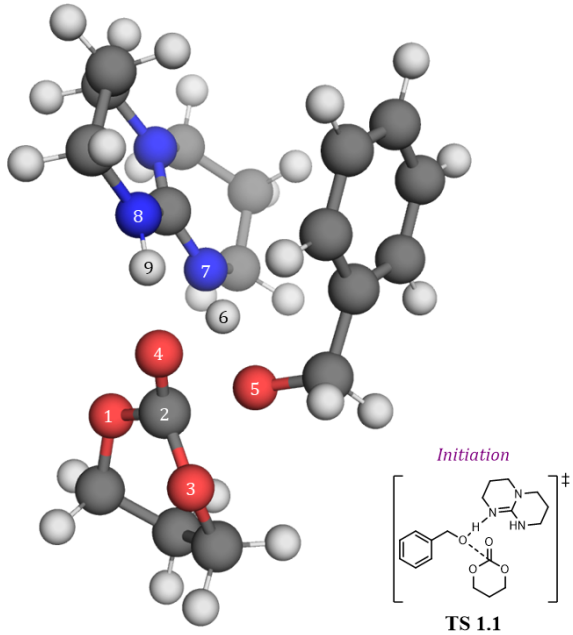

Figure 6.10: Molecular structure for the **TS 1.1** shown in **Figure 6.9** including atom labels

In this structure, the initiator is bound to the monomer at carbon C2, whose geometry is tetrahedral. Some values are presented in **Table 6.8**, and they show that the oxygen atoms O5, O1, O3 and O4 bound to the central carbon C2 produce angles around 110°, which correspond well to a tetrahedral geometry. Moreover, the single bond distances between these oxygens (O5, O1, O3) and this carbon C2 are 1.44, 1.41 and 1.48 Å, respectively, which are close to the theoretical value for these C-O distances (1.43 Å). The hydrogen bonds that the protonated catalyst ($HTBD^+$) is making have linear angles between the oxygen O3, hydrogen H6 and nitrogen N7 which are almost 180°, and the dihedral for O3-H6-H9-O4 is only 13.3°. These angles enable a stable tetrahedral geometry and allow the reaction to continue with the ROP by protonation of the outer oxygen O3 by the hydrogen H6 of the catalyst. The N-H distances for the $HTBD^+$ (H6-N7 and N8-H9) are around 1.05 Å, while the H-O distances between the catalyst and the main chain (O4-H9 and O3-H6) are quite long at 1.50

and 1.76 Å, respectively.

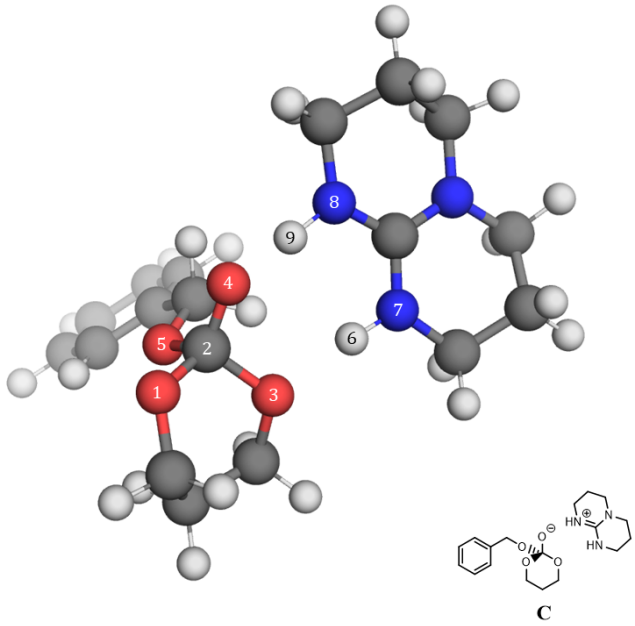

Figure 6.11: Molecular structure for the Intermediate **C** shown in **Figure 6.9** including atom labels

Table 6.8: Angles, dihedrals and distances for the geometry for the **TS 1.2** presented in **Figure 6.11**

Atom labels	Angle (°)
O1-C2-O3	108.0
O1-C2-O4	113.8
O3-H6-N7	173.6
O3-C2-O4	110.2
O5-C2-O4	115.6
C2-O3-H6-N7	-135.3
O3-H6-N7-N8	136.2
O3-H6-H9-O4	13.3

Atom labels	Distance (Å)
C2-O5	1.44
O3-H6	1.76
H6-N7	1.03
N8-H9	1.08
H9-O4	1.50
O1-C2	1.41
C2-O3	1.48
C2-O4	1.27

The transition state presented in **Figure 6.12** corresponds to **TS 1.2**, which is the ring-opening reaction shown in **Figure 6.9**. To clarify the transformation

involved during this transition state, some geometrical data is included in **Table 6.9**.

This transition state consists of a ring-opening reaction by the separation of the carbon C2 and the outer oxygen O3 and a simultaneous protonation of oxygen atom O3 by the H6 from the $HTBD^+$. The tetrahedral geometry illustrated in **Figure 6.11** is broken in this step.

The protonation of the outer oxygen O3 by the hydrogen H6 results in shorter distances for the oxygen atoms O5 and O1 bound to the carbon C2 (1.37 and 1.35 Å, respectively), and a larger one for the O3-C2 distance at 1.97 Å in comparison with the structure **Figure 6.11**, in which all these distances are around 1.43 Å. As a consequence of the ring-opening reaction, the geometry involved between the oxygens O1 and O4 and the carbon C2 becomes trigonal planar with a value of 120.2°.

The nature of the catalyst is its capacity to create hydrogen bonds and accommodate proton transfer reactions, and in the structure of **Figure 6.12** the capacity of TBD is to make hydrogen bonds with the main chain and keeping it near the catalyst. This is illustrated by the angle O4-H9-N8, and the reactivity related with the protonation is presented through the angle O3-H6-N7, both of which are linear with values close to 180°.

Table 6.9: Angles, dihedrals, and distances for the geometry for the **TS 1.2** represented in **Figure 6.12**

Atom labels	**Angle (°)**
O1-C2-O3	99.2
O1-C2-O4	120.2
O3-H6-N7	177.8
O4-H9-N8	175.7
O3-C2-O4	102.9
C2-O3-H6-N7	-132.6
O3-H6-N7-N8	153.6
H6-N7-N8-H9	-4.6

Atom labels	**Distance (Å)**
C2-O5	1.37
O3-H6	1.42
H6-N7	1.11
O1-O3	2.56
H9-O4	1.73
O1-C2	1.35
C2-O3	1.97
C2-O4	1.22

As seen above, the mechanistic pathway includes analogous transition states and intermediates depending on the number of propagations consid-

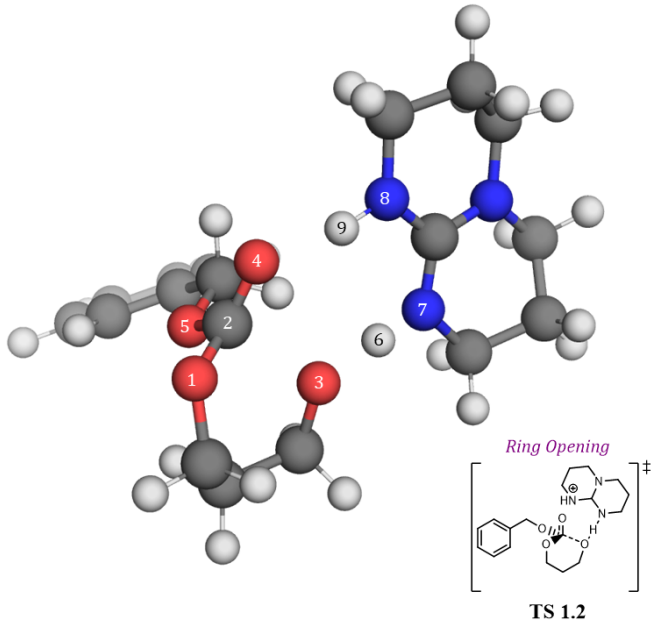

Figure 6.12: Molecular structure for the **TS 1.2** represented in **Figure 6.9** including atom labels

ered, which are directly related with the number of monomers added to the polymer chain. Therefore, the geometry involved in the initial transition state **TS 1.1** is analogous to the propagation-based **TS 2.1** and **TS 3.1**.

The main difference between the initiation and propagation steps is which molecule is deprotonated during the transition state, which may be the initiator BnOH (**TS 1.1**) or the terminal alcohol group from the *n*-polymer chain (**TS 2.1** and **TS 3.1**). The same occurs with the intermediate **C** and intermediates **G** and **K**, all of them have a tetrahedral carbonyl geometry around the carbon center, and hydrogen bonds with the protonated catalyst.

6.4.2 Ring Size

As introduced above, not only the typical six-membered cyclic carbonate is prone to undergo a ROP reaction[30,31,35,44,195,202,211,212,219,228,246], other cyclic carbonates such as five[232,236,247–250], seven[38,43,90,210,221,238,239,251] and even

eight-membered ones[226,240–244] are also prone to be polymerized under suitable conditions. As mentioned in the literature[220], larger rings (i.e., 6-, 7- and 8-MCCs) should provide thermodynamically stable polymers, although they are typically more difficult to synthesize. On the contrary, five-membered cyclic carbonates produce shorter polymer chains and sometimes cannot even undergo ROP[39,194]. *(Note that "larger polymer" in this case means a macromolecule that is the result of subsequent propagations involved during the reaction, and is not directly related to the ring size.)*

Taking into account all this information and understanding how the reaction works under the conditions shown in **Figure 6.7**, monomers with different ring sizes (five-, six- and seven-membered cyclic carbonates) were compared to see the differences among them (**Figure 6.13**). For all studied cases, a trimer formation is considered as a model system for the ROP reaction.

In **Figure 6.13**, the overall tendency for each monomer is visible after two propagation steps. Five- and seven-membered cyclic carbonates have more visible differences in each propagation part with opposite thermodynamic stability. The polymer derived from the 7MCC is relatively quite stable, but the one originating from the 5MCC relatively unstable, while the six-membered cyclic carbonate provides after ROP a slightly energetically more favoured macromolecule after each subsequent propagation. In more detail, the conversion of the five-membered cyclic carbonate (5MCC) is kinetically feasible with the lowest initiation transition state **TS 1.1** at 10.2 kcal·mol^{-1}, whereas the conversion of six- and seven-membered cyclic carbonates (6MCC and 7MCC) require 14.9 and 13.6 kcal·mol^{-1}, respectively. The first ring-opening (**TS 1.2**) is energetically more disfavoured than **TS 1.1** for both 5MCC and 6MCC with values 14.1 and 19.0 kcal·mol^{-1} in contrast to 7MCC, for which a value of 12.0 kcal·mol^{-1} was calculated.

The first propagation step, that includes the transition states **TS 2.1** and **TS 2.2** and their intermediates, have different tendencies for each monomer. The use of 5MCC produces slightly more unstable energies, with values of 12.4 and 15.8 kcal·mol^{-1} for **TS 2.1** and **TS 2.2**, respectively. These are close to the ones

determined for the 6MCC, and these latter values are slightly more favoured at 14.7 and 17.9 kcal·mol^{-1}. While five- and six-membered cyclic carbonates have similar energetic values in this part, the seven-membered cyclic carbonate distances itself from structure **F** onwards. It starts with a value of 11.4 kcal·mol^{-1} for **TS 2.1**, akin to the energies for the 5MCC and 6MCC based pathway. Then, the 7MCC-derived structures **F** and **G** are at 1.4 and 3.2 kcal·mol^{-1}, respectively, which are very different to the other two monomers: these values are 10.0 and 11.6 kcal·mol^{-1} for the 5MCC, and 11.5 and 13.1 kcal·mol^{-1} for the 6MCC.

The ring-opening transition state **TS 2.2** for the 7MCC is kinetically favoured at kcal·mol^{-1}. The intermediate structure **H** shows already the tendency for the next propagation step. The 5MCC-based pathway delivers the most unstable structure at 1.3 kcal·mol^{-1}, followed by a relatively close energetic value for the 6MCC at -2.5 kcal·mol^{-1} and a remarkably low energetic value of -13.1 kcal·mol^{-1} for the 7MCC based route. The second and last computed propagation step shows exactly the tendencies that have been reported in the literature[220]. The 5MCC-pathway shows the most unstable structures at 15.6 kcal·mol^{-1} for **TS 3.1** and 20.3 kcal·mol^{-1} for **TS 3.2**. In the middle are located the 6MCC-based structures for **TS 3.1** and **TS 3.2** with energies at 13.4 and 15.4 kcal·mol^{-1}, respectively. The 7MCC-pathway entails the most stable transition states with energetic values of 6.0 kcal·mol^{-1} for **TS 3.1** and 0.6 kcal·mol^{-1} for **TS 3.2**. This observed tendency is identical for structure **L** and the final oligomer (trimer): the 5MCC-pathway shows energies of 6.2 and 8.5 kcal·mol^{-1}, the 6MCC-route at -2.9 and 3.0 kcal·mol^{-1} and the 7MCC-manifold at -15.1 and -7.5 kcal·mol^{-1}, respectively. In essence, the trimer formation is exergonic for the ROP of 6MCC and 7MCC, but endergonic for the ROP of 5MCC.

On the one hand, the ROP of the seven-membered cyclic carbonate is significantly more thermodynamically favoured than the other monomers. This is not only applicable for almost all intermediates and transition states, but also for the overall tendency. The ROP of the six-membered cyclic carbonate is slightly less favoured energetically for each propagation step. It starts with relatively unstable structures at the initiation and the first propagation step,

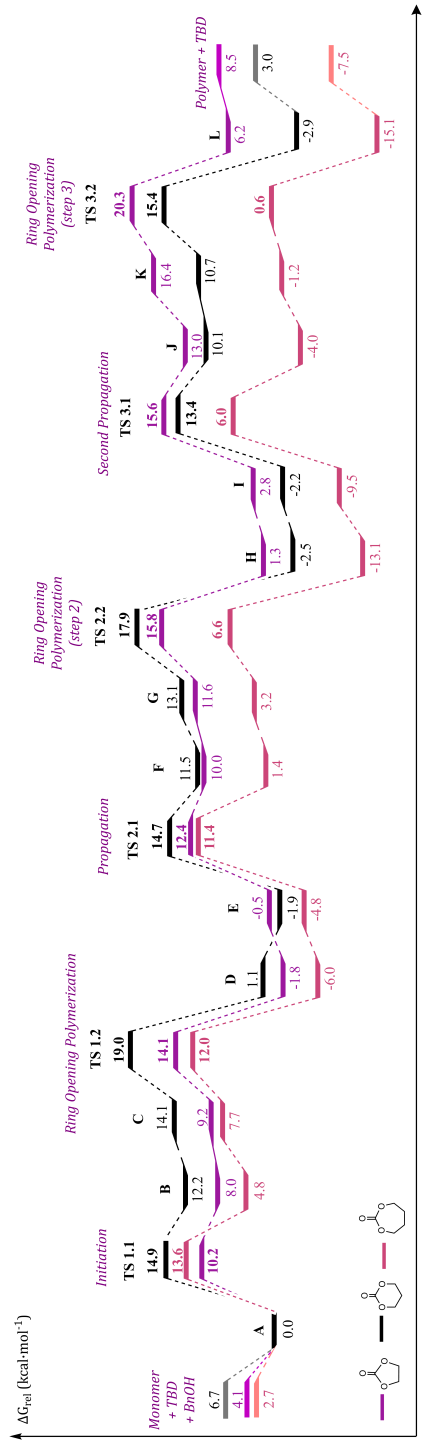

Figure 6.13: Five-, six- and seven-membered cyclic carbonates mechanistic profile comparative in kcal·mol^{-1}

and then evolves to become more feasible. The pathways based on the six- and seven-membered cyclic carbonate become, respectively, around 2 and 6 kcal·mol^{-1} thermodynamically more favoured with each consecutive propagation step. Contrary, the ROP of the five-membered cyclic carbonate starts with similar energies as noted with the other monomers, but then this ROP pathway becomes energetically more disfavoured with increasing values in each next propagation step.

The five- and six-membered cyclic carbonates have a similar tendency in each part, specifically, the transition states related to the ring-opening are energetically more disfavoured than the transition states related to initiation or propagation steps. In contrast, the seven-membered cyclic carbonate has the opposite behaviour. The stability of the final polymer structures after two propagations agrees with the expected behaviour and reported experimental data[39,220]:

- The 5MCC-pathway corresponds to the formation of the most unstable oligocarbonate chain and has an energetic value of kcal·mol^{-1}.
- The 6MCC-pathway is located between the 5MCC- and 7MCC-based one with an accessible oligomer at 3.0 kcal·mol^{-1}.
- The 7MCC-route leads to the most stable oligomeric chain at -7.5 kcal·mol^{-1}.

These results not only agree with the experimental behaviour of these monomers but also explain the tendency of each monomer to undergo more (7MCC, 6MCC) or less (5MCC) propagation steps.

Predictive correlation

As seen in the previous section, the trimer synthesis helps to see the tendency of the overall polymerization reaction, but with the initiation and first propagation parts is essentially enough to understand the reactivity and reduces the computational cost for each monomer. For this reason, the model system employed to represent the reactivity of a larger set of monomers consider only the formation of dimeric instead of trimeric structures.

In order to see more clearly the results and compare monomers between them, a correlation plot was designed (**Figure 6.14**). The *y* axis is representing the energy span of the reaction in kcal·mol^{-1} and on the *x* axis the thermodynamic stability of the dimer in relation to the respective monomers is given. These values are collected in **Table 6.10**.

To estimate the kinetic aspects of the process, we computed the energy span of the reaction as the difference between the most energetically disfavoured transition state and the thermodynamically most favoured minimum occurring before this transition state, as introduced by Kozuch[67].

Note that the value that describes the dimer stability (**Table 6.10**) is not the same that the value seen at the final structure of the mechanistic pathway. This difference is due to the reference structure that is considered, in this plot the stability of the polymer is referred to the initial monomers instead of the adduct **A**. Combining the energy span and the dimer stability versus the monomer, a predictable outcome for the ROP of the monomers can be gathered in a simple and intuitive plot (**Figure 6.14**).

The ROP reaction occurs at room temperature, hence, the maximum energetic span considered is below 25 kcal·mol^{-1}. This chosen boundary of the final dimer stability compared with the initial monomers is not an exact value, and for that reason, experimental results are useful to obtain knowledge whether the polymerization of a given monomer is truly feasible or not. The ideal expected monomer behaviour is localized in the lower left corner in **Figure 6.14** with an attractive (energy span) - (polymer stability). Cross-sections in this specific area of the plot mean that these ROP reactions will be energetically more favoured with a suitable and low enough thermodynamic stability for the, and hence, the respective monomer studied should be able to undergo a ROP reaction under these conditions.

Looking the **Figure 6.14** and the energy values included at **Table 6.10**, it is possible to see clearly the tendencies described above. The ROP of the 7MCC is located in the most stable region, with an energetic span of 17.4 kcal·mol^{-1} and the dimer synthesised is thermodynamically stable at -10.1kcal·mol^{-1}. The 5MCC-pathway has a very close value for the energetic span being 17.6

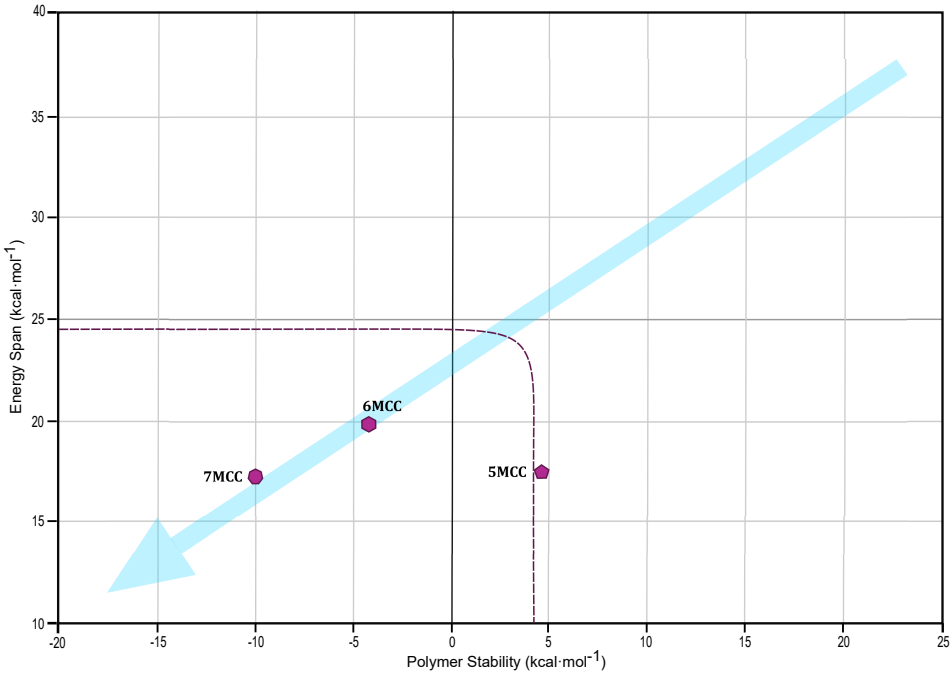

Figure 6.14: Correlation plot for five- (5MCC), six- (6MCC) and seven- (7MCC) membered cyclic carbonates represented as a purple pentagon, hexagon and heptagon respectively. The dashed line divides the polymerization from the non-polymerizable region. The blue arrow points at the most stable region in the plot

Table 6.10: Correlation plot values and legend for cyclic carbonates with different ring sizes in kcal·mol^{-1}

Monomer	Energy Span	Polymer stability
5MCC	17.6	4.4
6MCC	19.8	-3.8
7MCC	17.4	-10.1

kcal·mol^{-1}, but the dimer stability is located significantly higher at 4.4 kcal·mol^{-1} showing the difference with the tendencies of the reactions reported in the literature. The 6MCC-pathway has a higher energy span compared to both pathways starting from either the 5MCC or 7MCC and needs to surmount 19.8 kcal·mol^{-1}, and the dimer stability is located between the other two pathways at -3.8 kcal·mol^{-1}.

6.4.3 Real Case Studies

In this section, the polymerization of monomers tested experimentally under the same conditions as presented in **Figure 6.7** are considered to combine and validate the theoretical model against known experimental data. The reference structures are shown in **Figure 6.15**: Bicyc-OH, Bicyc-OTMS, Bicyc-Cyclohex[28], and CF_3-Ph, CF_3-Biphen and CF_3-Naph[223] which were tested in laboratory using TBD as a catalyst, toluene as a solvent at room temperature.

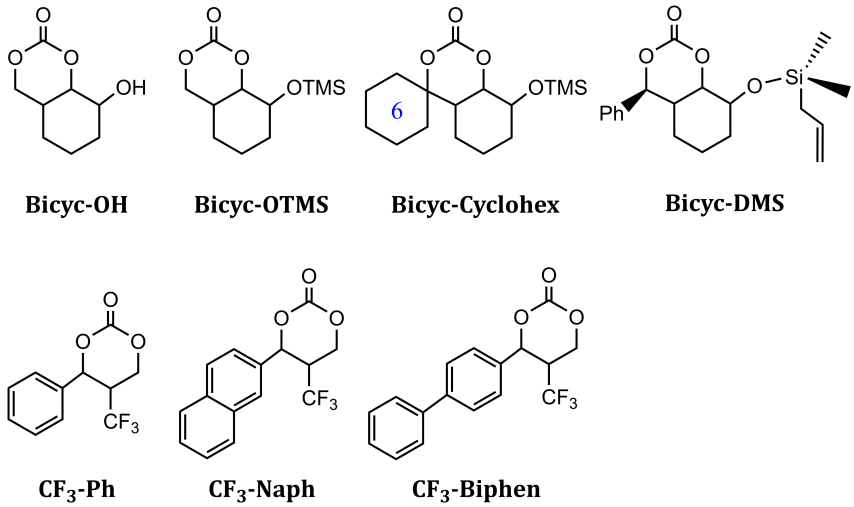

Figure 6.15: Monomers calculated from experimental results under the exact conditions

All of these monomers are accessible through reported syntheses and nearly all of them may undergo a successful ring-opening Polymerization reaction. Recent published results[28,223] show that by using the monomers CF_3-Ph, CF_3-Biphen, CF_3-Naph and Bicyc-OTMS it is possible to obtain large and stable polymer chains. The monomers Bicyc-DMS[252] and Bicyc-Cyclohex were tested in the laboratory by Kleij's group members (Dr. David Lamparelli and Alba Villar-Yanez (myself), respectively) obtaining unsuccessful results. It must be highlighted that also unsuccessful results bear importance since they can further shape the predictive computational model.

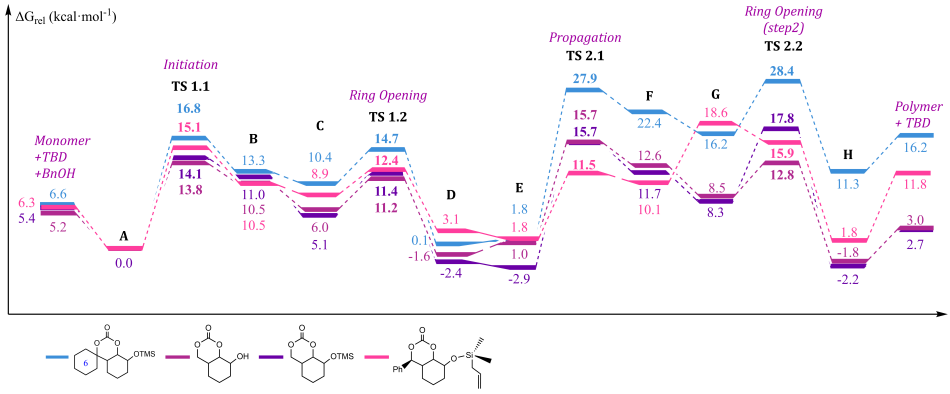

Figure 6.16: Relative Gibbs free energy profiles in kcal·mol^{-1} for bicyclic compounds: Bicyc-Cyclohex, Bicyc-OH, Bicyc-OTMS and Bicyc-DMS

In **Figure 6.16** a comparison of relative Gibbs energy profiles for the ROP of the bicyclic compounds is represented. The overall tendency of Bicyc-Cyclohex is producing a dimeric carbonate with lower thermodynamical stability as compared to the other compounds. The difference is not so large in the initiation part where the **TS 1.1** have values of 13.8, 14.1 and 15.1 kcal·mol^{-1} for the Bicyc-OH, Bicyc-OTMS and Bicyc-DMS, respectively, while for Bicyc-Cyclohex this amounts to 16.8 kcal·mol^{-1}. Hereafter, this is followed by the ring-opening transition state **TS 1.2**, that have similar energetic values of 11.2, 11.4, 12.4 and 14.7 kcal·mol^{-1} for Bicyc-OH, Bicyc-OTMS, Bicyc-DMS and Bicyc-Cyclohex.

During the propagation part, which includes **TS 2.1** (propagation step) and **TS 2.2** (ring-opening), the energies for the Bicyc-Cyclohex pathway are significantly higher with values of 27.9 and 28.4 kcal·mol^{-1}, respectively. This is in contrast with the other monomers, for which the propagation transition states **TS 2.1** in the case of Bicyc-OH and Bicyc-OTMS have lower values of 15.7 (for both) and 11.5 kcal·mol^{-1} for Bicyc-DMS. Then during the next and second ring-opening transition state **TS 2.2**, the pathways for Bicyc-OH, Bicyc-DMS and Bicyc-OTMS show values of 12.8, 15.9 and 17.8 kcal·mol^{-1}, respectively, being more energetically favoured than Bicyc-Cyclohex comparatively.

The reaction ends with the dimer and the catalyst gathered in structure **H** followed by their corresponding separated structures. In this last stage,

each monomer follows the same tendency as noted before, the Bicyc-Cyclohex pathway included the most disfavoured energies at 11.3 and 16.2 kcal·mol^{-1} followed by Bicyc-DMS with energies of 1.8 and 11.8 kcal·mol^{-1}. The Bicyc-OTMS manifold is the most favoured one displaying values of -2.2 and 2.7 kcal·mol^{-1}. Similar energetic values are observed for the Bicyc-OH route (-1.8 and 3.0 kcal·mol^{-1}). These combined computational observations agree with the experimental results, as the Bicyc-OTMS undergoes a successful ROP and the Bicyc-Cyclohex and Bicyc-DMS do not react. In the case of Bicyc-OH, the calculations predict that this mechanism should be feasible, but experimentally the reaction is limited (low molecular weight) because the alcohol group intervenes likely via chain-transfer events.

The reactivity of alcohols and alkoxides have an important role during the ROP reaction, hence, this property has to be considered for future calculations. Specifically, any alcohol or carboxyl group bound to the cyclic carbonate ring could interact during the ROP reaction and induce the formation of different polymeric structures (shorter or cross-linked/3D, instead of linear) or even not allow any reaction. Therefore, substituents with pendant alcohols connected to the cyclic carbonate will not be considered in this chapter.

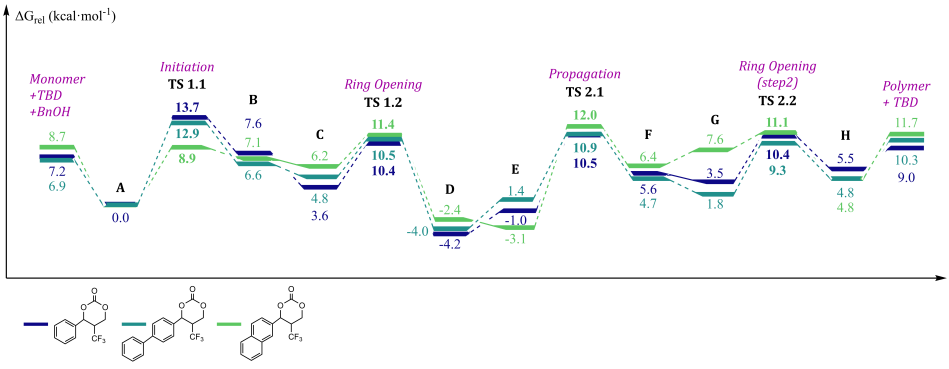

Figure 6.17: Relative Gibbs free energy profiles in kcal·mol^{-1} for the comparison between mechanistic Pathways for monomers that have CF_3 and aromatic group as a substituent: CF_3-Ph, CF_3-Biphen and CF_3-Naph

In the **Figure 6.17**, the Gibbs free energy profiles for the monomers CF_3-Ph, CF_3-Naph and CF_3-Biphen[223] are presented. These monomers have a CF_3

group and aromatic groups (phenyl, naphthalene or biphenyl) located at adjacent positions in the carbonate ring.

All three monomers have similar reactivity behaviour with similar energetic values and in particular for the transition states that are in the range from 8.9 to 13.7 kcal·mol^{-1}, and for the separated polymer and catalyst with values of 9.0-11.7 kcal·mol^{-1}. In general, the initiation and propagation steps are slightly disfavoured compared to the corresponding ring-opening steps. In more detail, the initiation (**TS 1.1**) corresponds to the highest transition state for CF_3-Biphen and CF_3-Ph (12.9 and 13.7 kcal·mol^{-1}) with an exception noted for the CF_3-Naph pathway which involves the most favoured transition state at 8.9 kcal·mol^{-1}.

The first ring-opening step (**TS 1.2**) shows very similar energies for used monomers at 10.4 kcal·mol^{-1} (for CF_3-Ph), 10.5 kcal·mol^{-1} (for CF_3-Biphen) and 11.4 kcal·mol^{-1} (for CF_3-Naph). Along the mechanistic pathway, the most stable structures are **D** with calculated energies of -4.2, -4.0 and -2.4 kcal·mol^{-1} and **E** with values of -1.0, 1.4 and -3.1 kcal·mol^{-1} for the pathway based on CF_3-Ph, CF_3-Biphen and CF_3-Naph, respectively. The ROP processes continue with the propagation and second ring-opening transition states (**TS 2.1** and **TS 2.2**) that are slightly more favoured than the previous ones having energetic values of 10.5 and 10.4 kcal·mol^{-1} for CF_3-Ph, 10.9 and 9.3 kcal·mol^{-1} for CF_3-Biphen, and 12.0 and 11.1 kcal·mol^{-1} for CF_3-Naph, respectively.

The final products **H** have values of 4.8 kcal·mol^{-1} for both CF_3-Biphen and CF_3-Naph, and 5.5 kcal·mol^{-1} for CF_3-Ph, whose structure is slightly less stable than computed for the intermediates **D** and **E**, thus helping the reaction to continue towards higher levels of propagation. The final dimeric structures are slightly less stable than the initial monomers meaning that these reactions are a bit endergonic.

In **Figure 6.18**, three additional monomers are given to extend the computational dataset, and these monomers are synthetically accessible following the same procedure as illustrated for cyclic carbonates presented in **Figure 6.16**[28]. They were chosen to evaluate the effect of adding different substituents, includ-

ing a methyl, a phenyl or two methyl groups in order to predict the reactivity based on the previous calculations and results. The monomer Bicyc-Ph differs from Bicyc-DMS only by the presence of a different alcohol protecting group, to examine the influence on the ROP reactivity without considering possible cross-linking reactions.

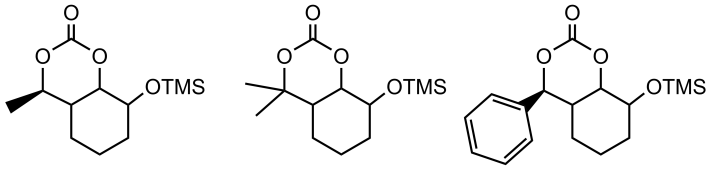

Bicyc-Me **Bicyc-DiMe** **Bicyc-Ph**

Figure 6.18: Monomers calculated inspired by the results attained for Bicyc-OH, Bicyc-OTMS[28], Bicyc-Cyclohex and Bicyc-DMS[252]

In **Figure 6.19** the mechanistic pathways are provided for the ROP of these latter monomers shown in **Figure 6.18**. It can be noted that Bicyc-DiMe will not be able to accommodate a successful ROP reaction. The main differences are shown at the propagation stage, where the propagation **TS 2.1** and ring-opening **TS 2.2** transition states are kinetically (much) disfavoured at 28.1 and 22.8 kcal·mol^{-1}. Moreover, the intermediates **F** and **G** are also energetically quite high with values of 23.9 and 17.2 kcal·mol^{-1}, respectively. The final dimer

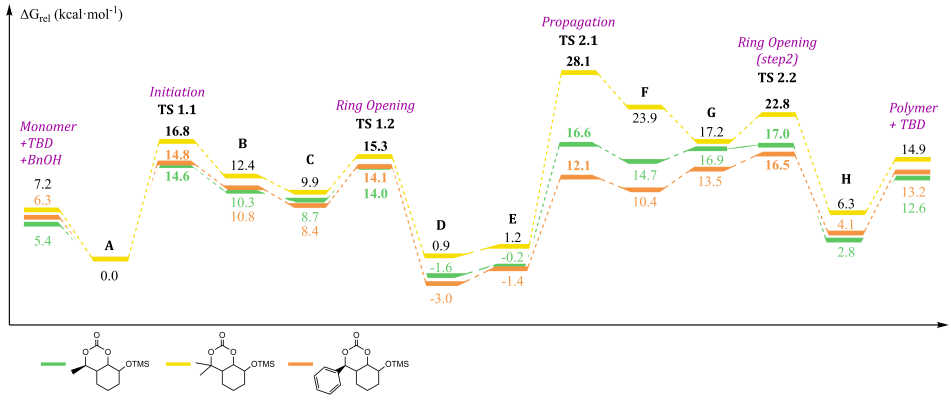

Figure 6.19: Relative Gibbs free energy profiles in kcal·mol^{-1} for the pathways involving Bicyc-Me, Bicyc-DiMe and Bicyc-Ph as monomers

structure is also 8.7 kcal·mol^{-1} more unstable than the initial monomer. In general, this reaction is not only endergonic, but also represents a high energy span, meaning that the ROP will be unlikely to occur.

Conversely, Bicyc-Me and Bicyc-Ph do not have a clear tendency to allow to predict their ROP ability. On one hand, the intermediates and transition states are accessible and energetically close for both monomers, with have a maximum value of 17.0 kcal·mol^{-1} for Bicyc-Me and 16.5 kcal·mol^{-1} for Bicyc-Ph. The initiation and ring-opening transition states **TS 1.1** and **TS 1.2** are located at 14.6 and 14.0 kcal·mol^{-1} for Bicyc-Me and at 14.8 and 14.1 kcal·mol^{-1} for Bicyc-Ph. Their computed ROP continues with the propagation (**TS 2.1**) and the second ring-opening step (**TS 2.2**) transition states amounting to 16.6 and 17.0 kcal·mol^{-1} for Bicyc-Me and 12.1 and 16.5 kcal·mol^{-1} for Bicyc-Ph. Therefore, the energy span for these polymerizations seem feasible under these conditions.

On the other hand, the final dimer free energies are similar to Bicyc-DiMe, having energetic values of 12.6, 13.2 kcal·mol^{-1} for Bicyc-Me and Bicyc-Ph, compared with the value of 14.9 kcal·mol^{-1} for Bicyc-DiMe. Thereby, these polymers are far more unstable than the initial monomers, making these ROP reaction endergonic and unlikely.

To analyse the results more deeply, a correlation plot depicted in **Figure 6.20** and its corresponding values written in **Table 6.11** are represented. At first sight, it is easy to see that the ROP of both Bicyc-Cyclohex and Bicyc-DiMe are clearly out of the desired range to yield isolable dimeric (or polymeric) products. Not only the transition states involved during the overall manifold are energetically disfavoured but also the final polymers are relatively unstable. That means that from a free energy perspective, resultant polymers will be too unstable with a strong tendency to depolymerize towards the initial cyclic monomer.

The pathway for Bicyc-DMS has an acceptable energy span, however the polymer stability is at 5.5 kcal·mol^{-1} and thus close to the (arbitrary) boundary of around 4 kcal·mol^{-1} and thus it seems unlikely that a successful ROP of this monomer can be executed. This hypothesis concurs with the experimental

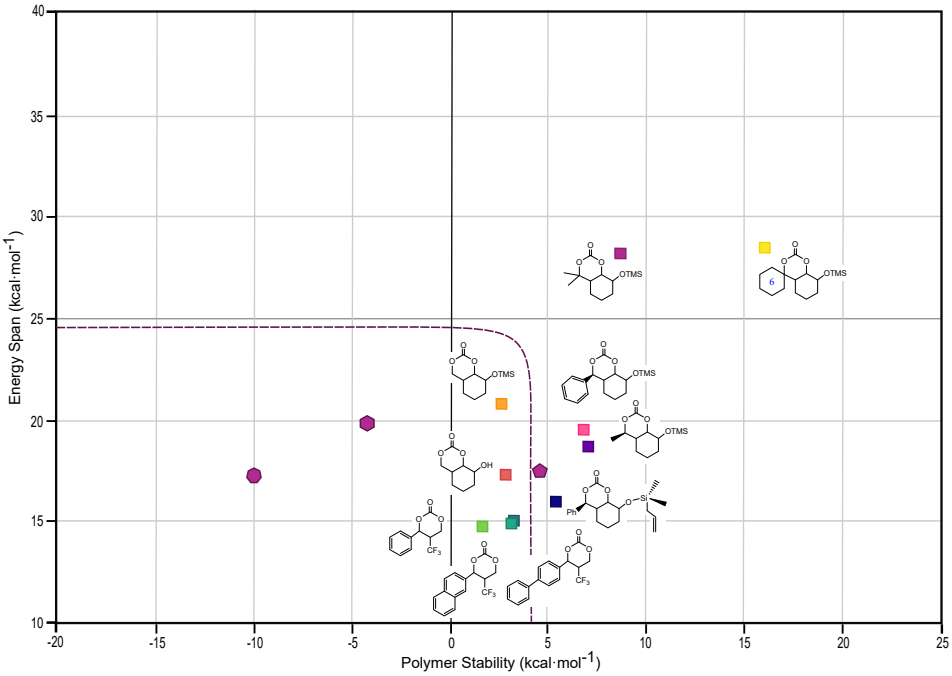

Figure 6.20: Correlation plot of the polymer stability vs. Energy span (both in kcal·mol^{-1}) for six-membered monomers tested in the Kleij laboratory and similar monomers computed [represented as squares]. Reference values for 5MCC, 6MCC and 7MCC from **Figure 6.14** are also included [represented as purple pentagon, hexagon and heptagon respectively]

results showing that the ROP is indeed not possible under ambient temperature conditions. The results for monomers Bicyc- Me and Bicyc-Ph are also placed outside the boundary region, and in these cases, the energetic span is reasonable but the final dimer stabilities are not low enough for a feasible ROP process.

The result collected for Bicyc-OH, Bicyc-OTMS, CF_3-Ph, CF_3-Naph and CF_3-Biphen show cross-points located in a stable range combining a low energy span and also an stable enough dimer. Due to the nature and position of the substituents, the CF_3-based monomers are located in a similar region with a value around of 15 kcal·mol^{-1} for the energy span, while the use of Bicyc-OH and Bicyc-OTMS present slightly higher energy span values of around 18.5 kcal·mol^{-1}.

Table 6.11: Correlation plot values and legend for six-membered monomers tested in Kleij's laboratory (and similar structures) in kcal·mol^{-1}

Monomer	Energy Span	Polymer stability	ROP Successful?
6MCC	19.8	-3.8	Yes
Bicyc-OH	17.3	3.0	Yes
Bicyc-OTMS	20.7	2.7	Yes
Bicyc-Cyclohex	28.4	16.2	No
Bicyc-DMS	15.9	5.5	No
CF_3-Ph	14.7	1.8	Yes
CF_3-Naph	15.1	2.9	Yes
CF_3-Biphen	14.9	3.3	Yes
Bicyc-Me	18.6	7.2	No
Bicyc-DiMe	28.1	8.7	No
Bicyc-Ph	19.5	6.9	No

An overall observation based on the combination of all results a seeming relation between a feasible ROP and how many positions in the ring are occupied. When the ring has two positions with substituents as present in Bicyc-OH, Bicyc-OTMS, CF_3-Ph, CF_3-Naph and CF_3-Biphen, the energetic span is not too high and the polymer stability is also acceptable, thus should enable a successful ROP reaction. When the ring has three positions occupied such as in Bicyc-Me and Bicyc-Ph, the ROP process looks possible from a kinetic point of view, but the dimer stability may be stable enough to allow to isolate a polymeric version. Finally, if the carbonate ring has four locations occupied as in Bicyc-Cyclohex and Bicyc-DiMe, it will not undergo a ROP reaction.

With these results in this section, it is possible to confirm that the computational model developed aligns well with the experimentally observed ROP reactivity under the conditions shown in**Figure 6.7** via a correlation of energy span and dimer stability to predict the reactivity for various known and unknown monomers.

6.4.4 Number of substituents

As seen in the section above, the number of substituents may have a key role for allowing a successful ROP. With this in mind, this section will study how many substituents can be introduced onto the cyclic carbonate towards a successful ROP reaction. To simplify this study, up to six "methyl" substituents were added to different positions in the 6MCC ring. All evaluated structures are presented in **Figure 6.21**.

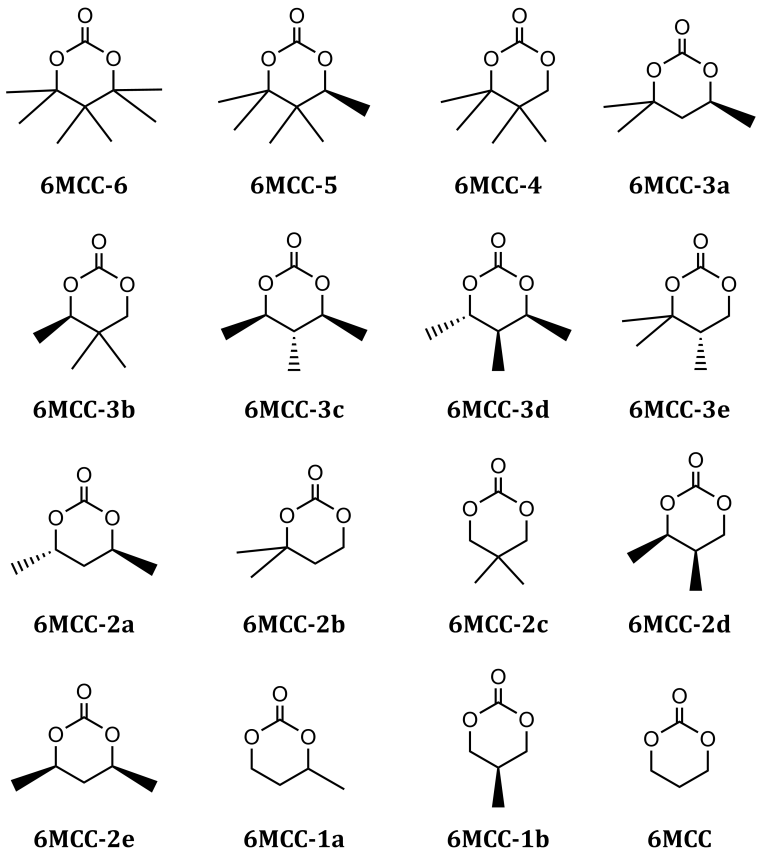

Figure 6.21: The calculated ROP monomers with a different number of methyl-substituents

In **Figure 6.22** the Gibbs free energy profiles for the ROP of the most substituted monomers 6MCC-6, 6MCC-5 and 6MCC-4 are presented. From the figure

it can be easily deduced that all these processes are energetically disfavoured having high values for the transition states and some of the intermediates. The initiation step **TS 1.1** is the lowest-energy transition state for each monomer at 16.9 kcal·mol^{-1} for 6MCC-6, 15.6 kcal·mol^{-1} for 6MCC-5 and 15.1 kcal·mol^{-1} for 6MCC-4. These processes continue with the first ring-opening step **TS 1.2** that is more energetically disfavoured than the previous one, but the values are still within an acceptable range to enable the ROP reaction. Specifically, the **TS 1.2** have values of 23.3, 19.5 and 17.7 kcal·mol^{-1} for 6MCC-6, 6MCC-4 and 6MCC-5, respectively. The intermediates **D** have very close energetic values for all structures being 7.8 kcal·mol^{-1} for both 6MCC-5 and 6MCC-4, and 7.9 kcal·mol^{-1} for 6MCC-6), while intermediates **E** have similar energetic values for 6MCC-6 and 6MCC-5 (7.7 and 7.3 kcal·mol^{-1}, respectively), and with a more stable structure for 6MCC-4 at 3.0 kcal·mol^{-1}. The propagation part, in contrast, follows a tendency more directly influenced by the number of substituents. The ROP of the most substituted monomer 6MCC-6 is at this stage the most disfavoured, followed by the ROP of 6MCC-5 and with the ROP of 6MCC-4 the most favoured comparatively. All of them have energetic values out of range at room temperature, namely, more than 25 kcal·mol^{-1} not only for the transition states **TS 2.1** and **TS 2.2**, but also for some intermediate structures. Due to this high energetic span, none of these monomers will be able to undergo a ROP reaction successfully.

In detail, the 6MCC-6 monomer has a propagation transition state **TS 2.1** located at 36.5 kcal·mol^{-1}, and this is followed by the intermediate structures **F** and **G** at 28.1 and 32.9 kcal·mol^{-1}. The second ring-opening transition state **TS 2.2** has an energetic value of 37.7 kcal·mol^{-1} being the highest transition state shown in **Figure 6.22**. The structure **H** is also relatively disfavoured with an energy value of 28.3 kcal·mol^{-1} and the final polymer stability is computed at over 25.5 kcal·mol^{-1}. As mentioned above, all of these transition states and intermediates are located over 25 kcal·mol^{-1}, and hence it is very likely that these structures are barely populated in the reaction mixture at room temperature.

Moreover, the final dimer product is so much disfavoured that it is unlikely to exist. Monomers 6MCC-5 and 6MCC-4 have energy-wise intermediates that

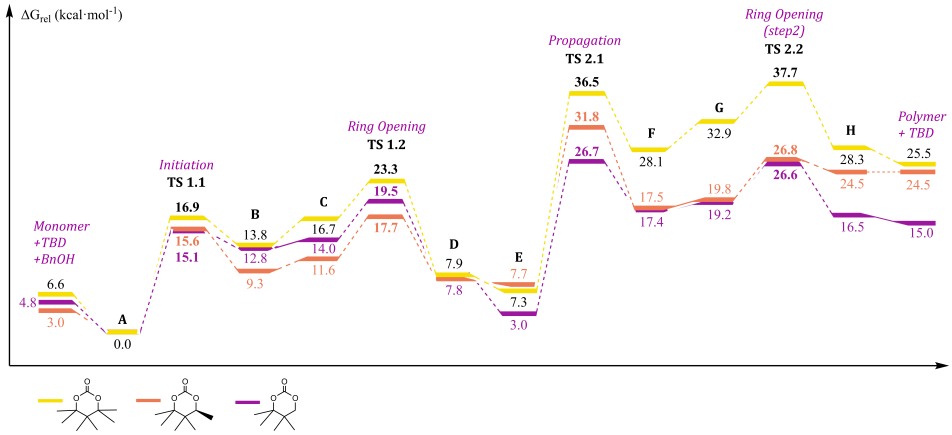

Figure 6.22: Relative Gibbs free energies in kcal·mol^{-1} for structures that have from 6 to 4 substituents: 6MCC-6, 6MCC-5 and 6MCC-4

are more reasonable as noted for **F** (17.5 and 17.4 kcal·mol^{-1}, respectively), **G** (19.8 and 19.2 kcal·mol^{-1}) and **H** (24.5 and 16.5 kcal·mol^{-1}). These values are in contrast to those related to the transition states **TS 2.1** and **TS 2.2**, which are much more disfavoured. Specifically, the propagation step **TS 2.1** has an energetic value of 31.8 kcal·mol^{-1} for 6MCC-5 and 26.7 kcal·mol^{-1} for 6MCC-4, and the second ring-opening-step **TS 2.2**, has energetic values quite close to the latter at 26.8 and 26.6 kcal·mol^{-1} for 6MCC-5 and 6MCC-4, respectively. The final dimer product in the manifold based on 6MCC-5 has a similar energy value as that of the 6MCC-6, (24.5 kcal·mol^{-1} in comparison with 25.5 kcal·mol^{-1}), while the 6MCC-4 a value of 15.0 kcal·mol^{-1} was determined, which is notably lower compared to the other monomers.

The **Figure 6.23** presents the Gibbs free energy profiles for the monomers with three substituents: 6MCC-3a, 6MCC-3b, 6MCC-3c, 6MCC-3d and 6MCC-3e. In contrast with the overall tendency shown in **Figure 6.22**, there is not a straightforward correlation noted for these monomers with the three methyl groups located in various positions on the carbonate ring.

The monomers 6MCC-3a and 6MCC-3e in general give the energetically most disfavoured profiles in this scheme. Their initiation step **TS 1.1** has a reasonable energy at 14.9 kcal·mol^{-1} for 6MCC-3a and a higher value for 6MCC-3e

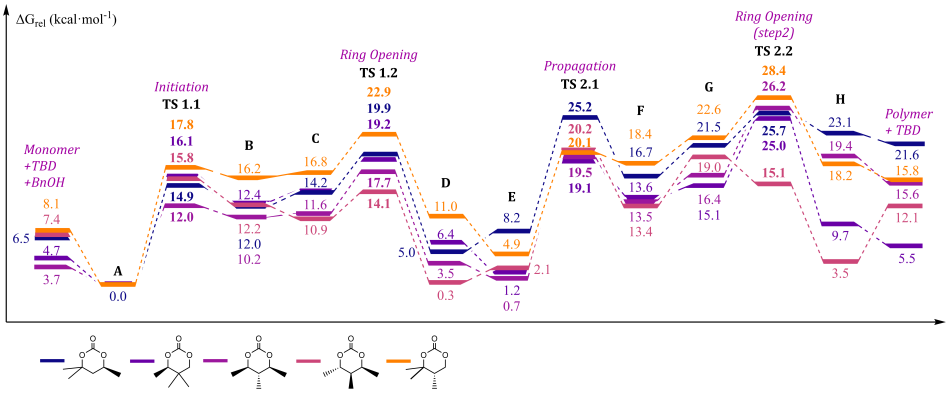

Figure 6.23: Relative Gibbs free energies in kcal·mol^{-1} for structures with three substituents: 6MCC-3a, 6MCC-3b, 6MCC-3c, 6MCC-3d and 6MCC-3e

at 17.8 kcal·mol^{-1}. The first ring-opening transition state **TS 1.2** are more disfavoured with values of 19.9 and 22.9 kcal·mol^{-1} for 6MCC-3a and 6MCC-3e, respectively. Their reaction then continues with even more disfavoured energy values for the propagation **TS 2.1** at 25.2 kcal·mol^{-1} (for 6MCC-3a) and 20.1 kcal·mol^{-1} (for 6MCC-3c). The second ring-opening transition states **TS 2.2** have also quite disfavoured energies with 25.7 kcal·mol^{-1} for 6MCC-3a, and 28.4 kcal·mol^{-1} for 6MCC-3e. The mechanistic description ends with the product **H** and the polymer, with slightly lower relative values of 23.1 and 21.6 kcal·mol^{-1} for 6MCC-3a and with more favoured energetic values for 6MCC-3e being 18.2 and 15.8 kcal·mol^{-1}, respectively. For both these monomers, their dimeric products are thermodynamically more unstable than the initial monomers. Additionally, most of the transition states involved during the ROP reaction are kinetically inaccessible, hence, the monomers 6MCC-3a and 6MCC-3e will not be easily polymerized under these conditions.

The monomers 6MCC-3b and 6MCC-3c have very different dispositions of the substituents, but nonetheless, have similar behaviour in the propagation and second ring-opening steps. In detail, the reaction starts with the initiation step **TS 1.1** which has for the 6MCC-3b pathway a value of 16.1 kcal·mol^{-1} and for the path involving 6MCC-3c being 12.0 kcal·mol^{-1}. The following ring-opening transition state **TS 1.2** has values of 19.2 and 17.7 kcal·mol^{-1} for the

pathways based on 6MCC-3b and 6MCC-3c, respectively. Structures **D** (at 6.4 kcal·mol^{-1} for the 6MCC-3b and at 3.5 kcal·mol^{-1} for the 6MCC-3c manifolds) are a bit more unstable than structures **E** in both pathways (1.2 kcal·mol^{-1} and 0.7 kcal·mol^{-1}). The propagation step **TS 2.1** is a bit high in energy with values of 19.1 and 19.5 kcal·mol^{-1} in the computed processes for 6MCC-3b and 6MCC-3c. Structures **F** and **G** are more similar in energy with energetic differences between these monomers around or below 1.5 kcal·mol^{-1}, and proceed with the second ring-opening transition state **TS 2.2** that has high values for both monomer cases being 25.0 kcal·mol^{-1} for 6MCC-3b and 26.2 kcal·mol^{-1} for 6MCC-3c. The energetic similarity ends at the final stage (**H**) and final dimeric products, which have energetic values of 9.7 and 5.5 kcal·mol^{-1}, and 19.4 and 15.6 kcal·mol^{-1}, respectively.

On one hand, for 6MCC-3c the dimer stability compared with the initial monomer has a value of 11.9 kcal·mol^{-1}, and together with the estimated energetic span of this reaction (25.5 kcal·mol^{-1}) predicts that this monomer will not be suitable to be polymerized under the standard conditions. On the other hand, is not easy to predict the reactivity for the 6MCC-3b monomer because the activation energy is around 25 kcal·mol^{-1}, which is close to the boundary value considered for ROP at room temperature. To help the prediction, the final polymer stability also has an important role. For the ROP 6MCC-3b monomer the dimer stability is 0.9 kcal·mol^{-1} and the energy span is 25.0 kcal·mol^{-1}. Therefore, this monomer could be potentially polymerized though likely only at elevated temperature. This case exemplifies the interest of retrieving additional experimental data to refine and shape the model thereby enhancing its predictive power.

After noting that 6MCC-3c cannot undergo a ROP, a question came up: Why are Bicyc-Me, Bicyc-Ph and Bicyc-DMS not so far from the ROP boundary area while having a more complex geometry than 6MCC-3c? Does the disposition of the substituents play an important role?

Note that monomers Bicyc-Me, Bicyc-Ph and Bicyc-DMS can be polymer-

ized according to the determined energy spans, but their dimer stability values are too high placing them outside the ROP region (see **Table 6.11** and **Figure 6.20**).

Simplification of the Bicyc-Me, Bicyc-Ph and Bicyc-DMS monomers by converting all their substituents into methyl groups and using the same stereochemistry, the result is the monomer 6MCC-3d. Although 6MCC-3c and 6MCC-3d are very similar, the change of stereochemistry makes a difference in the reactivity. In general, the ROP of monomer 6MCC-3d shows lower barriers compared to 6MCC-3a, 6MCC-3b, 6MCC-3c and 6MCC-3e. The initiation step **TS 1.1** has a similar value as observed for the other monomers (15.8 kcal·mol^{-1}), and I followed by structures **B** and **C** that also have similar values (12.2 and 10.9 kcal·mol^{-1}). The transition states related to the ring-opening steps (**TS 1.2** and **TS 2.2**) have more significant differences comparatively, with energetic values of 14.1 kcal·mol^{-1} for **TS 1.2** and 15.1 kcal·mol^{-1} for the **TS 2.2**. Therefore, these steps are energetically more feasible. The propagation step **TS 2.1**, located amidst the two ring-opening steps, has a value of 20.2 kcal·mol^{-1}, which is closer to the values related to the use of 6MCC-3b and 6MCC-3c. There is a remarkable energetic difference for intermediate **H** compared with those determined for 6MCC-3a, 6MCC-3c and 6MCC-3e, with 6MCC-3d being the most thermodynamically favoured one at 3.5 kcal·mol^{-1}, whereas the final dimer is located at 12.1 kcal·mol^{-1}, close to the value determined for 6MCC-3c. Overall, initiation and propagation as computed for the ROP of 6MCC-3d are higher in energy than the ring-opening steps in case of 6MCC-3c. This means that once the main structure is interacting with the monomer, the ring-opening reaction helps to create a stable product. Moreover, the stereochemistry has an important role, and results into a more stable dimer derived from 6MCC-3d located close to the boundary values while this is not the case for 6MCC-3c.

Considering the numbering of the substituents defined in **Figure 6.7**, the ROP reaction implies opening the ring at two possible side of the monomer being either where R_1 and R_2 are located or at the side that contains R_5 and R_6. The monomer 6MCC-3a is more sterically hindered in comparison with the other three-substituted monomers because it has substituents in R_5, R_6

and R_1. In other words, when the ring is opened in **TS 1.2** or **TS 2.2** the geometrically most favoured position is at the side that has one methyl group (R_1), contrary to the other side (R_5 and R_6) that includes two substituents. The 6MCC-3e is similar to 6MCC-3a, and in that case it has the side defined by R_1 and R_2 completely free, with all three substituents (R_5, R_6 and R_4) gathered in two contiguous positions. This nonsymmetrical positioning of the substituents reduces the number of possible reactive conformations. While the 6MCC-3c and 6MCC-3d have one substituent on each side, their molecular configuration is different. Finally, the 6MCC-3b has just one side occupied (at R_5) enhancing the number of configurations to react. Despite of these configurational differences, the energetic values are quite close during the initiation part, but become more distinct in the propagation part, and ends with dimeric products that have distinct energies and stabilities. As a consequence, the final polymer stability is directly related with the number of configurations related to the position of the substituents, with 6MCC-3a being the most disfavoured, 6MCC-3b most favoured, and 6MCC-3c and 6MCC-3d located between these two extremes with an energetic preference for 6MCC-3d among the last two examples. In summary, there is not a clear reactivity tendency for the triple-substituted monomers (**Figure 6.26**). Some of them have an energetic span and/or dimer stability located near the boundary values considered to create a feasible ROP under these conditions, while the others are outside this region and have relatively low ROP ability.

The **Figure 6.24** shows the Gibbs free energy profiles for those monomers having two substituents: 6MCC-2a, 6MCC-2b, 6MCC-2c, 6MCC-2d and 6MCC-2e. All of them presents similar overall behaviour and the TSs and intermediates are not overly high in energy allowing to predict that these monomers should undergo a ROP reaction under ambient temperature conditions. By analysing the results in more detail, is possible to appreciate the different tendencies related to the location of the substituents in this series of monomers.

In general, the most thermodynamically favoured profiles are for 6MCC-2c and 6MCC-2d due to the position of the two methyl groups. For 6MCC-2c, the

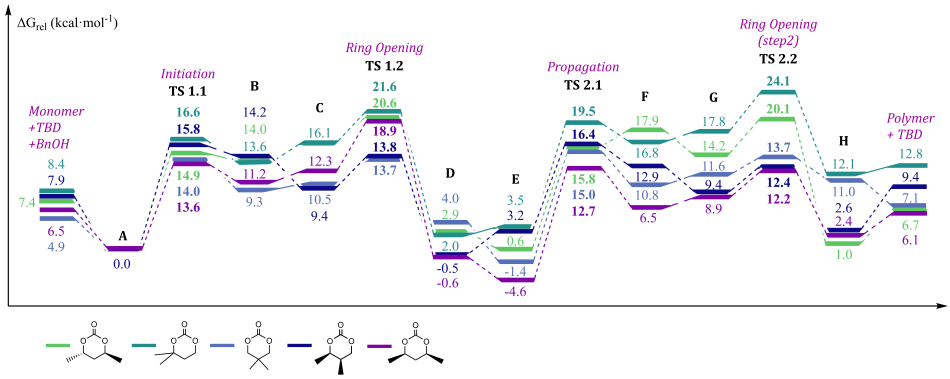

Figure 6.24: Relative Gibbs free energies in kcal·mol^{-1} for monomers with two substituents: 6MCC-2a, 6MCC-2b, 6MCC-2c, 6MCC-2d and 6MCC-2e

substituents (R_3 and R_4 in **Figure 6.7**)are present in a completely symmetrical way around the carbonate carbon, thus enhancing the reactivity due to a lack of orientational restriction with respect to the initiator and/or catalyst. For 6MCC-2d, the location of the substituents also enhances the ROP reaction due to a lack of steric hindrance with the methyl groups located far enough from to the reactive centre. Conversely, the ROP of 6MCC-2b represents the most energetically disfavoured profile. Although the ring-opening may be carried out near the side that remains unoccupied , the steric hindrance from the methyl groups located on both sides of the carbonate ring (R_5 and R_6 in **Figure 6.7**) results in energetically higher transition states than noted for the other monomers in **Figure 6.24**. The monomers 6MCC-2a and 6MCC-2e have similar substitutions but their stereochemistry is different, whereas the methyl positions for 6MCC-2a is the same as present in 6MCC-3d, and those in 6MCC-2e are similar to 6MCC-3c.

In detail, in **Figure 6.24**, the initiation transition step **TS 1.1** demonstrates similar energies for all monomers at this stage being 14.9 kcal·mol^{-1} for 6MCC-2a, 16.6 kcal·mol^{-1} for 6MCC-2b, 14.0 kcal·mol^{-1} for 6MCC-2c, 15.8 kcal·mol^{-1} for 6MCC-2d and 13.6 kcal·mol^{-1} for 6MCC-2e. The first ring-opening transition state **TS 1.2** show high values for the paths based on 6MCC-2b (21.6 kcal·mol^{-1}), 6MCC-2a (20.6 kcal·mol^{-1}) and 6MCC-2e (18.9 kcal·mol^{-1}), while

the computed values for 6MCC-3c and 6MCC-3d are lower and similar (13.7 and 13.8 kcal·mol^{-1}). During the propagation, the route based on 6MCC-2b has the most disfavoured transition states and intermediates with energetic values of 19.5 and 24.1 kcal·mol^{-1} for **TS 2.1** and **TS 2.2**, respectively. Notice that the ring-opening transition state (**TS 2.2**) value is near to the boundary of the ROP region but still within its outer limits to predict a ROP of this monomer at room temperature. The use of monomers 6MCC-3c and 6MCC-3d lead to close and favoured energies for the transition states and intermediates. The propagation **TS 2.1** has values of 15.0 and 16.4 kcal·mol^{-1} for 6MCC-2c and 6MCC-2d, respectively, which corresponds to their highest energetic value in their profile. The second-ring-opening transition state **TS 2.2** has almost equal values to their corresponding first ring-opening transition state (**TS 1.2**), being located at 13.7 and 12.4 kcal·mol^{-1} for 6MCC-2d and 6MCC-3c, respectively. Despite the structural similarity between 6MCC-2a and 6MCC-2e, the energetic profiles are not. Surprisingly, the ROP of 6MCC-2e is more favoured than that of 6MCC-2c and 6MCC-2d during the propagation part, with value of 12.7 and 12.2 kcal·mol^{-1} for **TS 2.1** and **TS 2.2**, respectively, and with the lowest energetic values for the intermediates **F** and **G**. However, the ROP of 6MCC-2a does not follow any tendency, and the propagation transition state **TS 2.1** has a value of 15.8 kcal·mol^{-1}, close to those computed for 6MCC-2c and 6MCC-2d. The following intermediates **F** and **G** have higher values close to that of 6MCC-2b, which is energetically the most disfavoured profile. Furthermore, the second ring-opening transition state **TS 2.2** has a high energy value of 20.1 kcal·mol^{-1}, which corresponds to the second most disfavoured profile after 6MCC-2b. Finally, the final product adduct **H** and the separated dimer structures show different tendencies for each monomer. The 6MCC-2b displays the most disfavoured energies with values amounting to 12.1 and 12.8 kcal·mol^{-1}, followed by the pathways that involve 6MCC-2c and 6MCC-2d with energetic values located somewhere in the middle of the entire series with opposite behaviour. While the structure of intermediate **H** derived from 6MCC-2c has a higher energetic value than the resultant dimer (11.0 vs. 7.1 kcal·mol^{-1}, respectively), the manifold based on 6MCC-2d illustrates a reversed behaviour

with energy values of 2.6 and 9.4 kcal·mol^{-1}. The most stable products are those from the utilization of 6MCC-2a and 6MCC-2e, and in these cases, both of these structures have similar values of 1.0 kcal·mol^{-1} (6MCC-2a) and 2.4 kcal·mol^{-1} (6MCC-2e) for structure **H**. The related dimer structures are located at 6.7 kcal·mol^{-1} (6MCC-2a) and 6.1 kcal·mol^{-1} (6MCC-2e).

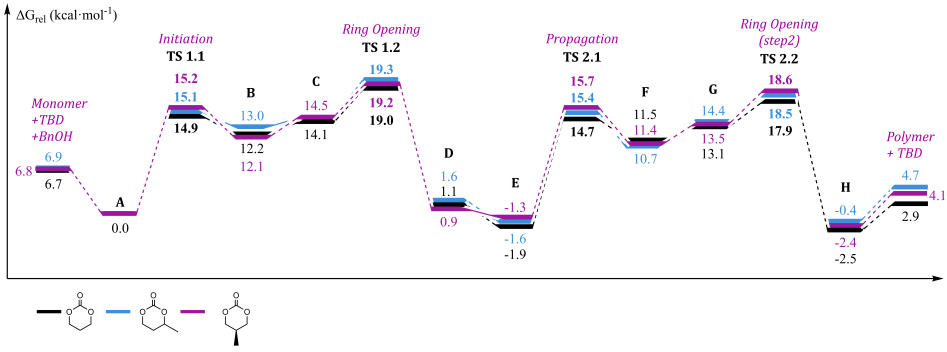

Figure 6.25: Relative Gibbs free energies in kcal·mol^{-1} for structures with zero or one substituents: 6MCC, 6MCC-1a and 6MCC-1b

Less substituted monomers with one or no substituents on the carbonate ring are shown in **Figure 6.25**. It is rather easy to observe that all monomers in this series (**Figure 6.25**) give acces to TSs and intermediates with very similar energetic values, and consequently, similar reactivity. The separated monomers in comparison with the adducts **A**, have energetic values around to 6.8 kcal·mol^{-1}. At the initial transition state **TS 1.1**, the energetic values are near 15 kcal·mol^{-1} and is followed by the first ring-opening **TS 1.2** that has values around 19 kcal·mol^{-1}. During the propagation part, the energetic profile for 6MCC is slightly more favoured than that of the monomer with one substituent (6MCC-1a and 6MCC-1b), but the difference is not really significant because it corresponds to a maximum of 2 kcal·mol^{-1}. The propagation transition state **TS 2.1** have values around 15.5 kcal·mol^{-1}, similar to the initial transition state **TS 1.1**, while the second ring-opening transition state **TS 2.2** is a bit lower compared to the first one (TS 1.2), with values of 18 kcal·mol^{-1} approximately. The final structure **H** is thermodynamically favoured for all monomer-based routes being -2.5 kcal·mol^{-1} for 6MCC, -0.4 kcal·mol^{-1} for 6MCC-1a and -2.4

kcal·mol^{-1} for 6MCC-1b. Finally, the separated dimer energy values are similar for the monomers with one substituent (4.7 kcal·mol^{-1} for 6MCC-1a and 4.1 kcal·mol^{-1} for 6MCC-1b), with the product of the ROP of 6MCC being slightly more favoured at 2.9 kcal·mol^{-1}.

In summary, it can be seen than all Gibbs free energy profiles presented in **Figure 6.25** follow the same tendency as that of 6MCC, hence, it is possible to predict that these monomers will emulate the same reactivity, with accessible transition states in every propagation step, obtaining a stable polymer. The energetic similarity could be explained by the lack of steric hindrance in these monomers, which enhances their reactivity towards ROP not being restricted to interact in just one possible and accessible orientation. The ideal ring-opening for 6MCC-1a occurs at the side that does not have any close by substituent. However, it is also possible to carry out the reaction by the side that has the methyl group closer to the reactive center. In the case of 6MCC-1b, the methyl is located in a symmetrical position, which means that it should interact with the catalyst/initiator in a similar way as 6MCC. Experimental data for 6MCC[31,35,38,39,195,220,228,246] and 6MCC-1a[224] reported in the literature confirm that these two monomers successfully undergo a ROP reaction using TBD as a catalyst at r.t. Therefore, these calculations agree with these experimental results and concur with the computational model described in this chapter.

The kinetic and thermodynamic ROP descriptors for the monomers presented in **Figure 6.21** are illustrated in **Figure 6.26** and gathered in **Table 6.12**. There is a clear tendency directly related with the number of substituents, with the ROP of 6MCC-6, 6MCC-5 and 6MCC-4 being not only out of the polymerization range at room temperature, but also their polymer (dimers) synthesised in all cases are thermodynamically disfavoured. Hence, none of these monomers are likely to undergo a ROP reaction under these conditions.

As noted above, the ROP of monomers with three substituents are more difficult to predict due to the variety of configurations and behaviours they may have. Some monomers such as 6MCC-3a, 6MCC-3c and 6MCC-3e are clearly out of the probable polymerization range, while 6MCC-3b and 6MCC-3d are

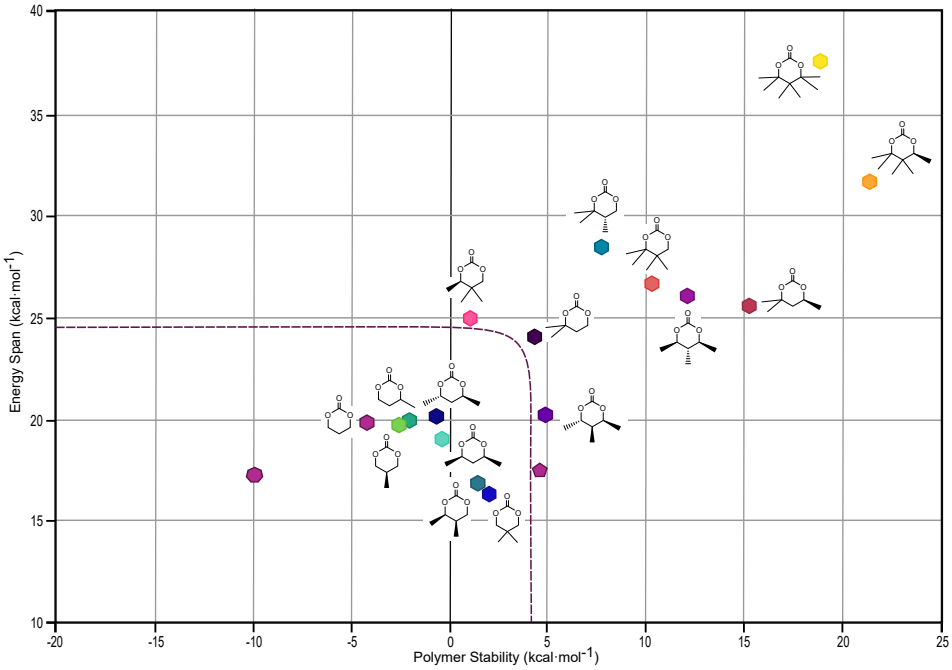

Figure 6.26: Correlation plot for dimer stability vs. their computed energy span (both in kcal·mol^{-1}) of monomers with different number of substituents [represented as hexagons]. Reference values for 5MCC, 6MCC and 7MCC are also included [represented as purple pentagon, hexagon and heptagon respectively]

placed close to its boundaries. On one hand, for 6MCC-3b the energetic span is near the limit of 25 kcal·mol^{-1}, thus making the dimer/polymer stability to play a key role. On the other hand, for 6MCC-3d a feasible energetic span was determined but its polymer stability is close to the boundary value at 4.8 kcal·mol^{-1} outside the feasible region. For monomers with two or less substituents the ROP is feasible, and the monomers shown in **Figure 6.26** perfectly fit in the acceptable ROP range. Nevertheless, for 6MCC-2b the computed energetic values are close to both boundaries (energy span of 24.1 kcal·mol^{-1} and a dimer stability of 4.5 kcal·mol^{-1}), but could still be feasible. The nonsymmetric positioning of the substituents in 6MCC-2b, 6MCC-3a and 6MCC-3e reduce their ROP potential causing higher energetic spans and dimer energies in comparison with other monomers having the same number of substituents. Finally, for monomers with one or no substituents (6MCC-1a, 6MCC-1b and 6MCC), the

Table 6.12: Correlation plot values and legend for monomers with different number of substituents in kcal·mol^{-1}

Monomer	Energy Span	Polymer stability	ROP Successful?
6MCC	19.8	-3.8	Yes
6MCC-1a	20.1	-2.2	Yes
6MCC-1b	19.8	-2.7	Yes
6MCC-2a	20.1	-0.7	Yes
6MCC-2b	24.1	4.5	Boundary
6MCC-2c	16.4	2.1	Yes
6MCC-2d	16.9	1.5	Yes
6MCC-2e	18.9	-0.4	Yes
6MCC-3a	25.7	15.1	No
6MCC-3b	25.0	0.9	Boundary
6MCC-3c	26.2	11.9	No
6MCC-3d	20.2	4.8	Boundary
6MCC-3e	28.4	7.7	No
6MCC-4	26.7	10.2	No
6MCC-5	31.8	21.5	No
6MCC-6	37.7	19.0	No

energetic span is relative small, and the final dimers are thermodynamically more stable than their initial monomers providing exergonic reactions. This feature helps the ROP reaction to advance thereby potentially leading to larger and stable polymer molecules.

6.4.5 Size and chemical nature of the substituents

In the previous section, the importance of the number of substituents was described, concluding that having one or two substituents bound to the ring of the carbonate monomer provides good ROP potential. Additionally, the position of these substituents enhances the reactivity if they are located in a symmetrical position. Considering this information, in this section we will evaluate substituents with a different size and nature located in the "favoured region", specifically, the positions chosen are R_3, R_4 (**Figure 6.7**) in the 6MCC ring.

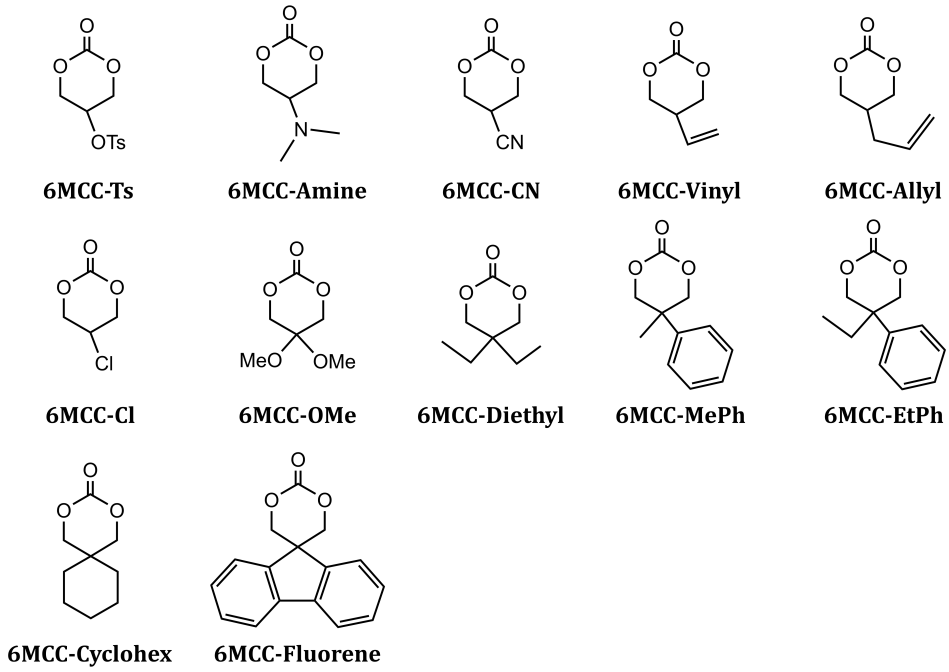

Figure 6.27: Monomers with one or two substituents in "favoured" positions in the monomer with a different nature and size

In the **Figure 6.27** all monomers considered in this study part of the study are depicted. There are six monomers with one substituent and six more with two substituents. For most monomers as 6MCC-Amine[38,41,44,226], 6MCC-OMe[38,219,228], 6MCC-Diethyl[38,218,219,247], 6MCC-MePh[219], 6MCC-EtPh[219] and 6MCC-Fluorene[227], there is experimental data in the literature related with their synthesis and/or polymerization. Nonetheless, the conditions reported are not always exactly to those studied in this chapter (**Figure 6.7**).

The Gibbs free energy profiles for six mono-substituted cyclic carbonates are given in **Figure 6.28**. All of them can undergo ROP and have similar energetic profiles although their substituents properties are different. In detail, the ROP of the monomers with electron-withdrawing groups (6MCC-CN and 6MCC-Cl) produce the most stable profiles, followed by the more electron-rich based monomer (6MCC-Amine) and the most sterically hindered monomer

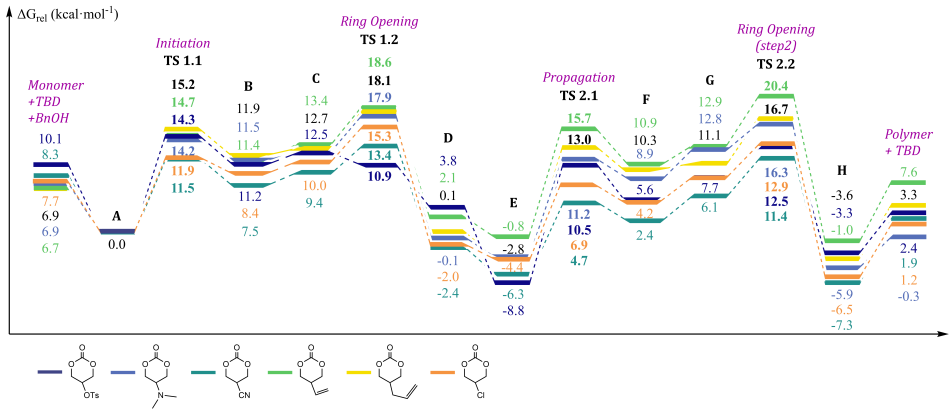

Figure 6.28: Relative Gibbs free energies in kcal·mol^{-1} for monomers with one substituent with a different nature and size: 6MCC-Ts, 6MCC-Amine, 6MCC-CN, 6MCC-Vinyl, 6MCC-Allyl and 6MCC-Cl

(6MCC-Ts). Based on the different nature and size of the functional groups involved, the most disfavoured computed profiles are those related to the 6MCC-Vinyl and 6MCC-Allyl.

The profiles for both 6MCC-CN and 6MCC-Cl have an initiation transition state **TS 1.1** with similar energies at 11.5 and 11.9 kcal·mol^{-1}, followed by structures **B** and **C** at 8.4 and 10.0 kcal·mol^{-1} for 6MCC-Cl, and 7.5 and 9.4 kcal·mol^{-1} for 6MCC-CN, respectively. The first ring-opening **TS 1.2** are slightly more disfavoured than the corresponding initiation transition state **TS 1.1** located at 15.3 kcal·mol^{-1} for 6MCC-Cl and at 13.4 kcal·mol^{-1} for 6MCC-CN. The structures **D** and **E** are thermodynamically more stable than the respective monomers, with values of -2.0 and -4.4 kcal·mol^{-1} (6MCC-Cl), and -2.4 and -6.3 kcal·mol^{-1} (6MCC-CN). The propagation part is more favoured than the previous stage, with transition states **TS 2.1** and **TS 2.2** having energetic values of 6.9 and 12.9 kcal·mol^{-1} for 6MCC-Cl, and 4.7 and 11.4 kcal·mol^{-1} for 6MCC-CN. The intermediates **F**, **G** and the product **H**, are the most stable structures in comparison to the other monomers, with values of 4.2, 7.7 and -6.5 kcal·mol^{-1} for 6MCC-Cl, and 2.4, 6.1 and -7.3 kcal·mol^{-1} for 6MCC-CN, respectively. The last structure (dimer) is energetically favoured for both monomers and have calculated energies equal to 1.9 kcal·mol^{-1} for 6MCC-CN, and 1.2 kcal·mol^{-1}

for 6MCC-Cl.

The other ROP profiles for monomers (6MCC-Ts, 6MCC-Amine, 6MCC-Vinyl and 6MCCAllyl) are a little more disfavoured than those of 6MCC-Cl and 6MCC-CN. As mentioned above, in general, the most disfavoured energetic profiles are for the monomers with the alkene groups, i.e., 6MCC-Vinyl and 6MCC-Allyl, while for 6MCC-Ts and 6MCC-Amine, the computed values are between the most stable profiles related to the monomers with an electron-withdrawing groups, and those that are most disfavoured related to the monomers bearing alkene groups.

For the initiation transition state **TS 1.1**, all monomers display very close values: 14.2 and 14.3 kcal·mol^{-1} for 6MCC-Amine and 6MCC-Ts, and 14.7 and 15.2 kcal·mol^{-1} for 6MCC-Vinyl and 6MCC-Allyl, respectively. The first ring-opening **TS 1.2** is a tiny bit more unstable than the initiation transition state, and also very similar energies are noted among the monomer series being 17.9, 18.1 and 18.6 kcal·mol^{-1} for 6MCC-Amine, 6MCC-Allyl and 6MCC-Vinyl, respectively. However, at this stage of the ROP for 6MCC-Ts, the energetic value the most favoured with a value of 10.9 kcal·mol^{-1}. The propagation transition state **TS 2.1** exhibit larger energetic differences among these monomers, but they are still rather close with the most favoured one calculated for 6MCC-Ts at 10.5 kcal·mol^{-1}, followed by 6MCC-Amine at 11.2 kcal·mol^{-1}. As mentioned above, during this step 6MCC-Allyl and 6MCC-Vinyl have intermediate structures that are relatively more unstable at 13.0 and 15.7 kcal·mol^{-1}, respectively. The same tendency continues at the ring-opening transition state **TS 2.2**, where the profile for 6MCC-Vinyl has an energetic value of 20.4 kcal·mol^{-1}, being more unstable compared to the other monomers with values of 16.7, 16.3 and 12.5 kcal·mol^{-1} for 6MCC-Allyl, 6MCC-Amine and 6MCC-Ts, respectively. The structure **H** and the dimer are thermodynamically favoured for all monomers, located at 5.9 and -0.3 kcal·mol^{-1} for 6MCC-Amine, at -3.3 and 2.4 kcal·mol^{-1} for 6MCC-Ts, at -1.0 and 7.6 kcal·mol^{-1} for 6MCC-Vinyl and at -3.6 and 3.3 kcal·mol^{-1} for 6MCC-Allyl.

Contrary to the monomers considered in **Figure 6.28**, 6MCC-Vinyl and 6MCC-Allyl offer the possibility to post-functionalize polycarbonates by virtue

of vinyl or allyl groups present in the backbone. Their presence creates polymers with interesting synthetic potential by using the olefins to make new bonds and structures useful to rigidify via crosslinking or further functionalize the macromolecule. The pendent alkene groups have successfully been used to post-functionalize the side-chains thereby creating different polymer properties[205,243]. Additionally, the vinyl and allyl groups have been used to synthesise bifunctional cyclic carbonates[253], which can be utilized to create cross-linked polycarbonates[254].

Considering that the substituent does not have any function during the process, and taking some considerations one step further, the ROP potential of 6MCC-Vinyl is comparable to the 5MCC discussed before in **Section 6.4.2**. The ROP of 6MCC-Vinyl is slightly energetically more disfavoured in each propagation step, obtaining thus a short and more unstable polymer product after each consecutive propagation. However, the ROP of 6MCC-Allyl seems to follow the same tendency as the profiles determined for the other monomers in **Figure 6.28**, being slightly more favoured after each propagation step. Despite these observations, both of these double-bond based monomers should easily undergo ROP due to their favourable energetic span and dimer stability (**Figure 6.30**).

In general, the ring-opening transition states (**TS 1.2** and **TS 2.2**) are energetically more disfavoured than their corresponding initiation (**TS 1.1**) or propagation (**TS 2.1**) transition states. Nevertheless, all of them are feasible at room temperature. The energetic values for the structures of the propagation part, are barely more accessible than the structures for the initiation part with the exception of 6MCC-Vinyl. The tendency for monomers with electron-withdrawing groups (6MCC-CN, 6MCC-Cl and 6MCC-Ts) is that their ROP is energetically more favourable than the monomers equipped with electron-donor groups (6MCC-Amine, 6MCC-Vinyl and 6MCC-Allyl). However, the energetic differences are not highly significant. The size of the substituents does neither has an important role, the pathway for most sterically hindered monomer 6MCC-Ts shows similar energetic values compared to the other monomers with smaller substituents. In conclusion, the position in the ring in

mono-substituted monomers is more important than the nature or size of the substituent, and all monomers examined (**Figure 6.28**) should be prone to be polymerized.

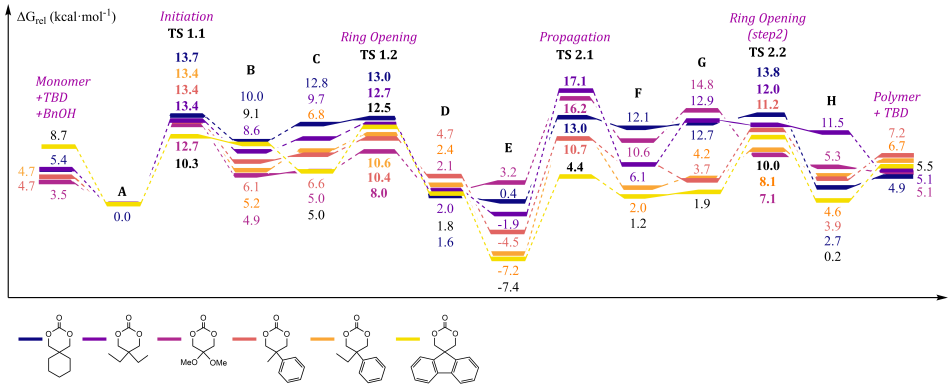

Figure 6.29: Relative Gibbs free energies in kcal·mol^{-1} for di-substituted structures with a different nature and size: 6MCC-Cyclohex, 6MCC-Diethyl, 6MCC-OMe, 6MCC-MePh, 6MCC-EtPh and 6MCC-Fluorene

The relative Gibbs energy profiles for disubstituted monomers are presented in **Figure 6.29**. On the one hand, for 6MCC-Cyclohex, 6MCC-Diethyl, 6MCC-OMe and 6MCC-Fluorene, not only the substituents are located in a favourable position (R_3, R_4 **Figure 6.7**), but are equal/symmetric as well. On the other hand, 6MCC-MePh and 6MCC-EtPh have different substituents including a phenyl and alkyl (methyl or ethyl) groups. The monomer tendencies shown in **Figure 6.29** are reasonably similar except for the profile related to the ROP of 6MCC-Fluorene, which has the most favoured energy values in almost all structures along the reaction pathway. Nevertheless, the energies compared with the other ROP profiles are not much different. As noted in **Figure 6.28**, the energetic tendencies for mono-substituted monomers are similar to those of di-substituted monomers (**Figure 6.29**). These tendencies embrace similar type of energetic values for the ROP pathways during the initiation part (from structure **A** to **D**), but they differ during the propagation part (from structure **E** to **H**). Specifically, the initiation transition state **TS 1.1** for the ROP of 6MCC-Diethyl, 6MCC-MePh and 6MCC-EtPh (13.4 kcal·mol^{-1}) have similar values, is

a little bit higher for 6MCC-Cyclohex (13.7 kcal·mol^{-1}), and more favourable for 6MCC-OMe and 6MCC-Fluorene (12.7 and 10.3 kcal·mol^{-1}, respectively). These values are close to those computed for the first ring-opening step **TS 1.2** that are at 13.0, 12.7 and 12.5 kcal·mol^{-1} for 6MCC-Cyclohex, 6MCC-Diethyl and 6MCC-Fluorene, respectively. In the middle of this range are the values calculated for 6MCC-MePh and 6MCC-EtPh amounting to 10.4 and 10.6 kcal·mol^{-1}. The most favoured energetic value is for the path for 6MCC-OMe at 8.0 kcal·mol^{-1} The main energetic differences are found within the structures **D** and **E**, which are more stable than their previous and subsequent structures. Intermediates **D** have similar values with 1.6, 1.8, 2.0, 2.1, 2.4 and 4.7 kcal·mol^{-1} for 6MCC-Cyclohex, 6MCC-Fluorene, 6MCC-Diethyl, 6MCC-OMe, 6MCC-EtPh and 6MCC-MePh, respectively. Structure **E** show more energetic diversity, and the most stable structures are those derived from 6MCC-Fluorene and 6MCC-EtPh at -7.4 and -7.2 kcal·mol^{-1}, followed by 6MCC-MePh and 6MCC-Diethyl being at -4.5 and -1.9 kcal·mol^{-1}, and with the values determined for 6MCC-Cyclohex and 6MCC-OMe the highest in the series at 0.4 and 3.2 kcal·mol^{-1}. The propagation transition state **TS 2.1** is the most unstable one in the ROP pathway for 6MCC-Diethyl and 6MCC-OMe located at 17.1 and 16.2 kcal·mol^{-1}, respectively, and is the most feasible for 6MCC-Fluorene at 4.4 kcal·mol^{-1}.

For the rest of the monomers, their energetic values are similar as their preceding transition states being 13.0 kcal·mol^{-1} for 6MCC-Cyclohex, and 10.7 kcal·mol^{-1} for both 6MCC-MePh and 6MCC-EtPh. The last ring-opening step **TS 2.2** is energetically comparable with **TS 1.2**, with 6MCC-Cyclohex and 6MCC-Diethyl again representing the most unstable structures with values of 13.8 and 12.0 kcal·mol^{-1}, respectively, and the most stable value observed for 6MCC-OMe at 7.1 kcal·mol^{-1}. In between these latter values are those from the profiles based on 6MCC-Fluorene (at 10.0 kcal·mol^{-1}), 6MCC-MePh (11.2 kcal·mol^{-1}) and 6MCC-EtPh (8.1 kcal·mol^{-1}).

Note that the computed manifolds for 6MCC-MePh and 6MCC-EtPh coincide or have (very) close values in each of their respective preceding transition states. However, in **TS 2.2** the energetic difference is larger about 3 kcal·mol^{-1}

approximately. For 6MCC-Fluorene, the initiation (**TS 1.1**) and propagation (**TS 2.1**) transition states are more stable than the respective ring-opening transition states (**TS 1.2** and **TS 2.2**), contrary to what is observed for 6MCC-OMe, whose profile shows the opposite behaviour having the most favoured transition states at the ring-opening stages. The final structures **H** and the dimers have quite similar energy values with the exception of 6MCC-Diethyl, for which **H** is located at 11.5 kcal·mol^{-1} (the most unstable structure among all of them) and 5.1 kcal·mol^{-1}, respectively. In the profiles of 6MCC-MePh and 6MCC-EtPh, the values are 3.9 and 4.6 kcal·mol^{-1} for structure **H**, and 7.2 and 6.7 kcal·mol^{-1} for the dimer, respectively. In the manifold calculated for 6MCC-OMe, the energies are 5.3 kcal·mol^{-1} (**H**) and 5.1 kcal·mol^{-1} (dimer). The related structures for 6MCC-Cyclohex and 6MCC-Fluorene have the most feasible energetic values being 2.7 and 0.2 kcal·mol^{-1} (structure **H**), and 4.9 and 5.5 kcal·mol^{-1} (dimer), respectively. In summary, all transition states are feasible at room temperature and almost all monomers presented in **Figure 6.29** have their final dimer energies lower than their corresponding initial monomers. Therefore, all of them should be prone to ROP delivering stable polymers.

Table 6.13: Correlation plot values and legend for monomers with different size and chemical nature of the substituents located in favoured positions in kcal·mol^{-1}

Monomer	Energy Span	Polymer stability	ROP Successful?
6MCC	19.8	-3.8	Yes
6MCC-Ts	21.3	-7.7	Yes
6MCC-Amine	19.1	-7.2	Yes
6MCC-CN	17.7	-6.4	Yes
6MCC-Vinyl	21.2	0.9	Yes
6MCC-Allyl	19.4	-3.6	Yes
6MCC-Cl	17.3	-6.5	Yes
6MCC-OMe	16.2	1.5	Yes
6MCC-Diethyl	19.0	-0.3	Yes
6MCC-MePh	15.7	2.5	Yes
6MCC-EtPh	17.8	2.0	Yes
6MCC-Cyclohex	13.8	-0.4	Yes
6MCC-Fluorene	17.3	-3.2	Yes

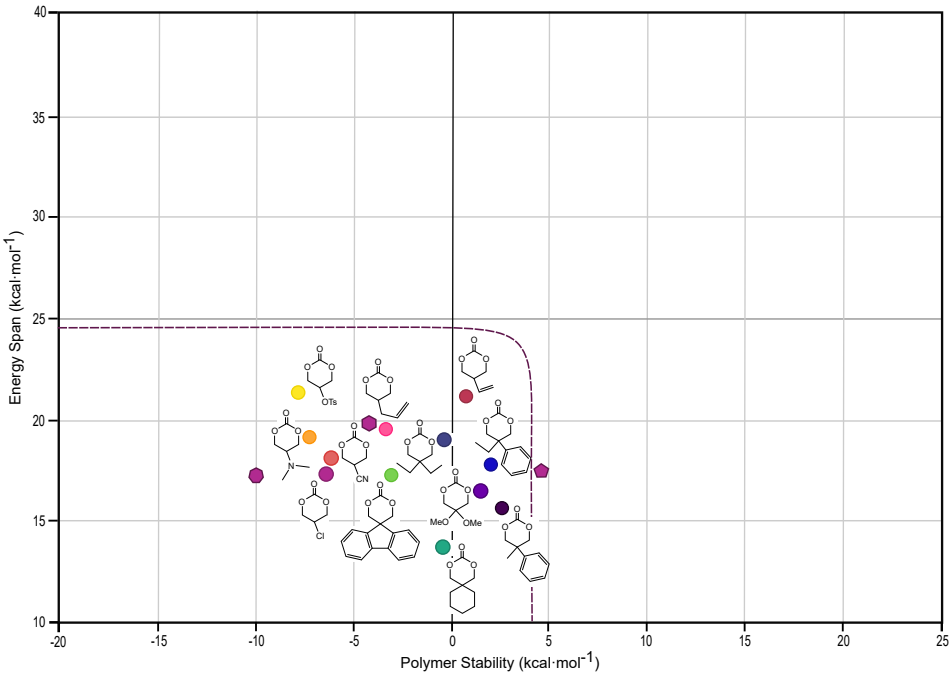

Figure 6.30: Correlation plot for polymer stability vs. Energy span (both in kcal·mol^{-1}) of monomers with different size and chemical nature for the substituents [represented as circles]. Reference values for 5MCC, 6MCC and 7MCC are also included [represented as purple pentagon, hexagon and heptagon respectively]

The energetic spans and dimer stabilities for the monomers represented in **Figure 6.27** are shown in **Figure 6.30** and their corresponding values are provided in **Table 6.13**. The mono-substituted monomers are in general located in the lower-left region, which means that they should be polymerizable (kinetically) and giving stable polymers (thermodynamics), while di-substituted monomers are located closer to the boundary of the ROP feasibility region. The mono-substituted monomers with electron-donating groups are placed in a more favourable region than the monomers with electron-withdrawing groups. Nevertheless, the energy spans and dimer stabilities for the most opposite-like monomers (6MCC-Amine and 6MCC-CN) are considerably close to one another. Therefore, based on our calculations there is no clear tendency related to the electronic nature of the monomer substituents.

For 6MCC-Allyl, 6MCC-Vinyl and 6MCC-Ts, the energetic span is higher

compared to the other monomers (**Figure 6.27**), with those for 6MCC-Vinyl and 6MCC-Ts being the highest with values close to 21 kcal·mol^{-1}. In general, the di-substituted monomers have lower energetic spans than the mono-substituted ones, however, their computed dimer stabilities are lower (i.e., higher energy values were calculated for these species). The most favoured di-substituted monomers in terms of ROP potential are the ones with a symmetrical substitution patterns with 6MCC-Fluorene and 6MCC-Cyclohex the most feasible ones. In the case of 6MCC-Fluorene, the energetic span is close to that of the mono-substituted monomers 6MCC-Cl, 6MCC-CN and 6MCC-Amine, while the energetic span value computed for 6MCC-Cyclohex is the lowest among the entire monomer series visualized in **Figure 6.27**. The 6MCC-MePh and 6MCC-EtPh have similar dimer stabilities and similar energy span values, with the monomer substituted by an ethyl group being slightly more disfavoured. The monomer 6MCC-OMe is located inside the feasible ROP region and thus the plot predicts that it may ring-open polymerized with a reasonable energy span. In conclusion, all of the calculated and visualized ROP data for this latter series of monomers seem to suggest that they can be polymerized under the standard ambient temperature conditions due to relatively low energetic spans and acceptable and low energies of the final dimers. Altogether, the combined data indicated that the location of the substituent in the ring is far more important than the chemical nature or size of the substituent.

6.4.6 Five-Membered Cyclic Carbonates

As mentioned above, several synthetic routes exists to obtain successfully five-membered cyclic carbonates (5MCC)[255–258]. Unfortunately, in general these molecules do not possess good potential for ROP, and in the sparse cases reported short and/or unstable polymers are observed in comparison to the ROP of the larger ring carbonates (6MCCs, 7MCCs and 8MCCs)[39,220]. Importantly, the 5MCC and 5MCC-Me can only can be ring-open polymerized at high temperatures, conditions that typically lead to decarboxylation thereby giving poly(ethylene-carbonate)s and not the target poly(carbonate)s. In **Figure 6.31**

some monomers are shown that have been previously prepared and reported in the literature: 5MCC[246,247,259,260], 5MCC-KetoPh[261], 5MCC-Cyc[91,235], 5MCC-Limonene[237], 5MCC-C=C[262,263] and 5MCC-Me[21,246,247,256,257,260,264,265]. Except for the *trans*-fused 5MCC-Cyc and 5MCC-Limonene, all other 5MCCs have not been reported as suitable monomers for ROP.

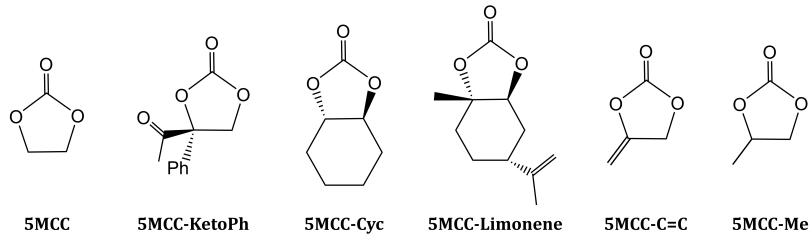

Figure 6.31: Five-membered cyclic carbonates monomers

In **Figure 6.32**, the relative Gibbs free energy profiles are presented for the monomers depicted in **Figure 6.31**. As already noted in **Section 6.4.2 - *Ring Size***, the ROP tendency for 5MCCs consists of various stages, with an initial stage (ring-opening by the initiator molecule, BnOH) that is kinetically feasible. However, at each subsequent step (alternating propagation and ring-opening of the next monomer), the process becomes energetically less favoured from a free energy point of view (i.e., an increasing ΔG is observed above the value of the respective monomer). The first part of the ROP shows similar values for all monomers, but the main differences occur in the second stage leading to the dimer. The most disfavoured profiles are those calculated for the monomers 5MCC-KetoPh, 5MCC-Me and 5MCC-C=C. As anticipated, the profile for 5MCC-Limonene is the most favoured one (negative ΔG), followed by the ones computed for 5MCC-Cyc and the non-substituted cyclic carbonate 5MCC.

In more detail, the separated, starting monomers 5MCC-Cyc and 5MCC have energies of 2.9 and 4.1 kcal·mol^{-1}, respectively, values that are followed by those computed for 5MCC-C=C (at 6.2 kcal·mol^{-1}) and the more disfavoured ones of 5MCC-Me, 5MCC-Limonene and 5MCC-KetoPh located at 7.2, 7.8 and 8.8 kcal·mol^{-1}. The 5MCC-Limonene has the lower energetic values for

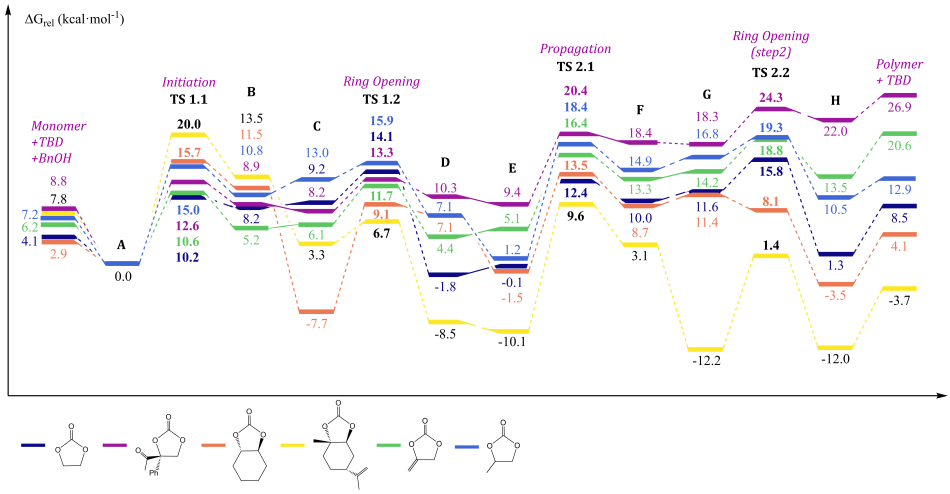

Figure 6.32: Relative Gibbs free energies in kcal·mol^{-1} for five-membered cyclic carbonates with different substituents: 5MCC, 5MCC-KetoPh, 5MCC-Cyc, 5MCC-Limonene, 5MCC-C=C and 5MCC-Me

almost all intermediates and transition states, with the exception of **TS 1.1**, which is relatively high at 20.0 kcal·mol^{-1} in comparison to those values of the other monomers (15.7 kcal·mol^{-1} for 5MCC-Cyc, 15.0 kcal·mol^{-1} for 5MCC-Me, 12.6 kcal·mol^{-1} for 5MCC-KetoPh, 10.6 kcal·mol^{-1} for 5MCC-C=C and 10.2 kcal·mol^{-1} for 5MCC).

In the first ring-opening transition state **TS 1.2**, the highest values are computed for the profiles of 5MCC-Me, 5MCC and 5MCC-KetoPh (15.9, 14.1 and 13.3 kcal·mol^{-1}, respectively), followed by that calculated for 5MCC-C=C (11.7 kcal·mol^{-1}) with the energies for the **TS 1.2** in the manifolds of 5MCC-Cyc and 5MCC-Limonene being most favored at 9.1 and 6.7 kcal·mol^{-1}. From this stage onwards, the profile for 5MCC-Limonene consistently shows the lowest energies, followed by the pathways determined for 5MCC-Cyc and 5MCC that are clearly above the profile of 5MCC-Limonene. The overall profiles computed for 5MCC-Me, 5MCC-C=C and 5MCC-KetoPh are energetically the most disfavoured ones. Moreover, in all energy profiles, with the exception of the ones determined for 5MCC-Cyc and 5MCC-Limonene, the propagation transition state **TS 2.1** has a lower energy value than the second ring-opening transition

state **TS 2.2**. Specifically, the least probable energetic paths are the ones related to the ROP of 5MCC-KetoPh, 5MCC-Me and 5MCC-C=C that display energy values of 20.4, 18.4, and 16.4 kcal·mol^{-1} for **TS 2.1**, and 24.3, 19.3 and 18.8 kcal·mol^{-1}, respectively, for **TS 2.2**. The use of monomers 5MCC-Cyc and 5MCC is energetically more feasible with values of 13.5 and 12.4 kcal·mol^{-1} for the propagation (**TS 2.1**), and 8.1 and 15.8 kcal·mol^{-1} for the second ring-opening (**TS 2.2**). Finally, the pathway based on the ROP of 5MCC-Limonene shows very low energetic values for the transition states **TS 2.1** and **TS 2.2** at 9.6 and 1.4 kcal·mol^{-1}, respectively. In between these transition states, the energies for intermediates **F** and **G** follow the same tendencies. The ones calculated for 5MCC-KetoPh are the highest with values around 18 kcal·mol^{-1}, followed by those calculated for 5MCC-Me and 5MCC-C=C with values near 15 kcal·mol^{-1}. Just below these latter ones are the data attained for monomers 5MCC and 5MCC-Cyc with similar values around 10.5 kcal·mol^{-1} for the aforementioned intermediates. The same intermediates that are derived 5MCC-Limonene have in this respect very low energies.

The reaction terminates (dimer stage) in a similar way as noted in the second ring-opening transition state, with structures **H** having computed values of 22.0, 13.5 and 10.5 kcal·mol^{-1} for 5MCC-KetoPh, 5MCC-C=C and 5MCC-Me, 1.3 and -3.5 kcal·mol^{-1} for 5MCC and 5MCC-Cyc, and finally, -12.0 kcal·mol^{-1} for 5MCC-Limonene. On the one hand, the final separate dimers are quite unstable for 5MCC-KetoPh, 5MCC-C=C and 5MCC-Me, which are at 26.9, 20.6 and 12.9 kcal·mol^{-1}. These energies are clearly too high to consider them as a stable product, hence, these monomers, even if they are kinetically feasible for ROP, are not able to provide stable and isolable polymers. On the other hand, the separate dimers for 5MCC, 5MCC-Cyc and 5MCC-Limonene have significant lower energetic values amounting to 8.5, 4.1 and -3.7 kcal·mol^{-1}, respectively. If we keep in mind that the corresponding energetic spans demonstrate kinetic feasibility for their ROP, we can safely assume that these monomers have potential to be ring-open polymerized towards isolable polymer species provided that depolymerization pathways are not equally operative.

To see more clearly which 5MCC monomers are predicted to be prone to

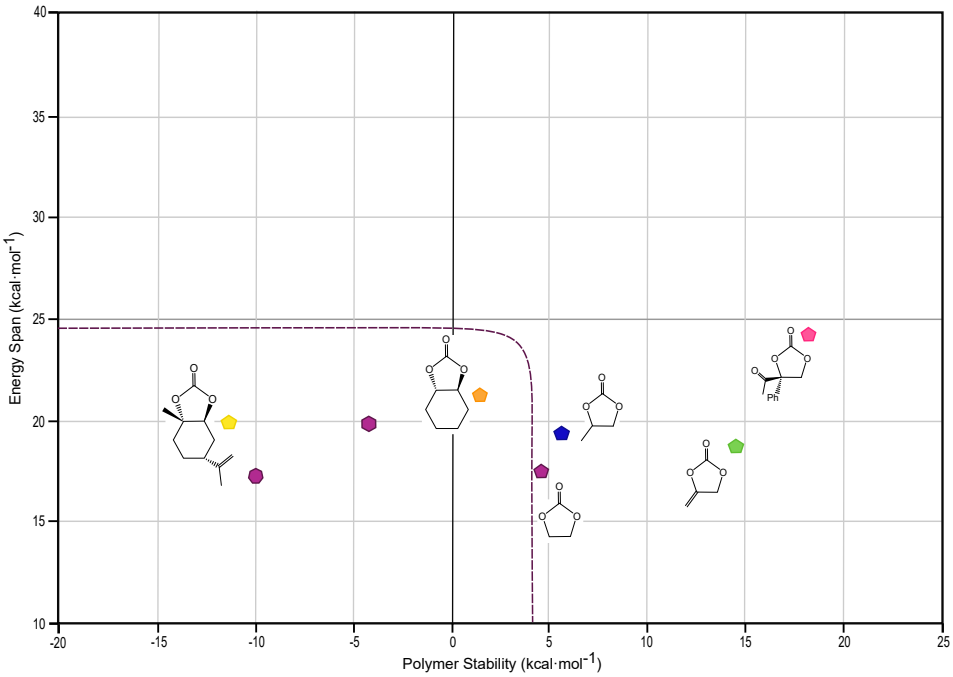

Figure 6.33: Correlation plot for polymer stability vs. Energy span (both in kcal·mol^{-1}) of five-membered cyclic carbonates (5MCC)s [represented as pentagons]. Reference values for 6MCC and 7MCC are also included [represented as purple hexagon and heptagon respectively]

Table 6.14: Correlation plot values and legend for five-membered cyclic carbonate monomers with different substituents located in favoured positions in kcal·mol^{-1}

Monomer	Energy Span	Polymer stability	ROP Successful?
5MCC	17.6	4.4	Boundary-No
5MCC-KetoPh	24.3	18.0	No
5MCC-Cyc	21.3	1.1	Yes
5MCC-Limonene	20.0	-11.5	Yes
5MCC-C=C	18.8	14.4	No
5MCC-Me	19.3	5.7	Boundary-No

ROP, a correlation plot is presented in **Figure 6.33** and selected energy values are listed in **Table 6.14**. At first sight, it is easy to recognize a relationship between the dimer stability and the tendencies seen in the propagation

part (**Figure 6.32**). Specifically, the profiles for 5MCC-KetoPh and 5MCC-C=C are the most disfavoured ones with a high energetic span and relative unstable dimer product. Close to the boundary of the ROP region are the values determined for both 5MCC-Me and 5MCC, which have reasonable energetic spans but their dimer stabilities are around +5 kcal·mol^{-1}. Finally, the values for 5MCC-Cyc and 5MCC-Limonene are the most prolific ones with both acceptable energy spans while based on relatively stable dimer species hence credible towards polymer formation.

In more detail, the relatively high energetic span for 5MCC-KetoPh at 24.3 kcal·mol^{-1} combined with a rather unstable dimer (18.0 kcal·mol^{-1}) makes this monomer unsuitable for ROP promoted by TBD/BnOH. For the monomer 5MCC-C=C, the energetic span is 18.8 kcal·mol^{-1} (thus feasible at room temperature), however, the corresponding dimer is quite unstable (14.4 kcal·mol^{-1}) and ROP of this 5MCC also looks unrealistic. These computed data for both these monomers is clearly out of the range considered to give successful ROP.

The 5MCC and 5MCC-Me monomer cases are more complicated to predict due to reasonable energetic spans (17.6 and 19.3 kcal·mol^{-1}, respectively) but with their dimer stabilities close but clearly outside the boundary region (5.7 kcal·mol^{-1}). The experimental data reported in the literature actually shows that these kind of monomers can be polymerized at high temperature using metal-based catalyst[231,233]. Additionally, in some of these polymerization procedures, decarboxylation of the monomer takes place under these conditions thus obtaining a polymer containing both carbonate and ether connections in the main polymer chain[229]. Therefore, we here conclude that 5MCC and 5MCC-Me are not sufficiently prone to undergo a successful ROP under the conditions reported in **Figure 6.7**, and this prediction coincides with the position of their computed date out of the boundary in the correlation plot (**Figure 6.33**).

The profile for 5MCC-Cyc shows a quite high energetic span of 21.3 kcal·mol^{-1}, but a very stable dimer at 1.1 kcal·mol^{-1}. Hence, this monomer should be prone towards ROP. The experimental data reported in the literature concurs with this prediction[235,236]. Finally, the most stable monomer is 5MCC-Limonene, being

structurally more complex in comparison with the other monomers reported in this section. However, several studies show that not only this monomer can be ring-open polymerized, but also stable polymers can be produced[237]. These data concur with the energetic values obtained (energy span of 20.0 kcal·mol^{-1}, and with a dimer stability of -11.5 kcal·mol^{-1}) and the favourable location within the ROP region of **Figure 6.33**.

In summary, in general the 5MCC monomers are more difficult to be polymerized than the larger-ring carbonates as there is a general tendency to produce intermediates and transition states that are increasingly more unstable after each consecutive propagation. Simple monomers with one or two substituents do not enhance the reactivity, while a cyclohexyl fused to the five-membered carbonate ring in a *trans*- conformation (5MCC-Cyc and 5MCC-Limonene) help to advance the ROP both from a kinetic and thermodynamic point of view.

6.4.7 Seven-Membered Cyclic Carbonates

As mentioned before, seven-membered cyclic carbonates (7MCCs) are more difficult monomers to be prepared, although they have better ROP potential as evidenced by several recent reports[39]. Due to their more challenging synthesis, only monomers that have been reported in the literature are here selected for computational studies (**Figure 6.34**). With this approach, it can be certified that these investigated 7MCCs are not only synthetically feasible, but also have ROP potential as supported by computation[38,90,91,210,220,238,239]. In addition, the monomer 7MCC-KetoMe has recently been demonstrated to undergo a successful ROP reaction using the same conditions that are considered in this study (cf., work done by Wangyu Shi from the Kleij group), helping to further validate the computational model.

The relative Gibbs free energies plotted in **Figure 6.35** are referred to the monomers shown in **Figure 6.34**. Overall, the computed energies indicate that the ROP of these monomers is thermodynamically more feasible as compared to the five- and six-membered monomers examined in the sections

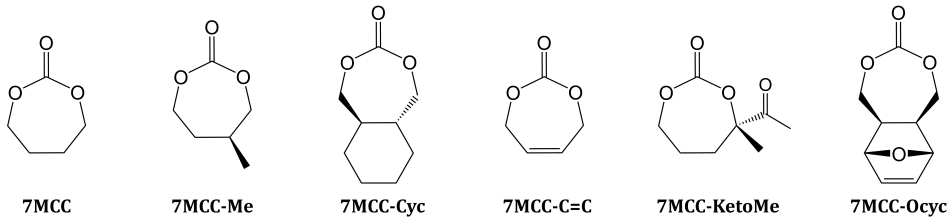

Figure 6.34: Seven-membered cyclic carbonates monomers

above. The ROP tendency for 7MCCs can be observed in **Figure 6.13**, showing that their initiation is more disfavoured than the following propagation steps, with declining energies in each subsequent cycle. The intermediates obtained as a product after the ring-opening transition states also illustrate the same tendency, as they are much more stable thermodynamically, and become energetically more feasible at the end of each propagation part. Since all these 7MCC monomers are prone to undergo a ROP reaction more easily than any other monomer described before (with the exception for 5MCC-Limonene), all comparative terms used in this section will be among the monomers presented in **Figure 6.34**.

As seen in the previous sections, the initiation part exhibits slightly different behaviour than the propagation part. In the latter, the stability tendencies for the intermediates and transition states derived from each monomer are clearer to follow. In **Figure 6.35**, the most favoured profile is the one computed for 7MCC-C=C, while the most disfavoured one corresponds to 7MCC-Cyc. Between these two extremes are located the pathways calculated for 7MCC and 7MCC-Me with rather similar values, followed by the data gathered for 7MCC-KetoMe and 7MCC-Ocyc. For all monomers, except for 7MCC-Cyc, the ring-opening transition states are energetically more favoured than their preceding initiation or propagation transition states.

In detail, the Gibbs free energy profiles presented in **Figure 6.35** start with the separate monomers, catalyst and initiator. The lowest energies for these types of ensembles are calculated for 7MCC-KetoMe and 7MCC with values of 2.0 and 2.7 kcal·mol^{-1}, followed by the profiles of 7MCC-Me and 7MCC-Cyc

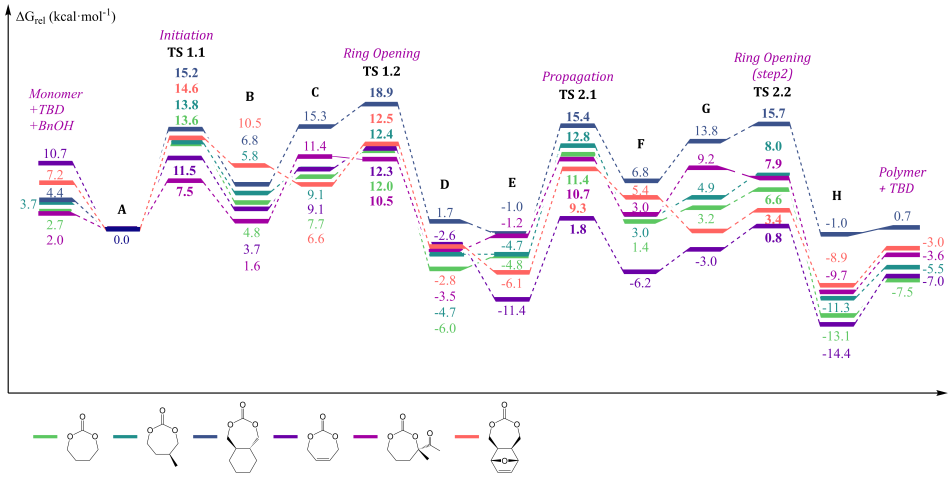

Figure 6.35: Relative Gibbs free energies in kcal·mol^{-1} for seven-membered cyclic carbonates having different substituents: 7MCC, 7MCC-Me, 7MCC-Cyc, 7MCC-C=C, 7MCC-KetoMe and 7MCC-Ocyc

with energies at 3.7 and 4.4 kcal·mol^{-1}. The ensembles computed for 7MCC-Ocyc and 7MCC-C=C are the most unstable ones at 7.2 and 10.7 kcal·mol^{-1}, respectively. The initiation transition state **TS 1.1** for the monomers have a fused cyclohexyl (7MCC-Cyc and 7MCC-Ocyc) have the highest energy values at 15.2 and 14.6 kcal·mol^{-1}, followed by the ones computed for 7MCC-Me and 7MCC with values amounting to 13.8 and 13.6 kcal·mol^{-1}. The manifolds for 7MCC-C=C and 7MCC-KetoMe show the lowest **TS 1.1** located at 11.5 and 7.5 kcal·mol^{-1}. The first ring-opening transition states **TS 1.2** has a similar behaviour as the ones observed for **TS 1.1**, with the TS calculated for 7MCC-Cyc being most disfavoured (18.9 kcal·mol^{-1}) and the TS for 7MCC-C=C being most favoured (10.5 kcal·mol^{-1}). The other monomers display **TS 1.2** that are really close in energy being at 12.0 kcal·mol^{-1} (7MCC), 12.3 kcal·mol^{-1} (7MCC-KetoMe), 12.4 kcal·mol^{-1} (7MCC-Me) and 12.5 kcal·mol^{-1} (7MCC-Ocyc).

As described in **Section 6.4.2 - *Ring Size***, the tendency for the propagation part of the mechanism is that it is energetically more favoured than the initiation part. During the propagation transition state **TS 2.1**, the 7MCC-Cyc derived structure is the most unstable at 15.4 kcal·mol^{-1}, contrary to the species derived from monomer 6MCC-C=C that shows at this stage the most favoured

energetic value (1.8 kcal·mol^{-1}). The **TS 2.1** computed for 7MCC and 7MCC-Me have rather similar values of 11.4 and 12.8 kcal·mol^{-1}, respectively, which are slightly higher than that of 7MCC-Ocyc and 7MCC-KetoMe which are 9.3 and 10.7 kcal·mol^{-1}. The second ring-opening **TS 2.2** has lower values than the preceding transition states, except for the profile of 7MCC-Cyc that demonstrates a different behaviour. The overall stability tendency is the same as noted for **TS 2.1** showing for 7MCC-Cyc the highest value (15.7 kcal·mol^{-1}), and for the 7MCC-C=C the lowest one at (0.8 kcal·mol^{-1}). The second more stable profile is noted for 7MCC-Ocyc with a value for **TS 2.1** of 3.4 kcal·mol^{-1}, followed by the one calculated for 7MCC at 6.6 kcal·mol^{-1}. The profiles for 7MCC-KetoMe and 7MCC-Me at this stage have values of 7.9 and 8.0 kcal·mol^{-1}, respectively.

The ROP reaction ends with rather stable products **H**. The most stable ones are those derived from 7MCC-C=C and 7MCC (at -14.4 and -13.1 kcal·mol^{-1}), followed by products **H** based on 7MCC-Me, 7MCC-KetoMe and 7MCC-Ocyc with energies of -11.3, -9.7 and -8.9 kcal·mol^{-1} and finally the product of 7MCC-Cyc at -1.0 kcal·mol^{-1}. The separate structures for the dimer and the recovered catalyst follow a similar tendency as seen with structure **H**. As observed before, the profiles of 7MCC and 7MCC-C=C show the most stable species with similar values of -7.5 and -7.0 kcal·mol^{-1}, followed by the pathway related to 7MCC-Me that has an energetic value of -5.5 kcal·mol^{-1}. The 7MCC-KetoMe and 7MCC-Ocyc related manifolds have here also similar values of -3.6 and -3.0 kcal·mol^{-1}, respectively, and the most unstable dimer species corresponds to the one resulting from 7MCC-Cyc at 0.7 kcal·mol^{-1}.
(Note that the polymer obtained from the 7MCC-C=C, corresponds to the cis-structure as reported in the literature[90])

The correlation plot presented in **Figure 6.36** and selected energy values are provided in **Table 6.15** confirm that all seven membered monomers are prone to ROP by TBD/BnOH. These data agrees with previous attained experimental results given in the literature[39,90,210,238,239]. The data obtained for 7MCC-C=C is located in the most favored ROP region, and the ROP of this monomer does not only display the lowest energy span compared to the other calculated

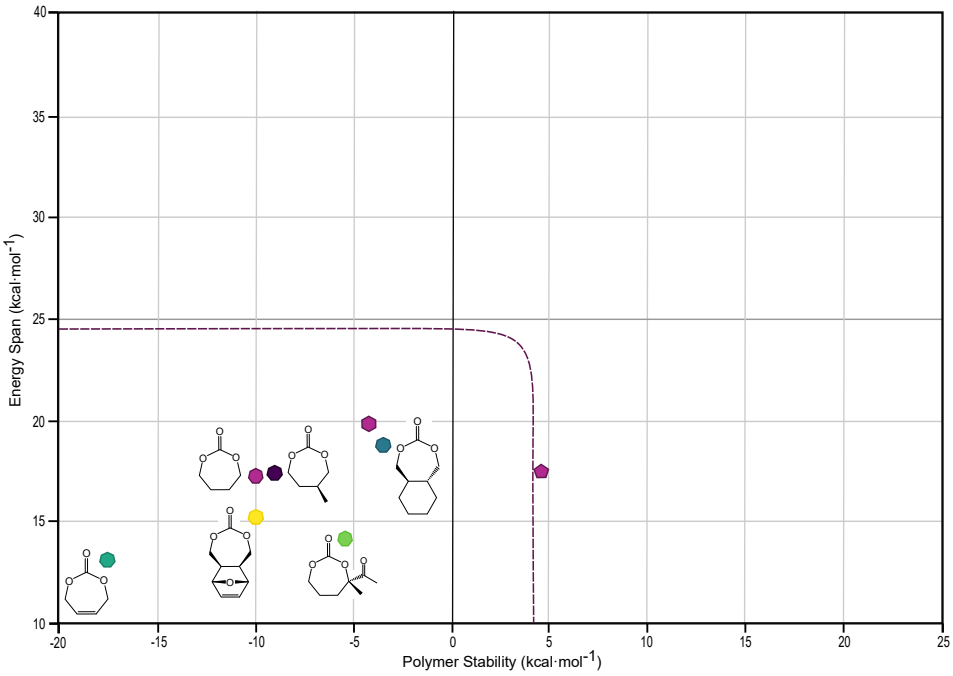

Figure 6.36: Correlation plot for polymer stability vs. Energy span (both in kcal·mol^{-1}) of seven-membered cyclic carbonates (7MCC)s [represented as heptagons]. Reference values for 5MCC and 6MCC are also included [represented as purple pentagon and hexagon respectively]

Table 6.15: Correlation plot values and legend for seven-membered cyclic carbonates in kcal·mol^{-1}

Monomer	Energy Span	Polymer stability	ROP Successful?
7MCC	17.4	-10.1	Yes
7MCC-Me	17.5	-9.2	Yes
7MCC-Cyc	18.9	-3.7	Yes
7MCC-C=C	13.2	-17.7	Yes
7MCC-KetoMe	14.2	-5.5	Yes
7MCC-Ocyc	15.4	-10.2	Yes

monomers (13.2 kcal·mol^{-1}), but also involves the most stable dimer at -17.7 kcal·mol^{-1}.

Located also in a favoured region of the plot, but contrary to 7MCC-C=C, the

calculated profile for the monomer 7MCC-Cyc displays a higher energy span and lower dimer stability with values of 18.9 and -3.7 kcal·mol^{-1}, respectively. The computed pathways for 7MCC and 7MCC-Me have quite close energy span values (17.4 and 17.5 kcal·mol^{-1}) and also dimer stabilities (at -10.1 and - 9.2 kcal·mol^{-1}). Despite 7MCC-Ocyc and 7MCC-KetoMe being structurally quite different, their energy spans are really similar (15.4 and 14.2 kcal·mol^{-1}, respectively), however, their related dimer stabilities illustrate that the one derived from 7MCC-Ocyc (-10.2 kcal·mol^{-1}) is more stable than the one obtained by ROP of 7MCC-KetoMe (-5.5 kcal·mol^{-1}).

In summary, the energy data (span and dimer stability) for all seven-membered cyclic carbonates are located well within the favoured ROP region in the correlation plot (**Figure 6.36**), which concurs with the behaviour observed in the ROP processes communicated in the literature. For all monomers (**Figure 6.34**), the energy span values clearly show their ROP potential from a kinetic point of view, and the dimer stabilities are significantly low, thus providing a thermodynamic driving force for the ROP of these monomers towards higher molecular weight polycarbonates.

6.4.8 Polymer stability

The polymer Gibbs free energy used in the predictive plot corresponds to the relative energy from the trimer or dimer as a single structure with its corresponding reactants. However, the oligomer/polymer chain may adopt several stable conformations depending on the nature of its substituents and the flexibility of the carbonate chain. After gathering all the data reported in the sections above, our aim was to examine whether the energies depicted in the predictive plot describe well enough these features in the oligomeric/polymeric structure. To further validate our data, some dimer/oligomer structures from each section above were re-calculated using a distinct procedure, and their corresponding Gibbs free energies were compared. Specifically, the cases chosen are related to the unsubstituted five-, six- and seven-membered cyclic carbonates (5MCC, 6MCC and 7MCC), the monomers tested under the same con-

ditions (Bicyc-OTMS and CF_3-Ph), the most energetically disfavoured structures originating from five- and six-membered cyclic carbonates (6MCC-6 and 5MCC-KetoPh), a 6MCC with a different substituent (6MCC-Amine and 6MCC-Cl), and a monomer with computed values close to the boundary ones (5MCC-Me).

The method used in this section starts with a GFN-xTB Molecular Dynamics simulation that explores the conformational space of the polymer at room temperature (*see computational details in **Section 6.3***). Above a thousand structures were sampled from the MD trajectory, which were divided into 5 clusters using a K-Means[245] clustering method. For each centre of cluster obtained, the geometry was re-optimized with Gaussian 16[62] at the same level outlined above (**Section 6.3**), and a vibrational analysis was also performed. Additionally, a standard state entropic corrections were applied[66]. In this way, the Gibbs free energies would be comparable.

The final averaged Gibbs free energy for the dimer(oligomer) was obtained by adding the energy of each conformer weighed according to a Boltzmann distribution (**Equation 6.1)** from the relative Gibbs free energies.

$$\frac{N_i}{N} = \frac{\exp^{(-E_i/kT)}}{\sum_j \exp^{(-E_i/kT)}} \tag{6.1}$$

Table 6.16 contains the energies computed with these two methods, and **Figure 6.37** corresponds to a predictive plot for ROP potential of the respective monomer based on both methods. In **Figure 6.37**, the data obtained in this section are represented as filled symbols and a darker boundary line, while the data from the sections above are represented as non-filled symbols, and the boundary line has a lighter colour.

Note that the colour that corresponds to each monomer does not always coincide with the coloured representations seen in the sections above. We implemented this change here to enhance the visualization of each structure in the plot.

The polymers derived from monomers without substituents and different carbonate ring sizes (5MCC, 6MCC and 7MCC) were first evaluated. Their aver-

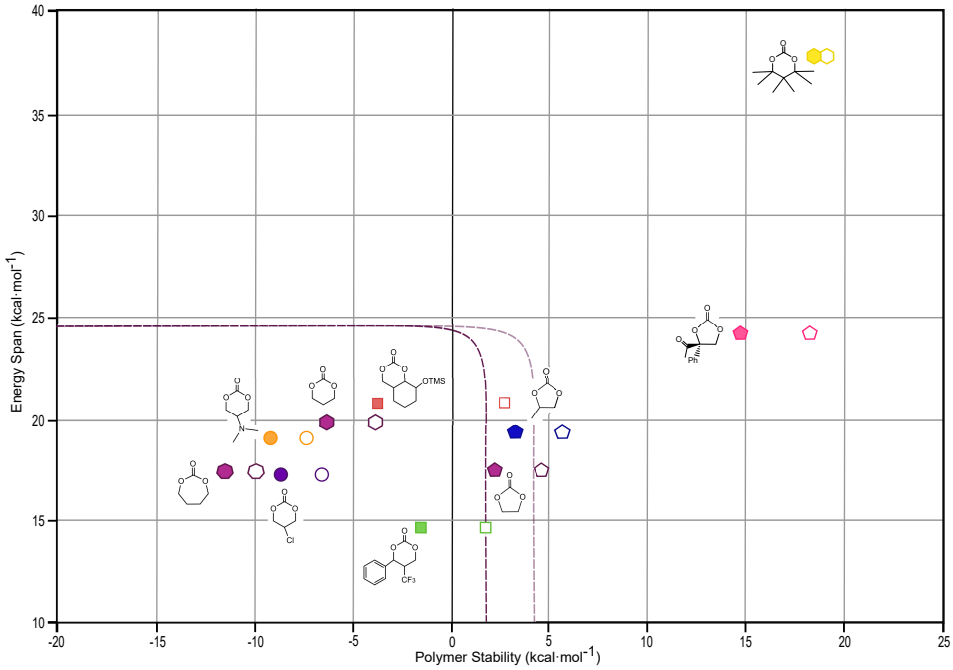

Figure 6.37: Correlation plot of the polymer stability (kcal·mol^{-1}) vs. Energy span (kcal·mol^{-1}). The filled symbols and the darker boundary line correspond to the Boltzmann-weighted energetic values, the non-filled symbols and the lighter boundary line are the reference values calculated in the sections above

aged Gibbs free energies are around 2 kcal·mol^{-1} more stable than the energies calculated above. The difference between these energies is not very large, and reinforces our hypothesis that the structures calculated initially describe well enough the studied mechanism at the given conditions.

For real case polymers experimentally shown to react, specifically Bicyc-OTMS[28] and CF_3-Ph[223], the average Gibbs free energy is also lower, therefore shifting their calculated ROP potential towards a more exergonic region (left side of the plot).

Profiles that are placed in an unfavourable region (high energy span and low dimer stability), such as determined for the highly-substituted 6MCC-6, and the 5MCC-KetoPh, were also examined by the alternative computational method. For both monomers more stable energetic values are found, however, these latter values are still are located in an unfavoured region (right side of

Table 6.16: Polymer relative Gibbs free energies compared with the relative weighted Boltzmann Gibbs free energies, both in kcal·mol^{-1}. The legend for the correlation plot (**Figure 6.37**) is also included

Monomer	ΔGibbs$_{rel}$	Boltzmann
5MCC	4.4	2.2
6MCC	-3.8	-6.2
7MCC	-10.1	-11.7
Bicyc-OTMS	2.7	-3.9
CF$_3$-Ph	1.8	-1.5
6MCC-6	19.0	18.6
5MCC-KetoPh	18.0	14.6
6MCC-Amine	-7.2	-9.2
6MCC-Cl	-6.6	-8.7
5MCC-Me	5.7	3.9

the plot). Specifically, for the 6MCC-6, the difference is less than kcal·mol^{-1} while for the 5MCC-KetoPh the difference is around kcal·mol^{-1} when comparing both methods.

As representative examples of polymers whose ROP was calculated to evaluate the chemical nature of the substituents, both 6MCC-Amine and 6MCC-Cl were selected. In both cases, the averaged energy method provides values that are more stable by about 2 kcal·mol^{-1}, placing them in a very similar region in the predictive plot. Finally, 5MCC-Me was evaluated because its ROP values were close to the boundary line. The averaged energetic value approach coincides in terms of ΔE and dimer stability similar to the trend observed for the other dimers computed in this section, and being more feasible by around 2 kcal·mol^{-1}.

In summary, it is possible to observe a clear trend regarding the relative Gibbs free energies obtained along this chapter with the averaged ones. Despite the energetic difference not always being the same, the Boltzmann averaged energetic values tend to be in a narrow range of kcal·mol^{-1} more stable. Consequently, if we would have computed all the averaged energies for all monomers discussed in this chapter, we would expect to obtain a very similar

predictive plot slightly shifted to a more stable ROP region and the boundary line would be shifted as well. Therefore, the polymer Gibbs free energies with the standard state entropic corrections computed throughout this chapter, describes sufficiently well the formation of the dimer structures, avoiding thus a higher computational cost resulting from the computational efforts needed to calculate the averaged Gibbs free energies.

6.5 Conclusions

An extensive study of the ROP of cyclic carbonates allowed unravelling the mechanistic pathway for a wide range of monomers and the creation of a reactivity predictive plot using TBD as a generic catalyst, BnOH as initiator under ambient temperature conditions. Therefore, all objectives outlined at the beginning of this chapter were achieved. Given the wide scope of this study, the conclusions below are segmented sections to give a detailed overview.

6.5.1 Mechanistic Pathway

The mechanistic pathway for ROP of cyclic carbonates using TBD as a catalyst and BnOH as an initiator in toluene solution at room temperature was unravelled. The nature of the TBD determines its reactivity due to the capacity to act/behave as a base and make hydrogen bonds with the carbonate oxygens and intermediate C-O bonds, hence, its presence is key in every transition state/intermediate. The mechanistic pathway consists of an initiation step followed by n propagation steps. Each step consists of two stages that include an initiation or propagation with a ring-opening step, involving thus two transition states and four intermediates. The reaction starts with an initiation step where the BnOH is deprotonated by the TBD and as a result, an alkoxide attacks the carbonate carbon from the cyclic carbonate, thus leading to an intermediate with a tetrahedral carbon. The second step is a ring-opening triggered by the protonated catalyst $HTBD^+$, it protonates the outer oxygen of the tetrahedral carbon intermediate, opening thereby the ring of the cyclic carbonate and

obtaining an oligomeric carbonate chain. The latter will then serve as the initiating species for the subsequent propagation towards a larger oligomers by deprotonation into an alkoxide, following the next ring-opening step. As many propagation steps may occur (propagation and ring-opening steps), the polymer chain will be growing until chain transfer occurs.

6.5.2 Ring Size

The ROP reaction was studied for cyclic carbonates with different ring sizes (5MCC, 6MCC, 7MCC) to evaluate the ring strain effect. A trimer formation was considered as a model system to compare the ROP reactivity trend. For the bigger ring systems 7MCC and 6MCC, each propagation step is thermodynamically more stable than the previous one (exergonic), while for the 5MCC the tendency is the opposite (endergonic). The 7MCC profile has in general significantly thermodynamically more stable intermediates and transition states along the reaction pathway. For the 6MCC and 5MCC, their ROP and involved energetic values start similarly, but at each propagation step, the 6MCC path is more favoured, contrary to profile computed for 5MCC that becomes more unstable.

6.5.3 Correlation plot

A useful predictive reactivity plot was designed where the data from the energy span of the ROP reaction (y axis) was plotted against the polymer stability (x axis). The monomers that are more favourable to undergo the ROP reaction are located as much diagonally left-down as possible in the plot. That region means represents reactions that are energetically feasible (kinetics), and the dimer obtained is also thermodynamically favoured. To separate the monomers that may undergo a successful ROP reaction from the others, a boundary line is represented near 25 kcal·mol^{-1} for the energy span with the chosen ROP process being computed at room temperature), and around 4 kcal·mol^{-1} for the polymer stability. This representation improves the visualization of the results, and allows the prediction of ROP propensity.

6.5.4 Real case studies

Monomers experimentally tested under the same conditions by Kleij group members were considered to validate the theoretical model by experimental data. The monomers CF_3-Ph, CF_3-Naph, CF_3-Biphen, Bicyc-OH and Bicyc-OTMS successfully undergo ROP as reported in the literature, while Bicyc-DMS and Bicyc-Cyclohex are not polymerizable having high values for the energy span and dimer stability. Other monomers analogous to Bicyc-OTMS were calculated, and Bicyc-DiMe was found to be likely unreactive, while Bicyc-Me and Bicyc-Ph were observed to be near the boundary of the ROP region with a reasonable energy span, though they do show moderate to high energetic values for dimer.

6.5.5 Number of substituents

The number of substituents plays a key role in the ROP reaction, and with this consideration, the optimal number of substituents was examined that can be present in the cyclic carbonate and allowing for an effective ROP reaction. To evaluate this effect, up to six methyl substituents were added to different positions in the 6MCC ring. The highly substituted monomers 6MCC-6, 6MCC-5, 6MCC-4 are energetically highly unlikely to undergo ROP, hence, they cannot be polymerized under these mild temperature conditions. The monomers with three substituents are generally not reactive enough in this ROP, but the disposition and stereochemistry of the substituents place some monomers (6MCC-3b and 6MCC-3d) close to the boundary of the ROP region. Almost all monomers with two substituents are placed in a favoured segment of the ROP region, except for 6MCC-2b, whose energy values are located near to polymerizable area. The mono-substituted monomers and 6MCC are all placed within a more favoured part of the ROP region, with similar energies for both the energy span and dimer stability. In summary, the maximum number of substituents present in a 6MCC monomer while ensuring potential ROP under these conditions is two. In general, monomers with three substituents will not (easily) undergo a successful polymerization. For di- and tri- substituted

monomers, the disposition of the substituents does also have an important role. In the most nonsymmetric dispositions, with two methyl groups on one side of the carbonate ring and attached to the same carbon center (6MCC-2b, 6MCC-3a, 6MCC-3e) correspond to rather disfavoured monomers.

6.5.6 Size and chemical nature of the substituents

To evaluate the effect of the chemical nature and size of the substituents in the ROP reaction, mono- and di-substituted six-membered cyclic carbonates with the substituents located in the same position in the ring were studied. Additionally, most of them are able to be synthesised or polymerized (preparative studies reported in the literature). All of them are able to undergo ROP, with the mono-substituted monomers placed in a more favoured ROP region compared to the di-substituted ones. The number of substituents and their positional symmetry in the ring have a more important role than their chemical nature or their size.

6.5.7 Five-membered cyclic carbonates (5MCCs)

The polymers from the simplest five-membered cyclic carbonates 5MCC and 5MCC-Me are located close to the boundary of the ROP region. These monomers are known to be ring-open polymerized, but only at high reaction temperature (with substantial loss of CO_2), and the ROP of 5MCC-KetoPh and 5MCC-C=C are both located in a very disfavoured region. In contrast, 5MCCs with a fused cyclohexyl group are prone to ROP due to their higher ring strain. The stereochemistry of these monomers has to be trans, because several studies report that the cis-isomer does not undergo the reaction. The *trans*-5MCC-Limonene monomer provides a highly stable dimer product upon ROP. This monomer is very versatile and it can be polymerized and depolymerized using the same catalyst (TBD) while changing the reaction temperature. The depolymerization reaction will be explained in detail in the next chapter of this Thesis).

6.5.8 Seven-membered cyclic carbonates (7MCCs)

The dimers (and likely their polymeric forms) from the seven-membered cyclic carbonates are extremely stable, all of them are placed in the most favoured region in the predictive plot, which concurs with the behaviour reported in the literature. The most stable monomer is the 7MCC-C=C, whose ROP results into a dimer with a low energy span and being thermodynamically stable.

6.5.9 Polymer stability

Some polymers were re-calculated using a distinct procedure to validate the data used along the chapter. The average Gibbs Free energy for the polymers tend to give more stable values within a narrow range of a few kcal·mol^{-1}. Therefore, the more simple and standard use of polymer Gibbs free energies with the standard state entropic corrections considered along this chapter adequately describes the dimer formation without the high computational cost associated when focusing on averaged Gibbs free energies.

UNIVERSITAT ROVIRA I VIRGILI
COMPUTATIONAL INSIGHTS OF CATALYTIC CARBON DIOXIDE VALORIZATION AND CIRCULAR RECYCLING PROCESSES
Alba Villar Yanez

CHAPTER

7 Depolymerization

7.1 Introduction

During the last decades, the inefficiency of plastic recycling processes has resulted in the accumulation of microplastics within various eco-systems, thus leading to focus in chemical recycling strategies of polymers to mitigate these adverse effects[266–269]. In an ideal scenario, recycling methods would produce the original monomers under suitable catalytic conditions, allowing for their re-polymerization into the same polymers and enabling the creation of circular loop opportunities[270–272]. Some recent advances in this area have been reported in the literature for polyesters[273], poly(dioxolanes)/ethers[274,275], and polyurethanes[276].

As explained in the previous chapter, aliphatic polycarbonates (APCs) have received attention due to their biocompatibility and potential degradability[277–280]. There are different synthetic routes to obtain them such as via polycondensation, Ring-Opening Polymerization (ROP) and Ring-Opening Copolymerization (ROCOP). The latter approach involves the use of epoxides and carbon dioxide (CO_2) to obtain polycarbonates[281–283]. The advantages of catalytic copolymerization is the simple access to the reactants involved CO_2 is considered green (non-toxic) and cheap, and epoxides having different structures and functional groups can alter some properties of the target polycarbonate such as thermal behaviour, crystallinity, hydrophilicity, etc.

Specifically, when cyclohexene oxide (CHO)[284–286] and limonene oxide (LO) monomers undergo ROCOP with CO_2, they produce polycarbonates with high glass transition temperatures (>100°C), which are useful towards thermoset plastics when they are in their amorphous state. The copolymerization of limonene oxide (LO) and CO_2 is challenging due to limited catalyst options[287–291]; however, the use of LO as a biobased monomer is increasing because of its functionality it creates in the resultant polymer (PLC)[292–300]. These advancements highlight how bulky monomers like LO are becoming more important in the development of more sustainable polycarbonates, and other polymers derived from (biobased) epoxides that are sterically constrained[301].

A relevant study was reported by de Koning and Sablong[302] who per-

formed a full depolymerization of poly(limonene carbonate) (PLC) into limonene oxide (LO) and CO_2, using the bicyclic guanidine TBD (1,5,7-triazabicyclo[4.4.0]dec-5-ene) as a catalyst at 110°C. However, the exact mechanism of this process remains unclear, and repolymerizing LO and CO_2 requires high pressures, thus impacting the overall energy profile and practicality of PLC recycling. Other studies regarding the depolymerization of similar polycarbonates such as poly(cyclohexene carbonate) (PCHC) have been reported[303–307], but only few of them lead to high yield of a cyclic carbonate with potential as a monomer in subsequent ROP.

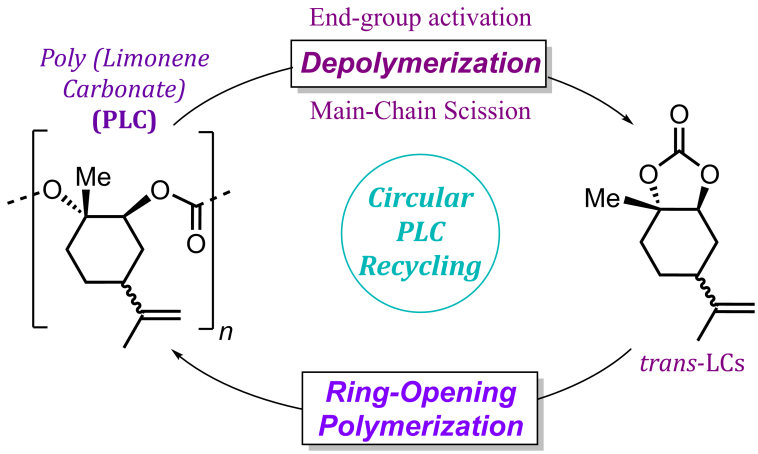

Figure 7.1: Circular recycling of biobased poly(limonene carbonate) through divergent degradation mechanisms and repolymerization (ROP) of *trans*-(limonene carbonate)

A more feasible approach for PLC recycling (not depending on higher-pressure copolymerization of LO and CO_2) is first obtaining *trans*-limonene carbonate as a major degradation product, followed by a Ring-Opening polymerization (ROP) reaction to deliver overall a circular process (**Figure 7.1**). As seen in the previous chapter, the ROP of five-membered cyclic carbonates is rare[308,309], but 5MCCs with a *trans*-configured fused ring such as limonene carbonate (LC) and cyclohexene carbonate (CHC) are amenable to be polymerized[198,235,236].

As seen along this thesis, TBD is a very versatile organocatalyst that behaves both as a base and/or as a proton-relay catalyst. In previous works from

the Kleij group, the formation of linear carbamates through a hydrogen-bond guided mechanism[310,311] was facilitated by TBD functioning as a proton-relay catalyst. In **Chapter 6 - *Ring-Opening Polymerization***, TBD's double function was crucial to facilitate the polymerization reaction. Therefore, we hypothesized that this hydrogen-bond activation mechanism could also play a key role in the depolymerization of polycarbonates.

In this chapter, we present evidence that TBD can serve as a versatile catalyst for the controlled degradation of poly(limonenecarbonate) (PLC) into *trans*-limonene carbonate *(trans*-LC) as the major reaction component and can subsequently undergo a ROP to regenerate PLC[237]. Moreover, mechanistic investigations including computational analysis and control experiments show that a mechanistically divergent depolymerization of PLC takes place combining complementary base-mediated end-group activation and a newly discovered, hydrogen-bond-promoted main-chain scission.

7.2 Objective/Motivation

The main objective outlines in this chapter is to understand the mechanistic pathways involved in the depolymerization process of poly(limonene carbonate) (PLC) using TBD as a catalyst and acetonitrile as a solvent at 80°C. Depending on where the depolymerization starts, two possible mechanisms are considered:

- **End-group depolymerization:** The reaction initiates at the terminal alcohol of the polymer chain, and the polymer depolymerizes by consecutive backbiting reactions.
- **Main-chain Scission:** The reaction begins somewhere in the main chain of PLC, where an initiator molecule activates a carbonyl group within the chain, resulting in the splitting of the polymer into two smaller chains.

To accomplish the main objective, both mechanisms will be studied and evaluated by means of DFT calculations supported by experimental results obtained by various Kleij group members.

7.3 Computational Details

Geometries and energies of all intermediates and transition states potentially involved in the reaction mechanism were computed at a DFT level using Gaussian16 rev. A.03[62] program with the ωB97X-D[191] functional, 6-311G**[192,193] basis set and SMD[65] implicit solvent model with acetonitrile parameters were employed in all the cases. Unconstrained geometry optimizations were complemented with vibrational analysis. Standard state entropic corrections were applied to the values of the Gibbs Free energies computed at 353.15K[66].

Full access to the dataset collection of computational calculations is available on the ioChem-BD repository[135] through:
https://doi.org/10.19061/iochem-bd-1-292

To obtain the initial structures for the transition states, a Potential Energy Surface (PES) scan was performed using the Gaussian16 program, revision A.03[62], at the same DFT level, temperature, and solvation model as described above. For certain structures, the PES scan was initially calculated using GFN2-xTB, version 6.4.1[83] (a program developed by Grimme), at 353.15K with the implicit solvent model GBSA2 with acetonitrile parameters. The resulting optimal molecular structures obtained from these calculations was then re-optimized with a vibrational analysis at the DFT level using Gaussian16 with the same conditions as described earlier.

7.4 Results and Discussion

The depolymerization reaction presented in **Figure 7.2** starts with the polycarbonate synthesised from *trans*-(limonene carbonate) (*trans*-LC), namely poly(limonene carbonate) (PLC), with TBD as a catalyst at 80°C in acetonitrile solution. The experimental results described in this chapter were performed by various Kleij group members (see: Dr. Lamparelli *et al.*)[237]. This depolymerization reaction achieves nearly complete conversion of PLC (with only 4%

remaining), yielding as a products *trans*-limonene carbonates (LC1 and LC2, 60%), along with a 36% yield of *cis*- and *trans*-limonene oxides (*trans*-LO and *cis*-LO)[237].

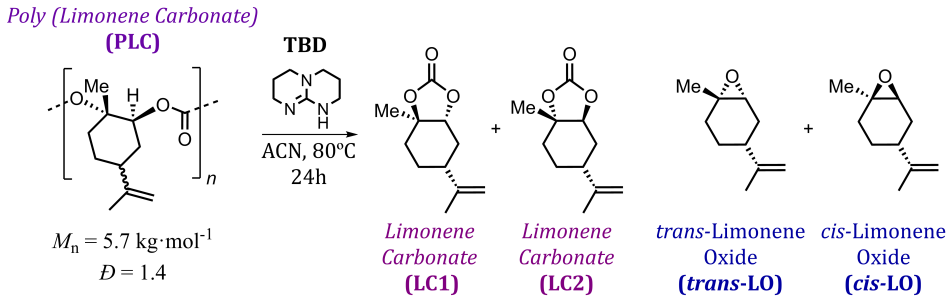

Figure 7.2: Scheme for the depolymerization of Poly(limonene carbonate) (PLC) and the reaction conditions

By using *trans*-LC, a repolymerization via ROP to regenerate PLC was tested using TBD as a catalyst, BnOH as an initiator in toluene solution at 80°C (M_n = 7.29 kg·mol^{-1}, Đ= 1.60). The mechanistic pathway of the ROP of *trans*-LC (5MCC-Limonene) is presented in **Chapter 6, Figure 6.32**. The energy span for the ROP reaction of 5MCC-Limonene at room temperature is 20.0 kcal·mol^{-1}, a barrier that is more than feasible at 80°C.

Several catalysts were tested in the laboratory to see whether they can accommodate the depolymerization of PLC, but among the N-heterocyclic bases studied, only TBD and DBU[a] achieved a high enough depolymerization conversion. While the use of TBD produced both LC and LO at high PLC conversion, the presence of DBU only resulted into LO formation at low PLC conversion (25%). As seen along this thesis, the role of TBD as a catalyst holds great potential due to its versatility. Not only it can behave as a base, but it is also able to make hydrogen bonds, and especially with the oxygen atoms of the cyclic carbonates and analogous heterocycles. The control experiment presented in **Figure 7.3 (a)** focuses on performing the reaction in the same conditions outlined above with another bicyclic guanidine catalyst. In this case, the use of

[a]Diazabicyclo[5.4.0]undec-7-ene

MTBD[b], with a similar chemical structure as TBD should not be able to make hydrogen bonds and induce proton relay steps in the overall manifold due to the N-bound methyl protecting group. As a consequence, the depolymerization does not occur. This result concurs with the idea that the reactivity related with the free -NH group of the TBD is crucial for depolymerization activity.

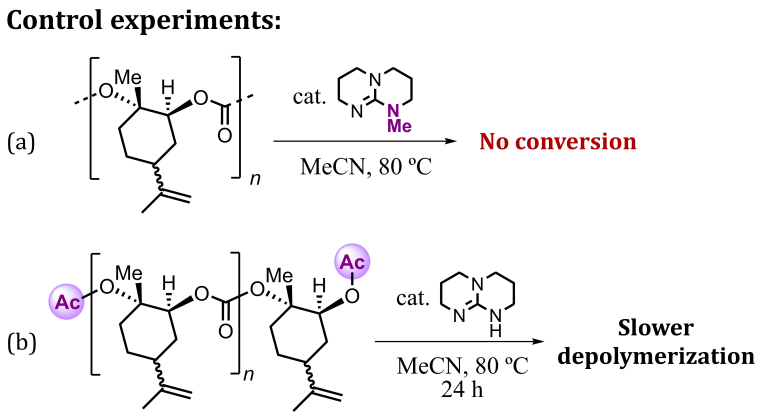

Figure 7.3: Control experiments for the depolymerization of poly(limonene carbonate)

The first depolymerization mechanism that comes to mind starts by activating one of the chain ends of the polymer induced by the catalyst TBD, resulting in consecutive reactions that depolymerize the entire polymer chain via consecutive backbiting steps. However, for very high molecular weight PLC, the catalyst likely encounters difficulties in locating a reactive end-group of the polymer, as each polymer chain possesses only two possible reactive sites. The reaction temperature aids in molecular mobility, thereby increasing the probability of finding a reactive centre. The control experiment presented in **Figure 7.3 (b)**, shows that by introducing chain-end protecting groups, inhibition of the end-group depolymerization mechanism occurs. Consequently, a slower but still feasible depolymerization takes place. This implies that another depolymerization mechanism occurs simultaneously, that could be randomly initiated within one of the repeat units of the polymer chain with the catalyst likely activating one of the carbonate group thereby starting a "main-chain scission"

[b] 7-Methyl-1,5,7-triazabicyclo(4.4.0)dec-5-ene

based depolymerization. As a result of this reaction, shorter polymer chains are obtained, enhancing the catalyst's ability to also initiate depolymerization via end-group activation.

Both mechanistically related reactions will be explained in detail and compared in the sections below. The model employed to study the mechanistic pathway is a trimer (an oligomer chain made up from 3 monomer units) as has been demonstrated to describe adequately the system in **Chapter 6**. Utilizing larger polymer chains for calculations would significantly increase the computational cost due to the increased number of atoms involved without obtaining significant improvements in the results, and hence we believe this approximation is reasonable.

7.4.1 End-group depolymerization

The end-group depolymerization mechanism cleaves polymer chains at their terminal units, which are typically more accessible than the internal units. In this case, the catalyst TBD makes the activation of the end-groups (OH) to initiate the depolymerization process. The mechanistic pathway involved can be understood as a series of consecutive reactions, in each of which a *trans*-limonene carbonate (*trans*-LC) is released from the main chain. Each part includes two transition states and four respective intermediates. The model compound used in this study is a trimeric oligocarbonate, hence, two *trans*-LC will be released during the mechanism described in this section.

The mechanistic pathway represented in the **Figure 7.4** starts with the separated structures of the trimer and the catalyst TBD with a relative Gibbs free energy of 5.5 kcal·mol^{-1}, while their adduct **A-e** is used as a reference (0.0 kcal·mol^{-1}). The first transition state **TS-1e** has an energetic value of 4.7 kcal·mol^{-1}, and consists of a deprotonation of the terminal alcohol group of the trimer by the catalyst (TBD). Simultaneously, this newly-created alkoxide approaches to the electrophilic carbon centre of the adjacent carbonate. The product of this interaction is the structure **B-e** at 5.6 kcal·mol^{-1}, which has a tetrahedral carbon centre with four O-substituents forming an ion pair with

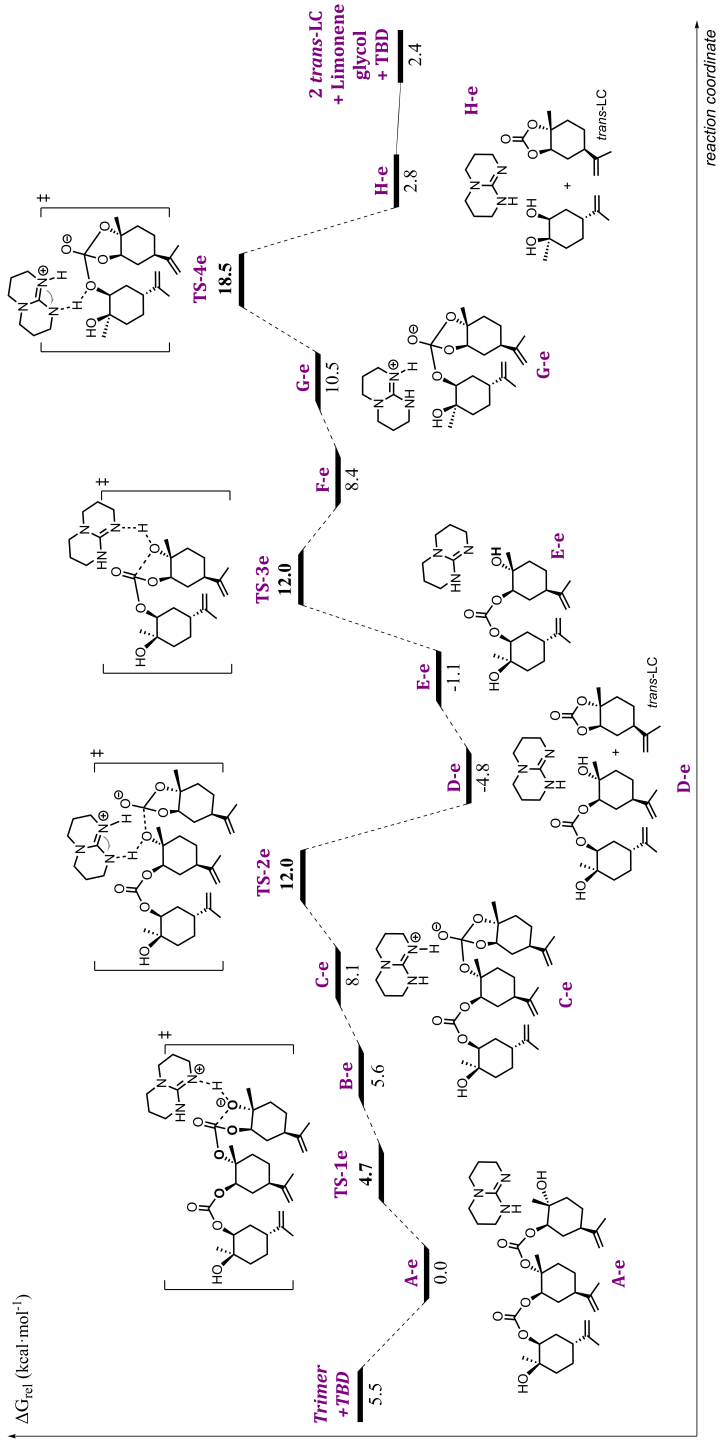

Figure 7.4: Relative Gibbs free energy reaction profile (in kcal·mol^{-1}) for the end-group based depolymerization of PLC

the protonated catalyst ($HTBD^+$), which maintains this geometry with hydrogen bonds between the anionic oxygens (outer and carbonyl) and the -NH group from the $HTBD^+$. The next intermediate **C-e** has an energetic value of 8.1 kcal·mol^{-1} and is highly similar to the previous one (**B-e**), the only difference is the orientation of the $HTBD^+$ hydrogen bonds, which in this case are made with the inner and carbonyl oxygens. Due to the catalyst orientation, the reaction leads to the next transition state **TS-2e** (12.0 kcal·mol^{-1}), in which the $HTBD^+$ protonates the nearest oxygen located in the main chain making an alcohol and a *trans*-limonene carbonate, both of which are represented in structure **D-e** (-4.8 kcal·mol^{-1}).

At this point, the second part of the end-group depolymerization starts, now the main chain is a dimeric unit with the catalyst. The dimer and the TBD are assembled in structure **E-e** (-1.1 kcal·mol^{-1}). The latter is followed by the transition state **TS-3e** (12.0 kcal·mol^{-1}) that describes a deprotonation of the outer oxygen while simultaneously approaching the carbonyl carbon. Intermediate **F-e** (8.4 kcal·mol^{-1}) has a tetrahedral centre, and the catalyst makes hydrogen bonds with two oxygen atoms producing structure **G-e** (10.5 kcal·mol^{-1}), which has the $HTBD^+$ located near the inner oxygen of the chain making a hydrogen bond. The last transition state, **TS-4e**, is the most energetically disfavoured one in this mechanism (18.5 kcal·mol^{-1}) and involves an oxygen protonation by $HTBD^+$ and the release of a second *trans*-limonene carbonate. The last intermediate **H-e** contains the adduct of the trans-LC, limonene glycol and the catalyst TBD with a relative Gibbs free energy of 2.8 kcal·mol^{-1}. The final products are the separated structures of the resultant two molecules of *trans*-LC, limonene glycol and the catalyst TBD, with a total energetic value of 2.4 kcal·mol^{-1}.

The energetic span[67] of this reaction is 23.3 kcal·mol^{-1}, which is totally feasible at 80°C. In summary, the end-group depolymerization of a trimeric model for PLC using TBD as a catalyst at 80°C in acetonitrile solution results into the release of one molecule of limonene glycol, *n trans*-limonene carbonates (depending of the original length of the polymer chain) and the recovered catalyst TBD.

Mechanistic Pathway Structures

For a more detailed analysis of the mechanism depicted in **Figure 7.4**, geometric parameters were illustrated with atom labels to describe their distances or angles related to their reactivity. As described earlier, the end-group depolymerization reaction involves a series of consecutive steps, each set of steps comprise two transition states and four respective intermediates thereby converting one monomer from the polymer chain. In **Figure 7.4** the first set of steps goes from **A-e** to **D-e**, and the second series from **E-e** to **H-e**. Therefore, this section will discuss the first two transition states to comprehend the overall reactivity, as the latter ones are analogous.

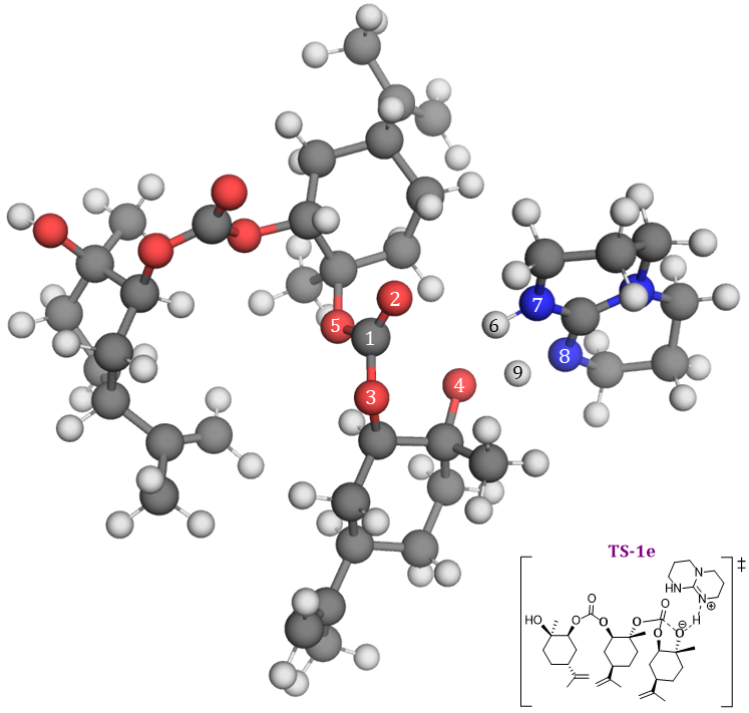

Figure 7.5: Molecular structure for the **TS-1e** shown in **Figure 7.4** including atom labels

The first transition state for the end-group activation mechanism **TS-1e** is presented in **Figure 7.5** and its key bond leghts and angles are detailed in **Ta-**

Table 7.1: Angles and distances for the geometry of **TS-1e** presented in **Figure 7.5**

Atom labels	**Angle (°)**
O3-C1-O4	76.0
O4-H9-N8	166.4
O3-C1-O2	121.3

Atom labels	**Distance (Å)**
C1-O4	2.80
O4-H9	1.36
H9-N8	1.15

ble 7.1. This transition state describes the deprotonation of the terminal alcohol (O4-H9) for the trimer as enabled by the nitrogen N8 from the TBD, while simultaneously the already created alkoxide species (O4) approaches the electrophilic carbonate carbon C1. The deprotonation involving the atoms O4, H9 and N8 shows a near linear arrangement (166.4°). However, this angle is not larger (cf., 180°) as a reaction needs to occur between the alkoxide (O4) and the carbonyl carbon C1, which are at a considerable distance of 2.8 Å (C1-O4). This distance is expected to decrease in the next intermediate when a tetrahedral centre is formed in structure **B-e**.

Table 7.2: Angles and distances for the geometry for the **TS-2e** presented in **Figure 7.6**

Atom labels	**Angle (°)**
O3-C1-O4	108.9
O3-C1-O5	100.6
O5-H9-N8	175.9
O3-C1-O2	121.6

Atom labels	**Distance (Å)**
C1-O4	1.38
C1-O5	1.92
O5-H9	1.56
H9-N8	1.06

The second transition state **TS-2e** from **Figure 7.4** is depicted in **Figure 7.6** and selected geometrical values are given in **Table 7.2**. In this transition state, the nearest oxygen located in the main chain (O5) is protonated by the $HTBD^+$ (H9), releasing a molecule of *trans*-LC and creating a terminal alcohol group in the remaining main chain (O5-H9). The protonation for the alkoxide O5 by H9 from the TBD again tends to form a linear arrangement between O5, H9 and N8 with a value of 175.9°. The other hydrogen H6 from the TBD makes an hydrogen bond with the carbonyl oxygen O2, enhancing its reactivity along this transition state. The angle for O4-C1-O3 (future carbonate in the *trans*-LC) amounts to 108.9°, and then evolves to the last structure **C-e** that includes a

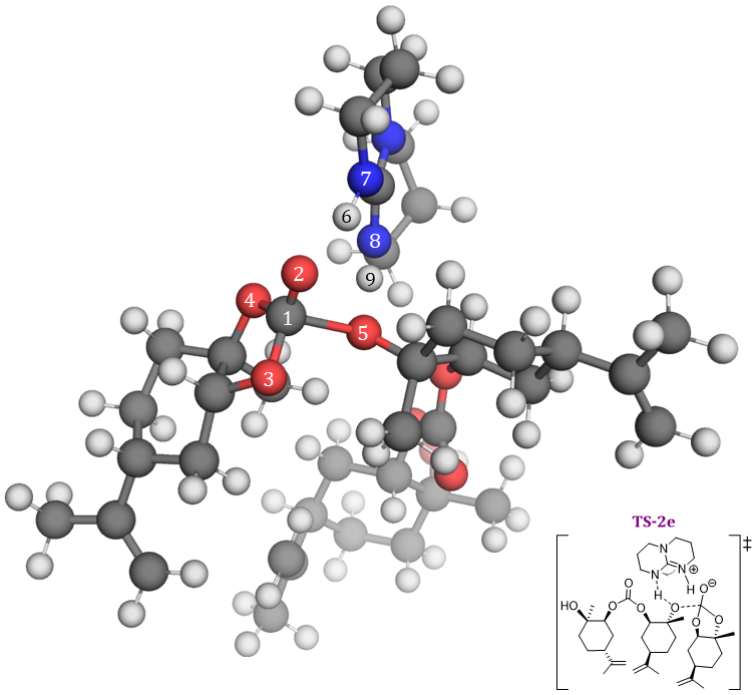

Figure 7.6: Molecular structure for the **TS-2e** shown in **Figure 7.4** including atom labels

tetrahedral carbon centre. However, the angle O3-C1-O5 now measures 100° due to the separation from the main chain, and the bond C1-O5 is 1.92 Å that is significantly longer than the distance between C1-O4 (1.38 Å) just released *trans*-LC.

7.4.2 Main-Chain Scission

The main-chain scission mechanism begins by activating a carbonate carbon of the polymer chain, leading to the rupture of the polymer chain into smaller segments. These segments can, from this moment onwards, undergo either fragmentation through end-group or main-chain scission pathways. The combination of both mechanisms accelerates the depolymerization of the polycarbonate, resulting in the formation of smaller polymer fragments that

will be divided into monomers (*trans*-LC) or limonene oxides (LOs).

The mechanism presented in **Figure 7.7** utilizes H_2O as a simple pronucleophile, which can be activated by TBD through hydrogen bonding. As occasional water is commonly present during these reactions, its low concentration has been shown not to be detrimental for TBD-based depolymerization[237].

The individual structures of the trimer, TBD and H_2O have an energetic value of 8.4 kcal·mol^{-1} over the reference, which is the adduct of these molecules in structure **A-m**. The first transition state, **TS-1m**, is the most energetically disfavoured one in this mechanism with an energetic value of 21.9 kcal·mol^{-1}. The water molecule is deprotonated by TBD, and as a result the hydroxide OH^- (a more productive nucleophile) attacks the carbonate carbon located in the middle of the chain. This reaction results into the intermediate structure **B-m** (16.0 kcal·mol^{-1}) which has a tetrahedral carbon centre due to its previous engagement with the hydroxide. In this latter structure the $HTBD^+$ remains close to the reactive centre due to hydrogen bonds present and involving different oxygen atoms of the carbonate. In the next structure, **C-m** located at 12.4 kcal·mol^{-1}, the $HTBD^+$ is located in a different orientation, thus enabling the geometry towards the following transition state **TS-2m** (15.2 kcal·mol^{-1}). During the second transition state **TS-2m**, the $HTBD^+$ protonates an inner oxygen of the polymer chain, producing a scission in the middle of the trimer, while the other part of the chain separates. The result is structure **D-m**, which is a formal dimer, and the catalyst recovered (TBD) combined with the just created hemi-ester of a carbonic acid derivative. This adduct is more thermodynamically stable than the structures determined before with an energetic value of -7.3 kcal·mol^{-1}. From this point onwards, the studied structures correspond to the monomer with the carbonate acid group, and the further reacting dimer will be considered in all the structures in order to be energetically comparable.

Note that in **Figure 7.7**, the following intermediates and transition states (from structure **D-m** onwards) are energetically more favoured than the ones described before. This variation may be due to the size of the main chain, which in this case is a monomer, hence, the energy values will likely depend on the size of the polycarbonate and exert some degree of entropic influence.

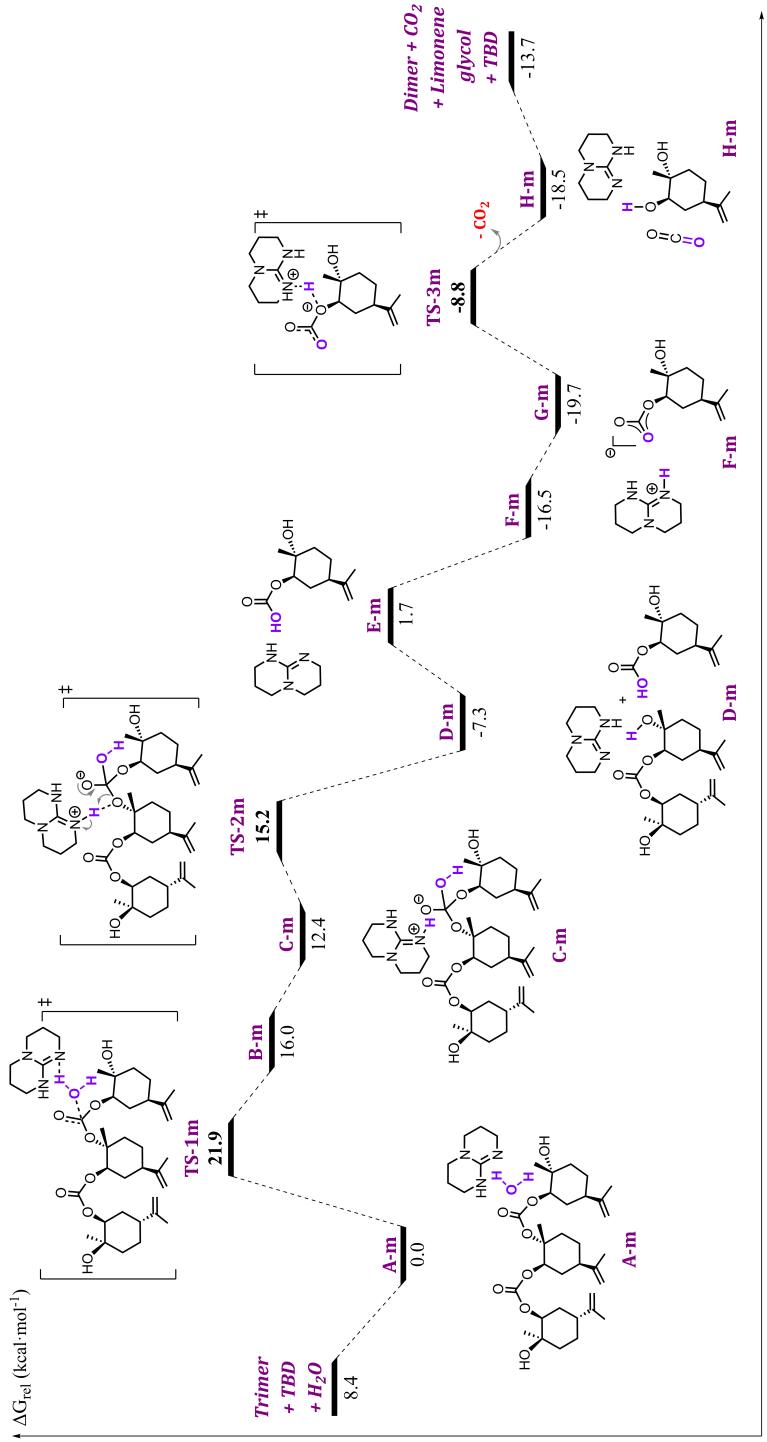

Figure 7.7: Relative Gibbs free energy profile in kcal·mol^{-1} and mechanistic scheme for the main-chain scission depolymerization

The structure **E-m** (1.7 kcal·mol^{-1}) includes the carbonic acid-based molecule and the TBD, that spontaneously evolve into the structure **F-m**, which is their adduct that contains a carbonate group and the protonated catalyst HTBD^{+} located at -16.5 kcal·mol^{-1}, and has a very similar geometry as **G-m** (-19.7 kcal·mol^{-1}). In the latter, the HTBD^{+} has changed its orientation, which in turn allows it to create new hydrogen bonds to enhance the reactivity of importance for the next transition state **TS-3m** (-8.8 kcal·mol^{-1}). During this last transition state, the HTBD^{+} protonates the inner oxygen of the carbonate group, which changing its original angle from ~120° (carbonate) to approximately 180° releasing thereby CO_2. This reaction ends with structure **H-m** (-18.5 kcal·mol^{-1}), which is the adduct of the recovered catalyst TBD, the limonene glycol and the CO_2 molecule. When separated, the addition of these molecules (including the dimer), has an energetic value of -13.7 kcal·mol^{-1}.

The energetic span[67] of this reaction is 21.9 kcal·mol^{-1}, which is completely feasible at 80°C. The mechanistic pathway for the depolymerization via main-chain scission requires a water molecule that behaves as a pronucleophile once its deprotonated by the catalyst to begin the reaction. Once the depolymerization starts, a cascade of reactions occurs to obtain a limonene glycol, a dimer from the cleaved chain, and a CO_2 molecule as products.

Mechanistic Pathway structures

For a more detailed analysis of the main-chain scission reaction, some structures from the overall mechanistic pathway presented in **Figure 7.7** will be discussed in this section to evaluate in more detail their structural parameters.

The first transition state **TS-1m** is presented in **Figure 7.8**, and its selected geometrical parameters are given in **Table 7.3**. This transition state shows a simultaneous reaction that involves a water molecule (H2-O1-H3), which is deprotonated by the N9 atom of TBD while the newly-created hydroxide O1-H2 attacks the carbonate carbon C4 from the trimer. In this structure, the angle in

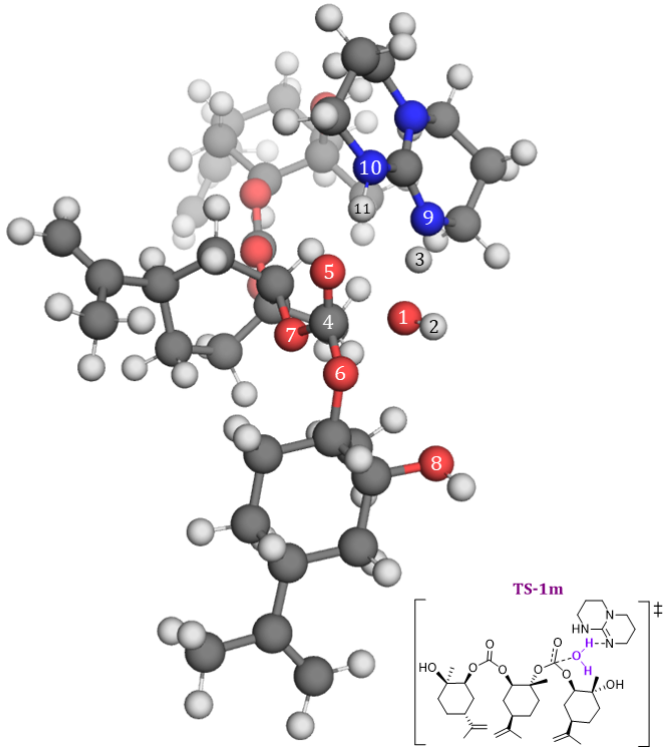

Figure 7.8: Molecular structure for the **TS-1m** presented in **Figure 7.4** including atom labels

Table 7.3: Angles and distances for the geometry for the **TS-1m** presented in **Figure 7.8**

Atom labels	Angle (°)
H2-O1-H3	111.1
O6-C4-O1	99.2
O1-H3-N9	177.0
C4-O1-H3	117.3
O5-H11-N10	164.6

Atom labels	Distance (Å)
O1-C4	1.97
O1-H3	1.50
O1-H2	0.96
H3-N9	1.09
O5-H11	1.79

the interacting water molecule is larger than the theoretical one with a value for H2-O1-H3 being 111.1° as a result of its partial deprotonated character mediated by H-bonding to TBD.

Moreover, the bond distance of O1-H3 is 1.50 Å due to the deprotonation made possible by the N9 atom of TBD with an almost linear arrangement for

O1-H3-N9 (177.0°), while O1-H2 keeps a typical bond length around 0.96 Å, while the O1-H3 bond distance is 1.50 Å due to the (partial) deprotonation enabled by the N9 atom of TBD with an almost linear arrangement for O1-H3-N9 (177.0°). As a consequence, the O1 atom from the alkoxide species comes closer to the carbonate carbon C4 with a distance of 1.97 Å. This interaction will generate a tetrahedral surrounded carbon C4 bound to the oxygens atoms O1, O5, O6 and O7. The angle related with oxygen atom O6 from the carbonate group and the oxygen from the hydroxide (O1) are set up to provide a tetrahedral arrangement around C4 in the next structure B-m (with O6-C4-O1 being 99.2°). Thus, these three molecules are able to react due to the hydrogen bonds made by the hydrogen H11 from the TBD with the oxygen O5 from the carbonate, with an angle O5-H11-N10 amounting to 164.6° and with a distance O5-H11 being 1.79 Å.

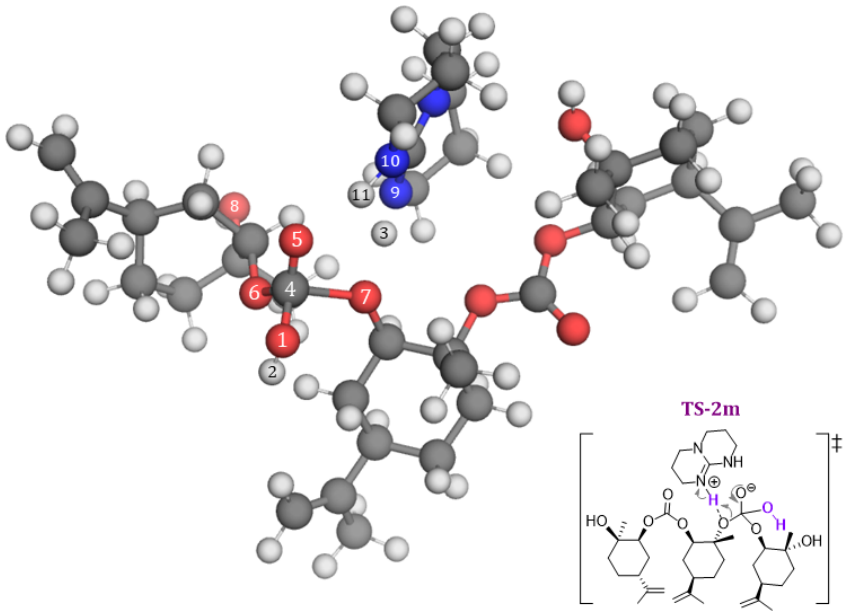

Figure 7.9: Molecular structure for the **TS-2m** presented in **Figure 7.7** including atom labels

The second transition state **TS-2m** presented in **Figure 7.9** and some of its geometrical values are listed in **Table 7.4**. This transition state consists of a

Table 7.4: Angles and distances for the geometry for the **TS-2m** presented in **Figure 7.9**

Atom labels	**Angle (°)**
O1-C4-O7	103.3
O6-C4-O1	108.0
O7-H3-N9	178.5
O5-H11-N10	166.5

Atom labels	**Distance (Å)**
O1-C4	1.36
O7-H3	1.62
C4-O7	1.84
H3-N9	1.05

middle-chain scission providing a dimeric carbonate and a hemi-ester of a carbonic acid derivative. The reaction starts with intermediate **C-m**, which contains a tetrahedral carbon C4 bound to their neighbouring oxygen atoms from the polymer chain (*i.e.*, O6 and O7), and the oxygen O1 from the hydroxide group in **TS-1m**. The scission is clearly observed by following the distance between the C4 carbon and the O7 whose value is 1.84 Å, and the related angles O1-C4-O7 (103.3°) and O6-C4-O1 (108.0°) close to tetrahedral ones. To complete the polymer chain scission, a proton transfer is made by the hydrogen H3 from the $HTBD^+$ and the oxygen atom from one part of the main chain (O7), and the relevant angle (O7-H3-N9) is almost perfectly linear at 178.5°. Additionally, the other hydrogen atom from the $HTBD^+$ (H11) makes a hydrogen bond with the oxygen atom O5 from the original carbonate unit, with an angle O5-H11-N10 being rather linear (166.5°). This hydrogen bond keeps the geometry together as to assist the chain scission.

Table 7.5: Angles and distances for the geometry for the **TS-3m** presented in **Figure 7.10**

Atom labels	**Angle (°)**
O1-C4-O5	160.8
O6-C4-O1	104.1
O6-H11-N10	157.6

Atom labels	**Distance (Å)**
O6-C4	2.18
C4-O5	1.17
O6-H11	1.61

The last transition state **TS-3m** geometry is presented in **Figure7.10** and some of its angles and bonds are added to **Table 7.5**. The outcome is CO_2 release (O1-C4-O5) from O6 in the anionic form of the carbonic acid-based molecule, while simultaneously, the H11 from the $HTBD^+$ protonates the just-

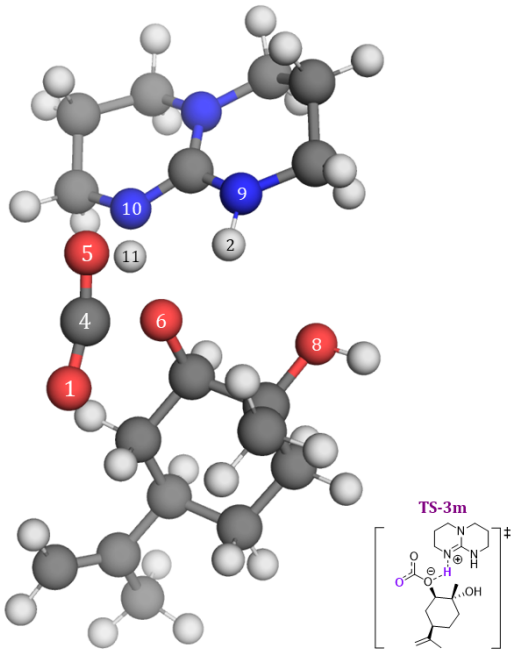

Figure 7.10: Molecular structure for the **TS-3m** presented in **Figure 7.7** including atom labels

created alkoxide O6. The angle from CO_2 O1-C4-O5 is 160.8°, which is somewhat in the middle of a typical trigonal geometry of the carbonate anion form (about 120°), and the final linear configuration of a carbon dioxide molecule, which is around 180°. The angle (O1-C4-O5) shows a geometry closer to that of CO_2 release, with distances for O6-C4 of 2.18 Å, and C4-O5 being 1.17 Å. Additionally, the proton transfer angle between the $HTBD^+$ and the alkoxide (O6-H11-N10) is less linear than compared with the previous angles, with a value of 157.6°. Note that **TS-3m** undergoes a significant geometrical transformation as it represents the transition state between **G-m**, which includes a carbonate anion, and **H-m** that corresponds to limonene glycol and a released CO_2 molecule. As a result, some angles and bonds in the **Figure7.10** lie within the range of these two geometries.

7.4.3 Depolymerization Mechanisms Evaluation

As seen in the sections above, both mechanisms (end-group depolymerization and main-chain scission) are feasible under the conditions reported in **Figure 7.2**, both experimentally and theoretically[237]. Therefore, we expect a combination of both mechanisms during the degradation of the poly(limonene carbonate) chains. In this section, we will briefly discuss the combination of both mechanisms by comparing them.

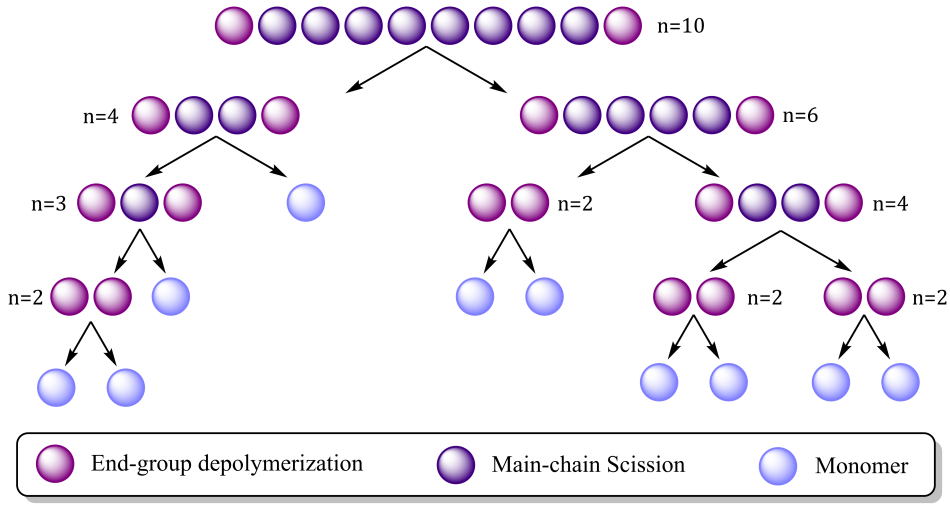

Figure 7.11: Schematic example of the depolymerization of a decamer

The pendent alcohol end-groups of the terminal groups tend to be more reactive, however, at the beginning of the reaction when the polymer chains are long, only two possible reactive sites are available for the end-group depolymerization mechanism. Therefore, the main-chain scission tends to be more easy to initiate the depolymerization, although a water molecule is needed to start the mechanism. To exemplify these concepts, a scheme of the depolymerization of a larger model (a decamer) is presented in **Figure 7.11**. In this schematic representation of the decamer, the violet bubbles represent where the "end-group depolymerization" would take place, the dark-purple bubbles represent where "main-chain scission" can occur, and the light blue bubbles represent the monomers obtained as final products of the depolymerization.

In the initial stage (when n = 10), the oligomeric chain has a higher number of carbonate groups that can participate in main-chain scission, increasing the probability to start cleaving the chain through this mechanism. In the example of **Figure 7.11**, we consider the scission of the decamer into large and unequal chains: a tetramer (n = 4) and a hexamer (n = 6). For the tetramer, it has an equal probability to undergo either mechanism. The end-group depolymerization mechanism (**Figure 7.11**, *left side*) decomposes this oligomer chain first into a trimer (n = 3) and releases a monomer, and subsequently the depolymerization results into a dimer (n = 2) and another respective monomer. For the hexamer, it has more carbonate groups of use for main-chain scission. Thus, we consider an nonsymmetric scission into a dimer (n = 2) and a tetramer (n = 4) (**Figure 7.11**, *right side*). In this case, the tetramer, is cleaved through the main-chain scission mechanism into two dimers, which will be depolymerized into their respective monomers. Taken into account this more complex starting point, there are thus many more combinations possible to break down the polymer chain of PLC.

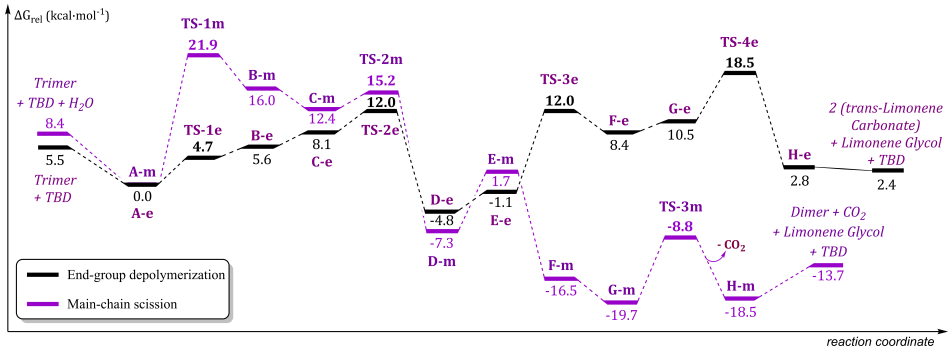

Figure 7.12: Energetic comparison between mechanistic pathways for PLC depolymerization

Energetically, both mechanisms are completely compatible, and in **Figure 7.12**, are presented the energetic profiles for both mechanisms. Note that the reference value for **A-m** includes the adduct of the trimer, the catalyst and a water molecule,while the **A-e** just includes the trimer and the catalyst. Despite the

fact that these mechanistic pathways are different, the energy spans for both reactions are very similar, 23.3 kcal·mol^{-1} for end-group based depolymerization and 21.9 kcal·mol^{-1} for main-chain scission based mechanism.

These energy span values demonstrate the feasibility of both processes according to experimental results. Moreover, a combination of both pathways is plausible, as the intermediate alcohol-terminated species produced through the main-chain scission mechanism can subsequently participate in end-group activation by TBD to further promoted polymer backbiting.

7.5 Conclusions

This chapter aims to understand the mechanistic pathways involved in the depolymerization process of polycarbonate derived from *trans*-(Limonene carbonate) (PLC) using TBD as a catalyst at 80°C in acetonitrile solution, exploring two different mechanisms: end-group depolymerization and main-chain scission. Both mechanisms were investigated through DFT calculations supported by experimental results obtained by various Kleij group members.

On one hand, the end-group depolymerization starts at the terminal alcohol of the polymer chain, initiating the decomposition of the PLC via a known backbiting reaction. On the other hand, the main-chain scission mechanism commences at a random position in the middle of the polymer chain, needs a (protic) water molecule as a pronucleophile, and splits the polymer chain into smaller segments. Both mechanisms are feasible under the conditions reported above, with energetic spans of 23.3 kcal·mol^{-1} for end-group depolymerization, and 21.9 kcal·mol^{-1} for main-chain scission mechanism. Therefore, this mechanistic study has unveiled new potential for polycarboante depolymerization through the combination of both end-group activation and main chain scission pathways.

Additionally, experimental studies evaluated the suitability of regenerating PLC from *trans*-LC via ROP using TBD, BnOH as an initiator in toluene solution at 80°C. The results demonstrate that PLC can be reformed and a combination of NMR and GPC analysis suggests that original polymer characteristics can be

preserved.

In conclusion, an efficient catalytic process for depolymerizing PLC using TBD as a versatile organocatalyst has been discovered. Mechanistic studies based on DFT calculations reveal that degradation of PLC can occur through the combination of end-group activation and/or a main chain scission pathway. Moreover, from the resultant *trans*-LC, repolymerization was successfully demonstrated using the same organocatalyst. All of these results represent a significant advancement in the recycling of PLC and more generally of polycarbonates, and a step closer to a circular use for these types of macromolecules.

CHAPTER

8 Summary and general conclusions

The work described in this thesis focuses on the recycling and circular use of CO_2 at by means of DFT calculations and reactivity prediction models. Carbon dioxide can be used as a renewable agent to synthesise cyclic carbonates that can be potentially polymerized into polycarbonates, which themselves may be depolymerized into its precursors. Each chapter in this thesis studies a step of this circular process, starting with the conversion of CO_2 into five-membered cyclic carbonates (5MCCs) from alkyne-1,2-diols using a Ag-based catalyst (**Chapter 4**). Then, the creation of larger carbonate rings such as six-membered cyclic carbonates (6MCC) from smaller ones (5MCC) with a unique organocatalytic strategy empowered by TBD (**Chapter 5**) was investigated. An extensive study of the Ring-Opening Polymerization (ROP) reaction for cyclic carbonates was performed exploring the mechanistic pathways of a wide range of monomers to generate a predictive reactivity plot to determine which monomers are prone to be polymerized and which are not (**Chapter 6**). Finally, a polycarbonate depolymerization mechanism catalyzed by TBD that selectively breaks down the polymer chain into a trans-cyclic carbonate, or an epoxide and CO_2, was studied (**Chapter 7**)).

In **Chapter 4: Using CO_2 to obtain Five-Membered Cyclic Carbonates with a Silver-based Catalyst** the mechanistic pathway involved in the synthesis of keto-substituted five-membered cyclic carbonates using alkyne-1,2-diol and CO_2 as a reactants, and promoted by a Ag-based catalyst was investigated. The catalyst is composed by a Buchwald phosphine-ligand (DavePhos or BrettPhos) coordinated to a silver(I) salt (AgOAc), and the substrate has a chiral centre, therefore, all possibilities were considered in the computational study, and were possible, supported by experimental data provided by Xuetong Li, offering a complete understanding of this reaction. For all mechanisms, the *R*-configured substrate is energetically more favoured than its *S*-isomer. The determining transition state for both the *R*- and *S*-pathway corresponds to a cyclic carbonate ring closure with an *E*-configuration which is energetically more favoured than the *Z* one. The mechanistic pathways catalysed by Ag(BrettPhos)OAc are energetically more accessible and follow very similar

manifolds compared to those promoted by Ag(DavePhos)OAc. Previous studies reported in the literature describe the formation of an α-alkylidene carbonate as the final product when using the same catalyst with a simple propargylic alcohol substrate. However, when using the alkyne-1,2-diol, the α–alkylidene carbonate is an intermediate. DFT studies reveal that this occurs due to the higher thermodynamic stability of the keto-carbonate (i.e., the final product), which aligns well with the experimental data.

In **Chapter 5: From Five- to Six-Membered Cyclic Carbonates** a unique organocatalytic manifold is described for the formation of six-membered cyclic carbonates (6MCCs) starting from five-membered cyclic carbonates (5MCCs) with a tertiary alcohol group, acetyl imidazole (AcIm) as an acylating agent and catalysed by 1,5,7-triazabicyclodec-5-ene (TBD) under mild conditions. DFT calculations were performed to study the mechanistic pathway involved in this reaction reinforced by experimental data provided by Chang Qiao. The overall mechanistic pathway can be described as an isomerization followed by O-acylation, and all intermediates and transition states are in a dynamic equilibrium until the 6MCC is acylated resulting in a thermodynamically highly stable product. The rate-determining transition state corresponds to the isomerization step, where the intermediate that has a tetrahedral carbon centre, is transformed from a 5MCC into a 6MCC. Alternative routes such as the "acylation of 5MCC" and the "isomerization of the initial 5MCC into a7MCC" were also investigated, but not being energetically feasible, concurring with control experiments.

In **Chapter 6: Ring-Opening Polymerization**, an extensive study of the Ring-Opening Polymerization (ROP) of cyclic carbonates has unravelled an overall mechanistic pathways for a wide range of monomers, and allowed to create a predictive reactivity plot.

- The ROP reaction of cyclic carbonates uses TBD as a catalyst, and benzyl alcohol (BnOH) as an initiator under mild conditions (r.t.). The mecha-

nistic pathway consists of an initiation step followed by multiple propagation steps. Each step involves two phases, an initiation or propagation, accompanied by ring-opening. The catalyst (TBD) is bifunctional, which is crucial throughout the reaction manifold since it can act both as a base and a proton-relay species with multiple H-bonding being important. To evaluate the ring strain effect, the ROP reaction for structurally related 5MCC, 6MCC and 7MCC were calculated and compared. The results coincide with the experimental behaviour reported in the literature: larger rings tend to provide energetically more favoured ROP potential in each consecutive propagation and tend to be exergonic, while the ROP for the 5MCC tends to be opposite (i.e., endergonic).

- A useful predictive reactivity plot was designed by plotting the energy span of the ROP reaction on the y-axis against the polymer stability on the x-axis. Monomers that are more favourable for the ROP reaction are positioned more diagonally left-down on the plot. Monomers experimentally tested under the same conditions by various Kleij group members were utilized to validate the theoretical model by experimental data.

- The number of substituents plays a key role in the ROP reaction. Therefore, the optimal number of substituents in the cyclic carbonate allowed for an effective ROP reaction was examined, by adding up to six methyl substituents to various positions on the 6MCC ring. The monomers that are most substituted (with 4 to 6 substituents) do not show ROP potential under the ambient temperature conditions, and their data points are all located in an unfavourable region in the predictive plot. Tri-substituted monomers are shown to be typically not reactive enough for ROP, though some of these provide data points that are placed close to the boundary. Monomers with two substituents are located in a favourable region except for one example placed close to the boundary of the ROP region. The disposition of the substituents for di- and tri- substituted monomers has an important role, and in general the symmetrical disposition of groups

is more favoured. The mono- and unsubstituted monomers are placed in a highly favourable segment of the ROP region in the predictive plot.

- To evaluate the effect of the chemical nature and size of the substituents in the ROP reaction, mono- and di-substituted six-membered cyclic carbonates with their substituents located in the same position on the ring were studied. These calculations show that the number of substituents and their positional symmetry in the ring have a more important role than their chemical nature or their size.

- Some 5MCCs and 7MCCs were further considered. As expected, the smaller ring 5MCCs are located in a region of the plot that does not support ROP ability. The exception to this are 5MCCs with a fused ring, which are clearly prone to ROP due to their higher ring strain. The 7MCCs are all located in an energetically favoured location in the predictive plot, which concurs with their experimentally observed behaviour reported in the literature.

- Certain polymers were recalculated using a different procedure to verify the data related with the polymer stability. This alternative method has as an output the average Gibbs Free energy, which tends to yield (slightly) more stable values within a narrow range of a few kcal·mol^{-1}. Therefore, the Gibbs free energies, along with the standard state entropic corrections, describes adequately enough the preselected dimer formation without the high computational cost associated with focusing on averaged Gibbs free energies.

In **Chapter 7: Depolymerization**, the mechanistic pathways involved in the depolymerization of poly(limonene carbonate), abbreviated as PLC, using TBD as a catalyst is presented by exploring two different mechanisms: (1) end-group based depolymerization, and (2) main-chain scission. Both mechanisms were investigated through DFT calculations supported by experimental data obtained from David Lamparelli. The combination of these mechanisms offers a

successful and efficient depolymerization that results into an appreciable yield of *trans*-limonene-carbonates (i.e., ROP monomers), and limonene-oxides and CO_2 as alternative/side products. The *trans*-configured cyclic carbonate obtained can be re-polymerized into PLC via ROP using the same organocatalyst, and this depolymerization/repolymerization sequence is a nice example of a potential circular use of polycarbonates.

Overall, the **General Conclusion** from the thesis work is that computational analysis of CO_2 valorization and recycling processes is of high value to offer not only a way to rationalize details of the operating manifolds that are not easily accessible via experimental techniques, but also help to establish new discoveries of mechanistic divergences and estimating the value of the mechanistic information in a wider context. For instance, the depolymerization of polycarbonates is gaining momentum, and the information gathered in **Chapter 7** of this thesis has unfolded new potential of catalysis as a key enabling tool in polymer/material recycling. This thesis also stresses the complementarity between both experimental and computational methods, and is clearly a powerful combination to address the future problems we have ahead of us.

Bibliography

[1] E. Parliament, Greenhouse Gas Emissions by Country and Sector (Infographic), https://www.europarl.europa.eu/topics/en/article/20180301STO98928/greenho gas-emissions-by-country-and-sector-infographic, **2018**.

[2] E. Parliament, Climate Change in Europe: Facts and Figures, https://www.europarl.europa.e change-in-europe-facts-and-figures, **2018**.

[3] E. Parliament, Circular Economy: Definition, Importance and Benefits, https://www.europarl.europa.eu/topics/en/article/20151201STO05603/circular-economy-definition-importance-and-benefits, **2023**.

[4] T. H. Levere, *Transforming Matter: A History of Chemistry from Alchemy to the Buckyball*, Johns Hopkins University Press, Baltimore, **2001**.

[5] P. W. Atkins, S. Cwi, *Química Física*, 8a ed, Editorial Médica Panamericana, Buenos Aires, **2008**.

[6] *Homogeneous Catalysis: Understanding the Art*, Springer Netherlands, Dordrecht, **2004**.

[7] S. Wu, R. Snajdrova, J. C. Moore, K. Baldenius, U. T. Bornscheuer, *Angewandte Chemie International Edition* **2021**, *60*, 88–119.

[8] E. Roduner, *Chem. Soc. Rev.* **2014**, *43*, 8226–8239.

[9] H. Cao, S. Liu, X. Wang, *Green Chemical Engineering* **2022**, *3*, 111–124.

[10] D. W. C. MacMillan, *Nature* **2008**, *455*, 304–308.

[11] M. H. Aukland, B. List, *Pure and Applied Chemistry* **2021**, *93*, 1371–1381.

[12] E. Fritz-Langhals, *Organic Process Research & Development* **2022**, *26*, 3015–3023.

[13] J. G. Kim, G. S. Lee, A. Lee, *Journal of Polymer Science* **2023**, pol.20230643.

[14] N. P. Outreach, The Nobel Prize in Chemistry 2013 Was Awarded Jointly to Martin Karplus, Michael Levitt and Arieh Warshel "for the Development of Multiscale Models for Complex Chemical Systems", https://www.nobelprize. **2013**.

[15] A. J. Kamphuis, F. Picchioni, P. P. Pescarmona, *Green Chemistry* **2019**, *21*, 406–448.

[16] P. Rollin, L. K. Soares, A. M. Barcellos, D. R. Araujo, E. J. Lenardão, R. G. Jacob, G. Perin, *Applied Sciences* **2021**, *11*, 5024.

[17] A.-A. G. Shaikh, S. Sivaram, *Chemical Reviews* **1996**, *96*, 951–976.

[18] P. P. Pescarmona, *Current Opinion in Green and Sustainable Chemistry* **2021**, *29*, 100457.

[19] L. Guo, K. J. Lamb, M. North, *Green Chemistry* **2021**, *23*, 77–118.

[20] J. L. Hedrick, V. Piunova, N. H. Park, T. Erdmann, P. L. Arrechea, *ACS Macro Letters* **2022**, *11*, 368–375.

[21] Á. Mesías-Salazar, Y. R. Yepes, J. Martínez, R. S. Rojas, *Catalysts* **2020**, *11*, 2.

[22] F. D. Bobbink, W. Gruszka, M. Hulla, S. Das, P. J. Dyson, *Chemical Communications* **2016**, *52*, 10787–10790.

[23] M. Honda, M. Tamura, K. Nakao, K. Suzuki, Y. Nakagawa, K. Tomishige, *ACS Catalysis* **2014**, *4*, 1893–1896.

[24] G. L. Gregory, M. Ulmann, A. Buchard, *RSC Advances* **2015**, *5*, 39404–39408.

[25] J. L. Payne, Z. Deng, A. L. Flach, J. N. Johnston, *Chemical Science* **2022**, *13*, 7318–7324.

[26] S. Minakata, I. Sasaki, T. Ide, *Angewandte Chemie International Edition* **2010**, *49*, 1309–1311.

[27] J. Rintjema, W. Guo, E. Martin, E. C. Escudero-Adán, A. W. Kleij, *Chemistry – A European Journal* **2015**, *21*, 10754–10762.

[28] C. Qiao, W. Shi, A. Brandolese, J. Benet-Buchholz, E. C. Escudero-Adán, A. W. Kleij, *Angewandte Chemie International Edition* **2022**, *61*, e202205053.

[29] S. Dabral, B. Bayarmagnai, M. Hermsen, J. Schießl, V. Mormul, A. S. K. Hashmi, T. Schaub, *Organic Letters* **2019**, *21*, 1422–1425.

[30] N. Ajellal, J.-F. Carpentier, C. Guillaume, S. M. Guillaume, M. Helou, V. Poirier, Y. Sarazin, A. Trifonov, *Dalton Transactions* **2010**, *39*, 8363.

[31] N. E. Kamber, W. Jeong, R. M. Waymouth, R. C. Pratt, B. G. G. Lohmeijer, J. L. Hedrick, *Chemical Reviews* **2007**, *107*, 5813–5840.

[32] S. Liu, C. Ren, N. Zhao, Y. Shen, Z. Li, *Macromolecular Rapid Communications* **2018**, *39*, 1800485.

[33] P. Olsén, K. Odelius, A.-C. Albertsson, *Biomacromolecules* **2016**, *17*, 699–709.

[34] C. Bonduelle, B. Martín-Vaca, F. P. Cossío, D. Bourissou, *Chemistry – A European Journal* **2008**, *14*, 5304–5312.

[35] F. Nederberg, B. G. G. Lohmeijer, F. Leibfarth, R. C. Pratt, J. Choi, A. P. Dove, R. M. Waymouth, J. L. Hedrick, *Biomacromolecules* **2007**, *8*, 153–160.

[36] J. Matsuo, F. Sanda, T. Endo, *Macromolecular Chemistry and Physics* **1998**, *199*, 97–102.

[37] J. Matsuo, F. Sanda, T. Endo, *Macromolecular Chemistry and Physics* **2000**, *201*, 585–596.

[38] W. Yu, E. Maynard, V. Chiaradia, M. C. Arno, A. P. Dove, *Chemical Reviews* **2021**, *121*, 10865–10907.

[39] *Organic Catalysis for Polymerisation*, (Eds.: A. Dove, H. Sardon, S. Naumann), Royal Society of Chemistry, London, **2019**.

[40] J. Matsuo, F. Sanda, T. Endo, *Journal of Polymer Science Part A: Polymer Chemistry* **1997**, *35*, 1375–1380.

[41] X. Zhang, M. Cai, Z. Zhong, R. Zhuo, *Macromolecular Rapid Communications* **2012**, *33*, 693–697.

[42] S.-H. Pyo, P. Persson, M. A. Mollaahmad, K. Sörensen, S. Lundmark, R. Hatti-Kaul, *Pure and Applied Chemistry* **2011**, *84*, 637–661.

[43] R. Wu, T. F. Al-Azemi, K. S. Bisht, *Biomacromolecules* **2008**, *9*, 2921–2928.

[44] L. Mespouille, O. Coulembier, M. Kawalec, A. P. Dove, P. Dubois, *Progress in Polymer Science* **2014**, *39*, 1144–1164.

[45] R. A. Clark, M. P. Shaver, *Chemical Reviews* **2024**, *124*, 2617–2650.

[46] R. Geyer, J. R. Jambeck, K. L. Law, *Science Advances* **2017**, *3*, e1700782.

[47] H. Auta, C. Emenike, S. Fauziah, *Environment International* **2017**, *102*, 165–176.

[48] E. Parliament, Microplastics: Sources, Effects and Solutions, https://www.europarl.eu sources-effects-and-solutions, **2018**.

[49] M. S. Savoca, A. G. McInturf, E. L. Hazen, *Global Change Biology* **2021**, *27*, 2188–2199.

[50] C. A. Velis, E. Cook, *Environmental Science & Technology* **2021**, *55*, 7186–7207.

[51] OECD, *Global Plastics Outlook: Economic Drivers, Environmental Impacts and Policy Options*, OECD, **2022**.

[52] K. Ragaert, L. Delva, K. Van Geem, *Waste Management* **2017**, *69*, 24–58.

[53] D. G. Bucknall, *Philosophical Transactions of the Royal Society A: Mathematical Physical and Engineering Sciences* **2020**, *378*, 20190268.

[54] G. W. Coates, Y. D. Y. L. Getzler, *Nature Reviews Materials* **2020**, *5*, 501–516.

[55] F. Jensen, *Introduction to Computational Chemistry*, 2nd ed, John Wiley & Sons, Chichester, England, **2007**.

[56] A. Szabo, N. S. Ostlund, *Modern Quantum Chemistry: Introduction to Advanced Electronic Structure Theory*, Dover Publications, Mineola, N.Y, **1996**.

[57] J. Bertran Rusca, *Química cuántica: fundamentos y aplicaciones computacionales*, Síntesis, Madrid, **2002**.

[58] E. Schrödinger, *Annalen der Physik* **1926**, *384*, 361–376.

[59] M. Born, R. Oppenheimer, *Annalen der Physik* **1927**, *389*, 457–484.

[60] M. Yanez, R. J. Boyd, *Comprehensive Computational Chemistry*, Elsevier, Amsterdam, **2024**.

[61] J. Tomasi, B. Mennucci, R. Cammi, *Chemical Reviews* **2005**, *105*, 2999–3094.

[62] M. J. Frisch et al., Gaussian~16 Revision A.03, Gaussian Inc. Wallingford CT, **2016**.

[63] S. Miertuš, E. Scrocco, J. Tomasi, *Chemical Physics* **1981**, *55*, 117–129.

[64] M. Cossi, V. Barone, R. Cammi, J. Tomasi, *Chemical Physics Letters* **1996**, *255*, 327–335.

[65] A. V. Marenich, C. J. Cramer, D. G. Truhlar, *The Journal of Physical Chemistry B* **2009**, *113*, 6378–6396.

[66] M. Besora, F. Maseras, *WIREs Computational Molecular Science* **2018**, *8*, e1372.

[67] S. Kozuch, *WIREs Computational Molecular Science* **2012**, *2*, 795–815.

[68] S. Kozuch, S. Shaik, *Accounts of Chemical Research* **2011**, *44*, 101–110.

[69] *Proceedings of the Royal Society of London. Series A - Mathematical and Physical Sciences* **1935**, *150*, 9–33.

[70] S. F. Sousa, P. A. Fernandes, M. J. Ramos, *The Journal of Physical Chemistry A* **2007**, *111*, 10439–10452.

[71] W. Koch, M. C. Holthausen, *A Chemist's Guide to Density Functional Theory*, 1st ed., Wiley, **2001**.

[72] P. Hohenberg, W. Kohn, *Physical Review* **1964**, *136*, B864–B871.

[73] W. Kohn, L. J. Sham, *Physical Review* **1965**, *140*, A1133–A1138.

[74] J.-D. Chai, M. Head-Gordon, *Physical Chemistry Chemical Physics* **2008**, *10*, 6615.

[75] J. P. Perdew, K. Burke, M. Ernzerhof, *Physical Review Letters* **1996**, *77*, 3865–3868.

[76] F. Weigend, R. Ahlrichs, *Physical Chemistry Chemical Physics* **2005**, *7*, 3297.

[77] A. Hellweg, D. Rappoport, *Physical Chemistry Chemical Physics* **2015**, *17*, 1010–1017.

[78] J. P. Perdew in AIP Conference Proceedings, *Vol. 577*, AIP, Antwerp (Belgium), **2001**, pp. 1–20.

[79] S. Grimme, *Journal of Computational Chemistry* **2006**, *27*, 1787–1799.

[80] S. Grimme, J. Antony, S. Ehrlich, H. Krieg, *The Journal of Chemical Physics* **2010**, *132*, 154104.

[81] S. Grimme, S. Ehrlich, L. Goerigk, *Journal of Computational Chemistry* **2011**, *32*, 1456–1465.

[82] C. Bannwarth, S. Ehlert, S. Grimme, *Journal of Chemical Theory and Computation* **2019**, *15*, 1652–1671.

[83] S. Grimme, C. Bannwarth, P. Shushkov, *Journal of Chemical Theory and Computation* **2017**, *13*, 1989–2009.

[84] T. Keijer, V. Bakker, J. C. Slootweg, *Nature Chemistry* **2019**, *11*, 190–195.

[85] J. Cantzler, F. Creutzig, E. Ayargarnchanakul, A. Javaid, L. Wong, W. Haas, *Environmental Research Letters* **2020**, *15*, 123001.

[86] E. C. D. Tan, P. Lamers, *Frontiers in Sustainability* **2021**, *2*, 701509.

[87] *Advances in Carbon Management Technologies: Volume 2, Biomass Utilization, Manufacturing, and Electricity Management*, First, (Eds.: S. K. Sikdar, F. Princiotta), CRC Press Taylor & Francis Group, Boca Raton, **2021**.

[88] C. Qiao, A. Villar-Yanez, J. Sprachmann, B. Limburg, C. Bo, A. W. Kleij, *Angewandte Chemie International Edition* **2020**, *59*, 18446–18451.

[89] C. Maquilón, F. Della Monica, B. Limburg, A. W. Kleij, *Advanced Synthesis & Catalysis* **2021**, *363*, 4033–4040.

[90] T. M. McGuire, C. Pérale, R. Castaing, G. Kociok-Köhn, A. Buchard, *Journal of the American Chemical Society* **2019**, *141*, 13301–13305.

[91] T. M. McGuire, E. M. López-Vidal, G. L. Gregory, A. Buchard, *Journal of CO2 Utilization* **2018**, *27*, 283–288.

[92] J. Vaitla, Y. Guttormsen, J. K. Mannisto, A. Nova, T. Repo, A. Bayer, K. H. Hopmann, *ACS Catalysis* **2017**, *7*, 7231–7244.

[93] W. Guo, V. Laserna, J. Rintjema, A. W. Kleij, *Advanced Synthesis & Catalysis* **2016**, *358*, 1602–1607.

[94] C. Lescot, D. U. Nielsen, I. S. Makarov, A. T. Lindhardt, K. Daasbjerg, T. Skrydstrup, *Journal of the American Chemical Society* **2014**, *136*, 6142–6147.

[95] P. K. Sahoo, Y. Zhang, S. Das, *ACS Catalysis* **2021**, *11*, 3414–3442.

[96] J. Rintjema, R. Epping, G. Fiorani, E. Martín, E. C. Escudero-Adán, A. W. Kleij, *Angewandte Chemie International Edition* **2016**, *55*, 3972–3976.

[97] M. Aresta, A. Dibenedetto, A. Angelini, *Chemical Reviews* **2014**, *114*, 1709–1742.

[98] J. Klankermayer, S. Wesselbaum, K. Beydoun, W. Leitner, *Angewandte Chemie International Edition* **2016**, *55*, 7296–7343.

[99] S. Dabral, T. Schaub, *Advanced Synthesis & Catalysis* **2019**, *361*, 223–246.

[100] W. Guo, J. E. Gómez, À. Cristòfol, J. Xie, A. W. Kleij, *Angewandte Chemie International Edition* **2018**, *57*, 13735–13747.

[101] V. Laserna, E. Martin, E. C. Escudero-Adán, A. W. Kleij, *ACS Catalysis* **2017**, *7*, 5478–5482.

[102] Q. Liu, L. Wu, R. Jackstell, M. Beller, *Nature Communications* **2015**, *6*, 5933.

[103] L. Zuo, T. Liu, X. Chang, W. Guo, *Molecules* **2019**, *24*, 3930.

[104] S. R. Lingampalli, M. M. Ayyub, C. N. R. Rao, *ACS Omega* **2017**, *2*, 2740–2748.

[105] S. Nitopi, E. Bertheussen, S. B. Scott, X. Liu, A. K. Engstfeld, S. Horch, B. Seger, I. E. L. Stephens, K. Chan, C. Hahn, J. K. Nørskov, T. F. Jaramillo, I. Chorkendorff, *Chemical Reviews* **2019**, *119*, 7610–7672.

[106] Q.-W. Song, Z.-H. Zhou, L.-N. He, *Green Chemistry* **2017**, *19*, 3707–3728.

[107] A. Tortajada, F. Juliá-Hernández, M. Börjesson, T. Moragas, R. Martin, *Angewandte Chemie International Edition* **2018**, *57*, 15948–15982.

[108] R. R. Shaikh, S. Pornpraprom, V. D'Elia, *ACS Catalysis* **2018**, *8*, 419–450.

[109] J. W. Comerford, I. D. V. Ingram, M. North, X. Wu, *Green Chemistry* **2015**, *17*, 1966–1987.

[110] M. Alves, B. Grignard, R. Mereau, C. Jerome, T. Tassaing, C. Detrembleur, *Catalysis Science & Technology* **2017**, *7*, 2651–2684.

[111] B. Yu, L.-N. He, *ChemSusChem* **2015**, *8*, 52–62.

[112] A. J. Kamphuis, F. Picchioni, P. P. Pescarmona, *Green Chemistry* **2019**, *21*, 406–448.

[113] F. Della Monica, A. W. Kleij, *Catalysis Science & Technology* **2020**, *10*, 3483–3501.

[114] B. Limburg, À. Cristòfol, F. Della Monica, A. W. Kleij, *ChemSusChem* **2020**, *13*, 6056–6065.

[115] A. Cai, A. W. Kleij, *Angewandte Chemie International Edition* **2019**, *58*, 14944–14949.

[116] À. Cristòfol, B. Limburg, A. W. Kleij, *Angewandte Chemie International Edition* **2021**, *60*, 15266–15270.

[117] B. Grignard, S. Gennen, C. Jérôme, A. W. Kleij, C. Detrembleur, *Chemical Society Reviews* **2019**, *48*, 4466–4514.

[118] N. Yadav, F. Seidi, D. Crespy, V. D'Elia, *ChemSusChem* **2019**, *12*, 724–754.

[119] F. Monie, B. Grignard, J.-M. Thomassin, R. Mereau, T. Tassaing, C. Jerome, C. Detrembleur, *Angewandte Chemie International Edition* **2020**, *59*, 17033–17041.

[120] G. L. Gregory, G. Kociok-Köhn, A. Buchard, *Polymer Chemistry* **2017**, *8*, 2093–2104.

[121] A. Gomez-Lopez, S. Panchireddy, B. Grignard, I. Calvo, C. Jerome, C. Detrembleur, H. Sardon, *ACS Sustainable Chemistry & Engineering* **2021**, *9*, 9541–9562.

[122] R. Huang, J. Rintjema, J. González-Fabra, E. Martín, E. C. Escudero-Adán, C. Bo, A. Urakawa, A. W. Kleij, *Nature Catalysis* **2018**, *2*, 62–70.

[123] S. Sopeña, M. Cozzolino, C. Maquilón, E. C. Escudero-Adán, M. Martínez Belmonte, A. W. Kleij, *Angewandte Chemie International Edition* **2018**, *57*, 11203–11207.

[124] Z.-H. Zhou, Q.-W. Song, L.-N. He, *ACS Omega* **2017**, *2*, 337–345.

[125] J.-Y. Li, L.-H. Han, Q.-C. Xu, Q.-W. Song, P. Liu, K. Zhang, *ACS Sustainable Chemistry & Engineering* **2019**, *7*, 3378–3388.

[126] H. Zhou, H. Zhang, S. Mu, W.-Z. Zhang, W.-M. Ren, X.-B. Lu, *Green Chemistry* **2019**, *21*, 6335–6341.

[127] P. Von Ragué Schleyer, *Journal of the American Chemical Society* **1961**, *83*, 1368–1373.

[128] R. M. Beesley, C. K. Ingold, J. F. Thorpe, *J. Chem. Soc. Trans.* **1915**, *107*, 1080–1106.

[129] M. E. Jung, *Synlett* **1990**, *1990*, 186–190.

[130] X. Li, A. Villar-Yanez, C. Ngassam Tounzoua, J. Benet-Buchholz, B. Grignard, C. Bo, C. Detrembleur, A. W. Kleij, *ACS Catalysis* **2022**, *12*, 2854–2860.

[131] T. Gavin Williams, A. K. Wilson, *The Journal of Chemical Physics* **2008**, *129*, 054108.

[132] M. Ernzerhof, G. E. Scuseria, *The Journal of Chemical Physics* **1999**, *110*, 5029–5036.

[133] S. Grimme, S. Ehrlich, L. Goerigk, *Journal of Computational Chemistry* **2011**, *32*, 1456–1465.

[134] S. Grimme, J. Antony, S. Ehrlich, H. Krieg, *The Journal of Chemical Physics* **2010**, *132*, 154104.

[135] M. Álvarez-Moreno, C. De Graaf, N. López, F. Maseras, J. M. Poblet, C. Bo, *Journal of Chemical Information and Modeling* **2015**, *55*, 95–103.

[136] J. Artz, T. E. Müller, K. Thenert, J. Kleinekorte, R. Meys, A. Sternberg, A. Bardow, W. Leitner, *Chemical Reviews* **2018**, *118*, 434–504.

[137] S. Liu, L. R. Winter, J. G. Chen, *ACS Catalysis* **2020**, *10*, 2855–2871.

[138] M. B. Ross, P. De Luna, Y. Li, C.-T. Dinh, D. Kim, P. Yang, E. H. Sargent, *Nature Catalysis* **2019**, *2*, 648–658.

[139] A. Goeppert, M. Czaun, J.-P. Jones, G. K. Surya Prakash, G. A. Olah, *Chem. Soc. Rev.* **2014**, *43*, 7995–8048.

[140] A. J. Kamphuis, F. Picchioni, P. P. Pescarmona, *Green Chemistry* **2019**, *21*, 406–448.

[141] B. Grignard, S. Gennen, C. Jérôme, A. W. Kleij, C. Detrembleur, *Chemical Society Reviews* **2019**, *48*, 4466–4514.

[142] S. J. Poland, D. J. Darensbourg, *Green Chem.* **2017**, *19*, 4990–5011.

[143] S. Paul, Y. Zhu, C. Romain, R. Brooks, P. K. Saini, C. K. Williams, *Chemical Communications* **2015**, *51*, 6459–6479.

[144] Q. Liu, L. Wu, R. Jackstell, M. Beller, *Nature Communications* **2015**, *6*, 5933.

[145] W. Guo, J. E. Gómez, À. Cristòfol, J. Xie, A. W. Kleij, *Angewandte Chemie International Edition* **2018**, *57*, 13735–13747.

[146] L. Song, Y.-X. Jiang, Z. Zhang, Y.-Y. Gui, X.-Y. Zhou, D.-G. Yu, *Chemical Communications* **2020**, *56*, 8355–8367.

[147] A. Tortajada, F. Juliá-Hernández, M. Börjesson, T. Moragas, R. Martin, *Angewandte Chemie International Edition* **2018**, *57*, 15948–15982.

[148] W. Guo, V. Laserna, J. Rintjema, A. W. Kleij, *Advanced Synthesis & Catalysis* **2016**, *358*, 1602–1607.

[149] D. U. Nielsen, X.-M. Hu, K. Daasbjerg, T. Skrydstrup, *Nature Catalysis* **2018**, *1*, 244–254.

[150] G. Fiorani, M. Stuck, C. Martín, M. M. Belmonte, E. Martin, E. C. Escudero-Adán, A. W. Kleij, *ChemSusChem* **2016**, *9*, 1304–1311.

[151] H. Zhou, H. Zhang, S. Mu, W.-Z. Zhang, W.-M. Ren, X.-B. Lu, *Green Chemistry* **2019**, *21*, 6335–6341.

[152] L. Longwitz, J. Steinbauer, A. Spannenberg, T. Werner, *ACS Catalysis* **2018**, *8*, 665–672.

[153] B. Yu, L.-N. He, *ChemSusChem* **2015**, *8*, 52–62.

[154] R. Yousefi, T. J. Struble, J. L. Payne, M. Vishe, N. D. Schley, J. N. Johnston, *Journal of the American Chemical Society* **2019**, *141*, 618–625.

[155] J. K. Mannisto, A. Sahari, K. Lagerblom, T. Niemi, M. Nieger, G. Sztanó, T. Repo, *Chemistry – A European Journal* **2019**, *25*, 10284–10289.

[156] M. Tamura, K. Noro, M. Honda, Y. Nakagawa, K. Tomishige, *Green Chemistry* **2013**, *15*, 1567.

[157] J. Hwang, D. Han, J. J. Oh, M. Cheong, H.-J. Koo, J. S. Lee, H. S. Kim, *Advanced Synthesis & Catalysis* **2019**, *361*, 297–306.

[158] G. Fiorani, W. Guo, A. W. Kleij, *Green Chemistry* **2015**, *17*, 1375–1389.

[159] M. Alves, B. Grignard, R. Mereau, C. Jerome, T. Tassaing, C. Detrembleur, *Catalysis Science & Technology* **2017**, *7*, 2651–2684.

[160] N. Liu, Y.-F. Xie, C. Wang, S.-J. Li, D. Wei, M. Li, B. Dai, *ACS Catalysis* **2018**, *8*, 9945–9957.

[161] R. R. Shaikh, S. Pornpraprom, V. D'Elia, *ACS Catalysis* **2018**, *8*, 419–450.

[162] J. W. Comerford, I. D. V. Ingram, M. North, X. Wu, *Green Chemistry* **2015**, *17*, 1966–1987.

[163] C. Martín, G. Fiorani, A. W. Kleij, *ACS Catalysis* **2015**, *5*, 1353–1370.

[164] T. M. McGuire, E. M. López-Vidal, G. L. Gregory, A. Buchard, *Journal of CO2 Utilization* **2018**, *27*, 283–288.

[165] G. L. Gregory, M. Ulmann, A. Buchard, *RSC Advances* **2015**, *5*, 39404–39408.

[166] M. Honda, M. Tamura, K. Nakao, K. Suzuki, Y. Nakagawa, K. Tomishige, *ACS Catalysis* **2014**, *4*, 1893–1896.

[167] T. Hirose, S. Shimizu, S. Qu, H. Shitara, K. Kodama, L. Wang, *RSC Advances* **2016**, *6*, 69040–69044.

[168] B. A. Vara, T. J. Struble, W. Wang, M. C. Dobish, J. N. Johnston, *Journal of the American Chemical Society* **2015**, *137*, 7302–7305.

[169] A. Hosseinian, S. Farshbaf, R. Mohammadi, A. Monfared, E. Vessally, *RSC Advances* **2018**, *8*, 17976–17988.

[170] C. J. Whiteoak, E. Martin, M. M. Belmonte, J. Benet-Buchholz, A. W. Kleij, *Advanced Synthesis & Catalysis* **2012**, *354*, 469–476.

[171] J. Rintjema, W. Guo, E. Martin, E. C. Escudero-Adán, A. W. Kleij, *Chemistry - A European Journal* **2015**, *21*, 10754–10762.

[172] B. R. Buckley, A. P. Patel, K. G. U. Wijayantha, *European Journal of Organic Chemistry* **2015**, *2015*, 474–478.

[173] D. J. Darensbourg, A. Horn Jr, A. I. Moncada, *Green Chemistry* **2010**, *12*, 1376.

[174] J. Vaitla, Y. Guttormsen, J. K. Mannisto, A. Nova, T. Repo, A. Bayer, K. H. Hopmann, *ACS Catalysis* **2017**, *7*, 7231–7244.

[175] B. D. W. Allen, C. P. Lakeland, J. P. A. Harrity, *Chemistry – A European Journal* **2017**, *23*, 13830–13857.

[176] G. L. Gregory, G. Kociok-Köhn, A. Buchard, *Polymer Chemistry* **2017**, *8*, 2093–2104.

[177] G. L. Gregory, L. M. Jenisch, B. Charles, G. Kociok-Köhn, A. Buchard, *Macromolecules* **2016**, *49*, 7165–7169.

[178] P. Brignou, J.-F. Carpentier, S. M. Guillaume, *Macromolecules* **2011**, *44*, 5127–5135.

[179] D. J. Darensbourg, A. I. Moncada, *Macromolecules* **2010**, *43*, 5996–6003.

[180] D. J. Darensbourg, A. I. Moncada, S.-H. Wei, *Macromolecules* **2011**, *44*, 2568–2576.

[181] M. Wadamoto, H. Yamamoto, *Journal of the American Chemical Society* **2005**, *127*, 14556–14557.

[182] G.-L. Chai, B. Zhu, J. Chang, *The Journal of Organic Chemistry* **2019**, *84*, 120–127.

[183] Y. Zhang, N. Li, N. Goyal, G. Li, H. Lee, B. Z. Lu, C. H. Senanayake, *The Journal of Organic Chemistry* **2013**, *78*, 5775–5781.

[184] J. Rintjema, R. Epping, G. Fiorani, E. Martín, E. C. Escudero-Adán, A. W. Kleij, *Angewandte Chemie International Edition* **2016**, *55*, 3972–3976.

[185] V. Laserna, E. Martin, E. C. Escudero-Adán, A. W. Kleij, *ACS Catalysis* **2017**, *7*, 5478–5482.

[186] S. Sopeña, M. Cozzolino, C. Maquilón, E. C. Escudero-Adán, M. Martínez Belmonte, A. W. Kleij, *Angewandte Chemie* **2018**, *130*, 11373–11377.

[187] R. Huang, J. Rintjema, J. González-Fabra, E. Martín, E. C. Escudero-Adán, C. Bo, A. Urakawa, A. W. Kleij, *Nature Catalysis* **2018**, *2*, 62–70.

[188] C. Maquilón, B. Limburg, V. Laserna, D. Garay-Ruiz, J. González-Fabra, C. Bo, M. Martínez Belmonte, E. C. Escudero-Adán, A. W. Kleij, *Organometallics* **2020**, *39*, 1642–1651.

[189] C. J. Whiteoak, N. Kielland, V. Laserna, E. C. Escudero-Adán, E. Martin, A. W. Kleij, *Journal of the American Chemical Society* **2013**, *135*, 1228–1231.

[190] C. J. Whiteoak, N. Kielland, V. Laserna, F. Castro-Gómez, E. Martin, E. C. Escudero-Adán, C. Bo, A. W. Kleij, *Chemistry - A European Journal* **2014**, *20*, 2264–2275.

[191] J.-D. Chai, M. Head-Gordon, *Physical Chemistry Chemical Physics* **2008**, *10*, 6615.

[192] R. Krishnan, J. S. Binkley, R. Seeger, J. A. Pople, *The Journal of Chemical Physics* **1980**, *72*, 650–654.

[193] A. D. McLean, G. S. Chandler, *The Journal of Chemical Physics* **1980**, *72*, 5639–5648.

[194] G. Hua, P. Olsén, J. Franzén, K. Odelius, *RSC Advances* **2018**, *8*, 39022–39028.

[195] G. L. Gregory, G. Kociok-Köhn, A. Buchard, *Polymer Chemistry* **2017**, *8*, 2093–2104.

[196] X.-B. Lu, W.-M. Ren, G.-P. Wu, *Accounts of Chemical Research* **2012**, *45*, 1721–1735.

[197] S. Paul, Y. Zhu, C. Romain, R. Brooks, P. K. Saini, C. K. Williams, *Chemical Communications* **2015**, *51*, 6459–6479.

[198] G. Trott, P. K. Saini, C. K. Williams, *Philosophical Transactions of the Royal Society A: Mathematical Physical and Engineering Sciences* **2016**, *374*, 20150085.

[199] X.-B. Lu, D. J. Darensbourg, *Chem. Soc. Rev.* **2012**, *41*, 1462–1484.

[200] B. Han, L. Zhang, H. Zhang, H. Ding, B. Liu, X. Wang, *Polymer Chemistry* **2016**, *7*, 4453–4457.

[201] R. C. Pratt, F. Nederberg, R. M. Waymouth, J. L. Hedrick, *Chem. Commun.* **2008**, 114–116.

[202] J. Chen, S. Kan, H. Xia, F. Zhou, X. Chen, X. Jiang, K. Guo, Z. Li, *Polymer* **2013**, *54*, 4177–4182.

[203] G. Kapiti, H. Keul, M. Möller, *Materials Today Communications* **2015**, *5*, 1–9.

[204] J.-C. Lee, M. H. Litt, *Macromolecules* **2000**, *33*, 1618–1627.

[205] F. He, Y.-P. Wang, G. Liu, H.-L. Jia, J. Feng, R.-X. Zhuo, *Polymer* **2008**, *49*, 1185–1190.

[206] H. R. Kricheldorf, J. Jenssen, *European Polymer Journal* **1989**, *25*, 1273–1279.

[207] M. Helou, O. Miserque, J.-M. Brusson, J.-F. Carpentier, S. M. Guillaume, *Advanced Synthesis & Catalysis* **2009**, *351*, 1312–1324.

[208] M. Helou, O. Miserque, J.-M. Brusson, J.-F. Carpentier, S. M. Guillaume, *Chemistry – A European Journal* **2008**, *14*, 8772–8775.

[209] P. Brignou, J.-F. Carpentier, S. M. Guillaume, *Macromolecules* **2011**, *44*, 5127–5135.

[210] P. Brignou, M. Priebe Gil, O. Casagrande, J.-F. Carpentier, S. M. Guillaume, *Macromolecules* **2010**, *43*, 8007–8017.

[211] F. Suriano, O. Coulembier, J. L. Hedrick, P. Dubois, *Polym. Chem.* **2011**, *2*, 528–533.

[212] D. Delcroix, B. Martín-Vaca, D. Bourissou, C. Navarro, *Macromolecules* **2010**, *43*, 8828–8835.

[213] J. Zhu, X. Luo, X. Li, *Polymers* **2023**, *15*, 720.

[214] H. Yang, M. Yan, S. Pispas, G. Zhang, *Macromolecular Chemistry and Physics* **2011**, *212*, 2589–2593.

[215] M. Azechi, K. Matsumoto, T. Endo, *Journal of Polymer Science Part A: Polymer Chemistry* **2013**, *51*, 1651–1655.

[216] A. T. Lonnecker, Y. H. Lim, K. L. Wooley, *ACS Macro Letters* **2017**, *6*, 748–753.

[217] M. Kawalec, A. P. Dove, L. Mespouille, P. Dubois, *Polym. Chem.* **2013**, *4*, 1260–1270.

[218] G. L. Gregory, M. Ulmann, A. Buchard, *RSC Advances* **2015**, *5*, 39404–39408.

[219] J. Matsuo, K. Aoki, F. Sanda, T. Endo, *Macromolecules* **1998**, *31*, 4432–4438.

[220] I. Nifant'ev, A. Shlyakhtin, V. Bagrov, B. Lozhkin, G. Zakirova, P. Ivchenko, O. Legon'kova, *Reaction Kinetics Mechanisms and Catalysis* **2016**, *117*, 447–476.

[221] I. Del Rosal, P. Brignou, S. M. Guillaume, J.-F. Carpentier, L. Maron, *Polymer Chemistry* **2011**, *2*, 2564.

[222] G. Rokicki, *Progress in Polymer Science* **2000**, *25*, 259–342.

[223] C. Maquilón, F. Della Monica, B. Limburg, A. W. Kleij, *Advanced Synthesis & Catalysis* **2021**, *363*, 4033–4040.

[224] G. Hua, J. Franzén, K. Odelius, *Macromolecules* **2019**, *52*, 2681–2690.

[225] C. A. DeRosa, A. M. Luke, K. Anderson, T. M. Reineke, W. B. Tolman, F. S. Bates, M. A. Hillmyer, *Macromolecules* **2021**, *54*, 5974–5984.

[226] Y. Dai, X. Zhang, *Polymer Chemistry* **2019**, *10*, 296–305.

[227] S. Venkataraman, J. L. Hedrick, Y. Y. Yang, *Polym. Chem.* **2014**, *5*, 2035–2040.

[228] M. Helou, O. Miserque, J.-M. Brusson, J.-F. Carpentier, S. M. Guillaume, *Chemistry – A European Journal* **2010**, *16*, 13805–13813.

[229] R. F. Storey, D. C. Hoffman, *Macromolecules* **1992**, *25*, 5369–5382.

[230] A. G. Patil, U. R. Kapadi, D. G. Hundiwale.

[231] K. Soga, Y. Tazuke, S. Hosoda, S. Ikeda, *Journal of Polymer Science: Polymer Chemistry Edition* **1977**, *15*, 219–229.

[232] R. Abdul-Karim, A. Hameed, M. I. Malik, *RSC Advances* **2017**, *7*, 11786–11795.

[233] R. Abdul-Karim, A. Hameed, M. I. Malik, *European Polymer Journal* **2018**, *105*, 95–106.

[234] J.-i. Kadokawa, Y. Iwasaki, H. Tagaya, *Macromolecular Rapid Communications* **2002**, *23*, 757–760.

[235] K. Tezuka, K. Komatsu, O. Haba, *Polymer Journal* **2013**, *45*, 1183–1187.

[236] W. Guerin, A. K. Diallo, E. Kirilov, M. Helou, M. Slawinski, J.-M. Brusson, J.-F. Carpentier, S. M. Guillaume, *Macromolecules* **2014**, *47*, 4230–4235.

[237] D. H. Lamparelli, A. Villar-Yanez, L. Dittrich, J. Rintjema, F. Bravo, C. Bo, A. W. Kleij, *Angewandte Chemie International Edition* **2023**, *62*, e202314659.

[238] W. Zhang, J. Dai, Y.-C. Wu, J.-X. Chen, S.-Y. Shan, Z. Cai, J.-B. Zhu, *ACS Macro Letters* **2022**, *11*, 173–178.

[239] Y.-C. Wu, H.-Z. Fan, W. Zhang, M.-Y. Wang, Z. Cai, J.-B. Zhu, *Macromolecules* **2022**, *55*, 9232–9241.

[240] S. Venkataraman, K. P. Mineart, V. M. Prabhu, J. L. Hedrick, Y. Y. Yang, *Polymer Chemistry* **2018**, *9*, 2434–2437.

[241] P. Bexis, J. De Winter, M. C. Arno, O. Coulembier, A. P. Dove, *Macromolecular Rapid Communications* **2021**, *42*, 2000378.

[242] F.-Y. Qiu, L. Yu, F.-S. Du, Z.-C. Li, *Macromolecular Rapid Communications* **2017**, *38*, 1700400.

[243] A. Y. Yuen, A. Bossion, A. Veloso, D. Mecerreyes, J. L. Hedrick, A. P. Dove, H. Sardon, *Polymer Chemistry* **2018**, *9*, 2458–2467.

[244] S. Venkataraman, V. W. L. Ng, D. J. Coady, H. W. Horn, G. O. Jones, T. S. Fung, H. Sardon, R. M. Waymouth, J. L. Hedrick, Y. Y. Yang, *Journal of the American Chemical Society* **2015**, *137*, 13851–13860.

[245] *Encyclopedia of Machine Learning*, (Eds.: C. Sammut, G. I. Webb), Springer US, Boston, MA, **2010**.

[246] Z. Abdel Baki, H. Dib, T. Sahin, *Polymers* **2022**, *14*, 2031.

[247] C. Jehanno, J. Demarteau, D. Mantione, M. C. Arno, F. Ruipérez, J. L. Hedrick, A. P. Dove, H. Sardon, *ACS Macro Letters* **2020**, *9*, 443–447.

[248] W. Guo, J. Gónzalez-Fabra, N. A. G. Bandeira, C. Bo, A. W. Kleij, *Angewandte Chemie* **2015**, *127*, 11852–11856.

[249] S. Sopeña, V. Laserna, W. Guo, E. Martin, E. C. Escudero-Adán, A. W. Kleij, *Advanced Synthesis & Catalysis* **2016**, *358*, 2172–2178.

[250] A. J. Kamphuis, F. Picchioni, P. P. Pescarmona, *Green Chemistry* **2019**, *21*, 406–448.

[251] R. P. Brannigan, A. Walder, A. P. Dove, *Journal of Polymer Science Part A: Polymer Chemistry* **2014**, *52*, 2279–2286.

[252] J. Ni, M. Lanzi, D. H. Lamparelli, A. W. Kleij, *Polymer Chemistry* **2023**, *14*, 4748–4753.

[253] T. Endo, K. Kakimoto, B. Ochiai, D. Nagai, *Macromolecules* **2005**, *38*, 8177–8182.

[254] R. L. Snyder, D. J. Fortman, G. X. De Hoe, M. A. Hillmyer, W. R. Dichtel, *Macromolecules* **2018**, *51*, 389–397.

[255] N. Yadav, F. Seidi, D. Crespy, V. D'Elia, *ChemSusChem* **2019**, *12*, 724–754.

[256] G. Fiorani, W. Guo, A. W. Kleij, *Green Chemistry* **2015**, *17*, 1375–1389.

[257] T. Weidlich, B. Kamenická, *Catalysts* **2022**, *12*, 298.

[258] Z. Guo, Y. Hu, S. Dong, L. Chen, L. Ma, Y. Zhou, L. Wang, J. Wang, *Chem Catalysis* **2022**, *2*, 519–530.

[259] W. Guo, J. E. Gómez, À. Cristòfol, J. Xie, A. W. Kleij, *Angewandte Chemie International Edition* **2018**, *57*, 13735–13747.

[260] J.-Q. Wang, K. Dong, W.-G. Cheng, J. Sun, S.-J. Zhang, *Catalysis Science & Technology* **2012**, *2*, 1480.

[261] X. Li, A. Villar-Yanez, C. Ngassam Tounzoua, J. Benet-Buchholz, B. Grignard, C. Bo, C. Detrembleur, A. W. Kleij, *ACS Catalysis* **2022**, *12*, 2854–2860.

[262] C. Ngassam Tounzoua, B. Grignard, C. Detrembleur, *Angewandte Chemie International Edition* **2022**, *61*, e202116066.

[263] Q.-W. Song, B. Yu, X.-D. Li, R. Ma, Z.-F. Diao, R.-G. Li, W. Li, L.-N. He, *Green Chemistry* **2014**, *16*, 1633.

[264] M. J. Ajitha, C. H. Suresh, *Tetrahedron Letters* **2011**, *52*, 5403–5406.

[265] X.-F. Liu, Q.-W. Song, S. Zhang, L.-N. He, *Catalysis Today* **2016**, *263*, 69–74.

[266] K. Zheng, Y. Wu, Z. Hu, S. Wang, X. Jiao, J. Zhu, Y. Sun, Y. Xie, *Chemical Society Reviews* **2023**, *52*, 8–29.

[267] A. O. C. Iroegbu, S. S. Ray, V. Mbarane, J. C. Bordado, J. P. Sardinha, *ACS Omega* **2021**, *6*, 19343–19355.

[268] T. P. Haider, C. Völker, J. Kramm, K. Landfester, F. R. Wurm, *Angewandte Chemie International Edition* **2019**, *58*, 50–62.

[269] G. W. Coates, Y. D. Y. L. Getzler, *Nature Reviews Materials* **2020**, *5*, 501–516.

[270] M. R. Johansen, T. B. Christensen, T. M. Ramos, K. Syberg, *Journal of Environmental Management* **2022**, *302*, 113975.

[271] J.-G. Rosenboom, R. Langer, G. Traverso, *Nature Reviews Materials* **2022**, *7*, 117–137.

[272] M. Bachmann, C. Zibunas, J. Hartmann, V. Tulus, S. Suh, G. Guillén-Gosálbez, A. Bardow, *Nature Sustainability* **2023**, *6*, 599–610.

[273] C. Li, L. Wang, Q. Yan, F. Liu, Y. Shen, Z. Li, *Angewandte Chemie International Edition* **2022**, *61*, e202201407.

[274] B. A. Abel, R. L. Snyder, G. W. Coates, *Science* **2021**, *373*, 783–789.

[275] H. G. Hester, B. A. Abel, G. W. Coates, *Journal of the American Chemical Society* **2023**, *145*, 8800–8804.

[276] D. T. Sheppard, K. Jin, L. S. Hamachi, W. Dean, D. J. Fortman, C. J. Ellison, W. R. Dichtel, *ACS Central Science* **2020**, *6*, 921–927.

[277] J. Xu, E. Feng, J. Song, *Journal of Applied Polymer Science* **2014**, *131*, app.39822.

[278] T. Artham, M. Doble, *Macromolecular Bioscience* **2008**, *8*, 14–24.

[279] W. Yu, E. Maynard, V. Chiaradia, M. C. Arno, A. P. Dove, *Chemical Reviews* **2021**, *121*, 10865–10907.

[280] R. P. Brannigan, A. P. Dove, *Biomaterials Science* **2017**, *5*, 9–21.

[281] S. Paul, Y. Zhu, C. Romain, R. Brooks, P. K. Saini, C. K. Williams, *Chemical Communications* **2015**, *51*, 6459–6479.

[282] X.-B. Lu, W.-M. Ren, G.-P. Wu, *Accounts of Chemical Research* **2012**, *45*, 1721–1735.

[283] G. A. Bhat, D. J. Darensbourg, *Green Chemistry* **2022**, *24*, 5007–5034.

[284] D. J. Darensbourg, *Chemical Reviews* **2007**, *107*, 2388–2410.

[285] S. Klaus, M. W. Lehenmeier, C. E. Anderson, B. Rieger, *Coordination Chemistry Reviews* **2011**, *255*, 1460–1479.

[286] M. I. Childers, J. M. Longo, N. J. Van Zee, A. M. LaPointe, G. W. Coates, *Chemical Reviews* **2014**, *114*, 8129–8152.

[287] O. Hauenstein, M. Reiter, S. Agarwal, B. Rieger, A. Greiner, *Green Chemistry* **2016**, *18*, 760–770.

[288] C. Li, R. J. Sablong, C. E. Koning, *Angewandte Chemie International Edition* **2016**, *55*, 11572–11576.

[289] M. Reiter, S. Vagin, A. Kronast, C. Jandl, B. Rieger, *Chemical Science* **2017**, *8*, 1876–1882.

[290] L. Peña Carrodeguas, J. González-Fabra, F. Castro-Gómez, C. Bo, A. W. Kleij, *Chemistry - A European Journal* **2015**, *21*, 6115–6122.

[291] C. Martín, A. W. Kleij, *Macromolecules* **2016**, *49*, 6285–6295.

[292] F. Auriemma, C. De Rosa, M. R. Di Caprio, R. Di Girolamo, W. C. Ellis, G. W. Coates, *Angewandte Chemie International Edition* **2015**, *54*, 1215–1218.

[293] O. Hauenstein, S. Agarwal, A. Greiner, *Nature Communications* **2016**, *7*, 11862.

[294] N. Kindermann, À. Cristòfol, A. W. Kleij, *ACS Catalysis* **2017**, *7*, 3860–3863.

[295] C. Li, R. J. Sablong, C. E. Koning, *European Polymer Journal* **2015**, *67*, 449–458.

[296] S. Brooks, D. Merckle, A. C. Weems, *ACS Sustainable Chemistry & Engineering* **2023**, *11*, 10252–10263.

[297] S. Neumann, L.-C. Leitner, H. Schmalz, S. Agarwal, A. Greiner, *ACS Sustainable Chemistry & Engineering* **2020**, *8*, 6442–6448.

[298] V. Bonamigo Moreira, J. Rintjema, F. Bravo, A. W. Kleij, L. Franco, J. Puiggalí, C. Alemán, E. Armelin, *ACS Sustainable Chemistry & Engineering* **2022**, *10*, 2708–2719.

[299] L. P. Carrodeguas, T. T. D. Chen, G. L. Gregory, G. S. Sulley, C. K. Williams, *Green Chemistry* **2020**, *22*, 8298–8307.

[300] T. Stößer, C. Li, J. Unruangsri, P. K. Saini, R. J. Sablong, M. A. R. Meier, C. K. Williams, C. Koning, *Polymer Chemistry* **2017**, *8*, 6099–6105.

[301] A. Brandolese, F. Della Monica, M. À. Pericàs, A. W. Kleij, *Macromolecules* **2022**, *55*, 2566–2573.

[302] C. Li, R. J. Sablong, R. A. T. M. Van Benthem, C. E. Koning, *ACS Macro Letters* **2017**, *6*, 684–688.

[303] W. C. Ellis, Y. Jung, M. Mulzer, R. Di Girolamo, E. B. Lobkovsky, G. W. Coates, *Chemical Science* **2014**, *5*, 4004.

[304] D. J. Darensbourg, S.-H. Wei, A. D. Yeung, W. C. Ellis, *Macromolecules* **2013**, *46*, 5850–5855.

[305] D. J. Darensbourg, S.-H. Wei, S. J. Wilson, *Macromolecules* **2013**, *46*, 3228–3233.

[306] Y. Liu, H. Zhou, J.-Z. Guo, W.-M. Ren, X.-B. Lu, *Angewandte Chemie International Edition* **2017**, *56*, 4862–4866.

[307] F. N. Singer, A. C. Deacy, T. M. McGuire, C. K. Williams, A. Buchard, *Angewandte Chemie International Edition* **2022**, *61*, e202201785.

[308] A. K. Diallo, E. Kirillov, M. Slawinski, J.-M. Brusson, S. M. Guillaume, J.-F. Carpentier, *Polymer Chemistry* **2015**, *6*, 1961–1971.

[309] M. Kawamoto, Y. Mori, A. Tsuge, T. Endo, *Journal of Polymer Science* **2022**, *60*, 1416–1421.

[310] W. Guo, J. Gónzalez-Fabra, N. A. G. Bandeira, C. Bo, A. W. Kleij, *Angewandte Chemie International Edition* **2015**, *54*, 11686–11690.

[311] S. Sopeña, V. Laserna, W. Guo, E. Martin, E. C. Escudero-Adán, A. W. Kleij, *Advanced Synthesis & Catalysis* **2016**, *358*, 2172–2178.

UNIVERSITAT ROVIRA I VIRGILI
COMPUTATIONAL INSIGHTS OF CATALYTIC CARBON DIOXIDE VALORIZATION AND CIRCULAR RECYCLING PROCESSES
Alba Villar Yanez

UNIVERSITAT
ROVIRA i VIRGILI